

Wire Flame Sprayed Aluminium Coatings onto Polymer and CFRP Substrates

Thesis submitted to the

University of Nottingham

for the degree of

Doctor of Philosophy

Geoffrey Lunn, MEng

Faculty of Engineering

University of Nottingham

November 2017

Preface

This thesis is submitted for the degree of Doctor of Philosophy at the University of Nottingham.

The research work was carried out under the supervision of Professor D.G. McCartney of the University of Nottingham and Dr M.A. Riley of TWI Ltd within the Faculty of Engineering, University of Nottingham and TWI Ltd.

It hereby certify that the work presented in this thesis is original, and suitable references are made to any work cited from the literature

Signed: _____ Date: _____

The following paper was pubished based on chapter 4 of this thesis:

G. D. Lunn, M. A. Riley, and D. G. McCartney, "A study of wire breakup and in-flight particle behavior during wire flame spraying of aluminum," Journal of Thermal Spray Technology, Sep 2017. [Online]. Available: https://doi.org/10.1007/s11666-017-0639-1

Abstract

Fibre reinforced polymer matrix composites (FRPs) are used in an increasing number of applications because of their attractive mechanical properties such as high specific strength and stiffness. However, for a number of applications, enhanced surface properties such as thermal and electrical conductivity and resistance to wear are required. Thermal spray coatings have the potential to be a technically suitable and cost effective means of achieving these surface properties. This thesis is a systematic study of the deposition of wire flame sprayed (WFS) pure aluminium onto two different carbon fibre reinforced polymer (CFRP) substrates; one epoxy and one PEEK based as well as unreinforced epoxy, PEEK and steel substrates.

The work investigates the following aspects: (i) characterisation of the flame spray plume; (ii) formation of splats on polymer and CFRP; (iii) how surface preparation (grit blasting), affects the surface features of PEEK and epoxy polymers and their respective CFRPs; (iv) the development of thick wire flame sprayed aluminium coatings deposited onto FRPs and the resultant adhesion between coating and substrate.

Particle diagnostic techniques as well as physical collection of in-flight particles were used to characterise the WFS plume. In order for the diagnostic system to detect the particles, external lighting was required, indicating that the particles were at temperatures of <1000°C. The particles detected by the system were shown to be travelling at high velocities $\approx$ 250 – 300 m.s^{-1}, 50 – 200 m.s^{-1} faster than most previous literature would suggest. Collection of the particles from the plume indicated that the particle diameters were log-normally distributed with a mean diameter of $\approx$ 25 µm. However, the particle diagnostic system could not detect particles $\lessapprox$45 µm, and thus only the largest particles in the plume could be characterised in terms of size and velocity. Overall, wire flame spraying generates a surprisingly stable particle stream.

Wipe tests, where isolated particles are deposited onto a substrate, were performed. The different splat characteristics on polymer, CFRP and metallic substrates were compared in both a qualitative and semi-quantitative manner. The splat morphology showed

that the particles deposited onto the substrates were molten on impact, and thus > 660℃. Splats deposited onto the polymer and CFRP substrates had large bulbous regions at their centre, due to gas evolution at the substrate interface and this limited the effective bonding area. Is postulated that bubbles could explode and formed ring shaped splats. This latter splat type was more prevalent on the epoxy based substrates, indicating a greater tendency for gas evolution on these substrates.

The different substrates were subjected to either a light or heavy grit-blast (LGB or HGB), and the surfaces characterised. The epoxy substrate was only slightly roughened and the damage induced was indicative of a brittle substrate, with material loss due to crack propagation. In contrast, grit-blasting of the PEEK substrate significantly roughened the surface via extensive plastic deformation. Finally, the CFRP substrates were extensively roughened by the grit-blasting process, exposing fibres and creating a distinctive bi-modal height distribution on the surface with deep valleys created due to the extensive loss of carbon fibres and high resin ridges left due to the resilience of the matrix.

WFS aluminium coatings were sprayed onto the different substrates with smooth, LGB and HGB surfaces. These experiments enabled pull-off adhesion tests to be conducted which showed clear differences between different sample types and surface preparations with results ranging from 1 MPa for as received CF-epoxy to 17.5 MPa for lightly grit-blasted CF-PEEK. The thermoplastic PEEK substrates typically had greater adhesion than the epoxy based ones and well adhered coatings could be deposited even onto smooth PEEK based substrates. The fracture face of substrates obtained from pull off tests showed structures indicative of local melting and flow in the case of thermoplastic PEEK which may account for the greater adhesion. Sectioned samples showed that there was extensive local interfacial cracking when fibres came into contact with the coating, indicating that the polymer phase has better coating adhesion than the fibre phase. Despite this, the FRP substrates typically had better coating adhesion than the polymer ones. It is believed that this is due to the significantly rougher surface of the FRP substrates.

Acknowledgements

I want to sincerely thank my supervisors Graham McCartney and Melissa Riley for their continued assistance, advice and patience throughout the research and writing up period. I would also like to acknowledge and thank Andy Tabecki, Gary Muggridge and Damian Whiteman for their advice and assistance in preparing samples.

This work was supported by the Engineering and Physical Sciences Research Council [grant number EP/L50502X/1 to the University of Nottingham] through an EPSRC Industrial CASE PhD studentship to G. D. Lunn. The project received additional sponsorship and support from TWI Ltd. It was enabled through, and undertaken at, the National Structural Integrity Research Centre (NSIRC), a postgraduate engineering facility for industry-led research into structural integrity established and managed by TWI Ltd through a network of both national and international Universities.

Contents

1 Introduction **1**

1.1 Introduction 1

2 Literature Review **5**

2.1 Introduction 5

2.2 Overview of thermal spray processes 6

2.2.1 Flame spray (FS) 7

2.2.2 Twin Wire Arc Spray (TWAS) 7

2.2.3 Plasma Spray (PS) 8

2.2.4 High Velocity Oxy-Fuel (HVOF) spraying 9

2.2.5 Cold Spray (CS) 9

2.3 Splat deposition 10

2.3.1 Introduction 10

2.3.2 Factors affecting splat type 12

2.4 Coating assessment - adhesion tests 18

2.4.1 General 18

2.4.2 Tensile adhesion tests 18

2.5 Residual stresses 20

2.5.1 Introduction 20

2.5.2 CTE mismatch 21

2.5.3 Quenching 21

2.5.4 Peening 22

2.6 Review of polymer composite materials 22

2.6.1 Introduction 22

2.6.2 Polymeric matrix phase 23

2.6.3 Reinforcement phase 25

2.6.4 Composite manufacture 26

2.7 Thermal spray onto polymers and fibre reinforced polymer composite materials . . . 27
2.7.1 Introduction . . . 27
2.7.2 Flame spray . . . 27
2.7.3 TWAS . . . 28
2.7.4 Plasma spray . . . 30
2.7.5 HVOF spraying . . . 34
2.7.6 Cold spraying . . . 34
2.7.7 Discussion of literature regarding thermal spraying onto FRP composites . . . 35
2.8 Literature review conclusions . . . 39

3 Experimental Methods **41**
3.1 Introduction . . . 41
3.2 Materials . . . 41
3.2.1 Substrate . . . 41
3.2.2 Wire feedstock . . . 45
3.3 Grit-blasting . . . 45
3.4 Wire flame spraying . . . 46
3.5 Wipe tests . . . 46
3.6 Metallographic preparation . . . 47
3.7 Optical microscopy . . . 48
3.8 Scanning Electron Microscopy (SEM) . . . 48
3.9 Focus variation microscopy (FVM) . . . 49
3.9.1 Roughness parameters . . . 50
3.9.2 Spacing parameters . . . 52
3.9.3 3-dimentional roughness parameters . . . 52

4 Wire Breakup and Particle Behaviour in Wire Flame Spray **53**
4.1 Introduction . . . 53
4.1.1 Literature review . . . 53
4.2 Objectives . . . 59
4.3 Approach . . . 60
4.4 Experimental methods . . . 60
4.4.1 Materials . . . 60
4.4.2 Wire flame spraying conditions . . . 61

4.4.3 Particle diagnostics . . . 61
4.4.4 Wire breakup analysis . . . 62
4.4.5 Particle collection . . . 63
4.4.6 Characterisation and quantification of particles . . . 63
4.5 Results . . . 64
4.5.1 Wire breakup . . . 64
4.5.2 In-flight particle measurements . . . 67
4.5.3 Heat input . . . 71
4.5.4 Wipe tests . . . 73
4.5.5 Collected particles . . . 73
4.6 Discussion . . . 75
4.6.1 Wire breakup/atomisation . . . 75
4.6.2 Number of detected particles . . . 77
4.6.3 Particle velocities . . . 77
4.7 Conclusions . . . 82

5 Splat Substrate Interaction **84**
5.1 Introduction . . . 84
5.2 Objectives . . . 84
5.3 Approach . . . 84
5.4 Experimental methods . . . 85
5.4.1 Substrate materials . . . 85
5.4.2 Wipe tests . . . 85
5.4.3 Analysis . . . 86
5.5 Results . . . 86
5.5.1 Overview of splat types . . . 86
5.5.2 Metallic substrates . . . 86
5.5.3 Un-abraded / polished polymers . . . 90
5.5.4 Roughened FRPs . . . 104
5.5.5 Reinforcement fibres . . . 104
5.6 Discussion . . . 108
5.6.1 General description/Flattening behaviour . . . 108
5.6.2 Morphology . . . 109
5.6.3 Gas formation mechanism . . . 110
5.6.4 Substrate features following splat removal . . . 112
5.6.5 Abraded CFRPs . . . 113

5.7 Conclusions 114

6 Effect of Surface Preparation on Metallic and Non-Metallic Substrates 116

6.1 Introduction 116

6.2 Literature Review 117

6.2.1 Characterising monolithic materials - Roughness parametrisation . 117

6.2.2 Relationship between roughness and coating adhesion 117

6.2.3 Surface preparation of polymers and FRPs 118

6.2.4 Solid particle erosion 118

6.2.5 Literature review summary 121

6.3 Motivation 122

6.4 Objective 122

6.5 Approach 122

6.6 Experimental methods 123

6.6.1 Substrate materials 123

6.6.2 Surface preparation 123

6.6.3 Surface characterisation / analysis 123

6.7 Results 124

6.7.1 Characterisation of substrates prior to treatment 124

6.7.2 Effect of grit-blasting 127

6.8 Discussion 142

6.9 Conclusions 148

7 Deposited Coatings 150

7.1 Introduction 150

7.2 Objective 151

7.3 Approach 151

7.4 Experimental methods 151

7.4.1 Substrate materials 151

7.4.2 Sample tests processing 152

7.5 Results 154

7.5.1 Coating thickness and weights 154

7.5.2 Tensile adhesion tests 155

7.5.3 Coating characterisation 159

7.6 Discussion 184

7.6.1 Introduction 184

7.6.2 Coating development . . . 185
7.6.3 Coating development model . . . 190
7.7 Conclusions . . . 191

8 Conclusions **193**
8.1 Wire flame spray plume . . . 193
8.2 Interaction of individual splats with the substrate . . . 194
8.3 Effect of grit blasting on substrate surfaces . . . 195
8.4 The adhesion strength and structure of multi-pass thick coatings . . . 195

9 Further work **197**

A Data sheets **219**

B Comparing contact and non-contact profilometry **225**
B.1 Introduction . . . 225
B.2 Experimental method . . . 225
B.2.1 Materials . . . 225
B.2.2 Methods . . . 225
B.3 Results and Discussion . . . 226
B.4 Conclusions . . . 226

C TWAS onto CF-epoxy composite **229**
C.1 Introduction . . . 229
C.2 Experimental method . . . 229
C.3 Results . . . 229

List of Tables

3.1 Published materials data for the CF-Epoxy composite used in this investigation (Tencate E722) [117] 42

3.2 Published materials data for CF-PEEK composite used in this investigation (TenCate Certex® TC1200) [118] 43

3.3 Published material data from epoxy technical data sheet (Easy composites EL2) [119] 44

3.4 Published material data from PEEK technical data sheet (Direct plastics) [120] 44

3.5 Grit-blasting parameters used throughout this investigation. Light grit-blast and heavy grit-blast parameters are typically referred to by their acronyms LGB and HGB respectively. 45

3.6 Baseline wire flame spray settings used for spraying throughout the study, where these are deviated from it is clearly noted 46

3.7 Different roughness parameters (from BS EN ISO 4287:1998) [127] 51

4.1 Effect of atomizing gas flow rate on particle velocity 69

4.2 Summary of particle velocities, diameters and number of detected particles at 160 mm stand-off distance for measurements at the beginning and end of three separate spray measurement sessions 69

5.1 Proportions of different splat types on each substrate material 87

5.2 Mean splat diameter (X) and standard deviation (σ) of the different splat morphologies on different (polished/as received) substrates 87

5.3 Percentage of splats which contain bulbous regions on different substrates with different morphologies 88

5.4 Percentage of splats which contain holes on different substrates with different morphologies 89

6.1 Different roughness parameters (from BS EN ISO 4287:1998 [127]) 117
6.2 Selected 2D roughness parameters of untreated substrates 124
6.3 Summary of carbon fibre cross section analysis showing the average minimum and maximum resin thickness showing that CF-PEEK has a greater range of resin thickness 127
6.4 Mass loss of grit-blasted samples (negative mass loss represents mass gain) Non reinforced epoxy samples had a different geometry 127
6.5 Selected 2D and 3D roughness parameter of unreinforced substrates . . . 129
6.6 Selected 2D and 3D roughness parameters of LGB and HGB carbon fibre reinforced polymers 139

7.1 Coating thickness measurements of WFS Al coatings on different substrates and preparations (Mean value from multiple measurements) 154
7.2 Coating mass measurements of WFS Al coatings on different substrates and preparations. Where single/few samples were tested, statistics are not included 154
7.3 Measured tensile adhesion strength for WFS Al coatings on the different substrates and preparations 156

List of Abbreviations

APS	Atmospheric plasma spray
BSE	Backscattered electron
CAPS	Controlled atmosphere plasma spray
CCD	Charged couple device
CF	Carbon fibre
CFR	Carbon fibre reinforced
CFRP	Carbon fibre reinforced polymers
CS	Cold spray
CTE	Coefficient of thermal expansion
CVD	Chemical vapour deposition
EDX	Energy dispersive X-ray spectroscopy
EMI	Electromagnetic interference
FEA	Finite element analysis
FIB	Focused ion beam
FRP	Fibre reinforced polymer
FS	Flame spray
FVM	Focus variation microscopy
GF	Glass fibre
GFRP	Glass fibre reinforced polymer
HGB	Heavy grit-blast
HVOF	High velocity oxygen fuel
IMS	Industrial mentholated spirit
L2V	Two focus velocimetry
LDA	Laser Doppler anemometry
LGB	Light grit-blast
PAN	Polyacrylonitrile
PEAK	polyaryl ether ketone
PEEK	Polyether ether ketone

PFS	Powder flame spray
PIV	Particle image velocimetry
PPS	Polyphenylene sulfide
PSV	Particle streak velocimetry
PVD	Physical vapour deposition
TAT	Tensile adhesion test
TBC	Thermal barrier coating
Tg	Glass transition temperature
TGA	Thermo-gravimetric analysis
Tm	Melting temperature
TS	Thermal spray
Tt	Transition temperature
TWAS	Twin wire arc spray
TWP	Two wavelength pyrometery
VPS	Vacuum plasma spray
WFS	Wire flame spray

Chapter 1

Introduction

1.1 Introduction

Fibre reinforced polymers (FRPs) - commonly referred to as composites - are being used in increasing quantities in many structural applications. For example, the rapid increase in their use in aircraft is illustrated in figure 1.1 [1]. This is because they can be designed and made to have extremely useful engineering properties. They can be extremely strong and stiff, typical tensile strength and elastic modulus values of unidirectional carbon fibre epoxy composites are 1260 MPa and 200 GPa respectively [2, p. 38]. These values compare very well with structural steels; however FRPs will typically have much lower densities, thus through their use significant weight savings can be achieved. In addition to these benefits FRPs are corrosion resistant and can be designed to be anisotropic, thus the material can be designed to have specific properties in different orientations, to match the components loading. There is a trend within many industries including the automotive and aerospace to replace metallic components with composite ones.

Despite the benefits of FRP components, there are several issues stopping their adoption in certain applications. FRPs have poor wear resistance compared with metallic materials [3]. They also have a low tolerance to heat, even some of the most heat tolerant FRPs – polyimides – can only work up to ≈ 315℃. These properties limit FRP use in high temperature or high erosion environments [4].

Protective coatings can potentially alleviate the above problems. Wear is predominantly a function of the surface of the component, so by adding a well adhered wear resistant coating, the composite's performance can be improved. The thermal tolerance of the material cannot be increased through the addition of a coating. However, a low thermal conductivity thermal barrier coating (e.g. zirconia) in conjunction with other

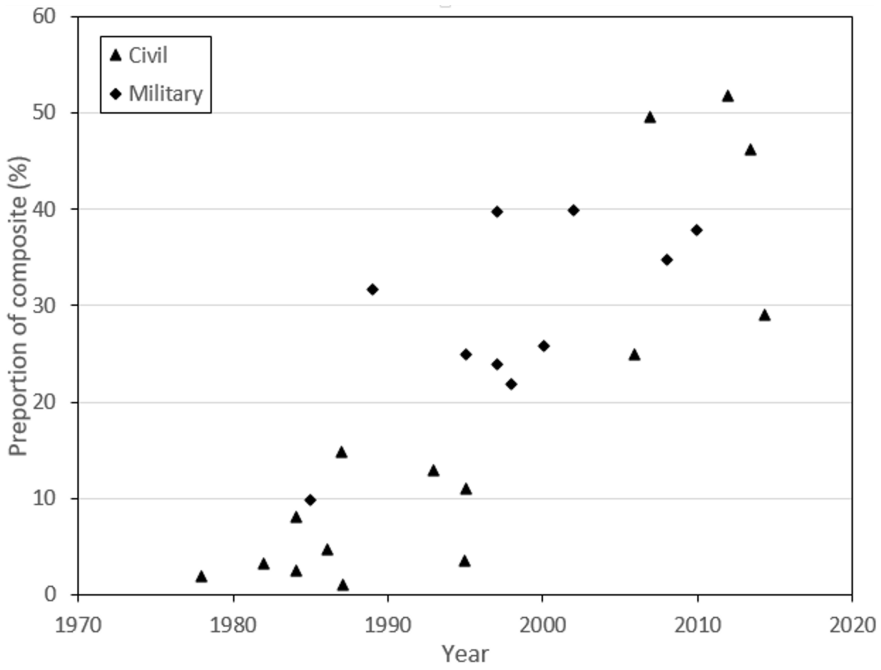


Figure 1.1: Plot showing the increasing proportion of composite materials used in different aircraft [1]

thermal management techniques (e.g. active cooling) can be used to extend the maximum service temperatures of FRP components. This approach is used successfully on metallic components with thermal barrier coatings (TBCs) being used in commercial aircraft engines since the early 1980s [5]. Coatings can also be used to add specialist properties to composite components. Aluminium has been sprayed on composites to add electrical conductivity [6] and for Electro-Magnetic Interference (EMI) shielding [7]. Thermal spray has also been suggested as a way of adding lightning strike protection to composite airframes [8].

There are many different methods to coat polymer based components; these include electroplating, PVD, CVD and thermal spray. Thermal spray is seen as a good method to coat FRPs as it is an economical process and is capable of coating non-conductive surfaces. Thermal spray involves propelling high temperature droplets of the coating material onto the component. These droplets adhere and build up to form a cohesive coating on the surface of the substrate. The droplets are heated and accelerated by different means depending on the type and specifics of the thermal spray technique.

TWI were the industrial sponsor of this project, providing funding, expertise and equipment. TWI has been actively researching and developing thermal spray coatings, including coating onto FRPs. They have expertise in the field as well as a full suite of thermal spray facilities, including Powder Flame Spray (PFS), Wire Flame Spray (WFS), High Velocity Oxy-Fuel (HVOF), Twin Wire Arc Spray (TWAS), Atmospheric Plasma

Spray (APS) and Cold Spray (CS).

The experimental trials in this thesis are primarily concerned with WFS of aluminium onto CFRP substrates. Low melting temperature thermal spray coatings, such as aluminium and zinc alloys, can been used to produce bond coats on FRPs. These low temperature bond coats cause limited thermal input into the substrate; act as an effective surface for another thermal spray coating to adhere to; and protect the temperature sensitive substrate from the high temperatures of the subsequent coating. These subsequent coatings are likely to be thermal barrier coatings (e.g. yttria stabilized zirconia) or wear resistant coatings (e.g. tungsten carbide cobalt) which would allow composite components (e.g. aero-engine bypass vane [4]) to be used in hotter or more erosive environments. Aluminium also has specific applications in its own right e.g. to increase thermal conductivity, electrical conductivity and Electro-Magnetic Interference (EMI) shielding. The bond strength is known to vary between spray processes, substrate material, surface conditions and spray parameters. However, the bond strength of the above, as with all thermally sprayed coatings onto FRPs, is low.

This project is primarily focused on understanding the adhesion mechanisms for successfully deposited coatings on FRP substrates, specifically:

- How thermal spray particles interact with FRP substrates
- What substrate conditions promote adhesion

This thesis is primarily concerned with Wire Flame Spraying (WFS) aluminium. Initially the properties of the WFS plume were investigated to understand its dynamics and the properties of the particles within it. Then the WFS gun was used to deposit onto variously prepared substrates including steel; thermoplastic and thermosetting polymers; fibres and composite materials. Properties of thermal spray splats and coatings were investigated as well as the failure mechanisms

The thesis is structured around this narrative and thus is it set out in the following chapters:

Literature review This chapter gives a general introduction to thermal spray and highlights previous investigations into thermally spraying onto FRPs.

Experimental methods This chapter introduces and describes the general experimental methods used in different parts of this thesis. Some specific techniques used in a particular investigations are outlined in their respective chapters.

Plume measurement This chapter documents investigations carried out into the properties of the wire flame spray plume.

Splat substrate interaction This chapter documents a series of wipe tests carried out using a custom jig. Isolated splats of aluminium were deposited onto a variety of difference substrates, the distribution, shape and microstructure are investigated.

Effect of surface preparation on substrate materials This chapter documents how the specific materials were affected by the preparation method (grit-blasting). It also documents in detail the surface properties of the substrates prior to thermal spray.

Deposited coatings This chapter documents spraying of coatings onto the various substrates with different surface preparations. It investigates the microstructure of the coatings and the adhesion strength obtained in each case. It investigates the fracture faces of the failed the coatings to glean information about the failure and adhesion mechanisms. The discussion in this chapter draws together many insights from previous chapters to create a model of how thermal spray coatings adhere to FRP materials and explain the mechanism for the observed results.

Chapter 2

Literature Review

2.1 Introduction

As stated in chapter 1, thermally sprayed coatings on CFRP substrates are not completely novel, and several such coatings have been used in specialist applications e.g. [9]. However, there is little work on this topic in the open literature and, what there is, is fragmented and not systematic. This literature review seeks to bring together this fragmented work and put it together to form a body of knowledge encompassing what is known about the topic. In order to do this, relevant studies are outlined and then common themes are brought out, establishing the state of the knowledge. Gaps in the knowledge are then identified, which the rest of the thesis will try to address. However, before doing this, it is important to first discuss thermal spray technologies more generally as well as briefly discuss composite materials. Thus, this literature review is broken into several sections:

- Overview of thermal spray techniques
- Overview of thermal spray coating properties (splat deposition, adhesion tests and residual stresses)
- Overview of composite materials
- Précis of the previous investigations in the literature
- Discussion of themes within the previous studies

2.2 Overview of thermal spray processes

Thermal spray (TS) is a term for a collection of similar coating processes. In these processes, precursor material - termed feedstock - is heated, atomised (if it is not already a powder) and accelerated toward a substrate material. The feedstock material is generally in the form of powder or a wire. In either case, the accelerated precursor material is in the form of small (generally 5 - 100 µm) molten or semi-molten droplets as it impacts on the substrate. These droplets impinge on the substrate, deform, cool and solidify. Multiple layers of these droplets are built up by successive passes of the thermal spray gun to form a coating. This can vary in thickness from tens of microns to several millimetres thick. The adhesion mechanism between the droplets and the substrate depends on the system, but it can be mechanical (i.e. due to keying), physical (i.e. due to secondary bonding) and/or metallurgical (i.e. due to chemical bonding or diffusion) [10, p. 129].

Due to the method of manufacture, TS coatings will typically have some level of porosity, oxide content (if metallic or cermet) and residual stress. The porosity is a result of the rapid cooling and the nature of coating formation through splat build up. It can be as high as 15% [11] in some TS coatings but in others can be as low as $\approx 1\%$. The oxide content is a result of the small feedstock particles being at elevated temperature whilst typically being exposed to oxygen. There are several reasons for residual stresses being formed within the coatings, concerned chiefly the rapid cooling and differences in themophysical properties between the coating and substrate material, these are discussed in greater detail in section 3. The extent to which these features occur is in part a function of which particular TS process is used to deposit the coating. The main types of thermal spray processes are:

- Flame spraying (FS)
- Twin wire arc spraying (TWAS)
- Plasma spraying (PS)
- High velocity oxy-fuel (HVOF) Spraying
- Cold spraying (CS)

The different types of thermal spray processes are generally classified depending on the method of particulate heating, and have different capabilities; some details of the different systems are described in the following sections.

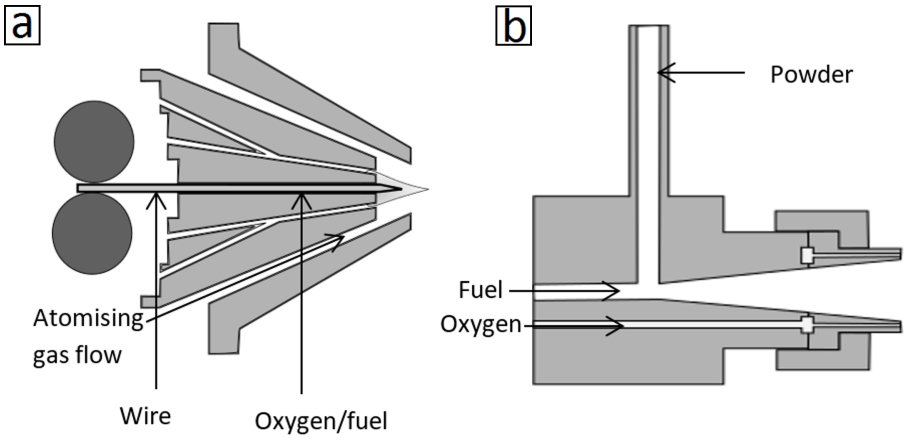


Figure 2.1: Simplified schematic of flame spray processes (a) wire fed, (b) powder fed

2.2.1 Flame spray (FS)

In FS the heat is provided by an oxygen-fuel flame burning at the tip of the nozzle, fuel gases typically used are propane, acetylene or hydrogen [12]. There are two varieties of flame spray processes, classified by the form of feedstock they require – wire or powder; these are outlined schematically in figure 2.1.

In WFS (figure 2.1a) the feedstock wire is fed into the flame and is thus melted by the heat. The molten wire is then atomised into small particles and propelled toward to substrate by an atomising gas (generally air). In PFS (figure 2.1b) powder is fed into the flame and accelerated toward the substrate. In PFS the particles are generally accelerated by the action of the flame, not an external gas/air supply as in the case of WFS.

Flame spray is a basic but versatile thermal spray process and can be used to spray a variety of materials including metals and polymers. FS particles are typically considered to have a low maximum particle velocity, up to 50 $m.s^{-1}$ for PFS [11] and 100 - 200 $m.s^{-1}$ for WFS [13, p. 284]. Low particle velocities can result in limited splat spreading during TS deposition [14]. Lower particle velocities and resultant reduced spreading of splats increases the amount/volume of voids between splats in the coating and so increases the porosity of the coating. Thus, WFS coatings are generally relatively porous (3 - 15 % [11]) with a high oxide content (in the case of metallic feedstock) in relation to other thermal spray processes [15].

2.2.2 Twin Wire Arc Spray (TWAS)

TWAS uses the action of an electric arc to melt the electrically conductive feedstock wire. Wire is fed from two different reels and has an electrical potential applied across

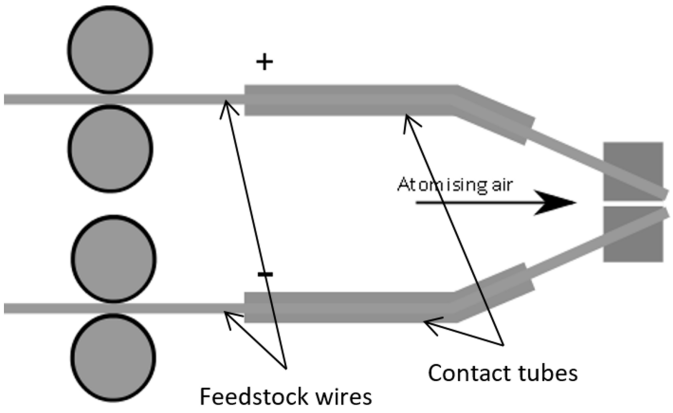


Figure 2.2: Simplified schematic of twin wire arc spray (TWAS) process showing conductive wires being negatively and positively biased causing aring and melting at the wire tip

which is, typically 20 – 40 V [10, p. 38]. An arc is formed between the two wires which can reach a temperature of 6000 K [10, p. 38]. A compressed gas stream is then used to atomise the molten wire and propel it toward the substrate (figure 2.2). Typical particle velocities from this process are around 150 $m.s^{-1}$ [11]. Coatings produced typically have porosity of 3 – 10 % [11]. This process can only thermally spray conductive wire but through the use of cored wire (powders contained within a conductive metallic sheath) it can spray non-conductive feedstock. The anode and cathode wires can also be made from dissimilar metals, forming a "pseudo-alloy" coating, e.g. [16].

2.2.3 Plasma Spray (PS)

Plasma spray (PS) involves heating a powder feedstock in a plasma jet and propelling it toward the substrate (figure 2.3). The plasma forming gases e.g. Ar, Ar/He, N_2 are ionised by the effect of the extreme heat of the electric arc within the gun [17]. The ionised gas expands and is expelled out of the outlet of the gun. Feedstock particles are often fed into the plasma stream as it exits the gun. Typical particle velocities are up to 450 $m.s^{-1}$ [11]. There are many different types of PS guns. They are differentiated by different factors including the powers at which they work, the gas velocities and powder injection point. Although it is a complex process, PS is very versatile and can spray the widest range of materials out of any of the thermal spray processes [15] i.e. metals, ceramics, polymers and cermets. Due to the high temperatures of the jet outlet that can reach over 12 000°C [15, p. 47] it is often used to spray ceramic feedstock. Porosity of coatings is typically 1-5 % [11] and bond strengths can be >70 MPa [15, p. 48]. Due to several factors, including oxidation of feedstock PS is sometimes carried out in a vacuum

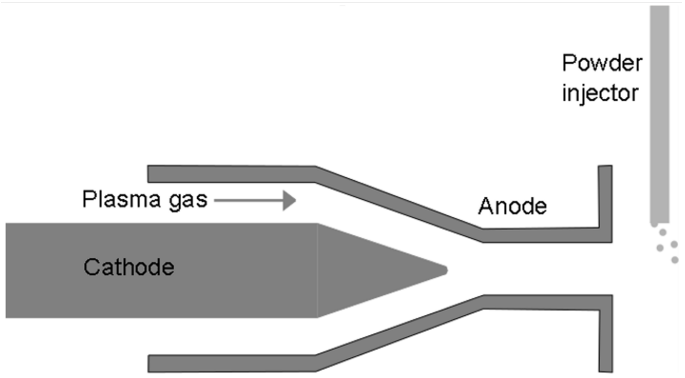


Figure 2.3: Simplified schematic of a DC external injection PS system where gas is fed between an arcing anode and cathod producing a plasma jet

(VPS) [10, 43] [18], or within a controlled atmosphere (CAPS) [10, 46]. However, the cost of VPS and CAPS make these processes uneconomical for most applications.

2.2.4 High Velocity Oxy-Fuel (HVOF) spraying

Similar to FS processes, high velocity oxy-fuel (HVOF) spraying uses a flame to heat the feedstock particles. However, unlike FS the combustion happens internally, within a combustion chamber or an air cap [19], thus high pressures are achieved; exceeding 240 kPa for standard HVOF and exceeding 820 kPa for Hyper-Velocity Oxy-Fuel [15]. Powder feedstock is fed (under pressure) into the combustion chamber exit. The particles are heated and propelled through a converging – diverging nozzle with the gas stream. The gas stream can be accelerated up to several Mach and the particles can reach velocities of up to 700 $m.s^{-1}$ or more [11]. High quality coatings can be achieved with coating adhesion (i.e. interfacial bond strength) in excess of 80 MPa [11] [20], and porosity typically less than 2 % [11] [21]. The high adhesion and low porosity of the coatings is due to the high impact velocity, and low level of oxidation is due to the typically lower temperatures of the particles. Feedstock is generally in the form of a powder, however there are wire-fed varieties (e.g. HVWire manufactured by High Velocity Technologies [22]).

2.2.5 Cold Spray (CS)

Cold spray (CS) is different from the other thermal spray processes in that the feedstock material need not necessarily be molten / semi-molten. Feedstock particles are propelled within a heated gas stream toward the substrate. If the particles reach a velocity – termed critical velocity (V_{crit}) – and do not exceed an erosion velocity (V_{err}) then they deform and form a coherent coating on the substrate. The gas stream may be composed

of different gases including preheated He or N_2. Cold spray is an effective way of forming coatings from a ductile feedstock. Hard, brittle materials cannot easily be sprayed. Well adhered low oxide coatings can be formed. This method of thermal spray is discussed very little in this thesis and for more information on the process the reader is directed to [15] or [23].

2.3 Splat deposition

2.3.1 Introduction

Thermal spray coatings are made up of individual lamella/splats which en masse make up the bulk thermal spray coating which is typically a few hundred microns thick. The first few splats form an initial layer and interact directly with the substrate. The subsequent splats adhere to the previously developed splats and do not directly interact with the substrate. Thus, these first splats are critical in determining the interfacial properties of the coating system, including the adhesion strength of the coating. Using a variety of different arrangements , typically involving spraying through orifices and shutters or mounting the substrates on fast moving turntables (e.g. [24] [25]) researchers have deposited splats onto polished substrates such that they are sufficiently isolated to be studied individually. The vast majority of this work has been carried out on metallic substrates and there is very little work looking at splat shapes on polymers or FRP substrates.

The aim of this section of the literature review is to outline the different mechanisms that lead to different splat morphologies. The bulk of this literature in this review is taken from studies of thermally spraying onto metallic substrates. Much of this literature included in this section is also discussed in several review articles and literature reviews [26] [27] [28] [29]; the introduction to [30] also contains a good précis of the available literature. The present literature review then moves to outlining some of the very limited experiments investigating splats on polymers and FRPs.

Studying splat morphology has proved important, not least because there is a strong indication that the morphology of the splats influences the properties of the coating including adhesion [31] [32] [33]. The majority of work investigating splat morphology has been carried out on smooth i.e. polished substrates. However, the parameters that have led to favourable splat morphology on smooth substrates have also been shown to lead to greater adhesion, reduced porosity and increased deposition efficiency on rough grit-blasted substrates [34], which are more typical of substrate surfaces employed during

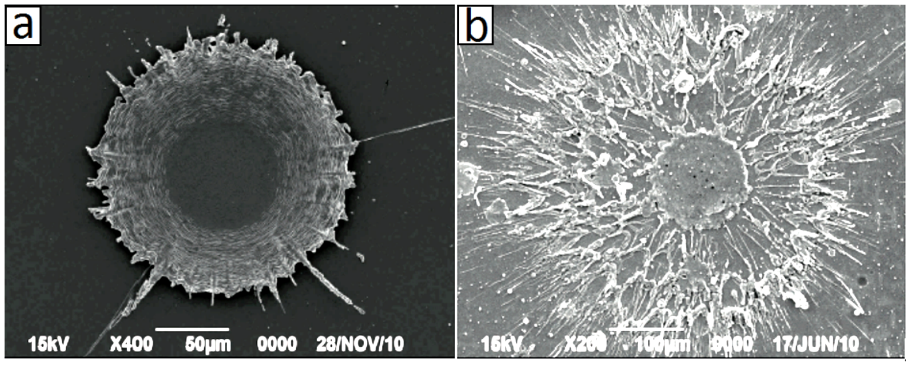


Figure 2.4: Representation of (a) disc type splat where the material is contained within a single regular splat (b) splash type where significant material is depsited around the central splat [29]

the thermal spray deposition of coatings for engineering applications.

The two most commonly discussed splats morphologies in terms of metallic substrates are disc and splash shaped. Disc shaped splats are characterised by a regular circle morphology with few / no protruding ligaments (figure 2.4a). Splash shaped splats are irregular, often characterised by a central splat surrounded by a ring or ligaments and debris forming around them [29] (figure 2.4b). The former is associated with greater adhesion than the latter [31] [32] [33]. In addition to the commonly discussed morphologies (disc and splash) a variety of different characteristic morphologies are discussed by different authors. For example, when spraying Ni-Cr onto aluminium and stainless steel, Tran et al. [35] distinguish two additional types; irregular splash and doughnut disc splat, the former being a non-round splash shape (figure 2.5b) and the latter being a round disc shape with a large hole in the middle (figure 2.5a). They also characterise what they term impact marks on the substrate where particle residue is present from where a particle hit the substrate but did not form a splat, presumably having rebounded. Other morphologies identified by different authors include "gravel" and "rugged" splats [33] associated with particles not fully molten upon substrate impact and "flower type" splats [36] which are formed due to the impacting particle locally melting the substrate. Many of these different morphologies may well be subsumed in the broad category of irregular splat. However, each of these types of splat morphology is probably formed due to different splashing regimes of thermal behaviour and fluid flow. Thus looking in the detail of the splat morphology helps reveal what is occurring when the thermal spray particle impacts the substrate. This makes observing the morphology useful for looking at mechanisms of coating build up which ultimately govern coating properties. However, from the perspective of increasing adhesion and reducing porosity, promoting disc shaped splats is believed to be an important requirement and much of the research focuses on these.

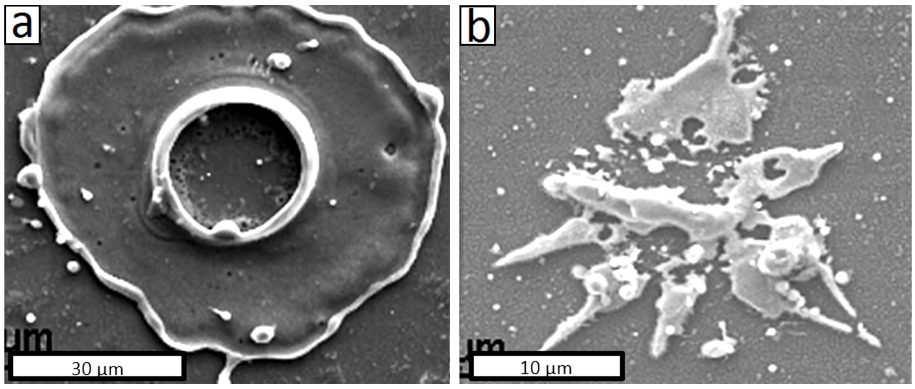


Figure 2.5: SEM images of (a) doughnut disc and (b) irregular splash Ni-Cr splats on polished metallic substrates [35]

2.3.2 Factors affecting splat type

Particle factors

The particle state upon impact would appear to be an important factor in determining the splat morphology. Different researchers have put forward models which seek to determine the splat diameter and other properties from particle parameters. Several factors influencing these models are summarised in [28]. One commonly quoted [28] [37] [38] [39] model is based on the Sommerfeld parameter (K). Defined in equation 2.1 where Re and We are the Reynolds number (equation 2.2) and Weber number (equation 2.3) of the droplets. In equation 2.2 and equation 2.3 ρ is droplet density ($kg.m^{-2}$), u is droplet velocity ($m.s^{-1}$), D is droplet diameter (m), μ is the dynamic viscosity of the droplet ($kg.m^{-1}.s^{-1}$) and σ is the surface tension of the droplet ($N.m^{-1}$). The Reynolds number represents the ratio of inertial forces over viscosity and the Weber number represents the ratio of initia over surface tension. Combined in the Sommerfeld parameter they mathematically represent the droplet's propensity to breakup upon impact.

$$K = We^{1/2}Re^{1/4} \tag{2.1}$$

$$Re = \frac{\rho u D}{\mu} \tag{2.2}$$

$$We = \frac{\rho u^2 D}{\sigma} \tag{2.3}$$

The Sommerfeld parameter was proposed in the context of experimental data drawn from impacting water and ethanol drops on a smooth surface. Thus, it is only relevant for fully molten particles, and does not consider solidification of the droplet, perhaps a

reasonable assumption if (as [30] states) solidification starts towards the end of spreading. The empirical model states that if K is less than 3 the droplet will rebound; if it is between 3 and 57.7 it will deposit and if it is greater than 57.7 it will splash on the surface. Using an involved experimental setup, Escure et al. [37] replicated the ethanol/water droplet experiment with alumina droplets on different substrates (304L, alumina and carbon). They identified two modes of splashing, one of which was related to the Sommerfeld parameter. This mode occurred at K>20 and involved a very small amount material ejection. The material was propelled a long distance (several millimetres) from the substrate and was likely entrained within the fluid flow [26], the disparity between measured critical K values was attributed to substrate roughness and experimental uncertainties. The other mode of splashing found in the study was more influenced by substrate temperature and particle velocity. The relevance of the Sommerfeld criteria has also been questioned because regular (non-splashed) disc shaped particles are abundant in the literature, despite typical plasma spraying leading to K values of 50 – 1800 [28] meaning that they should be a rarity. The strong effect substrate surface properties (discussed below) have on the splashing behaviour also makes the values seem of limited importance.

Substrate temperature

It has been shown that substrate temperature is a critical factor in determining splat morphology. As the temperature of the substrate is increased, the proportion of favourable (i.e. disc shaped) splats is also increased (e.g. [25] [40] [41] [39] [42]). Fukumoto et al. [25] defined the term transition temperature (Tt) to refer to the temperature at which half the splats are of the favourable disc morphology. The proportion of disc shaped splats dramatically increases in a small temperature range (100 – 200℃) around the Tt (figure 2.6). In the study, they determine the transition temperature on polished stainless steel for a variety of different metallic feedstock materials. Of the materials tested where a Tt was observed, it ranged from 114℃ for Cr to 337℃ for Ni.

In [25] Fukumoto et al. suggest that reason the substrate temperature is important in determining splashing behaviour is because it controls the splat cooling/solidification rate, and presumably that the Tt represented some critical value. This is in line with the freezing induced splashing mechanism in which the initial area in contact with the substrate of the spreading droplet solidifies forming a rim around the periphery hindering the flow of the molten liquid causing it to laterally jet described in [43]. Using Auger analysis, as well as observing disturbances in thin Au PVD coatings on substrates, Fukumoto et al. [25] demonstrated that splashing on cold substrates was caused by lateral jetting

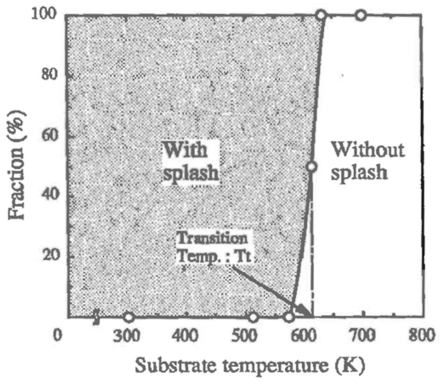


Figure 2.6: Figure showing the proportion of Ni splats splashing on a polished stainless steel substrate as a function of substrate temperature. As substrate temperature reaches the transition temperature, Tt, the proportion splashing dramatically reduces [25]

of material from the top part of the central portion of the splat (figure 2.7) rather than material flowing and subsequently breaking up. The study also found evidence in the splat microstructure of accelerated solidification in the central portion of splash splats. This backs up the hypothesis that splashing is caused by accelerated solidification of the central portion of the splat inhibiting flow, thus causing jetting/splashing.

There have been criticisms made of freezing induced splashing as a mechanism to describe the transition temperature. Chiefly, that the transition range is over such a small temperature window that the effect of this change in heat transfer is minimal [30]. An often mentioned possible mechanism for the transition temperature is that of adsorbents being removed from the substrate by heating prior to splat impact [45] [35] [46] [30]. If these are not removed by heating prior to spraying they are said to evolve from the substrate surface beneath the splat causing gas pockets, thus interrupting the development of disc shaped splats. These condensates/adsorbents have been observed in splats as nano-pores [47] and are shown to be more prevalent in the central portion of splashed splats than in disc splats [44]. Additional evidence of condensates/adsorbents being a driving factor for the Tt was shown by observing Cu splats in free-fall experiments in an argon atmosphere. It was shown that reducing the ambient pressure had a similar effect to increasing the substrate temperature i.e. the morphology of the splats changed from a splashed to a disc morphology. Given that reducing the pressure is another method to reduce the amount of condensates/adsorbents on the surface it suggests this may be a driving factor [48].

Irregular splashed splats have not always been attributed to jetting (where material detaches from the top of the splat due to restriction in the splat flattening caused by partial solidification of the splat (figure 2.7)). Numerical modelling has indicated that the liquid droplet can initially impact and spread on the surface forming a sheet. The central

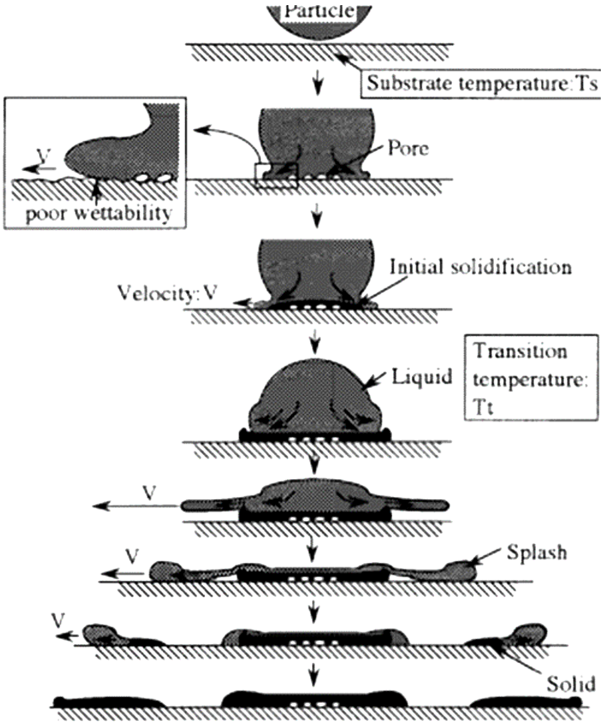


Figure 2.7: Illustration of particle deformation and splat formation on a substrate causing a splash type splat as described by Fukumoto and Huang. Material detaches from the central portion of the splat jetting to form irregular satellites [44]

region of this sheet having a higher thermal transfer than the rest of the splat would solidify. The outer part of the molten sheet having slower solidification can fragment leaving a central disc which solidified with fragmented metal round it [49] [26]. This formation was modelled and photographed on glass substrates [49]; a representative figure showing this is reproduced in figure 2.8.

Polymer and FRP substrates

Most of the splat morphology work mentioned up until this point has been carried out with metallic substrates. Very little work has been published investigating the way in which thermal spray particles interact with polymers and FRPs. Ganesan et al. [50] imaged single plasma sprayed copper splats on differently treated CFRP surfaces (chemically, mechanically and thermally); there is more discussion of this paper later in the chapter. From the images published in the study, no fibres are evident on the surface, and the substrates had a Ra of 7 - 9 µm. As the authors note, the morphology of splats is similar for all treatments. The splats appear to have similar morphology to other splats on CFRP imaged by the same research group [51]. In both cases, the splats are thick and relatively rough (e.g. figure 2.9) and seem similar to the splats which were semi-solid upon impact seen in [32] figure 2.10) perhaps suggesting that these were also

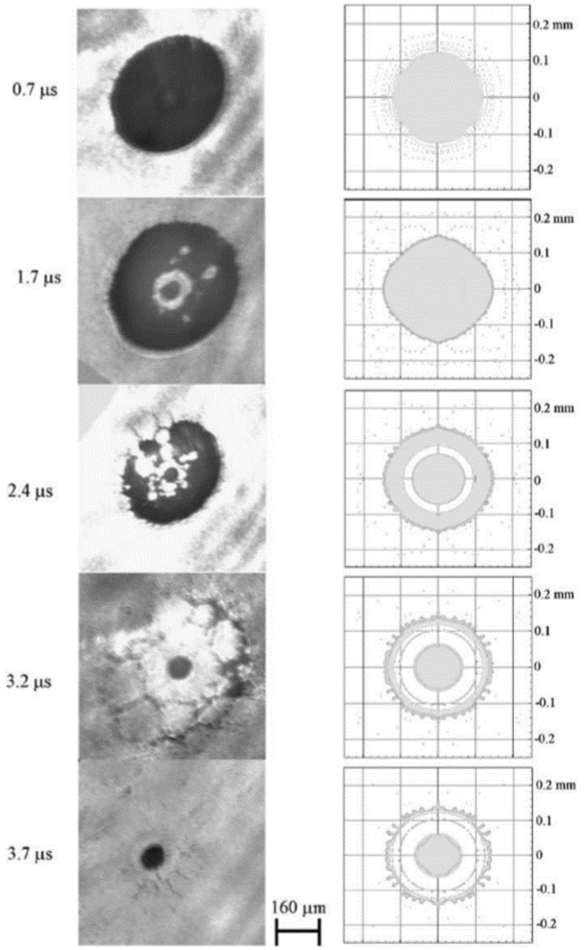


Figure 2.8: Photographs (left) and modelling results (right) showing the development of a Mo splash splat onto an unheated glass substrate, showing the initial spreading of the droplet, solidification of the central region and breakup of the slower to solidify periphery region [49]

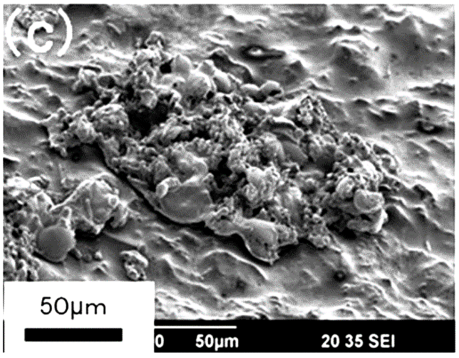


Figure 2.9: SEM image of PS Cu splat on grit-blasted CFRP. Image shows the rough Cu splat morphology on the FRP surface [50]

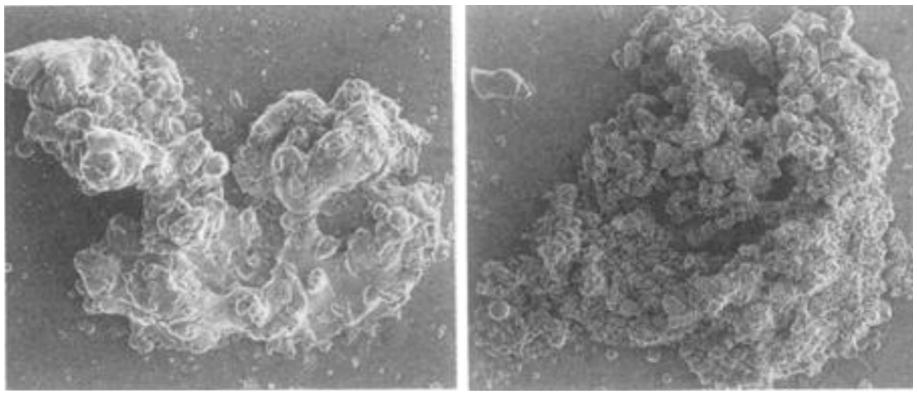


Figure 2.10: SEM images of splats formed on metallic substrate when impinging particles were not fully molten. Splats are characterised by the rough morphology seen in the images [32]

semi-solid upon substrate impact. In addition to these images, the authors use a high current focused ion beam (FIB) milling technique to carefully section splats within an SEM and observe their cross section. Through observation of the splats they propose that there is better contact between the splat and the substrate on the chemically treated substrate. However, the difference between the published FIB sections seems minimal.

Redza et al. [52] examined isolated splats on unidirectional CFRP substrates with a relatively high temperature thermoplastic polymer matrix (T_m = 250°C). The authors used a microwave plasma spray apparatus to deposit the chromium splats. The substrate had no surface preparation prior to the spraying. The carbon fibres (though visible) appeared to be covered with resin prior to spraying. After spraying, the polymer resin covering the fibres had been removed and the undamaged fibres were visible. Splats of Cr were visible on the surface preferentially adhering to the now exposed fibres. The deposited Cr particles appear to be very small (≈5 µm) and relatively regular and similar to those which the authors deposited onto 304 stainless steel [52] .

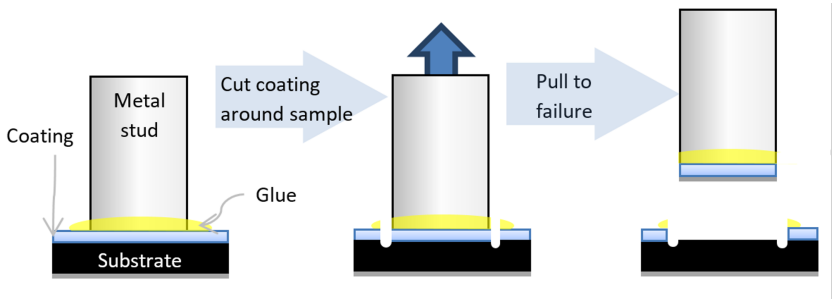


Figure 2.11: Simplified schematic representation of general tensile adhesion test. Involving the gluing of a metal stud to coating; scarfing of the surrounding coating; and pulling the stud to failure

2.4 Coating assessment - adhesion tests

2.4.1 General

A deposited coating can only protect the substrate as long as it is adhered to it. Thus it must be able to withstand the mechanical stresses experienced during service without debonding. This means effective assessment of coating adhesion strength is important.

There are myriad different adhesion tests, papers on the subject identify tens (80) [53] to hundreds (200) [54] of different adhesion tests of varying validity. Berndt and Lin provide an overview of the different tests as well as how to analyse them in [55] and [56]. Adhesion tests are used for different purposes within the thermal spray industry for characterising coatings, process development and quality control. The majority of the tests fall into one of several broad categories (tensile, shear, bending, and scratch). Within this study, tensile adhesion tests (TATs) were used to assess coating adhesion and so only these will be reviewed here.

2.4.2 Tensile adhesion tests

TATs are very common within the thermal spray industry. It should be noted that the in-service loading on coatings is rarely pure tensile, thus generally they do not necessarily introduce representative failures. Thus, the tests serve more for ranking coatings against one another [57]. Despite their flaws TATs are useful as they give a simple measure of coating adhesion. There are several common standard TATs, these include ASTM C633-13 [58], BS EN 582 [59] and ASTM D4541-95 [60]. The fundamental principle of these tests is to apply an increasing pure tensile force onto a deposited coating. This is done by attaching a test dolly / stud to the coating, applying an increasing tensile force, recording the value at which coating failure occurred; a simplified representation of this setup is shown in figure 2.11.

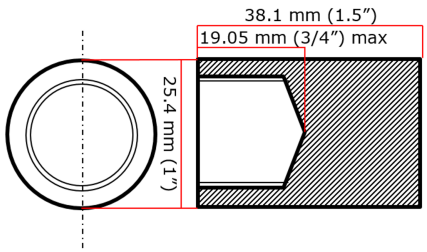


Figure 2.12: Simplified schematic of an ASTM C633-13 test stud (adapted from [58])

ASTM C633-13 and BS EN 582 are almost equivalent test standards. In both cases, coatings are prepared on end face of a defined test stud. Schematics for an ASTM C63-13 test stud is shown in figure 2.12 (the BS EN 582 test stud is very similar). The coating is then attached with adhesive to the end face of an identical test stud. Increasing force is than applied at a defined displacement rate (ASTM C633-13) or defined loading rate (BS EN 582) in pure tension until failure is induced. Failures can be cohesive (fracturing within the coating of substrate), adhesive (failing at the substrate / coating bond line), or mixed mode.

The adhesion of the coating is dependent upon the substrate material as well as the coating. Hence ideally the coated stud is manufactured from the same material as the substrate of the final system. Both ASTM C633-13 and BS EN 582 allow for stud to be made from steel but the end face covered with material representative of the substrate material.

ASTM D4541 is similar to the above TATs; however it is performed using a Portable Adhesion Tester (PAT). A test stud is attached to a flat section of the coating with adhesive and cured. The standard does not define a geometry of the test stud; the geometry is dependent upon the model of PAT used and the discretion of the tester. The coating immediately around the test stud can be cut to eliminate any contribution to in plane stresses. The stud is attached to the tester and increasing force is applied to the stud until the coating debonds.

In ASTM C633, ASTM D4541 and BS EN 582, the force required is divided by the area of the test stud to obtain the average stress on the coating at failure. The stress is necessarily non-uniform over the test stud, this will lead to an underestimation of the adhesion strength. In 1993 [61], it was shown that increasing the length of the ASTM C633-79 stud by 50 % (1", 25.4 mm) would increase the uniformity of the stress field and give more representative results. The modern version of the test stud is now 1.5" (38.1) as shown in figure 2.12.

As with any experimental test, there is some scatter in the obtained results from the

above tests; thus to reduce uncertainty to an acceptable level several repeats are required to fulfil the standard – ASTM C633-13 requires at least 5 repeats of each test [58]. This number of repeats reduces the level of uncertainty to around 15 % [62]. Interestingly, when Kuroda et al. [63] introduced a defined intentional crack around the circumference of an ASTM C633/BS EN 582 style stud, the scatter in the results obtained was reduced. The authors suggested that without this intentional crack the failure was determined by the circumferential geometry (roughness etc.). Tsui et al. [57] agree that in a TAT the coating failure is dependent on flaws in the specimen edge. Thus, presumably by inducing a controlled stress raiser in place uncontrolled ones, Kuroda et al. [63] reduced the scatter.

Comparing adhesion test results across studies should be done with care, even if both tests are TATs and performed on the same coating/substrate system. The thicknesses of the coatings are rarely common, and adhesion tests used are often not performed rigorously to a common standard. These points are of concern if one wants to compare studies to try and elucidate common themes. Thicker coatings tend to have lower adhesion strengths possibly due to higher residual stresses in the coating acting against adhesion, or as Lin and Berndt [56] suggest due to glue infiltration or improved stress transfer over the coating. In any case this effect is seen in many studies including [50] where the thicker coatings had lower adhesion. Studies within TWI have also shown that even different tensile tests standards, ASTM C633 and ASTM D4541 do not necessarily yield the same results, especially when testing lower adhesion strength coatings [64]. This is in part because of shear and peeling effects being less controlled in ASTM D4541 standard (PAT method). Due to these facts, adhesion results can only rigorously be compared within single studies.

2.5 Residual stresses

2.5.1 Introduction

As splats deposit and coatings form, residual stresses are generated within thermal spray coatings which vary through the coating thickness and into the substrate itself. In general, residual stresses are formed due to a misfit between the substrate and the coating. This misfit leads to elastic energy being stored in the induced strain of the coating and substrate. As the thickness of the coating increases, the magnitude of the stored elastic energy increases, as do the residual stresses [65]. Residual stresses can result in spallation and cracking of the deposited coatings [65]. These residual stresses can be compressive [66], or tensile [67] and substantial in value, in the region of several hundred

MPa [66] [67]. Tensile residual stresses can limit the possible thickness of a coating, because the stresses (from this elastic stain energy) work against adhesive forces and when they reach a critical value, may overcome the adhesive forces, even without an externally applied load. Thus, controlling residual stresses is important to a successful coating system. There are three main mechanisms for residual stress build-up quoted in literature [68] [66] these are discussed in sections 2.5.2 - 2.5.4:

- Coefficient of thermal expansion (CTE) mismatch
- Quenching
- Peening

2.5.2 CTE mismatch

During the spraying of a thermal spray coating both the substrate and coating are at elevated temperatures. As the materials cool to room temperature after spraying they will both contract in accordance with their respective CTEs. Generally, the materials will have different CTEs and may also be cooling from different temperatures, thus each material's contraction will constrained by the other and a system of residual stresses are set up in the coating and substrate. The magnitude and type – compressive or tensile – is controlled by the elastic modulus values and CTEs of coating and substrate materials. It should be noted that when discussing the properties of the coating material (e.g. elastic modulus), these may be very different from those of the equivalent bulk material and so for accurate modelling must be directly measured [65].

2.5.3 Quenching

Quenching stresses come about as the result of cooling of the thermal spray particles on the substrate. As a spray particle hits the substrate it can be at a temperature of several hundred ℃ for metallic alloys, and several thousand ℃ in the case of ceramics. As it impinges the surface, there is high heat flow through the droplet to the substrate and an associated temperature drop in the droplet. Due to the droplet almost invariably having a positive CTE the droplets will contract upon solidification with an associated volume change (normally a decrease). However, the droplet is constrained by the substrate which it is adhered to. Thus a system of opposing residual stresses is created, tensile in the splat and compressive on the substrate, or previously deposited layer [68]. The magnitude of the quenching stress can be estimated by considering the CTE of the

impinging particle and the temperature difference between the particle and the substrate; these considerations are encapsulated in equation 2.4 [69] [65].

$$\sigma \approx E_d \alpha_d (T_d - T_s) \tag{2.4}$$

Where E_d is the Young's modulus of the droplet, α_d is the CTE of the droplet, and T_d and T_s are the temperatures of the droplet and substrate respectively. This simple model predicts the maximum possible quenching stresses exerted, using it can give quenching stresses in the order of 0.1 - several GPa [69] [65]. In reality, these levels of stress levels may be reduced by stress relaxation processes in the splat and equation 2.4 represents a maximum which is not reached [69].

2.5.4 Peening

In high velocity thermal spray processes, i.e. HVOF and CS, particles impinging the substrate can be travelling at high speeds - 700 $m.s^{-1}$ or greater - thus can have significant momentum. When the high momentum thermal spray particles hit the substrate, or previously deposited particles they can cause significant local stresses to be imparted onto what they hit. This can induce plastic deformation (spreading) of the uppermost surface (substrate or previously deposited coating). This plastic deformation of the outermost surface causes a compressive residual stress on the outer surface, with a balancing tensile residual stress nearer the substrate. Peening effects are most significant in the higher velocity thermal spray processes, i.e. HVOF and CS [66]. Peening effects become much less significant in the higher particle temperature, lower velocity processes e.g. PS. As liquid droplets do not cause peening effects. When peening stresses are significant, cold worked microstructures are found within the coating [70].

2.6 Review of polymer composite materials

2.6.1 Introduction

Composites are characterised as having distinct multiple phases which act together to give the material a specific set of properties. These properties are different from those which each constituent material has alone. In respect to this work, the composite materials that are being considered are fibre reinforced polymers (FRP). In these systems a reinforcing phase, comprising strong, stiff thin fibres is held together and protected by a polymer matrix phase which transfers and distributes the load across the fibres.

Typical reinforcing fibre types are aramid, carbon and glass fibres , and around 10 µm in diameter [71]. Typical polymer matrix materials include thermosetting resins (e.g. are vinyl esters, epoxies and some polyimides) and thermoplastic resins (e.g. polyphenylene sulfide (PPS) and polyether ether ketone (PEEK)).

FRP materials can be extremely strong and stiff. A typical tensile strength and elastic modulus of unidirectional carbon fibre epoxy composite can be 1260 MPa and 200 GPa respectively [2, p. 38] with densities around 1600 $kg.m^{-3}$ [72]. However, the exact properties of the material will depend on many different factors, including the:

- Chemistry of each phase
- Ratio of matrix to reinforcement
- Physical form of the reinforcement
- Reinforcement orientation
- Method of production
- Direction of testing with respect to fibre orientation

2.6.2 Polymeric matrix phase

Polymers are high molecular weight organic materials made up of long chains of repeating monomer units covalently bonded together to form polymer chains. One of the simplest polymer materials is polyethylene (PE). PE has a repeating unit (monomer) that is made up of saturated carbon and hydrogen atoms (figure 2.13). There can be thousands of repeating monomers forming a single polymer chain. The length of these will determine the molecular weight of the polymer which has implications for its mechanical [73] and thermal properties [74, p. 475]. Different polymers will be made up of different monomer units that contain different functional groups; these will change the chemical and mechanical properties of the polymer. For example replacing one of the hydrogen atoms in each PE monomer with a phenyl group would turn it into a polystyrene monomer. Thus changing the properties of the polymer e.g. increasing the melting temperature from around 115℃ (for low density (LD)PE) to 240℃ (for isotactic polystyrene) [74, p. 801]. In addition to the base polymer, additives (fillers, plasticisers, etc.) are also typically added to a polymers material to improve properties e.g. ductility, strength and oxidation resistance or to reduce the cost of the plastic.

Some polymers form permanent covalent bonds between the different polymer chains to create cross-linked polymers; these polymers (e.g. epoxy, vinyl esters) are called

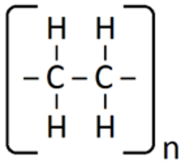


Figure 2.13: Schematic representation of repeating monomer unit in polyethylene

thermosetting polymers and cannot be made to melt and flow by heating. The highly interlinked polymers yields a brittle solid; however these are generally toughened to improve their ductility. Thermoplastics do not form these covalent cross links and upon heating the polymer chains are freer to move and the material can soften and melt. These materials are also typically tougher than thermosetting polymers [75].

The structure of the monomer/polymer also influences the crystallinity of the polymer, i.e. what percentage of the polymers volume is made of structures with long range order rather than amorphous phase (cooling rate also has a significant effect on the degree of crystallization). Complex polymers with large functional groups and unsaturated bonds are less likely to form ordered structures and have less crystallinity. In actuality, crystallinity of a polymer ranges from 0 – around 95% [74, p. 456]; thus, even the most crystalline polymers will have at least some amorphous regions. The presence of these two regions have a significant effect on the behaviour of the polymers, for instance how they respond to temperature change. The crystalline phase has distinct phase change at a melting temperature (Tm) (or range). The amorphous phase does not show a distinct Tm. Instead, above a temperature (termed glass transition temperature (Tg)), the amorphous phase behaves as a very viscous fluid, its viscosity decreasing at the temperature rises. Below the Tg the polymer chains lose their mobility and the material behaves as a glass, hence the term Tg [76, p. 76]. The mechanical properties of a thermoplastic depend on the test temperature in relation to the glass transition temperature. Low temperature and/or high strain rate lead to high modulus but brittle behaviour but the converse is true for temperatures above Tg and lower strain rates.

There are several polymer resin types commonly used in FRP manufacture; this study focuses on two main resin types namely (thermoset epoxy and thermoplastic polyetheretherkeytone (PEEK)). These are briefly discussed below.

Epoxies are the most common resin type used in high performance composites [75]; they contain epoxide functional groups (figure 2.14) at each end of the monomer. These functional groups react with functional groups (e.g. epoxide or amine) in other epoxy monomers or hardeners to form polymer chains (polymerise) [2, p. 18] and cure. Clearly a hardener requires at least two of these groups to allow it to link to at least two monomers.



Figure 2.14: Schematic representation of an epoxide group

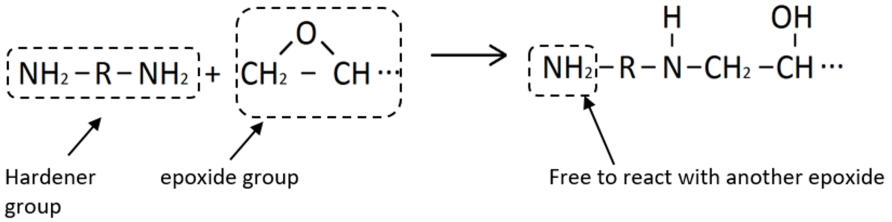


Figure 2.15: Example reaction between hardener containing two amine functional groups and epoxide functional group [76, p. 280]

An example reaction between an epoxide group and an amine hardener is shown in figure 2.15 [76, p. 280]. Epoxy resins are typically simple to process and once cured (typically with the aid of heat and pressure), they result in highly cross-linked amorphous thermosetting polymer materials. The properties of the specific material depend on the epoxy, curing agent and conditions used and a typical cast epoxy can have tensile strength of ≈ 20 - 80 MPa [2, p. 19] and a maximum working temperature of ≈ 120 – 135℃ [75].

PEEK is a semi-crystalline thermoplastic. Its monomer unit is depicted in figure 2.16. It is known for having a very high temperature capability with a Tg of 142℃, and a melting temperature of 343℃ [77].

2.6.3 Reinforcement phase

As mentioned above, typical fibre-reinforcement materials are carbon, glass or aramid fibre. Within these broad categories there is differentiation in size structure, chemistry and strength. These are important factors in determining the overall material properties of the composite. For example, carbon fibre reinforcements are typically derived from either polyacrylonitrile (PAN) or mesophase pitch (pitch) precursors, the former generally having higher strength than the later [78].

Fibre reinforcements may be incorporated into the polymer matrix in different forms, and this will also play an important role in the properties of the FRP composite. One form the reinforcement can take is as short lengths of fibre. These are incorporated

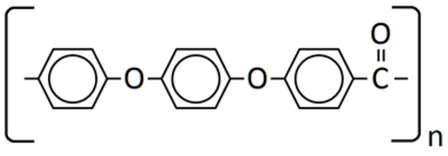


Figure 2.16: Schematic representation of repeating PEEK monomer unit

into the matrix in a random orientation; thus the material can have largely isotropic properties. This method of incorporation is a relatively economic way or producing composites and standard plastic processing techniques can be employed [79]. In this case, the properties of the composite are heavily influenced by the length of the fibres, as well as their volume fraction within the composite. In order to be an effective reinforcement the fibre length should be greater than the critical length (lc). The critical length is defined as the minimum fibre length where maximum fibre loading is achieved. Where the reinforcement length is equal lc, the maximum loading is only achieved at the middle point along of the fibre. As the length of the fibre increases, load transference to it will improve, thus more of the length of the fibre will achieve the maximum loading [74, p. 519].

Fibre reinforcements can also be incorporated into the polymer matrix as continuous strands. The present study is focusing on FRPs where the reinforcements are in the form of woven fabrics; such materials will have anisotropic mechanical properties depending on fibre orientation. There are several different types of weave used including plain, twill, satin and uni-directional. The choice of weave for a particular application will depend on several factors but drape-ability (how the cloth will conform to shapes) is important for more complex shapes. Fibre reinforcement cloth is often supplied already impregnated with the resin material; this is termed pre-preg material.

2.6.4 Composite manufacture

Fibre reinforced polymer composites are cured/solidified within or around a mould to define shape of the part as polymer resin sets. There are many different methods for doing this; the method favoured will depend on the specific application, geometry and the properties of the resin used. This work does not purport to discuss them is any detail but some basic details of general composite manufacturing are discussed below. Reference [80] provides a comprehensive introduction to the topic.

The simplest method of composite manufacture is hand layup on an open mould. In this process fibre and thermosetting resin are applied by hand to the prepared mould. Preparation involves coating the surface of the mould with a release agent to allow for the finished part removal. After this, a gel coat will often be applied prior to the resin or the first ply in order to ensure a good and consistent tool face. This is followed by a skin coat of resin (a thick initial resin layer). After this, layers of reinforcement cloth (plys) are placed, and resin manually worked into the fibres. The layup is compressed and consolidated manually with rollers and cured [80, p. 132]. Depending on the part and

resin this may be cured under elevated temperature and/or pressure. Pre-preg material can also be moulded in a similar manner to the above. However, gel coats are not typically applied and curing is typical done under elevated temperature and pressure.

In addition, through the use of thermoplastic pre-pregs, thermoplastic composites can be processed via this route. Thermoplastic prepregs can also be processed using a hot press technique. In this technique the pre-preg is laid up into a mould (coated in release agent). Another matching mould it brought down so that the moulds sandwich the pre-preg material, these apply heat and pressure so that the material heats and consolidates. After a time the part is cooled and then the mould is removed [80, p. 216]. Typically, the surfaces in contact with a mould (the tool face) will be smooth – mirroring the finish of the mould.

2.7 Thermal spray onto polymers and fibre reinforced polymer composite materials

2.7.1 Introduction

Although thermal spraying of metals onto polymers was first reported by Ingham and Shepard in reference [81], which was published in 1943, there is little work reported in the open literature until the late 1980s. In recent years, there has been a significant increase in interest especially concerning thermal spraying of metals, ceramics and cermets onto FRPs, much of it concerned with improving resistance to wear.

2.7.2 Flame spray

With regard to the methods used in the present study, little work has been reported in the open literature on flame spraying of coatings onto FRPs. There have been two sets of trials found in the literature discussed briefly below.

Sutter et al. [82] [83] [84] conducted a variety of investigations whose aim was to improve the erosion resistance of a carbon-Kevlar® epoxy FRP aero-engine bypass vane by thermally spraying it with an erosion resistant coating. These researchers investigated the use of two different coating systems, SANRES and SANPRES. These are both proprietary and consisted of a TS bond coat and a PS WC-Co topcoat. The difference between the systems was in the bond coat, the former had no polymer component within it and was deposited with a wire flame spray gun (Metco 12E). The latter bond coat contained a polymer component and was deposited by plasma spray. Due to the pro-

prietary nature of the systems, very little information was included about the materials or coating process other than the substrates were "carefully" grit-blasted with alumina prior to coating and that the bond-coats were 76 µm thick. The coatings deposited onto the FRP bypass vanes were shown to improve the erosion resistance that was observed under test.

Recently researchers at the University of Alberta have used powder FS (PFS) to produce Al [6] and Al-Si [85] [86] coatings on basalt and glass fibre reinforced epoxy tubes. The general aim of the work appears to have been the application of electrically conductive coatings onto FRP pipes as damage detection sensors. Huonnic et al [6] found that conductive Al coatings could be obtained by PFS onto grit-blasted FRP tubes with a Ra of 5.8 µm. Coatings could not be deposited onto non-grit-blasted tubes with a Ra of 1.5 µm. The coated tubes were found to leak and fail at a 17% lower internal pressure than the un-coated control samples; this was attributed damage occurring due to grit-blasting. Gonzalez et al. [85] managed to obtain successful FS coatings on tubular samples without grit-blasting the surface. This was achieved by impregnating the surface of the composite during layup with 80 mesh garnet sand. This method of surface treatment allowed the PFS coating to build-up but prevented to coated samples failing at the lower pressures. Using this method, the coated samples failed at a 1% higher internal pressure than the untreated ones.

The same preparation/coating method has subsequently been used by other researchers at the University of Alberta to flame spray NiCrAlY [87] onto CFRP as a ≈100 µm thick coating for use as a conductive element for a resistive heater. The purpose of the investigation was to study the heating/de-icing capability of the coated substrate and as such there was little characterisation of the coating although the authors do not note deficiencies in the coating. The approach of thermally spraying composite parts for in-flight de-icing is already used in industry, e.g. for the Agusta Westland AW101 (Merlin) main rotor blade [9] as well in the leading edge of the Boeing 787 dreamliner [88]. These parts are both produced by GKN Aerospace. Due to the commercial nature of these components there is limited information about these in the open literature.

2.7.3 TWAS

The first application of TWAS coatings to FRP substrates found in the literature was detailed in Lugsheider et al. [89]. This study was primarily focused on investigating the most effective type of pre-treatment for increasing tensile and shear adhesion strength of the coating. Deposits were subsequently tested with tensile adhesion tests and in a shear

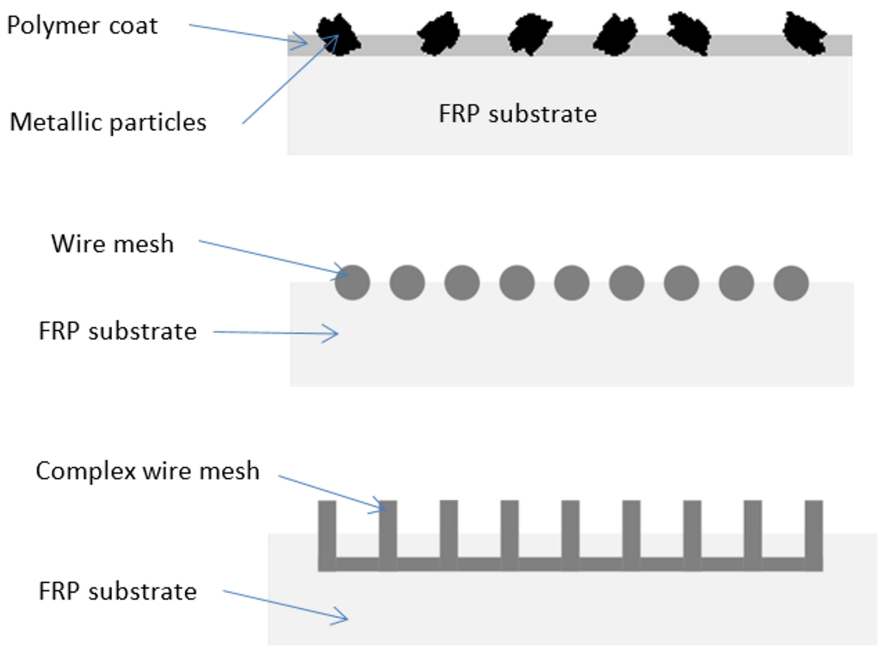


Figure 2.17: Schematic of differently modified substrates to prepare for thermal spray

rolling fatigue setup. The paper reported four different preparation types, namely:

I Grit-blasting.

II Gluing a layer of metal particles on the surface of the substrate with a high temperature thermosetting polymer (figure 2.17 top).

III Embedding wire into the surface of the laminate and lightly grit-blasting the surface to expose the top half of the wire (figure 2.17 middle).

IV Embedding of a complex 3D wire matt within the layup such that small wires protruded out of the substrate, normal to the surface (figure 2.17 bottom).

TWAS was used to coat the prepared samples with NiCu 70/30. In the study, additional samples were plasma sprayed with a nickel based alloy. Few details about the actual spray setup were included except that air jets had been used to cool the samples during spraying. All of the pre-treatments resulted in successful coating deposition and multiple samples were tested. When tested in tension, preparation II had a similar adhesion to grit-blasting (≈20 MPa) with preparations III and IV having lower adhesion. However, the impregnated wire (preparation III) did perform significantly better in rolling fatigue with the PS Ni based coating. Kim et al. [90] employed a hybrid TWAS/HVOF system in an attempt to coat epoxy resin tubes with NiTi/Al; in the study, the substrates were not grit-blasted prior to spraying. The attempted coatings did not adhere, which was attributed to softening of the substrate and the particle impact and the lack of carbon

fibres. The study had some limited success with a TS Zn-based bond coat but, in order to obtain acceptable adhesion to a CFRP tube without grit-blasting, stainless steel leafing pigment was first glued to the tube prior to TS application of the topcoat. Recently, several studies originating from the Harbin Institute of Technology have also used TWAS to coat FRPs [3] [91] [92]. These studies are all concerned with thermally spraying two layer (bond and top coat) erosion resistant coatings onto FRPs. However, [3] focuses on surface preparation, [91] on bond coat material, and [92] on bond coat application. In [3], a Zn bond coat was deposited by TWAS onto carbon fibre reinforced polyimide substrates. The substrates had been subject to different surface abrasion regimes; grit-blasting with one of multiple different pressures (0.2 – 0.8 MPa) using one of two different grit sizes (28 or 46 mesh), or manual abrasion with one of several different grades of sand paper (60 – 1000 mesh). The maximum shear adhesion value (9.4 MPa) was obtained by grit-blasting with the lowest blast pressure (0.2 MPa) but the coarsest grit (28 mesh) tested. The various grades of sand paper gave relatively low shear adhesion strength, ranging from 3 – 5 MPa. The results imply that the coating adhesion benefits from a rough surface, but too much grit-blasting was detrimental to the adhesion; the authors state that this is due to substrate damage. In [91], different bond coats were applied to the CFR (carbon fibre reinforced)-polyimide substrates prior to the PS application of an Al_2O_3 topcoat. The TWAS applied bond coats were Al and Zn, in addition Al, Zn, Cu and Ni_3Al were applied as bond coats using PS (the Cu and Ni_3Al were unsuccessful due to thermal damage). The TWAS Al coating also thermally damaged the substrate, and thus gave the lowest shear adhesion strength (≈7.5 MPa). The TWAS Zn coating did not damage the substrate and had adhesion values in line with the PS Zn (10.9 MPa) and Al (11.9 MPa) which were not seen to thermally damage the substrate. In [92], Zn-Al was deposited by TWAS at different arc powers, ranging from 25 – 45 kW. It was observed that higher adhesion strengths were obtained at higher spraying powers, peaking at 40 kW (13.8 MPa) and then reducing at 45 kW where there was evidence of thermal damage to the substrate. It is stated that the fracture faces showed that at 40 kW, there is evidence of good bonding between the coating and the fibres which is not apparent at the lower spraying powers. The facture faces indicated that at high spraying powers, the Al bonded well to the carbon fibres.

2.7.4 Plasma spray

The majority of work concerning thermally spraying coatings onto FRPs and polymers has been carried out using PS techniques. One of the first research papers found on this

topic was a 1989 conference paper by Ducos [93]. In this work, glass fibre reinforced polymers were PS with different materials, B_4C, Al and Al_2O_3 (the latter with a polycarbonate base coat) and CFR Epoxy was coated with Ca stabilised ZrO_2. Few details are given about the work or coatings but the importance of spraying in a controlled atmosphere is stressed as well as the need for sufficient cooling of the substrates. This was achieved by spraying in a low pressure argon atmosphere and using liquid argon to cool the substrate whilst spraying. The paper states that a sprayed polymer bond coat (as used for spraying the Al_2O_3 coating) must be thermoplastic to be effective. This is so that sprayed particles are "sealed into the undercoat" during spraying. In addition, the paper introduces an additional surface activation technique (plasma treatment) prior to spraying. Few details on the process are given, and reported results show the plasma treatment increased the adhesion results from < 1 MPa in all cases to $\approx$2– 9.5 MPa depending on the coating/substrate system. No mention is made of any physical preparation (e.g. grit-blasting) of the substrate. This would account for the poor adhesion of the untreated samples as there would be little to no keying. Presumably after surface activation, there would be some sort of chemical adhesion accounting for the increased adhesion, or at least the plasma activation might have roughened the surface slightly.

In a 1995 conference paper [94], Henne and Schitter outlined investigations where polyphenylene sulphide (PPS) and polyaryletherketone (PAEK) thermoplastic polymers were successfully plasma sprayed onto steel and CFR-phenolic resin substrates. In addition plasma sprayed metallic (NiCr 80/20) and ceramic (Al2O3 TiO_2 97/3) topcoats were successfully applied to the thermoplastic coatings. It was stated that applying PS coatings to the CFRP substrates is more challenging than to the metallic substrates because of the potential for thermal damage. The study observed "open" porosity in the sprayed coatings and attributed this to out-gassing from the CFRP matrix during heating. The study stated that the open porosity observed in cross sections was reduced when PPS was sprayed instead of PAEK due to its lower melting temperature.

The aim of Reardon in [95] was to develop a PS bond coat which would allow the application of functional topcoats to polymer substrates. Several different substrates were sprayed including two different glass reinforced plastics (polycarbonate and cured phenolic resin). The bond coat was applied after lightly grit-blasting the surface so as not to expose the fibres. The final bond coat consisted of 300 series stainless steel, epoxy and nylon. They determined that proportions of 95, 2.5 and 2.5 % respectively are optimal (these work out to be approximately 75, 12.5 and 12.5 % respectively in terms of volume percentage). Interfacial bond strengths of 10.6 and 6.1 MPa for the

bond coat were obtained for the glass reinforced polycarbonate and cured phenolic resin respectively. Interestingly, when a top coat of Fe-Mo was applied on top of the bond coat the adhesion of the system increased to 17.9 and 12.4 MPa respectively. Reardon pre-heated the substrate to 65℃ prior to spraying them; no obvious thermal degradation is noted in the paper. However, it is clear that the fracture surfaces of the adhesion test coupons must have been examined as mention is made of residual material remaining on the adhesion tests. They state that more residue is typically found on thermoplastic then the thermosetting ones indicating better adhesion to those substrates.

Alonso et al. [96] investigated several different 2-phase bond coats deposed by air PS onto CF epoxy substrates. An erosion resistant top coat (Al_2O_3 or WC-Co) was then applied on the bond coat. The substrates were all lightly grit-blasted prior to the application of the bond coat. The study reports concern about possible thermal damage to the substrate, and thus cooling air jets were used. A relatively large stand-off distance was also used, presumably for the same reason. The bond coats investigated had mostly a variety of Al-glass mixtures. There were two glass powder sizes used (50 and 100 µm) and a range of glass weight percentages (10 – 35 %). These bond coats gave reasonable tensile adhesion (7 – 11 MPa). The highest of these adhesion strengths (11.2 MPa) was produced with the larger (100 µm) glass powder at the lowest weight proportion of glass (10 %) tested. Higher adhesion strengths were obtained with AlSi/polyester (15.4 MPa) and stainless steel/plastic (16.3 MPa) bond coats but neither of these coatings were capable of having the Al_2O_3 or WC-Co applied as they damaged the deposited bond coat.

Ashari and Tucker [97] briefly outline several different investigations into plasma spraying erosion resistant coatings onto different FRPs. Although they do not state many details or show mechanical data for the coatings they highlight what in their approach has been successful. They state that direct application of wear resistant coatings (e.g. WC-Co) was not possible and that bond coats must first be applied for CFRP (direct application was found to be possible on GFRP). Several bond coats were found to be successful including Ni (plated and PS), as well as PS PEEK, nylon and polyimide.

Huang et al. [98] [99] investigated different Al and Zn bond coats deposited by APS for an yttria stabilised zirconia (YSZ) thermal barrier top coat. Prior to coating the CFR-polyimide substrate, it was ground with abrasive paper; the grinding removed most of the polyimide resin leaving mostly exposed fibres on the surface. X-ray diffraction (XRD) of the deposited coatings revealed a low oxide content and appreciable residual stresses. Thermal shock tests of the coated substrates revealed that the Zn base coat

had a greater thermal shock life than the Al base coat. It also showed that the thinnest Al coat investigated (30 µm) in combination with the thickest YSZ top coat (130 µm) gave the best thermal shock life when using an Al base coat.

More recently researchers from the Centre for Composite Materials and Structures at the Harbin Institute of Technology have used plasma spray to coat FRP substrates [100] [101]. The studies are broadly similar to the research group's work investigating TWAS. Song et al [100] investigated the effect of PS power on coating quality. In the study, PS PbSn coatings were deposited with different plasma powers ranging from 35 – 45 kW. The lower power settings led to deposited splats on the surface not being fully molten on impact and thus to low adhesion. Adhesion was seen to increase with increasing power up to a peak of 14.2 MPa at a power of 40 kW. Above this, there was thermal damage to the substrate and a reduced adhesion strength. Guanghong et al. [101] conducted similar work with Al bond coats on FRP substrates. They were deposited with different plasma powers and at stand-off distances. It was observed that the lowest shear adhesion strength (1.7 MPa) was obtained when spraying with the lowest power (0.98 kW) and the highest stand-off distance (190 mm). The spray particles deposited at these conditions were seen to be less molten upon impact that those sprayed at the other conditions. The highest adhesions recorded (5.21 MPa) were using the highest power (1.17 kW) conditions at the greater stand-off distance (190 mm).

Ganesan et al. [50] investigated the effect of different CFRP surface treatments on an Cu coatings deposited by APS (this study is briefly mentioned in 3.2.3). Samples were treated in one of three ways: chemically (with a variety of reagents giving a Ra of 7.8 µm); thermally (with pre-exposure to the plasma plume giving a Ra of 6.8 µm); or mechanically (with grit-blasting giving a Ra of 9.3 µm). XPS of the treated surfaces showed a change in surface chemistry on the chemically and thermally treated samples. The morphology of the splats for all of the surface preparations is said to be the same, from the images of the surface it appears that fibres are not exposed on the surface. Adhesion tests showed a small rise in tensile adhesion (to around ≈2.6 MPa) for the chemically treated samples and a small decrease (to ≈1.5 MPa) for the thermally treated samples in reference to the adhesion of the grit blasted sample (≈2.3 MPa). These changes are within the error quoted in their figure and they attribute the slight (apparently insignificant) rise in adhesion for the chemically treated surface sample having increased surface energy and a higher proportion of C-O and C-N groups identified in the XPS.

2.7.5 HVOF spraying

Ivosevic et al. [102] [103] [104] [105] [106] investigated the use of HVOF spraying to deposit erosion resistant coatings onto carbon fibre reinforced polyimide substrates. Their approach was to 'functionally grade' the coatings i.e. blend the coating make-up from 100 % polyimide polymer to 100 % WC-Co. Thus ensuring affinity between the substrate and coating as well as grading the coefficient of thermal expansion (CTE) mismatch across the coating system. Prior to application, the CFR polyimide was lightly grit-blasted with 60 mesh Al_2O_3 grit and the coating was heated whilst spraying. The polyimide layer was found to contain a high volume fraction of pores; the authors state that this was likely due to gases produced in the polyimide coating due to residual condensate products and polymerisation occurring. The coating system failed mostly cohesively in the substrate at 5.3 – 8.4 MPa. In the as-manufactured condition (i.e. without preparation or coating), the substrate failed in tension at an average stress of 17.5 MPa , indicating that the coating process had damaged the substrate. The authors suggest that this may be due to damage sustained whilst grit-blasting of the composite i.e. damaging fibres.

In addition to the work above, Dixit et al. [107] successfully used HVOF spraying to coat a high temperature CFRP with Ni-based base coats and a WC-Co-Cr erosion resistant top coat. No adhesion measurements are reported but the coatings performed well in erosion testing. The authors used very fine grit (100 grit) to blast the substrate and emphasise the need for sufficient application of substrate cooling during spraying. The substrates were also plasma cleaned prior to spraying.

2.7.6 Cold spraying

Several researchers have tried to deposit metallic coatings onto polymers [108] [109] and FRPs [109] [110] [111] [112] using a cold spray process. However, attempts have had only limited success. Some metals e.g. tin can sometimes be deposited but typically materials imbed in the plastic and coherent coatings are not formed. Researchers have often resorted to depositing a bond coat with a traditional thermal spray process prior to cold spray deposition. Despite the difficulties, there are several different studies in this area, a good review of them is given in [113] but further detail is not given here.

2.7.7 Discussion of literature regarding thermal spraying onto FRP composites

The literature outlined above indicates than many previous studies involved a trial and error approach so the purpose of this section is to try to extract systematic understanding from rather disparate literature.

Surface preparation / bonding mechanism

Interfacial adhesion of traditional thermal spray coatings onto metallic substrates is often attributed to a mixture of physical, chemical and mechanical mechanisms. The contribution of each mechanism for a particular coating system is difficult to ascertain; however, all factors may play a part. When thermally spraying metallic coatings onto polymer based substrates, most authors report that without prior abrasion, coatings build-up was not possible [6] [90]. This indicates that most, if not all, of the adhesion strength of thermal spray coatings onto polymers/FRPs comes from mechanical keying. Therefore, some degree of abrasion is required for a thermal spray coating to adhere. However, the literature is less clear as to what constitutes appropriate abrasion for polymers and FRPs and which features of an abraded surface define one that is well prepared.

When plasma spraying polymer/stainless steel bond coats onto FRPs, Reardon [95] asserts that an optimal grit-blasting treatment would not expose any underlying fibres. It is unclear if this assertion has an evidential basis. However, given that the coating contained polymer components, it may have had a particular affinity for the polymer surface. Applying this hypothesis could limit the extent of surface preparation as the polymer layer on the surface of a typical FRP can be thin and taking care not to expose fibres would severely limit the scope to develop significant roughness on a FRP substrate.

Other authors are less explicit about any surface morphology recommendations. Despite this, there are indications from their work that more severe grit-blasting and exposed fibres are beneficial. Zhu et al [114] noted infiltration of their HVOF sprayed Zn bond coat into carbon fibres and suggest that this was positive. Wang et al. [92] observed carbon fibres embedded within their TWAS Zn-Al coating after it had been removed during adhesion testing. The authors suggest that this cohesive failure within the fibre phase of the substrate is evidence that there is good adhesion between their coating and carbon fibres, implying that exposed fibres are positive for coating adhesion. Ivosevic et al [105] [106] also observed a level of cohesive failure within their CFRP substrate during coating adhesion tests. This was evidenced by fibres being present on the failed HVOF-sprayed polyimide coatings. These failures happened at significantly lower stresses than

the cohesive strength of the control samples. The authors attribute this to damage caused to the underlying substrate as a result of grit-blasting. This highlights the problems with grit-blasting a CFRP substrate too severely as it can reduce its cohesive strength. This is likely because it exposes and fractures the carbon fibres at the surface, weakening the cohesive strength of the surface layer.

Lie et al. [3] highlights the importance of ensuring the correct level of substrate grit-blasting. In their study, CFRP substrates were grit-blasted with various grit-sizes and pressures before coating them and performing adhesion tests. The results showed that for the finer grit investigated, increasing the pressure of grit-blast rapidly increased the shear adhesion strength of the coating up to a blast pressure of 0.4 MPa (58 psi). The adhesion strength then remained relatively constant, with some indication of a slight downward trend. For the coarser grit tested, the highest shear strength was attained at the lowest reported blast pressure. This was also the highest reported obtained in the study. In this case, as the pressure increased, there was a trend of reducing shear adhesion strength. This study shows that some abrasion is required to attain adhesion but if this is too aggressive, the adhesion strength of the sprayed coating was reduced, presumably introducing a component of cohesive failure within the substrate. This effect could also be in part due to exposing different proportions of the different phases (resin and fibre) on the surface and differential adhesion to the two phases.

Another method used to achieve interfacial coating adhesion is the use a composite bond layer. This bond coat contains a polymeric phase which can adhere to the substrate and an additional phase e.g. stainless steel [95] [96] which metallic coatings have a more effective bond to. This metallic phase may possibly act as an asperity for mechanical adhesion. Similar bond coats can also act to smooth large CTE differences [103]. Instead of thermally spraying bond coats, some authors have glued or impregnated their composites with hard particles prior to spraying [90] [6]. Instead of abrading the surface or using a bond coat, some researchers have attempted to modify the chemistry of the substrate to promote adhesion. This approach is rare and the results obtained have been mixed, with the mechanisms unclear. Ganesan et al. [50] treated the surface of CFRP samples with a mixture of reagents and thereby increased the concentration of O and N species on the surface and increased the substrate's surface energy. The effects of this treatment on the thermal spray coating were marginal at best. In contrast, Ducos [93] found significantly increased adhesion of coatings (100 – 1500 %) after his plasma treatment. The proposed mechanism for this significant improvement was that the ion bombardment removed adsorbed gas and "created sites" for the coating to adhere. It is unclear exactly what is

meant by the last statement but the mechanism could be due to a cleaning action (as utilised in [107]), micro-roughening (as induced in [115]) or functionalising the surface, perhaps allowing for some chemical bonding. The above literature makes it clear that surfaces must typically be roughened prior to thermally spraying the substrates. However, there is little knowledge regarding the morphology of the substrate required in order to optimise adhesion or the mechanisms involved.

Thermal damage to the substrate

Heat input into the substrate is an unavoidable consequence of thermal spraying. The heating of the substrate probably stems from both being in the vicinity of the heat source used for melting the feedstock material and directly from the impact of molten feedstock particles. Excessive heat input has been shown to damage the polymer/FRP substrates causing cohesive failure within the substrate [91]. Researchers have claimed that it has led to out-gassing from the substrate into the coating causing porosity [94]. Many studies try to pre-empt this possibility with simple strategies such as cooling air jets [107] [89], fast passes [89], long stand-off distances [96] or more extreme measures such as cryogenic liquid cooling [93] [116]. Liu et al. [91] plasma sprayed Al, Zn, Cu and Ni_3Al onto a very high temperature tolerant (371℃) fibre reinforced polyimide substrate. The low melting temperature feedstock materials (Zn and Al) had reasonable adhesion to the substrate. This is in contrast to the higher melting temperature materials (Cu and Ni_3Al) sprayed with similar (though not identical) parameters which had very poor adhesion. The latter had caused thermal damage in the resin phase of the substrates, reportedly causing the resin to no longer adhere the fibre phase. This study indicates the general trend that higher melting temperature feedstock materials are more prone to cause damage to the polymer based substrate than lower melting temperature ones. However, even very low temperature feedstock materials can thermally damage an FRP substrate material, and the spraying parameters will have an influence this. Song et al. [100] plasma sprayed a PbSn alloy (melting temperature 232℃) onto a heat tolerant (372℃) CFRP substrate. They found that the coating adhesion increased with the plasma power; this was associated with more fully melted particles. However, above a critical set of parameters the adhesion reduced and thermal damage was evident on the substrate.

The method of thermal spray can also affect the heat input into the substrate. In Liu et al. [91] (discussed above) in addition to plasma spraying Al they also deposited Al coatings using TWAS. They found that the TWAS coating resulted in reduced adhesion

and reduced observable thermal damage to the substrate. Although it could well be argued that the TWAS parameters could be optimised in order to reduce thermal damage and increase adhesion, it does highlight that some thermal spray processes typically impart more heat input than others. Flame spray is typically associated with low heat input. This is demonstrated by Huonnic et al. [6]; aluminium was flame sprayed onto basalt fibres reinforced epoxy tubes and without any thermal precautions, no damage was reported.

From the above literature, it is clear that most researchers try to reduce the thermal input into a polymer substrate. However, there are a few instances where pre-heating of the substrate has been carried out. These have either been because of the specifics of the feedstock [102] or have had limited benefit [91]. In [102], the researchers were spraying a polyimide onto a FRP surface and the heating was introduced to aid the curing of the resin. In [91], a slight increase in shear adhesion strength (from $\approx$ 12 MPa - 14 MPa) was seen when applying a PS Al coating to a thermosetting polyimide substrate when the substrate was first pre-heated to 250℃.

Substrate properties

There has been apparently very little work investigating the effect of different substrate properties on thermal spray coating quality. There is some anecdotal evidence that glass fibres may be beneficial for deposition of some coatings. Ashari & Tucker [97] reported that chromium oxide could be directly deposited onto glass fibre reinforced polymer, but required a bond coat to be applied to a carbon fibre reinforced polymer (CFRP). Within the body of literature, it is reported that FRPs with different polymer matrix types have been used as substrates. Often the polymer phases used have relatively high operating temperatures [92] [3] [99]. In most of the reported studies, the resin phase of the FRP was a thermosetting polymer. However, in [95] a bond coat made up of nylon, epoxy and stainless steel was sprayed onto different polymers. In this work the observation was made that higher bond strengths were achieved when spraying onto thermoplastics rather than thermosetting polymers. In addition to this, in [93], Ducos states that the polymer bond coats applied to aid further TS coatings to adhere must be made from thermoplastic in order to be successful suggesting that thermoplastic matrices might be more suited as substrates for thermal spray

2.8 Literature review conclusions

The literature has shown that, although there are examples of successful deposition of metallic and ceramic thermally sprayed coatings onto CFRP, adhesion strengths are variable (<1 MPa - >20 MPa) and there are numerous difficulties and unknowns with spraying onto the FRPs mentioned below.

A recurring theme in the literature is concern about thermal damage to the polymer, some investigations have claimed to demonstrate this damage. Despite the concern there has been little systematic investigation into the use of a low heat input thermal spray technique such as flame spray. Where this technique has been employed, thermal damage has not been reported in the literature.

The primary bonding mechanism appears to be mechanical keying; evidence for any other type of bonding seems very limited. Grit-blasting is used as the principal surface preparation step prior to deposition of a thermal spray coating. There is some evidence of this causing damage to fibres and matrix but there has been little detailed and systematic characterisation of this prepared surface prior to spraying.

Furthermore, there is little work investigating whether the thermal spray coating adheres to both fibre and resin phases. The little work that does exist appears to imply that exposed fibres promote adhesion.

Finally, there is little work investigating the influence of the polymer matrix phase on the adhesion of thermal spray coatings to FRPs. Most studies have been on FRPs with thermosetting polymer matrix. Few studies have involved thermoplastic polymers as the matrix phase. The few that do exist [94] [95] appear to show that greater coating adhesion strengths can be achieved than with thermosetting polymers.

The rest of the thesis is structured to address each of these points. The investigation in focused on WFS as there appears to be very little work using this technology and there are indications that the low heat input of this technique is beneficial for temperature sensitive substrates. However, there is little work characterising the plume of WFS, thus the first results chapter investigates the properties of the WFS plume. The aim of this is to understand the properties of the impinging particles as well as the heat input into the substrate.

The second results chapter investigates how initial particles interact with polymer based substrates and whether they behave differently on different phases and polymer types. A common thermosetting and thermoplastic polymer/FRP were chosen in order as determine differences between these types of polymers.

The third results chapter fully characterises the surfaces of the prepared substrates

prior to coating. This is important so that differences can be mapped to differences in adhesion and microstructure.

The final results chapter characterises and tests WFS coatings deposited onto the different substrates. The results of these investigations are combined with the results of the previous chapters in order to draw out mechanistic insight into the coating process.

Chapter 3

Experimental Methods

3.1 Introduction

This chapter outlines the materials and the general experimental methods used throughout this thesis. Techniques which are primarily used in an individual section are not outlined here, instead they are explained within the relevant results chapters.

3.2 Materials

3.2.1 Substrate

Two different carbon fibre reinforced polymer (CFRP) materials have been used in these investigations, one epoxy based (CF-epoxy) and one PEEK based (CF-PEEK). These materials were chosen because they are typical aerospace grade CFRP systems; the former has a thermosetting matrix and later thermoplastic matrix. In addition to the fibre reinforced polymers (FRPs), materials representing the unreinforced polymer matrix were also used as substrates. Steel substrates were also sprayed as a base for comparison. Relevant available published properties (e.g. glass transition temperature, thermo-degradation properties etc.) for these materials are included below, and data sheets for these materials are reproduced in appendix A.

CF-Epoxy

The CF-epoxy substrate used in these investigations is constructed from TenCate E722 pre-impregnated carbon fibre cloth (pre-preg). It is a typical toughened epoxy based pre-preg with 2/2 Twill weave, with each individual fibre approximately 7 µm in diameter. A balanced 9 ply stack was used to create the final laminate (0°, 90° and +/- 45° plys).



Figure 3.1: Photograph of the as received surface of the CF-epoxy used throughout this study (Tencate E722), (a) smooth tool-face and (b) rougher non-tool-face

Table 3.1: Published materials data for the CF-Epoxy composite used in this investigation (Tencate E722) [117]

Property	Value
Tensile strength (MPa)	595
Stiffness (GPa)	59.1
Cure temperature (°C)	120

The final thickness of the composite was 2.3 mm and the weight was 3.2 kg.m^{-2}. The tool face has a smooth (Ra = 0.2 µm) texture, the non-tool face has a rough (Ra = 13.11 µm) texture. Both faces are completely covered with epoxy, and are shown in figure 3.1, relevant available properties are reproduced in table 3.1.

CF-PEEK

The CF-PEEK laminate used in these investigations is made from TenCate Certex® TC1200 pre-preg carbon fibre cloth. It is a thermoplastic pre-preg with a 4/1 twill weave, with each individual fibre approximately 7 µm in diameter. A balanced 4 ply stack was used to create the final laminate (0° and 90°). The final thickness of the composite was 1.3 mm and the weight was 1.9 kg.m^{-2}. Due to the manufacturing route of the composite, both sides of the laminate had a smooth (Ra = 0.8 µm) tool face surface with some of the underlying weave structure showing through in the topography of the final surface. The faces of the laminate are completely covered with PEEK resin. A picture of the substrate is shown in figure 3.2, relevant available properties are reproduced in table 3.2.



Figure 3.2: Photograph of the as received surface of the CF-PEEK used throughout this study (TC1200 CFRP), both sides were in contact with the tool and had the same surface finish

Table 3.2: Published materials data for CF-PEEK composite used in this investigation (TenCate Certex® TC1200) [118]

Property	Value
Tensile strength (MPa)	776
Stiffness (GPa)	51.1
Max service temperature (°C)	121
Glass transition temperature (°C)	143
Melting temperature (°C)	343

Table 3.3: Published material data from epoxy technical data sheet (Easy composites EL2) [119]

Property	Value
Hardness (Shore D)	84 - 88
Linear shrinkage (%)	0.5
Tensile strength (MPa)	70 - 80
Heat distortion temperature (°C)	82 - 88

Table 3.4: Published material data from PEEK technical data sheet (Direct plastics) [120]

Property		Value
Ball indentation hardness (MPa)		253
Modulus of elasticity (MPa)		4200
Tensile strength (MPa)		116
Elongation at break (%)		15
Glass transition temperature (°C)		150
Melting temperature (°C)		341
Heat distortion temperature (°C)		162
Coefficient of linear thermal expansion ($10^{-6}K^{-1}$)	23 – 60 °C	50
	23 – 100 °C	50
	100 – 150 °C	70

Epoxy polymer

It was not possible to obtain an identical polymer to that used as the matrix phase in the CF-epoxy. Instead a two part cold cure epoxy (Easy composites EL2) was used to represent the unreinforced thermosetting epoxy matrix. The resin was mixed as per manufactures guidelines and cast under vacuum in a bell jar. After curing, the epoxy was polished to 1/4 micron finish. Some pertinent material properties from the data sheet are shown in table 3.3, the full data sheet is reproduced in appendix A.

PEEK polymer

The exact makeup of the PEEK polymer used as the matrix phase in the CF-PEEK was unknown so a commercially available 6 mm PEEK sheet (Direct Plastics Ltd) was used as a substrate. Prior to processing, the PEEK substrates were polished to 1/4 micron finish. Some pertinent material properties from the data sheet are shown in table 3.4, the full data sheet is reproduced in appendix A.

C15 low-carbon steel

This is a standard grade of steel defined BS EN 10277 - 2: 2008, of nominal composition Fe-0.15% C- 0.55% Mn. It is a soft (98 – 178 HB) low-carbon steel. It was chosen because it is common and easily machinable. This material was used as a standard metallic substrate for comparison to the polymeric and composite materials in a number of thermal spray experiments.

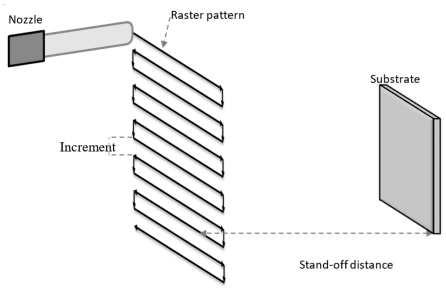


Figure 3.3: Schematic illustrating a generic raster pattern as used to both grit-blast and coat the substrates

Table 3.5: Grit-blasting parameters used throughout this investigation. Light grit-blast and heavy grit-blast parameters are typically referred to by their acronyms LGB and HGB respectively.

Parameter	Light grit-blast	Heavy grit-blast
Nozzle	Ti25-8 DV	CSD-X-8 / B
Static Pressure (psi) [MPa]	26 [0.18]	40 [0.28]
Working Pressure (psi) [MPa]	20 [0.14]	35 [0.24]
Traverse speed ($mm.s^{-1}$)	180	200
Stand-off (mm)	150	150
Spray angle (°)	90	90
Raster increment (mm)	10	10
Grit mass flow rate ($g.s^{-1}$)	9	12

3.2.2 Wire feedstock

Aluminium wire (Metallisation O1E) of 2.3 mm diameter has been used throughout this investigation. This has a purity of 99% otherwise known as the AA 1100 alloy grade The data sheet for this feedstock is included in appendix A.

3.3 Grit-blasting

Grit-blasting was carried out using a mechanised pressure fed Hodge Clemco 2452NC Blast Machine within an isolated grit-blasting cell. For repeatability, the movement of the nozzle was automated using an OTC 6 axis robot. The robot moved the nozzle at a fixed stand-off distance from the surface of the substrate, rastering over the surface with a defined traverse speed and raster increment as described in figure 3.3. All grit-blasting was carried out with 80 mesh virgin brown alumina grit. Two different sets of parameters have been used for the blasting of the materials; Heavy (HGB) and Light (LGB). HGB refers to the more aggressive blasting parameters and LGB refers to the less aggressive set. The general settings are outlined in table 3.5.

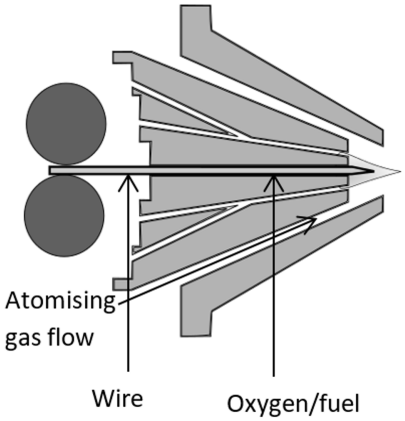


Figure 3.4: Simplified schematic of the wire flame spray gun showing how wire is fed into and external oxy-fuel flame which atomising gas is directed to

Table 3.6: Baseline wire flame spray settings used for spraying throughout the study, where these are deviated from it is clearly noted

Feedstock material	Al (2.3 mm diameter)
Feed rate ($mm.s^{-1}$)	40
Stand-off (mm)	160
Traverse speed ($mm.s^{-1}$)	1000
Raster separation (mm)	8
Spray angle (°)	90
Atomising Air ($l_n.s^{-1}$)	7.7
O_2 ($l_n.s^{-1}$)	1.25
C_3H_8 ($l_n.s^{-1}$)	0.25

3.4 Wire flame spraying

Wire flame spraying was conducted using a Metallisation MK73 flame spray system (figure 3.4). Industrial propane was used as the fuel gas in a stoichiometric oxygen-fuel ratio. All gasses were monitored using mass flow meters and the baseline settings used are shown in table 3.6. For positional repeatability the gun movement was controlled using an OTC 6 axis robot an industrial robot. When coatings were produced, the gun was rastered over the substrate as shown in figure 3.3.

3.5 Wipe tests

Wipe tests are samples which have been exposed to the thermal spray plume for very short amount of time such that they have a sparse population of individual splats deposited on them. In this study a wipe test rig was designed and constructed. The rig consisted of a mask with a thin 2 x 40 mm slot mounted on an inverted pendulum. The samples were mounted behind the mask and the mask was passed over the sample such that the sample would be exposed to the plume for a short amount of time. The pendulum moved by a

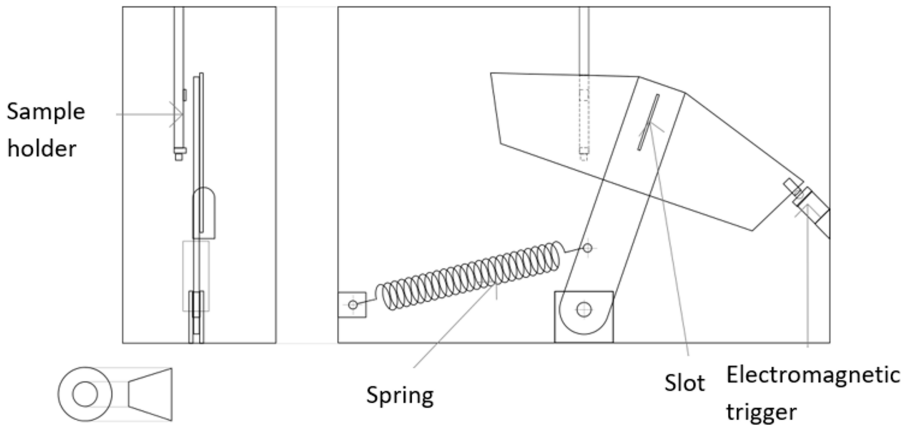


Figure 3.5: Schematic representation of wipe test jig used in investigation. The slot passed briefly over the substrate allowing the sample exposure to plume

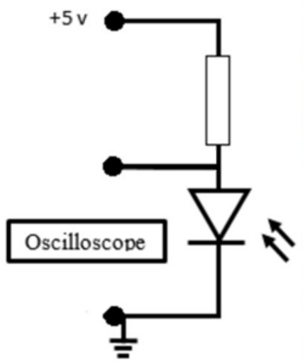


Figure 3.6: Photograph of light gate acquiring shutter open time data

spring and triggered with an electromagnet, a schematic of this is shown in figure 3.5. The velocity of the pendulum was calculated with a light gate and oscilloscope as shown in figure 3.6. It was found that the pendulum and slit arrangement exposed a point of the sample to the spray plume for 0.3 ms.

3.6 Metallographic preparation

Metallographic samples were cut/sectioned with an ATA Brillant [sic] 220 using appropriate abrasive slitting wheels. Samples were always cold mounted in Struers Epofix, this was done to ensure that the high pressures/temperatures associated with hot mounting in bakelite did not affect the coatings or the temperature sensitive substrates. Samples were then ground using a Buehler Phoenix 330 variable speed grinder / polisher using progressively finer SiC papers (60, 120, 320, 600, 1200 and 2500 grit). Samples were polished with a Metoserve 250 grinder/polisher using progressively finer diamond pastes (3, 1 and 1/4 µm). Where required samples were then finally polished on an ATA Saphir

560 with an OP-U solution.

3.7 Optical microscopy

Various different optical microscopes were used to image samples at a variety of different objective lenses (2.5 - 50x). Images were captured using specialist software (Leica application suite version 4.4.0 and Olympus stream essentials version 1.9.2). Digital processing of these images was carried out using ImageJ/FIJI Version 1.45b.

3.8 Scanning Electron Microscopy (SEM)

SEM was used to capture high magnification images of the samples. It is an established technique and many reference texts exist explaining the fundamentals of the process e.g. [121] [122]. These can be referred to should the reader require an in-depth explanation of the process. Images have a large depth of field meaning the technique is particularly useful for characterising rough samples, like those examined in this study. The technique typically requires samples to be electrically conductive; thus, prior to imaging thin (nm) Au coatings were deposited onto non-conductive specimens using an Edwards S150B sputter coater.

SEM Imaging was carried out using a Zeiss EVO LS15 equipped with a field emission (LaB6) element as the electron source generating the electron beam. Images were taken using the secondary electron (SE) and back scattered electron (BSE) detectors, these detect different types of electrons emitted from the sample due to interactions with the electron beam. The former (SE mode) detects low energy electrons emitted from the sample as the electron beam inelastically interacts with the volume near the surface of the sample. This mode highlights sharp edges and thus was useful for characterising the roughness / topography of the samples. The latter (BSE mode) uses back scattered (reflected) electrons resulting from elastic collisions of the electron beam with the sample. Elements with higher atomic weights back scatter greater numbers of electrons, thus the technique was useful for highlighting elemental composition change. These electrons can come from a greater depth than secondary electron and the maximum resolution is less. This is because of the characteristic tear drop shape of the interaction volume shown in figure 3.7. As the depth increases, the area of interaction increases and thus the resolution becomes less [123]. However, in this mode the images are less affected by small amounts of sample charging. This characteristic was particularly useful as many of the rougher samples in this study had some amount of charging, even after sputter coating.

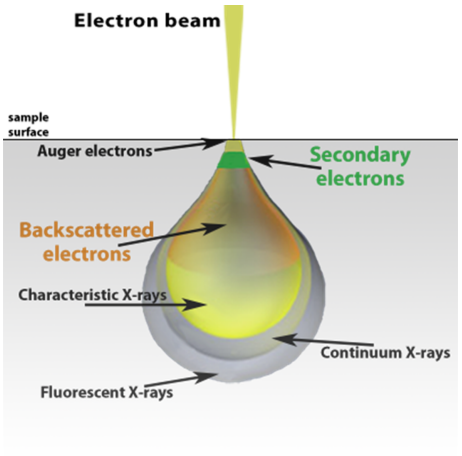


Figure 3.7: Schematic of electron beam/sample interaction volumes illustrating where different electron signals come from within the sample showing that as depth increases the interaction area increases, reducing maximum resolution [123]

In addition to SE and BSE imaging, energy dispersive X-ray (EDX) spectra and maps were taken using Oxford instruments (X-MAX^N). The technique detects characteristic X-rays emitted from atoms as high energy electrons move to occupy lower energy states after an inelastic collision. The X-rays can come from deeper in the sample [123] than BSE or SE and thus the technique typically has a lower spatial resolution. With reference to standards, this technique can identify elemental makeup in a semi-quantitative in way. However, in this study it was used qualitatively to map surface areas and to broadly identify elements. Where possible the accelerating voltage was 20 kV and the working distance was 8.5 mm; however due to practical or sample difficulties this was not always possible.

3.9 Focus variation microscopy (FVM)

3-dimensional surface topography measurements (depth images) were taken using a focus variation microscope (FVM) (Alicona infinite focus SL). This is a relatively new technique of topographical measurement which is somewhat similar to confocal microscopy [124]. The technique gives topographical and real colour representations of the measurand surface. The depth images are constructed from a serious of low depth of field images of the same location taken at different focal distances. Due to the low depth of field of the images, each region of the surface is only in sharp focus at the correct focal length (i.e. in one image). Algorithms determine in which image each region of the surface is sharpest, this is done with metric maximising the local standard deviation of the pixel values [125]. This gives the distance between the sensor and each region of the image and thus a 3D topographical map (depth image) of the surface can be constructed. The

technique allows for external lighting and utilising a ring light, features as steep as 80 - 87° can be imaged [125] [126].

Images were taken using different objective lenses (5 – 50x), the most appropriate lens was chosen for each sample and the level of features for be distinguished. The higher magnification lenses led to reduced depth of field, thus a greater vertical resolution of up to 20 nm for the 50x lens [126]. Increasing the objective magnification also increased the lateral and longitudinal resolution with the accompanying reduction in measurement area. However, the samples were mounted on a motorised stage such that multiple depth images could be taken and stitched together to form a larger image.

This measurement technique can have trouble measuring very smooth and transparent samples due to difficulty adequately detecting the sharpest focal distance [125]. Thus, there was some difficulty measuring the surface of the smooth polymer and composite samples which had some level of transparency. In these samples, the roughness parameters obtained (discussed below) did not initially match equivalent measurements taken using a contact profilometer (Taylor Hobson Form Talysurf 40). The semi-transparent nature of the sample meant there was difficulty in determining the in-focus focal plane. The problem was overcome by sputter coating the samples prior to measurement. This problem is discussed, and evidence is presented in Appendix B.

When measuring roughness, the appropriate objective lens and filtering frequencies are a function of the topography of the substrate. In this work, the objective lens and filtering frequencies were chosen in line with the manufacturer's recommendations and measurements were generally carried out in accordance with BS EN ISO 4287:1998.

3.9.1 Roughness parameters

In these investigations (as well as in the wider literature), surfaces roughness have typically been characterised by roughness (R) numbers e.g. Ra. R numbers are statistical measures of filtered topographical data. These topographical data are in the form of line traces; in this work these were extracted from depth images, however, more typically measured with a stylus measurement device e.g. Taylor Hobson Form Talysurf 40. These line traces are band pass filtered to remove low frequency form and waviness as well as high frequency noise prior to characterising the roughness (graphically illustrated in figure 3.8). The most commonly used of these R numbers is Ra, which is the average absolute deviation from the mean of the data. Rq is the variance from the mean line, and Rsk is the skewness of the data around the mean line. Clearly, this single number is necessarily a simplification of the surface and only reveals an individual statistic about

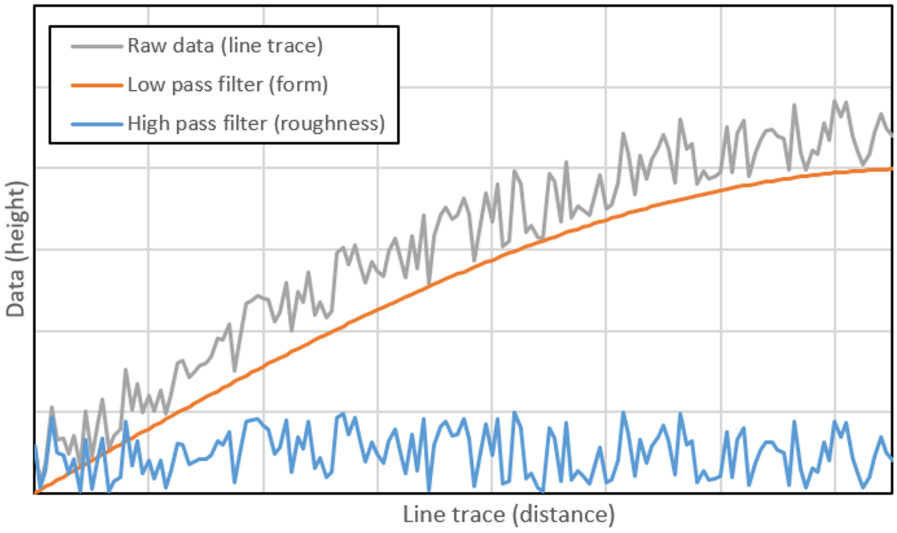


Figure 3.8: Illustrative plot showing raw line trace data and how it is high and low pass filtered to remove leave roughness and waviness data respectively

Table 3.7: Different roughness parameters (from BS EN ISO 4287:1998) [127]

Roughness parameter	Calculation	Description
Ra	$\frac{1}{n}\sum_{i=1}^{n}\lvert z_i\rvert$	The average absolute height of perturbations on the surface from the average profile height. This measure is also known as the Arithmetic Average (AA)
Rz	$\lvert z_{min}\rvert + \lvert z_{max}\rvert$	This is the height difference between the lowest valley and the highest peak in the sample length.
Rq	$\sqrt{\frac{1}{n}\sum_{i=1}^{n} z_i^2}$	This is the Root Mean Squared (RMS) value of the surface height over the sampling length
Rsk	$\frac{1}{R_q^3}(\frac{1}{n}\sum_{i=0}^{n} z_i^3)$	This is the skewness of the distribution of the points measured along a sampling length. i.e. whether it is positively or negatively skewed. This highlights the effect of isolated features

the surface topography. There are many different R numbers which give different statistical information about the surface (each denoted by different suffixes), thus there is not necessarily any relationship between R parameters. Any relationship that may exist is completely surface dependent [7, p. 69]. A non-exhaustive list of different roughness parameters are shown in table 3.7 [127]. The parameters shown in the table are defined for a single sample length. In practice several sample lengths are measured within an evaluation length; these are averaged to calculate the parameter [128, p. 3].

As stated previously, before calculating roughness parameters raw topographical data are filtered so that the results are not affected by lower frequency form, waviness features or noise [129]. In addition to R numbers there are Waviness (W) numbers and Primary (P) numbers, which are calculated using the same approach as outlined in table 3.7. However W numbers are filtered with a lower frequency band pass filter so that waviness

is measured and P numbers are calculated from the primary profile, i.e. no prior filtering (other than to remove measurement noise) is applied [127]. The filtering cut-off values depend on the sample and measurement equipment; some default figures are shown in [127].

3.9.2 Spacing parameters

Spacing parameters look at the spacing of topographical features on the surface, they can characterise topographies filtered for primary, roughness or waviness measurements, and are denoted as such, e.g. RSm. As with R numbers, there are different types of S numbers that denote different characteristics of the surface. A commonly used S parameter is Sm, the mean profile width within a sampling length, i.e. the average distance between the trace dropping below a defined height, often 10 % of Rz [127]. In addition to height and spacing parameters there are hybrid parameters which take into account both spacing and height, one such parameter is Rδq which is the root mean squared (RMS) of the gradient over the sampling length, as defined in equation 3.1.

$$R\Delta_q = \sqrt{\sum_{i=1}^{n} (\frac{\Delta z}{\Delta x})^2} \tag{3.1}$$

3.9.3 3-dimentional roughness parameters

Recently non-contact 3d profilometers (e.g. Alicona infinite focus SL) have become more common, these allow the collection of a 3d instead of a 2d data set. In order to analyse these 3d data sets surface (S) parameters have been defined in [127]. Many of these S numbers are 3d equivalents of R numbers e.g. Sa is the direct equivalent of Ra but with a the third dimension added, i.e. the average is taken over the defined area, not length. Limited use has been made of these in this study for three main reasons. They give similar information to their R equivalents; there are complications in defining the appropriate filter for the samples; and all of the current relevant literature use R not S numbers.

$$Sa = \frac{1}{XY} \sum_{x=1}^{x=X} \sum_{y=1}^{y=Y} |z(x,y)| \tag{3.2}$$

Chapter 4

Wire Breakup and Particle Behaviour in Wire Flame Spray

4.1 Introduction

This thesis is primarily concerned with using WFS to coat FRPs. FRPs are sensitive to hot erosive environments, thus WFS (which is generally regarded as having low particle velocities (50 - 200 $m.s^{-1}$) and heat input) [15] [13] appears to be an attractive process for the application. However, very little work has been published where the break-up of the wire and the properties of the plume have actually been measured. This chapter is concerned with using modern particle diagnostic techniques to investigate wire break-up and measure these properties. This work is important to confirm the suitability of the process for the application and to understand the properties of the particles so that these can be taken into account in further analysis of the coating system. Much of the work in this chapter has been separately published by the author in the Journal of Thermal Spray Technology [130].

4.1.1 Literature review

This literature review gives a general introduction to modern particle diagnostic systems, briefly discussing their operation, mentioning some of the major commercial variants and their application to wire-fed processes. A point is made to outline the few studies where WFS particle properties have been measured in the literature.

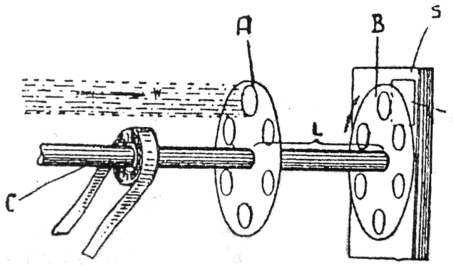


Figure 4.1: Schematic of mechanical arrangement to determine thermal spray particle velocity by spraying through two spinning discs (a & b) onto a sample (s) [131]

Early velocity measurement

Velocity measurements of particles within the thermal spray plume have been attempted as far back as 1926 [131]. Early measurements were conducted using specially designed mechanical apparatuses e.g. Figure 4.1 (reproduced from [131]). Two identical discs with holes spaced around the periphery are mounted on a shaft at a fixed distance from each other such that the holes in the two discs align with each other. The shaft is spun at a known angular velocity and a thermal spray gun is positioned such that it sprays through the holes/onto the discs as the discs rotate. A sample placed on the other side of the rotating discs so that particles which pass through the holes in both discs will deposit on it. The mass deposited onto the sample is a function of the geometry of the apparatus, particle velocity and angular velocity of the discs. Thus, by measuring mass deposited as a function of angular velocity the particle velocities can be determined. The book [131] gives typical measured particle velocities for flame sprayed particles (likely WFS) of 120 and 140 $m.s^{-1}$ for brass and zinc respectively at 0.1 m from the nozzle. Mechanical methods such as these have typically been considered unreliable [132] and more technologically advanced techniques such as Laser Doppler anemometry (LDA), two focus velocimetry (L2V) and particle image velocimetry (PIV) have since been developed. These techniques are briefly outlined in the following paragraphs before an overview of the main industrial particle diagnostic systems is given.

Laser Doppler anemometry (LDA)

LDA is outlined and discussed in many references including [133, p. 193 - 194] and [134], it works by directing in-phase laser beams toward each other at a known angle so that they meet and interact at a point. The coherent light beams interact and cause interference patterns with known spacing to form. As a particle passes between the pattern and the detector it blocks part of the interference pattern from an optical detector (Figure 4.3). As the particle moves across the bright and dark fringes it blocks different amounts of

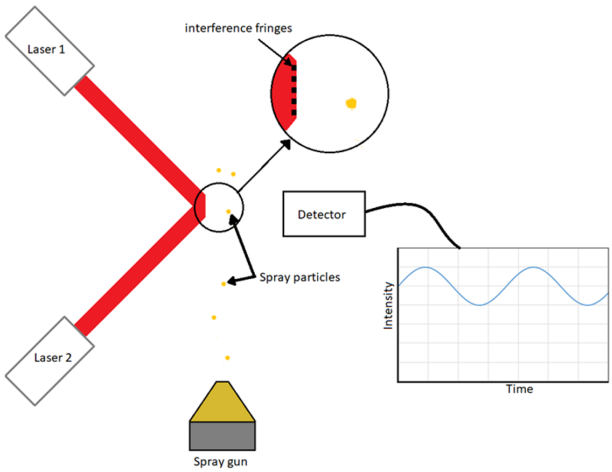


Figure 4.2: Simplified schematic of laser Doppler velocimetry showing how particles pass formed light fringes causing a signal in the detector which is a function of the particle velocity (normal to the fringes)

light from reaching the detector, thus by processing the intensity of light the particle velocity perpendicular to the fringes can be determined. Additional signal processing can determine some size information.

Laser two focus velocimetry (L2V)

This method is also outlined in [133, p. 195] and [134] as well as many other reference texts. The general principle is to have two parallel focused laser beams in close proximity in the measurement volume as particles pass through the individual beams they scatter light which can then be detected. The time offset between the scattering events in the two beams allows for velocity determination. Such a system was used in [135] to determine particle velocity in the plume of a TWAS gun spraying steel.

Particle image velocimetry (PIV)

PIV is discussed in many sources including [133, p. 195 - 197], [136] and [137]. The technique involves taking images of the particles within the measurement volume in quick succession. Particles are either imaged once per a frame or of there are multiple exposures of the same particles in a single frame. The former can require the camera/detector to have a very high frame rate and the later requires a fast strobing light source. Images are then processed to determine the particle velocities; this is either done by tracking and pairing up the individual particles in the image(s), or breaking down the image into sections and performing auto/cross-correlations to determine the average particle movement in each of these areas.

Industrial sensors

From the late 1990s robust industrial particle diagnostic tools utilising of some of the techniques mentioned above have been on the market. Some of the main commercial variants available today are the DPV (TECNAR Automation Ltd., St Bruno, Canada), the Accuraspray system (TECNAR Automation Ltd., St Bruno, Canada) and Spray-Watch (Oseir, Tampere, Finland). Instead of using lasers to illuminate particles as done in LDA and L2V, the hot thermal spray particles are detected from their own emitted infrared (IR) light. The intensity of the IR light is also used to determine the particle temperature through the use of two wavelength pyrometery (TWP) [138]. Relatively cold thermal spray particles (<1000℃) do not emit enough IR radiation to be detected and lasers are used to illuminate them for detection, therefore particle temperature cannot be determined in these cases.

The Accuraspray and the DPV systems use a measurement method which is similar to the L2V method (described in 1.1.2). IR Light emitted from the particles is detected by a photodiode at two closely spaced measurement volumes. The offset of the signals allows for time-of-flight velocity measurements and TWP of the detected light can be used to determine particle temperature. One of the main differences between the systems is the distance between measurement regions, and thus the size of the measurement volume. The measurement volume for the DPV is around 1 mm^3 and for the Accuraspray is >150 mm^3. The small measurement volume of the DPV system means that (assuming the particle loading of the gas stream is low), it is reasonable to assume that the infrared light passing the sensor at any point is emitted from a single particle, thus each datum point recorded is representative of a single particle and the signal intensity can be used to determine particle size. With the larger volume of the Accuraspray, the signals come from multiple particles and thus they represent an average measurement. This also means that particle size cannot be determined [139].

The SprayWatch system is based around a relatively high speed camera and takes a PIV based approach. The system either directly implements PIV or utilises the similar technique called particle streak velocimetry (PSV). When the particles are hot/bright enough to not require additional laser lighting the PSV approach is used. In this mode, the exposure times of the camera are set sufficiently long such each particle forms a streak across the image, the length and direction of these streaks allows for simple time of flight calculation of velocity and the width allows the diameters of the particles to be calculated. The emitted light also allows an ensemble TWP temperature measurement.

When the particles do not emit sufficient IR radiation for direct detection a laser

strobe is used to illuminate the particles and more traditional PIV approach is taken. The system can either be configured to use a sheet or backlit laser, i.e. normal to or opposite the particle detector. The laser strobe flashes three times within each exposure and thus the images are triple exposed resulting in three images of the same particles in each image. A particle tracking based approach is used to determine individual particle velocity vectors and the diameter of the particles is measured normal to the velocity vector [140].

Wipe tests

In addition to modern particle diagnostic systems, in order to understand how particles interact with the substrate, wipe tests are often also used to assess the flattening behaviour of the particles as they splat on the substrate. A wipe test is where a substrate is exposed to the thermal spray plume for a very short time period (fractions of a second); thus isolated splats are deposited and an instantaneous assessment of the plume can be made. This methodology is discussed in greater detail in chapter 3 .

Particle diagnostics in TWAS

Despite the availability of sophisticated particle diagnostics, relatively little attention has been paid to using the technique to investigate wire fed thermal spray processes i.e. WFS and TWAS. These processes are potentially more complex as they involve wire breakup and subsequent heat and momentum transfer to particles which may further breakup. Wire breakup phenomena have been studied to some extent within the TWAS literature [141] [142] [143] [144]. In [141] [142] [143], wire melting and disintegration was imaged during the TWAS process and the effects of changing process parameters were investigated. In [141], Hussary and Hederlein imaged the melting carbon steel feedstock during disintegration. The study noted that there was a diffuse arc attachment on the anode and a concentrated one on the cathode as shown in Figure 4.3 (a). The diffuse arc attachment on the anode led to diffuse heating which formed a thin layer of molten steel on the anode. The atomising air caused this to form a protruding sheet, which is visible on the anode in Figure 4.3b. This sheet would grow and eventually collapse disintegrating the sheet into large drops. The more localised heating in cathode typically did not typically yield a molten sheet; however, increasing the atomising gas pressure and arc current induced the cathode to form a sheet more akin to the anode sheet. The discussion was further developed in [142], where a similar experimental method (involving imaging the primary wire breakup of an arc sprayed steel wire) was followed. Similar wire

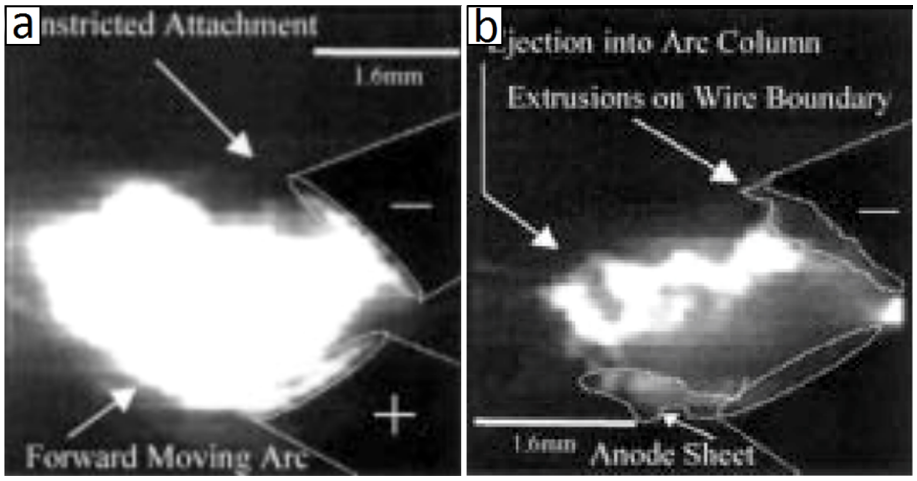


Figure 4.3: Stills from wire atomisation video (a) shows diffuse arc attachment on the anode and constrained arc attachment on the cathode, (b) shows protruding liquid metal sheet on anode [141]

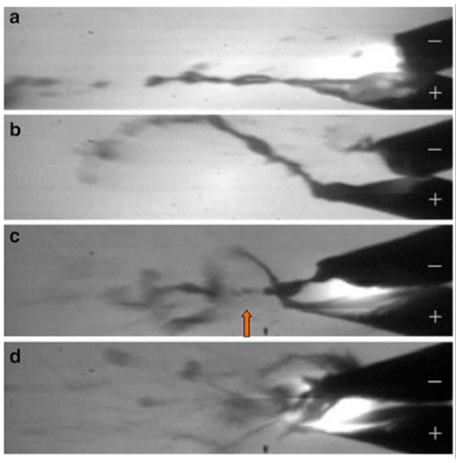


Figure 4.4: Image showing anode sheet breakup mechanisms, (a) Rayleigh axisymmetric breakup, (b & c) Rayleigh non-axisymmetric and (d) membrane breakup [142]

sheets were formed and the anode sheet breakup was characterised as either Rayleigh axisymmetric breakup, Rayleigh non-axisymmetric breakup or membrane type breakup; these breakup mechanisms are displayed in Figure 4.4.

The anode in Figure 4.4a is a typical example of Rayleigh axisymmetric breakup, small axisymmetric waves are formed due to the interplay between external aerodynamic forces and the surface tension. When the amplitude becomes large the sheet breaks up [145, p. 132]. The anodes in Figure 4.4b and c are typical examples of Rayleigh non-axisymmetric breakup. In addition to the asymmetric waves in the previous mode the sheet has a sinusoidal wave [145, p. 132] and [145, p. 589]. The cathode in Figure 4.4d shows membrane type breakup, the mechanism initiates from holes forming in the sheet [23, p. 589].

Tillmann and Abdulgader [143] used a very similar methodology to observe the wire

breakup in a solid steel and cored wires in a TWAS process. A cored wire is a conductive hollow wire sheath containing typically non-conductive feedstock (in this case 50 % fused WC-W_2C). Cored wires allow non-conductive materials to be sprayed via TWAS which requires a conductive feedstock. The distinctive anode sheet was observed on the solid steel wire but not on the cored wire.

Particle diagnostics in wire flame spray

WFS has received least analysis using these methodologies. This could well be due to the low added value applications for which it is typically employed, e.g. cathodic protective coatings on pipes [146]. Due to this lack of attention there is little information surrounding the properties of the wire flame spray plume available. In reference literature, powder flame spray and wire flame spray are typically grouped together and velocities quoted for them are 50 - 100 $m.s^{-1}$ [15] or 100 - 200 $m.s^{-1}$ [13] but it is difficult to find evidential basis for these figures. In one study, Dykhuizen & Neiser [147] measured particle velocities in a WFS system spraying copper at a single location 70 mm from the gun in order to develop a closed loop control system. In this context, they measured particle velocities of 50 - 400 $m.s^{-1}$ [147], somewhat higher than typically quoted. The authors comment on the difficulty of detecting WFS Cu particles due to their low temperatures and emissivity. Neiser et al. also measured particle velocities of the related process; wire-fed HVOF. Their work detected particle velocities of 140 - 270 $m.s^{-1}$ [148] 40 mm downstream from the gun. Work carried out investigating powder flame spray found particle properties $<$50 $m.s^{-1}$ ([14]); these are more akin to the often quoted figures.

In order to assess the suitability of WFS for spraying onto thermally sensitive FRP substrates it is important to have a better understanding of the properties of the thermal spray particles upon impingement. Given the thermally sensitive nature of the substrate, it is also important to assess the stability of the process. It is also important to understand particle properties to develop a mechanistic understanding of adhesion at the surface.

4.2 Objectives

- Measure the particle properties in the wire flame spray plume
- Assess the repeatability of the WFS process
- Assess the robustness of the process to parameter change
- Map how the particle properties change throughout the plume

- Determine the applicability of the SprayWatch particle diagnostic system for process monitoring of WFS Al
- Observe and describe the wire break-up
- Determine the applicability of WFS for the coatings of polymers and FRPs
- Determine heat input into the substrate

4.3 Approach

The general approach taken to fulfilling these objectives was to setup and obtain data using a commercially available particle diagnostic system (SprayWatch 2i). Repeatability was assessed by measuring particle properties (at a particular point in the plume) during different spray runs over the course of several months. To establish the effect of process parameters, these were intentionally varied within certain limits and the particle properties at different points were measured. The system was also used to record images of the wire breakup.

The suitability of the particle diagnostic system to measure particle properties was assessed by analysing the output data, critically evaluating the system and - where possible - verifying the output against physical measurements.

The heat input into to a CFRP substrate was also assessed by recording the temperature of the substrate just below the substrate surface.

4.4 Experimental methods

4.4.1 Materials

Feedstock

The feedstock used in this investigation was the same as was used throughout this thesis, industrially pure aluminium Metallisation 01E more detail about this feedstock is given in the experimental methods chapter.

Substrate

Wipe tests The spraying experiments for wipe deposits involved deposits onto polished mild steel.

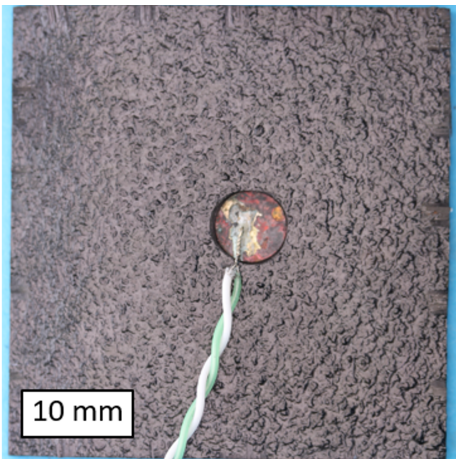


Figure 4.5: Photograph of the back face of the instrumented CF-epoxy coupon (without insulating tape backing)

Substrate temperature measurements Substrate temperature measurements were carried out by spraying onto on a 40 x 40 mm E722 Epoxy reinforced CF. Details on this material are given in the experimental methods chapter. The substrate had a flat hole milled in the centre of the substrate from the back. The hole was 1 mm short of the substrate surface. In this hole was placed a K-type thermocouple welded to a 5 mm copper stud (figure 4.5). The hole was backfilled with thermally insulating high temperature tape.

4.4.2 Wire flame spraying conditions

Wire flame spray was carried out with a Metallisation MK 73 in line with the baseline parameters outlined in the Experimental Methods chapter. In addition to the baseline parameters, the atomising air was varied to +/- 20 % of this baseline value. Where this has been done it is clearly highlighted

4.4.3 Particle diagnostics

The particle diagnostic system (SprayWatch 2i, Oseir, Finland) is shown schematically in Figure 4.6. In this configuration the particle detector takes shadow-graph images of the plume illuminated by the laser. Within a single exposure the laser strobe illuminates the image three times at timed intervals. This treble exposure means that each particle is shown three times in a single image. Image analysis is then used to detect triplets; their size is then determined from the particle images and their velocity by the particle spacing. This configuration was used because it was not possible to detect WFS particles based on their emitted IR radiation. Prior to this study, initial work was carried out to

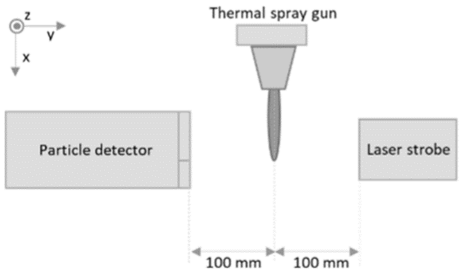


Figure 4.6: Schematic diagram of the setup for measuring in-flight particle parameters using a backlit arrangement. The origin (x = y = z = 0) is at the center of the nozzle exit, and the x directionis along the plume axis. The arrow indicates the typical measurement region

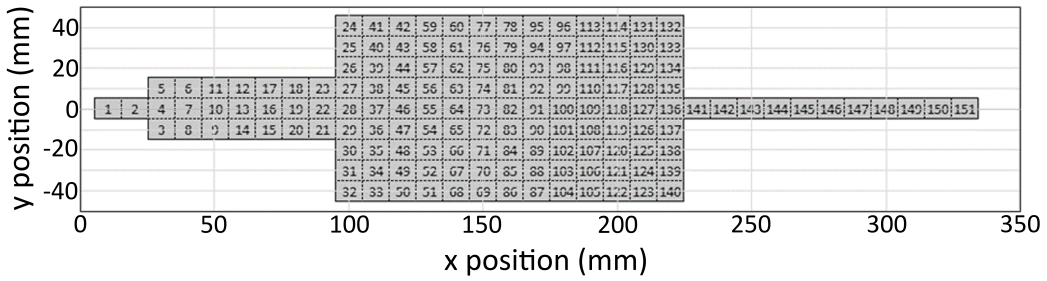


Figure 4.7: Schematic diagram of the locations within the x-y plane (z = 0) for particle parameter measurements within the spray plume

identify the appropriate interval length between laser pulses. The interval chosen was 0.5 µs as it ensured the individual triplets were distinct but easily identified as triplets.

The system was set up such that the plume was located directly between the particle detector and the laser strobe and 100 mm from each. The particle detector was fitted with a close-up lens and had a measurement volume of 10.9 x 10.2 x 11.6 mm. The location of this measurement volume was moved in the plume in the x and z direction by moving the flame spray gun in relation to the particle detector in line with figure 4.7. Thus, 151 individual regions spaced 10 mm apart were measured with a small 1.2 mm overlap. Data were analysed at specific locations, in addition the detected particle data from each run were merged together to give an overall description of how the whole plume behaved.

4.4.4 Wire breakup analysis

The particle diagnostic equipment was also used to take images of the wire during breakup. In these images, the laser strobe was set to illuminate once every frame at a frame rate of 3 frames per a second, in this way it was possible to observe wire breakup mechanisms.

In addition to the wire breakup images, after the WFS gun was extinguished, the wire

tips were collected and examined. SEM images were taken of the external morphology of collected wire tips using an EVO LS15 SEM (Zeiss, Germany)

4.4.5 Particle collection

In flight capture

Particles were allowed to solidify in flight and collected. They were collected on wet filter paper at a very large (1 m) stand-off distance. The large stand-off distance was used to ensure that the particles were solid before impact on the filter paper. Particles were removed from the paper and put in suspension in Industrial Methylated Spirits (IMS). The suspension was then placed on slides in small quantities and the IMS was allowed to evaporate, leaving the captured particles.

Wipe tests

Splats were collected using the wipe test rig; this is discussed in greater detail chapter 3 & 5.

4.4.6 Characterisation and quantification of particles

Captured spray particles

Volume measurements of the particles were undertaken of using focus variation microscopy (Infinite focus SL, Alicona Imaging GmbH, Austria). The measurements were difficult to achieve using this method because of the shape of the particles (with re-entrant angles e.g. Figure 4.9 (a) leading to possible systematic overestimation of particle volumes with this line of sight metrology process as illustrated in Figure 4.9 (b). However, minimum (volume in the top half of the particles) Figure 4.9 (c), and maximum (total measured volume) figure 4.9 (mid) bounds were placed on the volume for each particle measured. The midpoint between the two bounds was calculated and used as a volume estimate. In addition to volume measurements, SEM images were taken of the external morphology of collected particles using an EVO LS15 SEM (Zeiss, Germany)

Wipe test splats

The volume of these particles was also measured with focus variation microscopy. This was readily achieved as the shape of the splats (flat, without re-entrant angles) lends itself to volume measurement by this method. In addition to volume measurement,

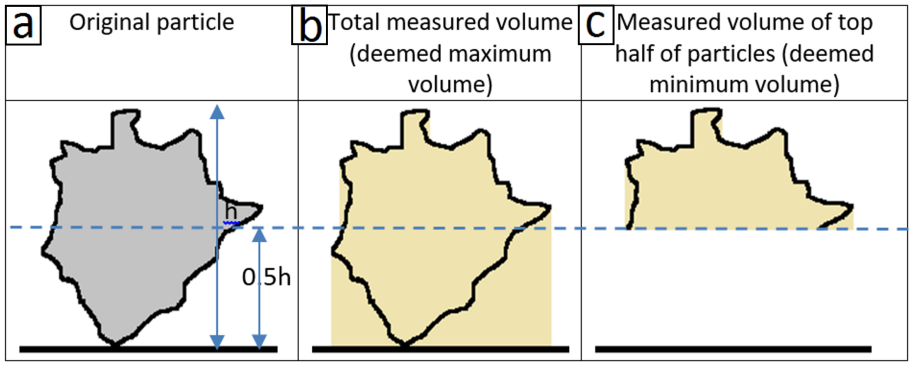


Figure 4.8: Schematic diagram showing (a) example particle with re-entrant angle (b) measured volume of particle (c) measured volume of top half of particle

macro optical images were taken of the wipe tests and Fiji image analysis software [18] was used to segment and record the location of each splat.

4.5 Results

4.5.1 Wire breakup

Figure 4.9 shows six non-consecutive images of the wire tip taken over a 40 s time period. The end of the flame spray gun is indicated by the dashed line on the left side of each image. From the images it is clear that the wire formed a conical shape with a mean angle of 9.5° ; this angle was relatively constant in all of the images with a standard deviation of 1.4°. The wire emerged from the end of the gun with a relatively constant diameter, mean of 1.02 mm (standard deviation of 0.05 mm), significantly thinner than the diameter of the initial feedstock, 2.3 mm. Thus, the cone must have started to thin within the gun, and out of sight of the camera. Assuming the cone angle remains the same within the air cap, the total length of the conical section is 7.5 mm.

The series of images in figure 4.9 show the process of wire breakup. Figure 4.9a clearly shows waves of molten aluminium were pushed toward the end of the wire tip. Figure 4.9a - d show that these waves of material increased the size of the molten pool of material suspended from the end of the wire tip. The images show that the molten metal pool formed a thin liquid jet which was subjected to the aerodynamic forces within the plume often forming waves as shown in figure 4.9b - d. These waves sometimes thinned and broke up into irregular shaped droplets as in figure 4.9d, or larger sections of the ligament broke off at once creating larger irregular shaped molten particles as highlighted in images figure 4.9e and figure 4.9f.

After the initial breakup, the molten wire fragments quickly breakup further. Within

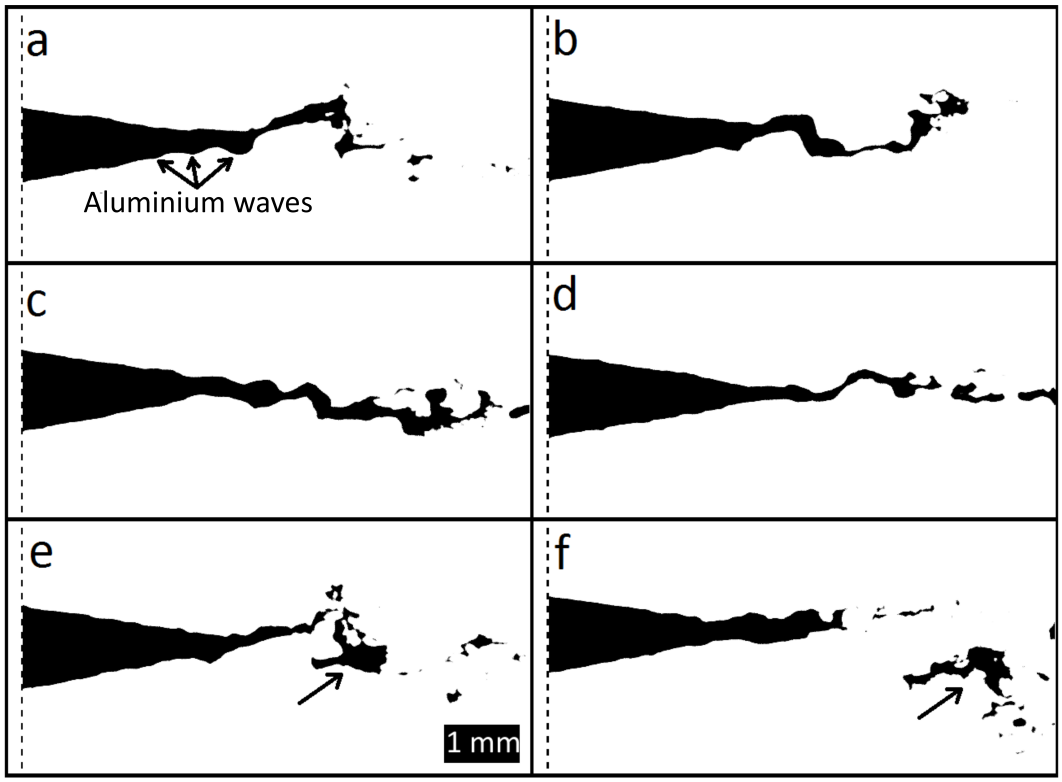


Figure 4.9: Set of six non-sequential wire tip images taken with SprayWatch and a laser strobe backlight. The vertical dashed lines indicated the position of the end of the thermal spray gun

5 mm from the end of the wire tip (10 mm from the nozzle exit), the particles have the same appearance as in the rest of the plume. Figure 4.10 shows an image taken by SprayWatch at this point, it should be noted that each particles is imaged three times in this figure due the requirements of the PIV particle tracking algorithm.

The effect of atomising air flow rate on the wire breakup was investigated by varying it +/- 20 % from its baseline value. Images of the atomising wire taken at the different settings look almost identical to those at the baseline values and the diameter of the wire at the end of the gun did not significantly change by varying the atomising air flow rate (1.07 and 1.17 mm for -20% and + 20% respectively), nor did the angle of the cone (8.8°and 9.5°for -20% and + 20% respectively). The length of the wire extension in the individual frames was plotted as a histogram. Figure 4.11 displays the histograms for the three different atomising gas condition. The peak of the three distributions are very similar (between 4 - 5 mm) indicating that the modal averages or wire length are not significantly different for the three settings. The higher atomising gas flow rates has a slightly narrower distribution; this indicates that there is slightly less variability on the tip length at the higher atomising flows. However, the magnitude of this effect is small and not necessarily significant.



Figure 4.10: Typical image from the centreline of the plume starting at 10mm from the gun nozzle showing large wire droplets from breakup (seen in figure 4.9) have broken down into small particles. (this image is triple exposed in order for PIV speed and size analysis to be performed). Particles are travelling left to right in this image

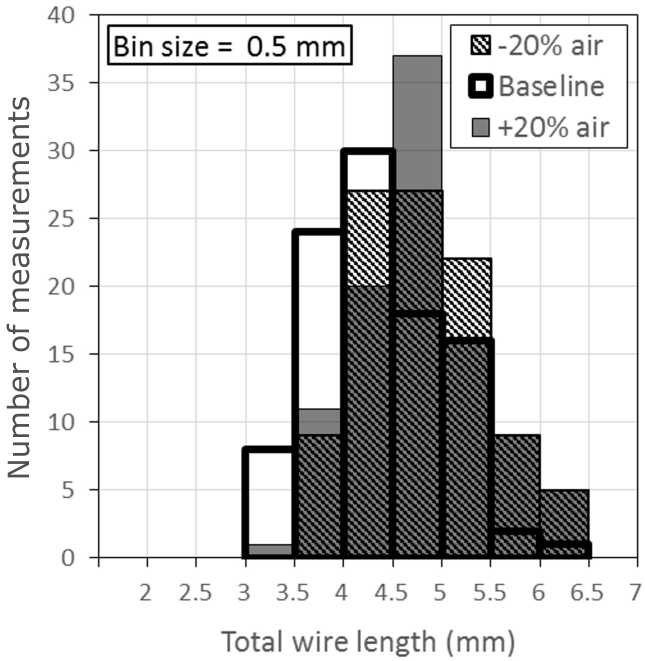


Figure 4.11: Histogram showing the distribution of wire tip length (measured from the gun exit). Data are shown for the baseline air flow rate and for deviations of +/- 20% from the baseline value

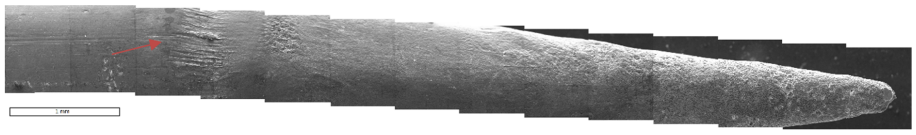


Figure 4.12: Composite image (made from multiple SE SEM images) of WFS wire tip showing length of conical area after thermal spray (arrow indicates end of conical region)

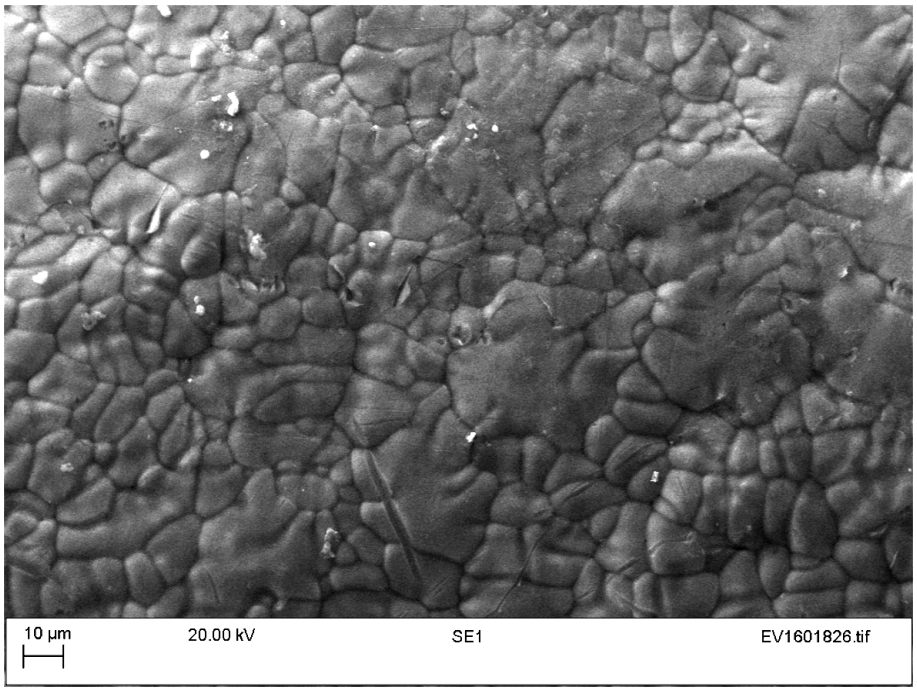


Figure 4.13: SEM image showing dendritic surface structure of conical area of Al wire tip after thermal spray

Wire tips and particle morphology

After the gun was extinguished, the wire tips were imaged. Figure 4.12 shows a composite image of the wire constructed from many different SEM images. It shows that the length of the conical regions of the wire tips to be 6.6 mm. The image also shows the surface of the conical region to have a texture. Figure 4.13 shows this texture in more detail, and it is indicative of a dendritic structure formed due to rapid re-solidification. This structure is not evident further back from this region where the wire maintains its 2.3 mm diameter.

4.5.2 In-flight particle measurements

Velocity

The mean measured velocity of the spray particles at a spraying distance of 160 mm along the centreline (+/- 5 mm) was 287 $m.s^{-1}$, the median velocity was 281 $m.s^{-1}$ and the standard deviation of the sample data was 62 $m.s^{-1}$. A histogram of the individual

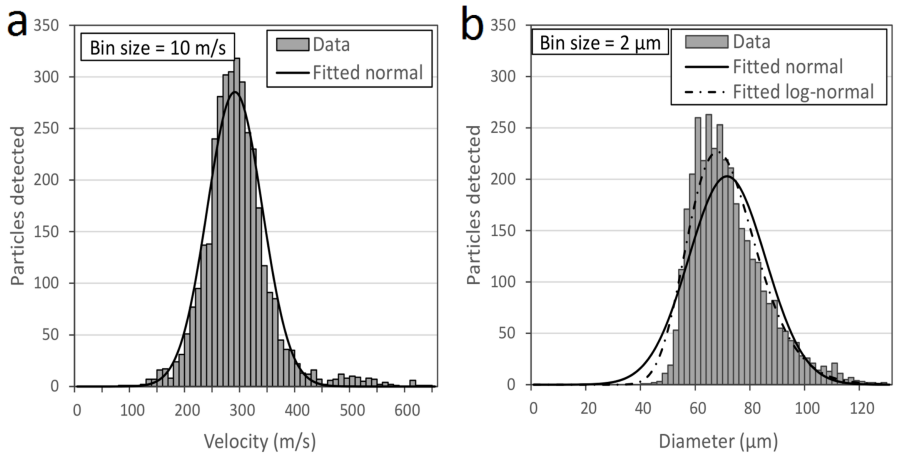


Figure 4.14: Histograms showing the distribution of (a) particle velocity measurements and (b) particle diameter measurements. Solid lines show fitted distributions. In (a) a normal distribution and in (b) a log-normal distribution

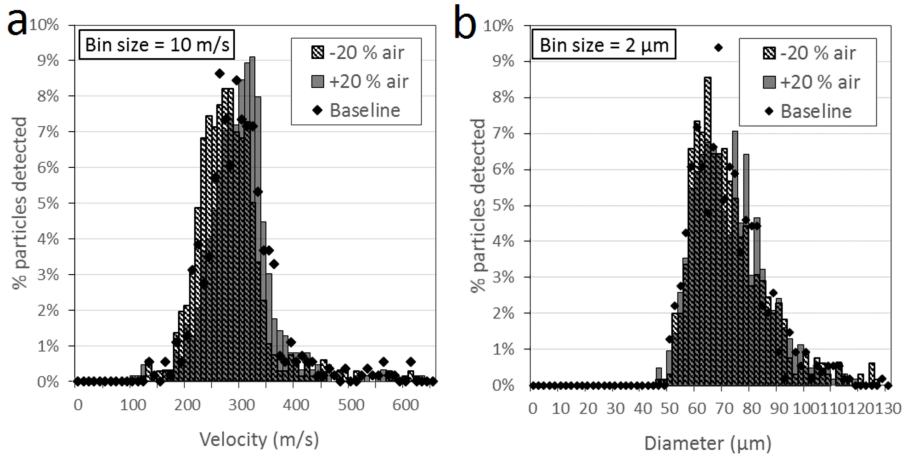


Figure 4.15: Histograms showing the distributions of (a) particle velocity and (b) particle diameter. Measurements taken on the plume centerline at a distance of 160 mm from the exit of the gun. Data are shown for the baseline air flow rate and for deviations of ±20% from the baseline value

measured particle velocities is shown in figure 4.14a. A normal distribution curve has been fitted to this data and plotted on the figure which appears to fit well. It should be noted that the fitted distribution has a modified standard deviation of 50 $m.s^{-1}$. This figure has been used because the calculated figure was affected by the very high velocity data points which are likely from noise in the data. Higher atomising gas flow rates led to marginally higher particle velocities as shown in figure 4.15a; however, the difference was well within one standard deviation (table 4.1)

Size

The mean measured particle diameter measured was 71 µm, the median diameter was 68 µm, and the data had a standard deviation of 14 µm. A histogram of the individual

Table 4.1: Effect of atomizing gas flow rate on particle velocity

	Atomising gas flow rate		
	-20 %	Baseline	+ 20 %
Mean velocity ($m.s^{-1}$)	272	287	294
Standard deviation ($m.s^{-1}$)	63	62	63

Table 4.2: Summary of particle velocities, diameters and number of detected particles at 160 mm stand-off distance for measurements at the beginning and end of three separate spray measurement sessions

	Spray session 1		Spray session 2		Spray session 3	
	Start	End	Start	End	Start	End
Mean velocity ($m.s^{-1}$)	272	286	285	291	298	294
Standard deviation ($m.s^{-1}$)	45	67	51	68	70	63
mean diameter (µm)	70	71	70	70	71	72
Standard deviation (µm)	14	15	13	13	14	15
Number of particles detected	775	713	507	544	542	495

measured particle diameters is shown in figure 4.14b. Fitted normal (solid line) and log-normal (dashed line) distribution curves have been also been plotted on the figure. The log-normal distribution appears to fit the data better than a normal distribution but neither fit particularly well at the low diameter end of the distribution. The measured particle size distributions are broadly similar at the higher and lower atomizing gas flows (figure 4.15b), with a noticeable lower size cut-off at around 50 µm for all atomising air flows tested.

Repeatability Figure 4.16 shows the velocity and diameter measurements of all the detected particles with time. This data is for baseline parameters at the 160 mm stand-off distance. The figures show that over the course of a measurement run (approximately 40 s) there was no statistically significant trend in velocity or diameter with time indicating that the plume was stable over the course of a measurement run. Repeat runs were performed at the start and end of each spray session. Statistics for each of these repeated measurements are shown in table 4.2. The results show that average velocity and particle size within plume was consistent over the course of spray session (approximately and hour of continual spraying) as well as from spray session to spray session (spaced over the course of several months). The only figure with any notable difference between spray sessions was that of number of particles detected. More particles were detected in the first session than in the subsequent two; the number detected in the different spray runs within the same spray run were relatively consistent.

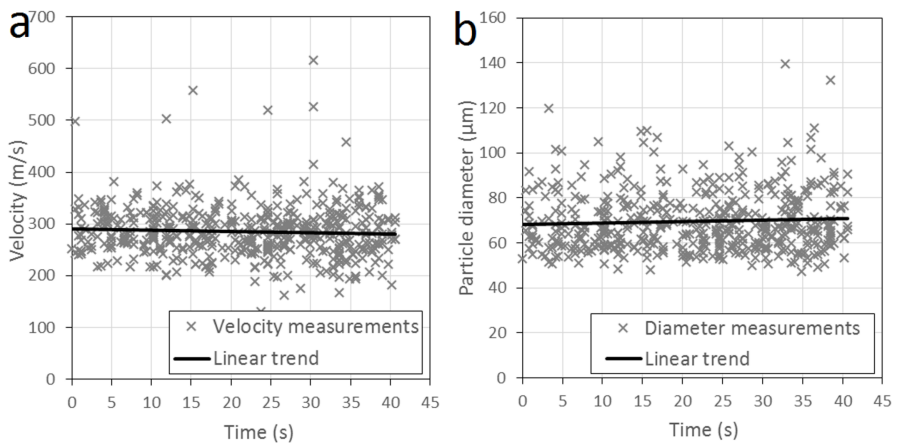


Figure 4.16: SprayWatch measurements showing the variation of (a) particle velocity and (b) particle diameter with spraying time. Measurements taken on the plume centerline at a distance of 160 mm from the exit of the gun

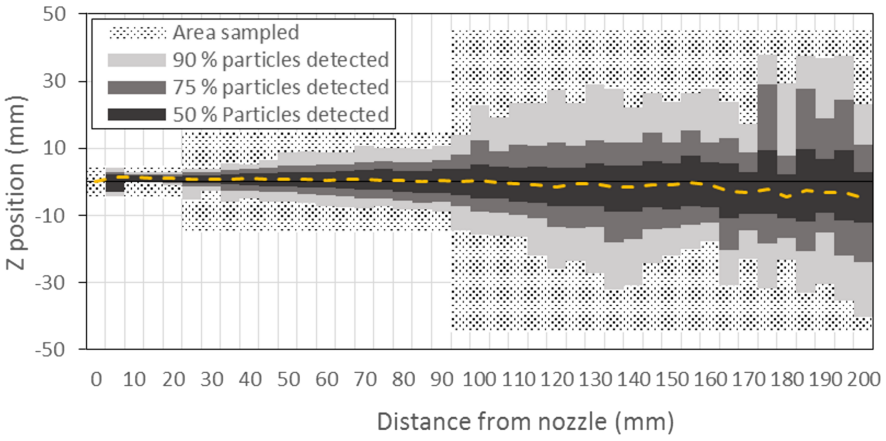


Figure 4.17: Contour plot detailing the distribution of particles at different standoff distances within the plume. Colored area represents where 90, 75 and 50% of the particles are detected

Position

Figure 4.17 represents the plume width as a function of stand-off distance (axial axis). The axial axis has been discretised into 5 mm bins and the boundaries within those bins represent the 50^{th}, 75^{th} and 90^{th} percentile of the radial distance where the particles were found, the lighter dashed area represents the total measurement area. The figure demonstrates that the width of the thermal spray plume is shown to increase with stand-off distance. However, even at 200 mm it remained relatively narrow with 50 % of the detected particles within +/- 7.5 mm of the centreline of the plume.

The average velocity of the particles detected at each point within the plume has been calculated. The measurement area had been resolved into a 1 mm grid in x and z as defined in figure 4.6 and the average velocity plotted as a colour-map in figure 4.18. The figure shows that the velocities of the particles are greatest in the central cone of the

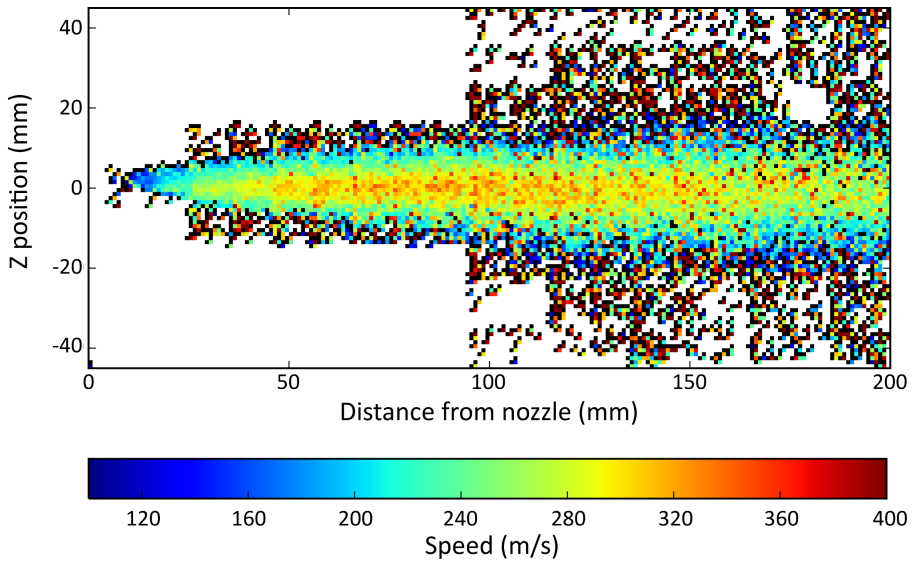


Figure 4.18: Plot showing the mean particle speed at each measured location within the spray plume

plume and decrease radially away from the centre of it, where the velocities fell to around 200 m.s^{-1}. At these locations (greater than +/- 20 mm from the centreline throughout most the plume) the numbers of detected particles were small enough that they can be considered little more than noise. The particle velocity within the central cone increased until ≈ 70 mm from the nozzle exit and it then remained relatively constant up to ≈ 150 mm, and then started to gradually decline. Nevertheless, the detected velocities were typically still > 250 m.s^{-1} until the end of stand-off distances measured (figure 4.19). The detected particle diameters were shown to be practically constant along the centreline throughout the entire measurement region (figure 4.20).

4.5.3 Heat input

As mentioned in section 4.3, the Al particles did not emit enough IR radiation in order to detect them without the use of external laser illumination. Thus no temperature measurements could be made of the particles, thus indicating that the particles are likely under 1000℃.

The measured of temperatures of the substrate during thermal spray are plotted in figure 4.21. The traces for a single surface coat (consisting of a single raster pattern) and a 10 surface coat layers are shown in the plot. The data show that at 1 mm from the substrate face, the temperature stayed below 90℃; this is despite ten coats being applied in quick succession. This result implies that any damage occurring in the composite due to Al WFS will be localised to the very top surface. It should be noted that this top

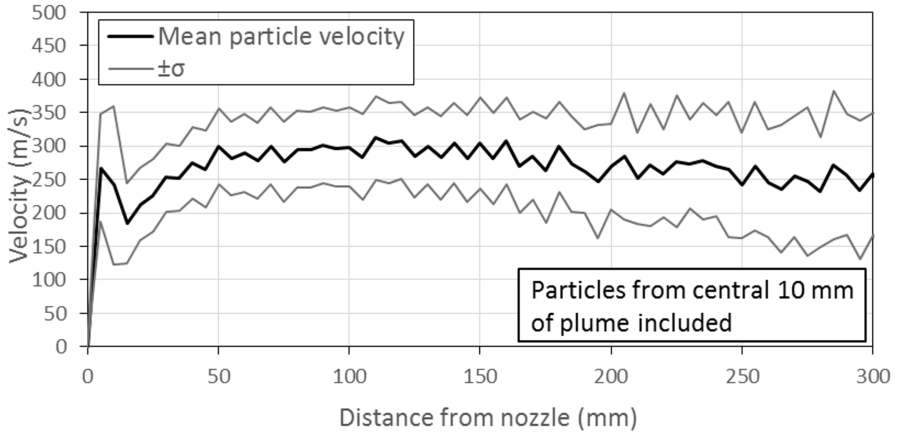


Figure 4.19: The effect of distance from the nozzle exit on the mean particle velocity in the central 10 mm of the spray plume from SprayWatch measurements. Also shown are lines for +/- one standard deviation (σ) from the mean

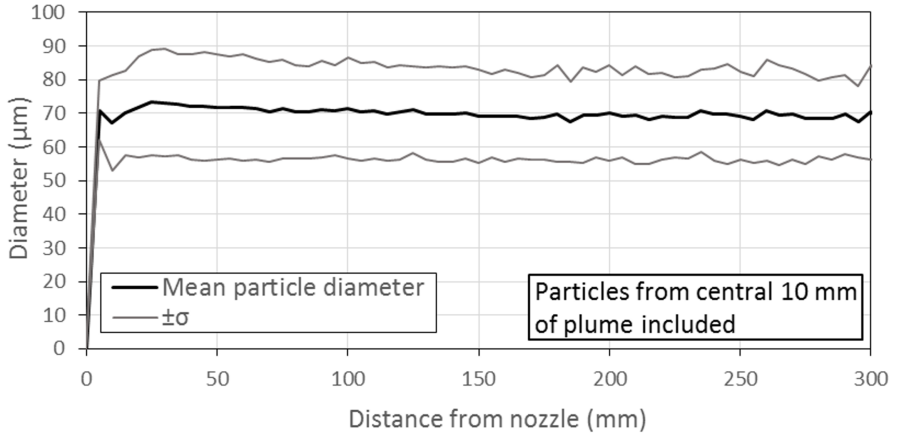


Figure 4.20: The effect of distance from the nozzle exit on the mean particle diameter in the central 10 mm of the spray plume from SprayWatch measurements. Also shown are lines for +/- one standard deviation (σ) from the mean

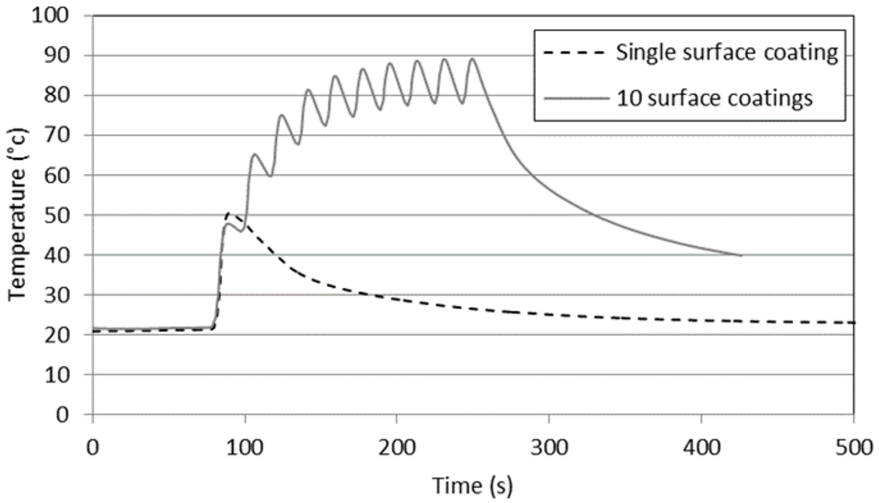


Figure 4.21: Plot showing measured bulk surface temperature of FRP during WFS of aluminium for a single coating and 10 coatings

surface is likely to be of critical importance for coating adhesion.

4.5.4 Wipe tests

Figure 4.22 shows the spatial distribution of splats in the z axis (as defined in figure 4.6) for 5 wipe tests on polished steel. The location of these splats is shown to be normally distributed in this axis for the 5 wipe test samples. Particle distribution data from the particle diagnostic system for the same region is also plotted. There is some scatter in the data, but the wipe tests (which represent 0.3 x 10^{-3}s of spray time) seem to have a relatively constant Gaussian distribution, which is consistent with the equivalent data obtained from the particle diagnostic system which is also plotted on the graph. In order to make the spraywatch data comparable to the wipe test data, only the particles +/- 20 mm from the centreline at 160 mm stand-off distance is included in this figure.

The volume of selected splats was readily obtained using the FVM technique. The measured splat volumes were converted into an equivalent particle diameter assuming the particles were spherical. The calculated particle diameters are plotted in a histogram in the turquoise colour in figure 4.23. The distribution displayed in the histogram appears to either be normal with a large positive skew, or a log-normal distribution.

4.5.5 Collected particles

The collected particles from the thermal spray plume were shown to be typically non-spherical this is indicated by SEM imaging as shown in figure 4.24. The majority were shown to be approximately cylindrical with length in the order of 10 µm. However, there were some substantially larger particles in the order of 100 µm, which tended to be more

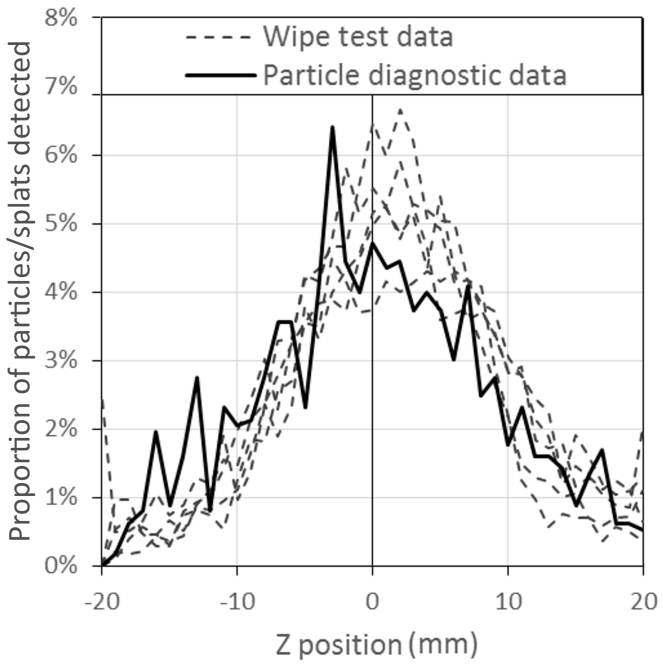


Figure 4.22: Graph showing the spatial distribution of numbers of particles measured along the z direction at a distance of 160 mm from the nozzle exit. Data obtained from wipe test coupons and SprayWatch (particle diagnostic) measurements

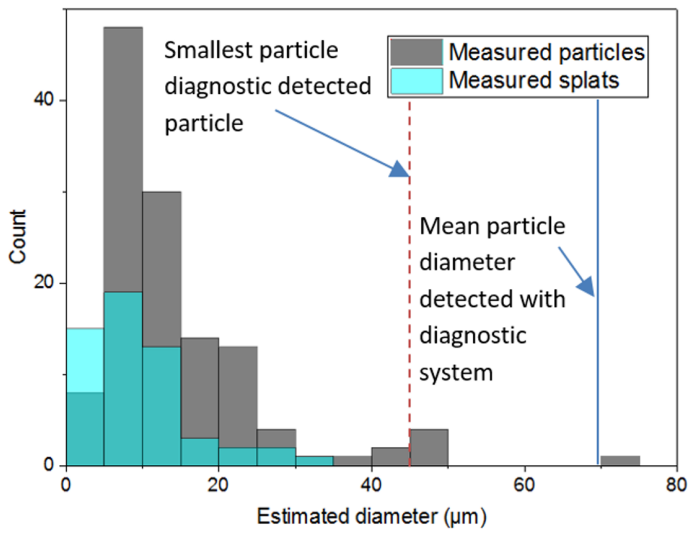


Figure 4.23: Histogram showing the calculated diameter of collected particles and splats showing indicating the two yield similar diameters, both of which are much smaller than those measured through particle diagnostics

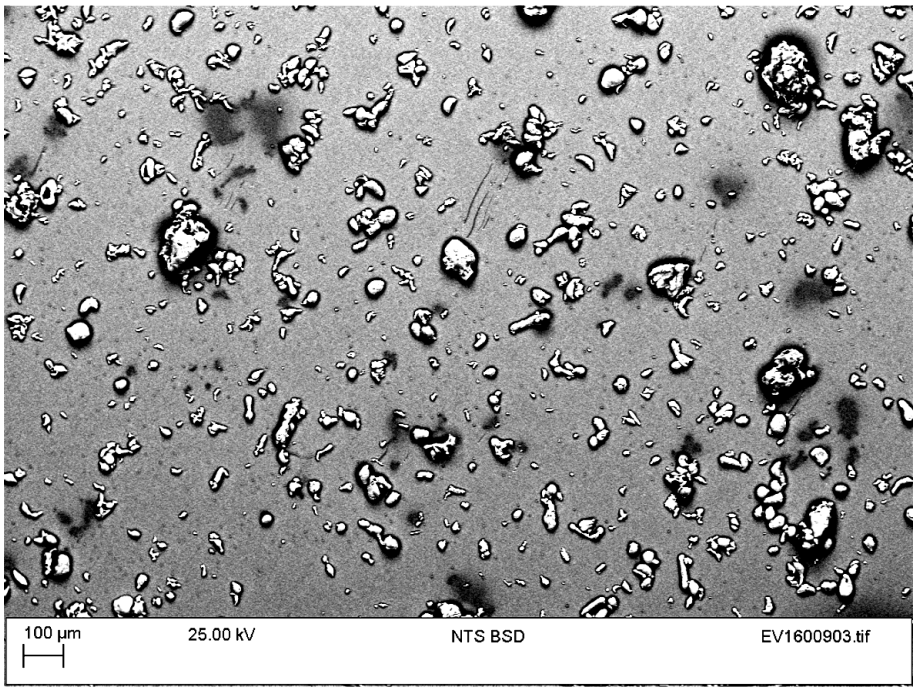


Figure 4.24: BSE SEM image of collected thermal spray particles on a microscope slide showing the size (≈50 µm) and morphology (non-spherical) of the particles (black areas are an artefact of sample preparation)

spherical. The volume of a random sample of 126 particles was measured; these volumes were converted to an equivalent diameter, the mean (particle based) volume is 67,000 μm^2, this equates to a diameter of 25 µm for a perfectly spherical particle. The equivalent diameter of the collected particles is displayed as the grey histogram in figure 4.23, the measured sizes and distibution appear to be in line with the diameters calculated from the splat volumes. As before, the distribution appears to either resemble a heavily positively skewed normal distribution, or a log-normal distribution. The appropriateness of a log-normal fit is demonstrated by the relatively good straight line fit in the log-normal plot shown in figure 4.25. A log-normal plot plots the ordered data points against what the data points would be expected to be if the data fitted the fitted log-normal distribution perfectly; thus, the straight line indicates a good fit to the model. It is interesting to note that very few of the equivalent diameters of the particles are anywhere near as large as those measured with the SprayWatch equipment.

4.6 Discussion

4.6.1 Wire breakup/atomisation

Wire was successfully imaged as it atomised. There were no significant differences observed in the wire breakup when modifying the atomising air flow (+/- 20 % from the

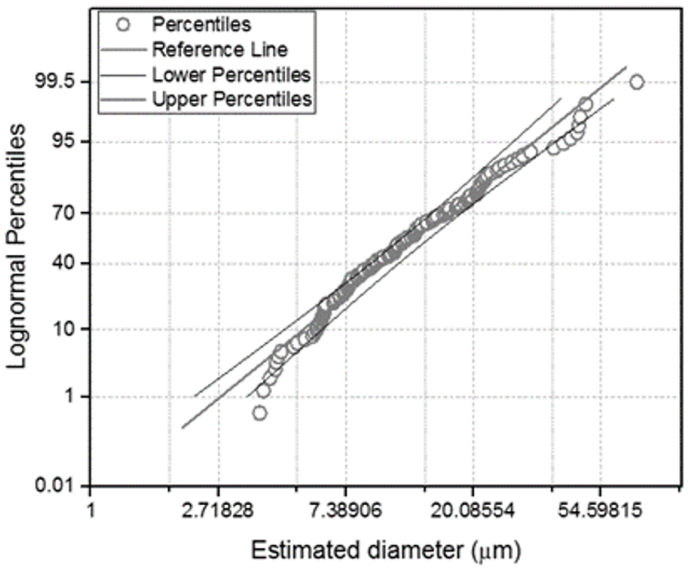


Figure 4.25: Log-normal plot of the effective diameter of collected particles showing they fit a log-normal distribution)

baseline value). Waves of metal are clearly observed on the molten surface of the wire. In the wire flame spray process a shearing force is applied by the fast moving atomising air flowing over the molten surface. This is probably responsible for transporting molten metal to the tip of the wire where, because of viscous forces, it forms a molten tip or jet. This appears to be in line with previous discussions of liquid jet disintegration both generally [149] and in the context of twin wire arc spray [141] [142] [143] [144]. The disintegrating WFS wire bares close resemblance to the anode within the TWAS process this seems reasonable as the flame will induces diffuse, non-localised heating along the wire which is more akin to the anode heating profile. As with the anode sheet in the TWAS process, the propensity for the jet to break-up is expressed by the Weber number (equation 4.1).

$$We = (v^2 l \rho)/\gamma \tag{4.1}$$

where v is the atomising air velocity, l is the length of the molten zone at the tip, ρ is the atomising air density and γ is the surface tension of liquid metal. The value of the Weber number determines the break-up regime. The images taken in this investigation appear to indicate a mainly non-axisymmetric form of breakup (although there are some examples of axisymmetric and membrane type breakup). This implies a Weber number of 15 - 25 for all air flow rates employed [142] and suggests that primary atomisation is similar in both wire flame and twin wire arc spraying. However, the estimate for the Weber number calculated from the air volume flow rate and γ from [150] gives a Weber

number of 300 - 600 and this range of values would suggest membrane type breakup would be dominant. This discrepancy is probably due to difficulties in the estimation of the Weber number for two reasons. First, the oxidation of the molten aluminium could affect the surface tension of the liquid metal at the tip and secondly, the flow dynamics and flow conditions of the atomising air at the nozzle exit need to be calculated more precisely using, for example, a computational fluid dynamics approach. Secondary atomisation of the particles was seen to occur very quickly after initial wire breakup; in most cases the wire had disintegrated into small particles 5 mm after initial breakup, around 10 mm from the nozzle exit. Due to the low frame rate and relatively low resolution of the images it is not possible to comment on the mechanisms by which this happened.

4.6.2 Number of detected particles

The particles in the plume had relatively constant properties throughout the different spray runs and spray sessions. However there was some disparity between the numbers of detected particles in the different spray sessions, there were around 30 % fewer particles detected in the later spray sessions compared to the first. However repeat runs within a single spray session yielded the same results. The likely reason for this is small misalignments between the WFS gun and the particle detector/camera. Small misalignments in the thermal spray gun around its z axis can result in areas of the plume being outside of the depth of field of the PIV camera; this is schematically illustrated in figure 4.26. Figure 4.27 shows the magnitude of the plume centreline translation at a stand-off distance of 160 mm with different misalignments. It also uses the measured particle distribution at 160 mm (and assuming an axisymmetric distribution) to estimate the proportion of the particles in the plume remaining within the depth of field at different misalignment angles. The figure shows that with perfect alignment, around 35 % of the detected particles will be within the 11.6 mm depth of field of the camera, assuming that the first spray session was perfectly aligned a misalignment of just +/- 2.5° would account for the around 30 % drop in detected particles, but would impact the measured velocity measurement by less than 0.1 %.

4.6.3 Particle velocities

Repeated measurements of the plume with the particle diagnostic system over the course of several months indicate that the plume is stable in terms of particle velocity and particle size. There are issues with the particle sizing which will be discussed later. However, the average particle velocities measured are in the region of 250 - 300 $m.s^{-1}$.

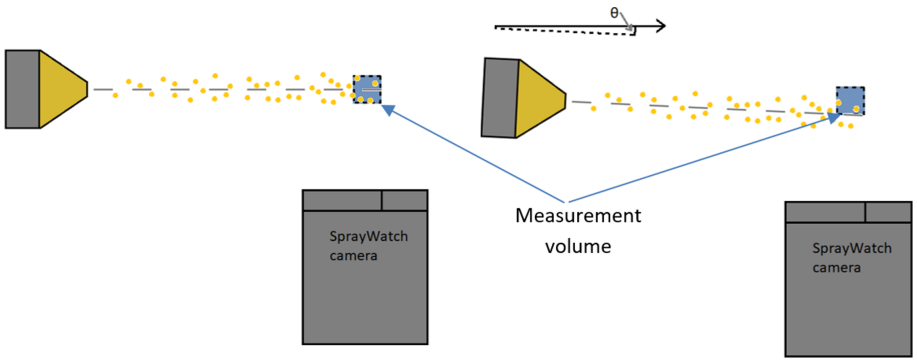


Figure 4.26: Schematic demonstrating how a small gun/detector misalignment reduced detected particles in the plume as more particles are no longer within the depth of field of the camera

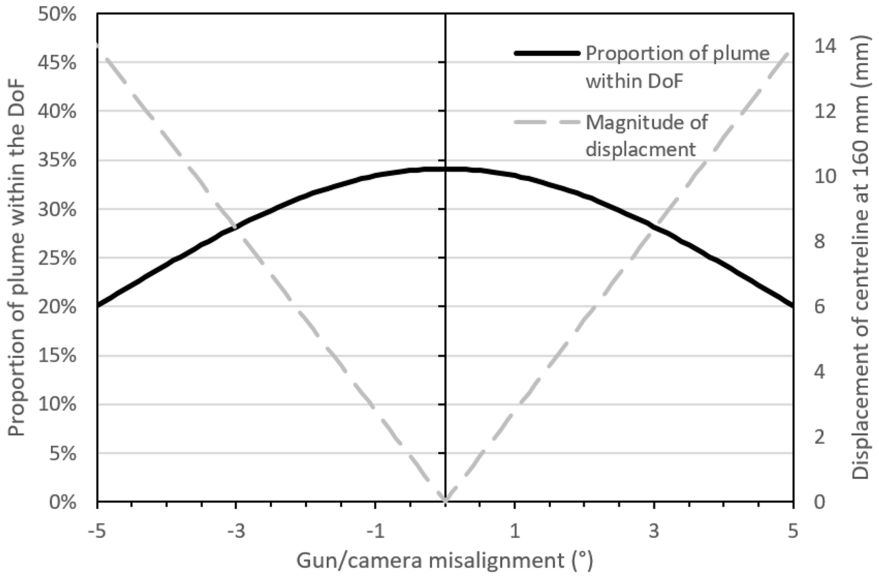


Figure 4.27: Effect of angular misalignment and percent of particles in plume outside of measurement volume

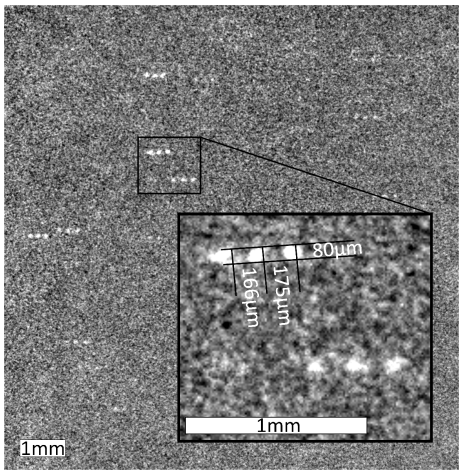


Figure 4.28: Representative image taken from the SprayWatch system with measurements shown for a single particle triplet in the enlarged area of the box (inset)

The measurement of a particle involves treble exposing images such that each particle is imaged three times per an exposure; an example image is shown in figure 4.28. The distance between each rendering of the particle is ≈ 170 µm, which given the time interval between laser pulses chosen (0.5 µs) equates to a velocity of 320 $m.s^{-1}$. It is of note that the resolution of the diagnostic system used was 1000 x 1000 pixels. Combined with the optics, this means that each pixel represents 10.6 µm, or 20 $m.s^{-1}$. Thus, the minimum velocity realistically measureable (given the time interval) is 100 $m.s^{-1}$. If the time period was increased slower speeds could be measured. This time interval was chosen during preliminary experiments to ensure that the particles were far enough apart that they were distinct but close enough together that they could readily be detected as triplets. The images suggest that the interval chosen was about correct and there is no evidence of particles which are blurred together in a streak because the interval is too small.

These measured particle velocities are higher than the typical reference values which tend to group WFS and PFS together and suggest that particle velocities are below 200 $m.s^{-1}$ [1]. The velocities reported in this study agree well with the single location measurements performed by Dykhuizen & Neiser who measured particle velocities in the range of 50 - 400 $m.s^{-1}$ [147] which is one of the only other reported studies measuring WFS particle properties. Given that there are some (limited) studies which suggest that PFS velocities are in line with reference texts [14], it suggests that WFS particle velocities can be significantly greater than PFS. In addition to the run to run stability of the particle velocities, the velocities were relatively insensitive to both stand-off distance and relatively large (+/- 20%) changes in atomising gas flow rate. The distribution of particles in the plume was also seen to be relatively stable as the stand-off distance changed. This suggests that the WFS process (as run in these investigations) was relatively robust in

these parameters. This repeatability and robustness is positive if sensitive materials are to be coated, as it implies that even if process variables change slightly day to day the coating quality should be relatively constant. No particle or gas temperatures could be measured from within the plume. The only temperature measurements recorded were 1 mm from the surface of a CFRP coupon, these stayed below 90℃, meaning that within the bulk of the substrate, thermal damage should not occur. This again suggests that the process may well be suitable for the coating CFRPs. However locally on the surface the temperature may well raise to a level which could damage the polymer surface.

Particle size There was very little change in the particle diagnostic system detected particle size with position or atomising gas; also the data did not seem to fit a standard distribution (e.g. normal, lognormal). The distribution of particles detected by the diagnostic system appeared to peak at ≈65 µm and the number detected reduced as particle size reduced below that, detecting no particles smaller than ≈45 µm. This limitation is not surprising as the low resolution of the particle diagnostic system meant each pixel in represented 10.6 μm^2, thus a 60µm particle was only 6 pixels wide. Using the splat volume data, an inferred particle size distribution was created. The particles detected with the particle diagnostic technique were larger than any inferred from measured splat volume. This suggests that the particle diagnostic system is only detecting the largest particles in the plume. There is additional evidence that the particle diagnostic system is failing to detect all the spray particles. The collected data at the different measurement locations has been combined to give 100 individual snapshots of the entire plume. Picking a plane at (150 mm from the nozzle tip), a volume flux of 92 $mm^3.s^{-1}$ was calculated. This gave a wide range of 15 - 53% of volume flux detected by the system depending on the shape assumptions (compared to the volume flow rate calculated using the wire feed rate). The 53% volume ratio depends on the particles being perfect spheres, and as such is likely represents an upper bound for detected flux ratio. This upper bound of volume ratio is higher than the theoretical maximum detectable ratio in terms of particle numbers based on the depth of field argument in section 4.6.2. However, it is important to note that the 53% is an upper limit and the two detection ratios are not measuring quite the same thing and thus not necessarily mutually exclusive.

The ratio of detected particles and volume flux can also be calculated using statistical methods. There were enough collected particles to fit a distribution, the data fitted a log-normal distribution well, where ln(Diameter) $\sim$ N(2.5, 0.6). Assuming this measured particle size distribution is the same as that of particles in the plume, the log normal

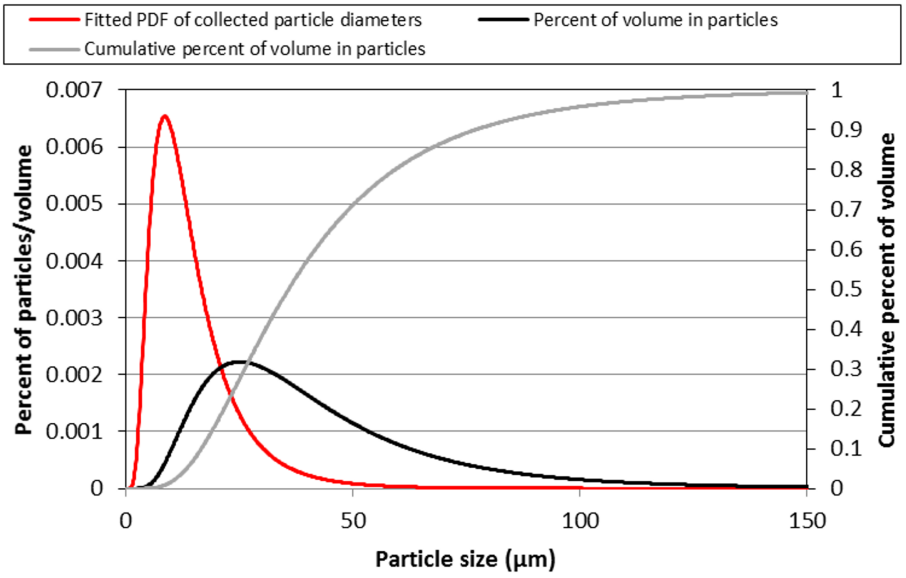


Figure 4.29: Plot showing the fitted log-normal particle diameter distribution of collected particles (red), proportion of sprayed volume coming from each different particle sizes (black) and cumulative proportion of volume coming from the different measured particle size

distribution can be used to calculate the percentage of particles in the plume which were greater than the minimum detectible size for the particle diagnostic system; using this methodology and assuming a minimum detection limit of 50 µm, a detected proportion of 0.93% is obtained. This information is plotted in figure 4.29; assuming spherical geometry, this accounts yields a percent volume detection of 29%. This is around the centre of the estimate based on the volume conservation argument discussed above.

Applicability of results to all particles There are features of the data that imply the results obtained examining the largest particles (i.e. what was detected with the particle diagnostic system) are representative of the particles as a whole. Firstly, the spatial distribution of particles obtained from the particle diagnostic system has been shown to be representative of what is deposited on a wipe test (figure 4.22). In addition, there is no correlation shown in the data between velocity and particle size (figure 4.30), this implies that the velocities of the measured particles are likely to be somewhat representative of the smaller particles. However, given the small range of particle sizes detected, this is far from compelling evidence. However Planche et al. [14] correlated particle size and velocity for several powder fed processes (PFS, PS and HVOF). They found a general negative correlation between particle size and velocity, i.e. as particle size increased the velocity decreased. The trend was more significant for the higher velocity processes specifically HVOF, and less significant for the lower velocity processes such as PS. The data collected in this study falls between these two velocity ranges in the Plache et al.

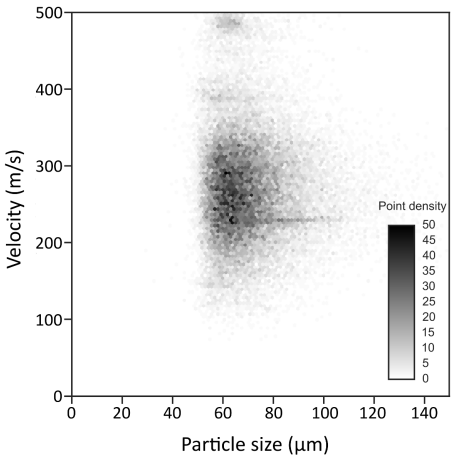


Figure 4.30: Binned frequency scatter plot of particle size and particle velocity obtained from SprayWatch measurements showing there is no significant correlation

study, and their data only includes particles up to ≈ 55 µm in powder fed processes. Despite these caveats, it implies that the measured particle speeds in the SprayWatch data may be a slight underestimation of the true average particle speeds; but they should be somewhat indicative of the true values. It is likely that a more modern SprayWatch model with a higher CCD pixel count would be able to detect smaller particles and thus allow more concrete statements about particle properties to be determined.

4.7 Conclusions

- PSV / PIV has been successfully used to determine the wire breakup and in flight particle behaviour of the WFS process for an aluminium feedstock.
- The WFS feedstock breaks up in a non-axisymmetric Rayleigh manor in a similar way to TWAS.
- Velocities for the detected particles were in the order of 200 - 350 m.s $^{-1}$. The measured velocities were greatest in the centre of plume and decreased little with distance from the gun. The velocities were also relatively constant when varying the flow of atomising air +/- 20%.
- Analysis of the measured diameter data suggests that the diagnostic system (as it was set up in these experiments) only detects particles above 50 - 60 µm. This limitation (due to the low resolution of the particle detector) means that only the largest particles (accounting for ≈ 30% of the volume could be detected.
- The spatial distribution of detected particles in the plume was measured by analysing particle diagnostic data from multiple runs. This distribution correlated well with

splat distribution data on wipe tests. The plume of detected particles was shown to remain relatively narrow, even at large stand-off distances.

- In all, the process has been seen to be relatively stable (in parameters measured) to deliberate change in stand-off distance and atomising air flow rate. It has also been seen to be relatively repeatable over several months in the measured parameters.
- The measured temperature 1 mm from the composite surface remained below 90℃ implying that the bulk of the CFRP material is not thermally damaged by WFS coating in Al.

Chapter 5

Splat Substrate Interaction

5.1 Introduction

The literature regarding thermal spray particles impacting on metallic substrates is well developed, even if there are fundamental questions left unanswered about the exact causes of different splat shapes; this literature is discussed in the literature review chapter. It is clear that study of the splat morphologies can help reveal what is happening on the surface during the spraying and aid understanding of how coating adhesion develops. However, there do not appear to be in-depth investigations of how particles impinge on polymer and FRP substrates and form splats. The purpose of this chapter is to thus investigate how splats form on polymer and FRP materials, to characterise the types of splats which are formed on the surface and investigate how and where they adhere to the substrate.

5.2 Objectives

- Investigate splat morphology on smooth polymer and FRP substrates to determine the effect of the polymer substrate
- To determine if and where aluminium splats preferentially deposit on the two phase substrate

5.3 Approach

The general experimental approach taken in this work was to momentarily expose a range of different substrates to the WFS plume, such that a collection of isolated splats

were deposited. The morphology and location of these splats were then examined so conclusions could be drawn about how spats behaved upon impact and how this was affected by the substrate.

5.4 Experimental methods

5.4.1 Substrate materials

The substrate materials used in this chapter are listed below. Details on these substrates can be found in chapter 3. The square brackets after the substrate material in the list below denote which surface preparations were investigated for each substrate. LGB and HGB denote high grit-blast and low grit-blast settings (as defined in chapter 3), polished denotes that the substrate was polished to 0.25 µm finish and as received means that the substrate was sprayed in the state that the substrate was received from the manufacturer. Detailed surface characterisation of the roughened substrates are not reported here but can be found in chapter 6.

- Steel (C15) [polished]
- Unreinforced polymers
  - Epoxy Easy composites (EL2) [polished]
  - PEEK [polished]
- Dry Reinforcement fibres
  - Carbon fibre [As received]
  - Glass fibre [As received]
- CFRP
  - CF-epoxy (Tencate E722) [As received, LGB & HGB]
  - CF-PEEK (Tencate Cetex® TC1200) [As received, LGB & HGB]

5.4.2 Wipe tests

Thermal spraying

Thermal spraying was carried using the WFS apparatus and the baseline parameters outlined in chapter 3.

Wipe test

The wipe test rig and methodology outlined in Chapter 3 were used to create the samples for analysis.

5.4.3 Analysis

Optical microscopy, SEM and FVM were used to investigate and image the splats and these techniques are previously outlined in chapter 3. Detailed qualitative observations were made of the morphology and distribution of splats using high magnification optical and SEM images.

5.5 Results

5.5.1 Overview of splat types

Optical microscopy surveys were conducted on the different sprayed substrate materials in their smooth state (i.e. the FRP samples were as received, and the metallic and polymer samples were polished). In these surveys, multiple substrates were imaged per sample type and multiple images were taken per a sample. The images were captured using a 10X objective lense and recorded at a 1600 x 1200 pixel resolution. Over 100 splats were imaged and categorised for each substrate type. The splats were manually categorised into one of 4 broad categories (defined below), examples of each of these are shown in figure 5.1.

- Regular (Relatively circular and formed from a continuous coherent splat)
- Irregular (Non-circular and formed from a continuous coherent splat)
- Ring (Large round splats predominantly formed of a large outer ring section without significant material in the middle)
- Fragmented (irregular non-continuous splat)

In addition to putting the splats into categories, bulbous features and holes are identified, examples of these features are shown in figure 5.1.

5.5.2 Metallic substrates

As can be observed from figure 5.2, the majority of the deposited splats on polished steel were coherent and relatively circular. Analysis of multiple optical microscopy images

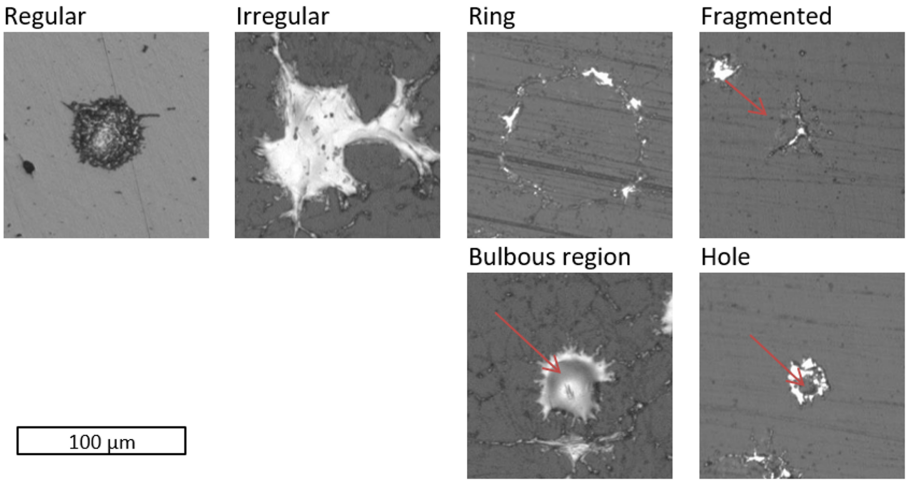


Figure 5.1: Optical microscopy images of (top) representative splats in each defined splat category and (bottom) bulbous features and holes

Table 5.1: Proportions of different splat types on each substrate material

Substrate type	Preportion of different splat type (%)				
	Regular	Irregular	Ring	Fragmented	Rebound
Steel	95	5	0	0	0
epoxy	28	39	21	11	1
CF-epoxy	34	45	16	3	1
PEEK	46	48	4	1	1
CF-PEEK	33	62	3	2	0

(>100 splats on steel substrates) showed that 95 % of the splats fitted this category and had an average diameter of 34 µm (table 5.1, table 5.2 & figure 5.3). The remaining 5% of splats were (what are described here as) irregular splats i.e. non-circular but still coherent. Within the splats on the steel substrates, bulbous regions and holes had a low incidence of 9 and 3% respectively (table 5.3 and table 5.4). Where splats did have bulbous regions and holes they were typically small in relation to the size of the splat (e.g. figure 5.4).

Examining the splats at higher resolution (in the SEM) showed that the surface

Table 5.2: Mean splat diameter (X) and standard deviation (σ) of the different splat morphologies on different (polished/as received) substrates

Splat morphology	Substrate									
	Steel		Epoxy		CF-epoxy		PEEK		CF-PEEK	
	X (µm)	σ (µm)	X (µm)	σ (µm)	X (µm)	σ (µm)	X (µm)	σ (µm)	X (µm)	σ (µm)
Regular	34	19	16	10	19	9	25	13	20	11
Irregular	43	16	15	8	26	19	24	18	23	22
Ring	-	-	69	34	66	37	48	36	32	13
Fragmented	0	0	29	27	27	15	51	23	26	17
All morphologies	34	19	28	29	30	26	26	18	23	19

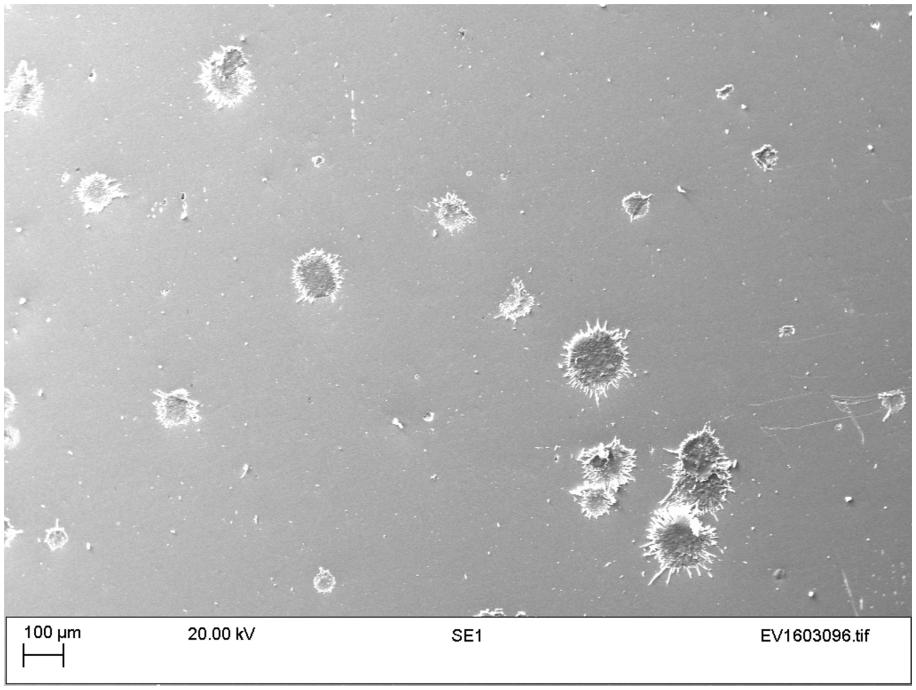


Figure 5.2: Representative SE SEM image of Al splats on polished steel substrate showing their regularity

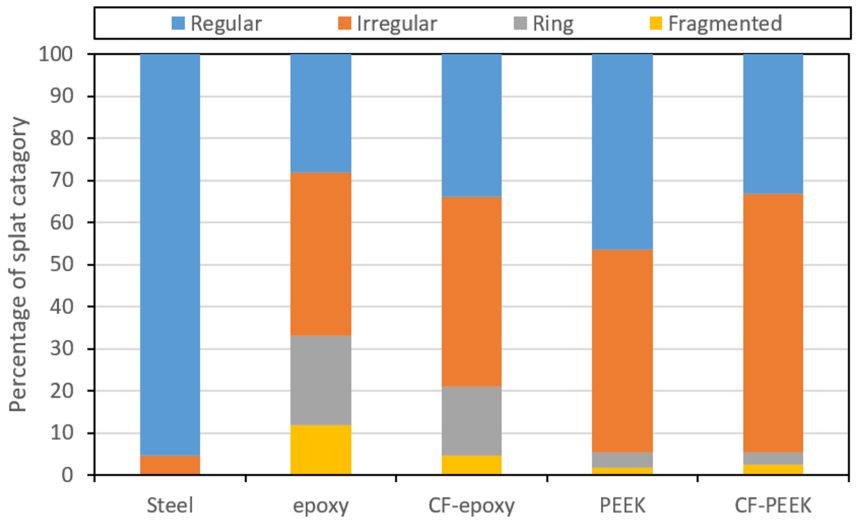


Figure 5.3: Bar chart of the proportion of different types of splat detected on different un-abraded (smooth) substrates

Table 5.3: Percentage of splats which contain bulbous regions on different substrates with different morphologies

Splat morphology	Substrate				
	Steel	Epoxy	CF-epoxy	PEEK	CF-PEEK
Regular (%)	9	66	78	70	78
Irregular (%)	11	23	45	44	44
Ring (%)	-	2	5	0	17
Fragmented (%)	-	9	18	0	0
All splats (%)	9	29	49	54	53

Table 5.4: Percentage of splats which contain holes on different substrates with different morphologies

Splat morphology	Substrate				
	Steel	Epoxy	CF-epoxy	PEEK	CF-PEEK
Regular (%)	3	18	33	17	29
Irregular (%)	0	20	31	26	22
Ring (%)	-	2	3	0	17
Fragmented (%)	-	13	18	0	20
All splats (%)	3	15	27	21	24

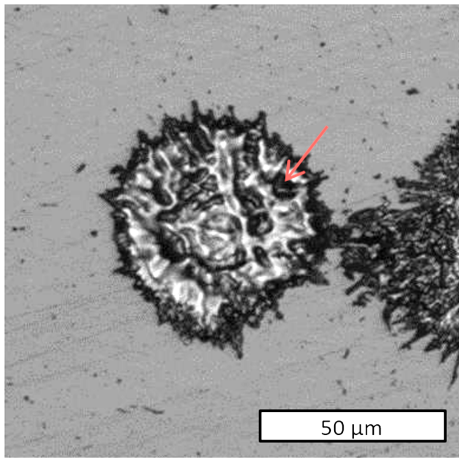


Figure 5.4: OM image of typical Al splat on a polished steel substrate showing that holes are small compared to the overall diameter of splat

of the splat is rough and pores are present underneath the surface. These points are demonstrated by SE (figure 5.5a) and BSE (figure 5.5b) images. The back scattered image of the splat, with its greater interaction depth, reveals that parts of the upper surface are very thin and cover a pore.

The splats deposited on steel were easily removed with carbon tape and figure 5.6 shows features of the underside of a number of splats. There are regions where the removal appears to have resulted in cohesive failure within the splat as shown in figure 5.6a-b. This is characterised by a depression in the centre of the splat with a brittle fracture face

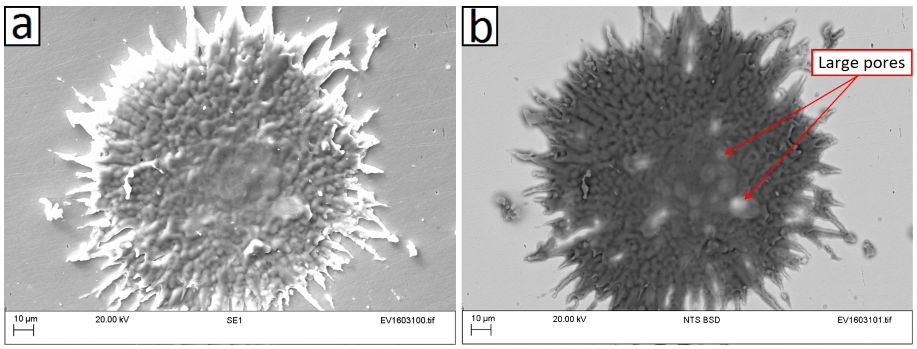


Figure 5.5: SE SEM image of a single Al splats on a polished steel substrate, (a) SE and (b) BSE images. The BSE image shows that there are small subsurface voids not apparent in SE images

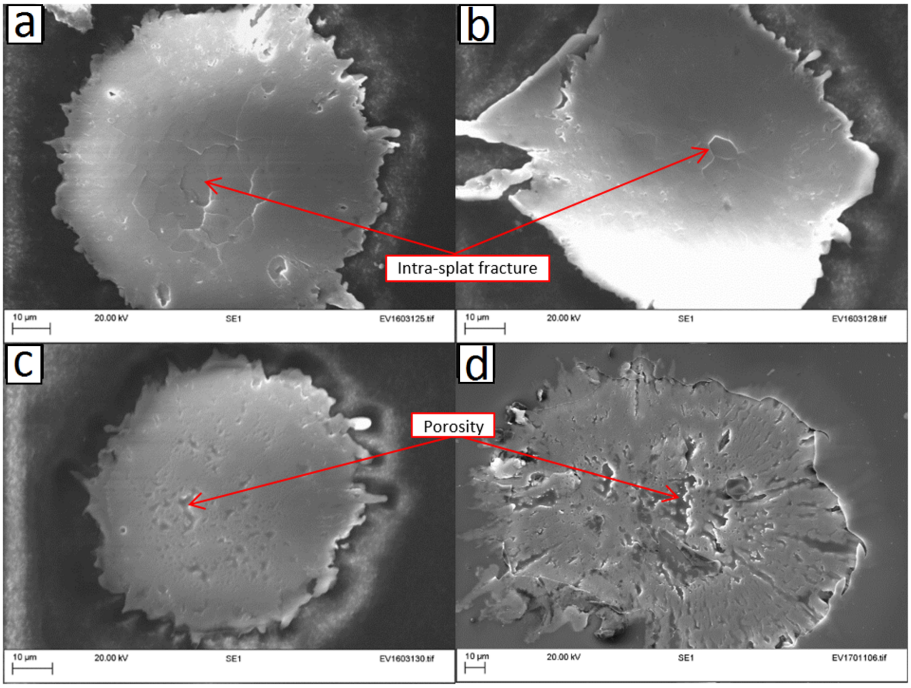


Figure 5.6: SEM images of the underside of a selection of Al splats removed from a polished steel substrate. a and b show cohesive failure, c and d show pores

where the aluminium has possibly failed along grain boundaries. The underside of other splats showed pores, in most cases the pores were nano-micrometre scale as shown in figure 5.6c; however in a minority of cases the pores were larger as shown in figure 5.6d. Figure 5.6d also shows the presence of marks spreading radially outwards. These marks appear to be radially elongated pores.

Figure 5.7 shows the apparent brittle fracture face in figure 5.6a under higher magnification highlighting the possible intergranular fracture. At these higher magnifications, smaller nano-metre scale pores become evident.

After the removal of the splats, the substrate was imaged since there were areas where splats were still in place. However, even where splats had been removed, there were some regions where parts of splats were in place. Figure 5.8 shows a BSE image of one such area, with the remnants of a removed splat on the substrate. This residue may be associated with a splat that failed cohesively leaving some of the splat remaining on the substrate which appears bright in its lower atomic number.

5.5.3 Un-abraded / polished polymers

The characteristics of the splats obtained on the as received FRP and polished polymers were broadly very similar. This is because the surface of the as-received CF-epoxy substrate is almost completely made up of epoxy resin (this is demonstrated in chapter

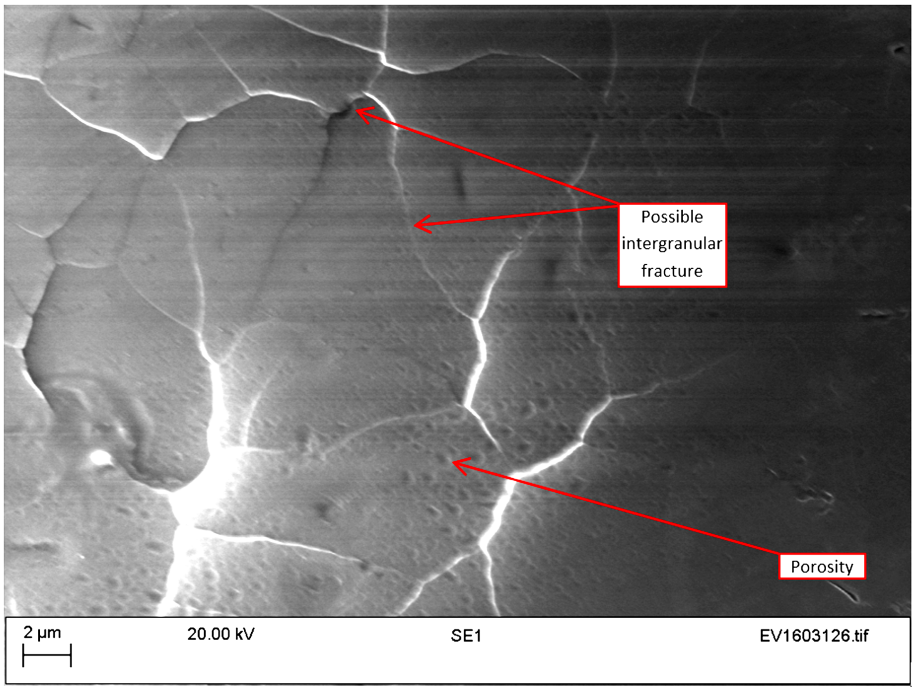


Figure 5.7: SE SEM image of fracture face of Al splat (close up of figure 5.6a)

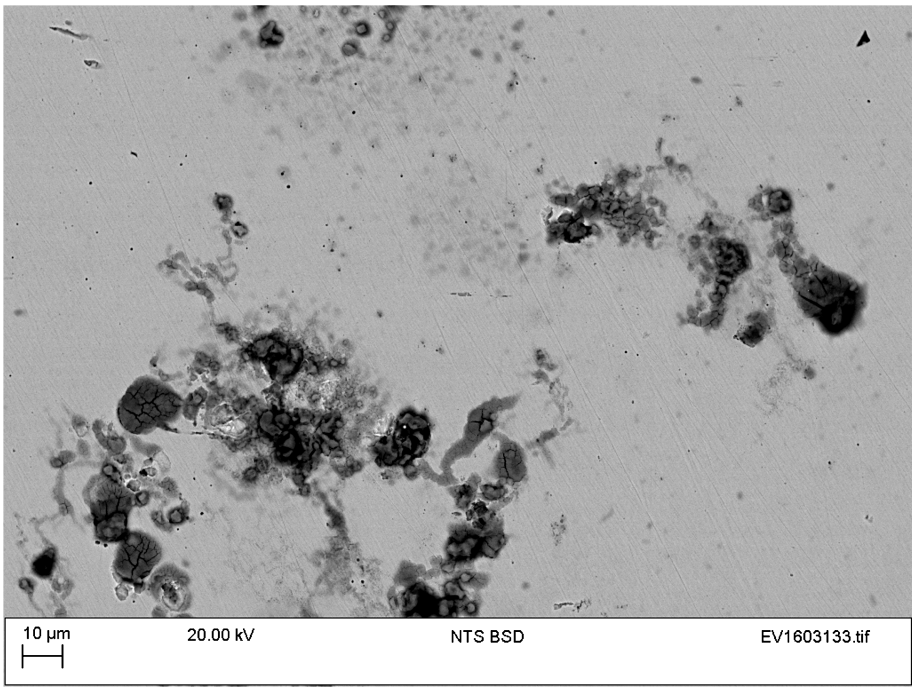


Figure 5.8: BSE SEM image of steel substrate after splat removal, darker regions indicate aluminium residue after splat removal

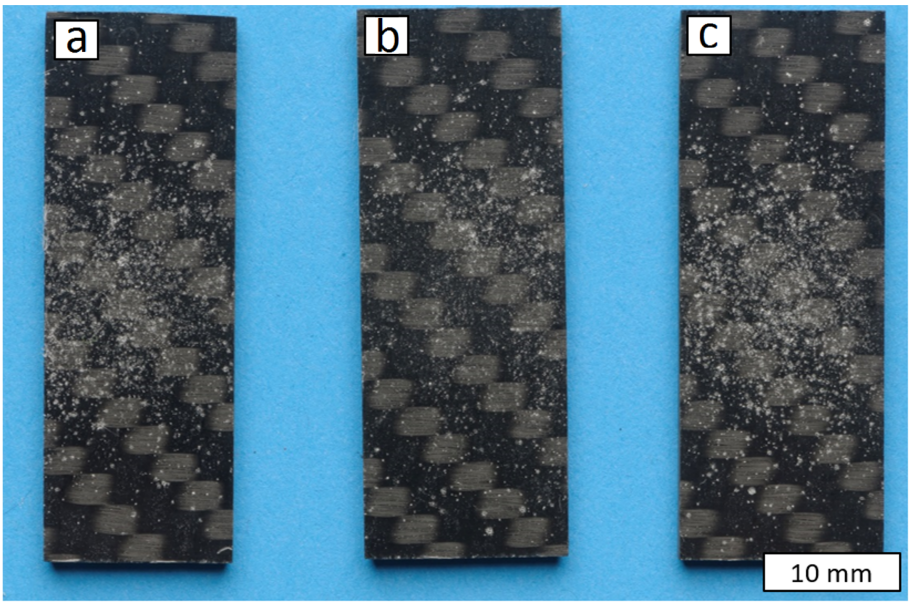


Figure 5.9: Photograph of 3 representative wipe tests on as-received CF-epoxy substrates showing deposited splats against a background of the polymer weave

6); thus the surface presented to the incoming spray particles are very similar. Thus the results of the investigations carried out on as received FRPs are reported alongside the results of the respective polished unreinforced polymers.

Epoxy / as received CFR-epoxy

Aluminium splats were successfully deposited onto both polished epoxy and as received CF-epoxy substrates, as shown (for as received CF-epoxy) in figure 5.9. A representative SEM image showing the general splat morphology is shown in figure 5.10; this image is of polished epoxy but very similar images were obtained on as received CF-epoxy. This is to be expected as the surfaces of the substrates are very similar as mentioned in section 5.5.3. Due to the size of the rings, they appear to be dominant. However, all types of splat categories defined in this study were found on the surface during the OM survey. The proportions of the different types are similar for the epoxy (28 % regular, 39 % irregular, 21 % ring and 11 % fragmented) and the CF-epoxy (34 % regular, 45 % irregular, 16 % ring and 3 % fragmented) (figure 5.3). Of these, a majority of the regular splats (66 % and 78 % for the epoxy and CF-epoxy respectively) contained bulbous regions and significant numbers contained holes (see table 5.3 and table 5.4).

Representative OM images of regular, irregular and fragmented splats obtained on polished epoxy are shown and labelled in figure 5.11. Several of the splat types have bulbous regions and holes which are representative of the splats as a whole. Splats were removed from the surface of the sample with carbon tape. The undersides of several

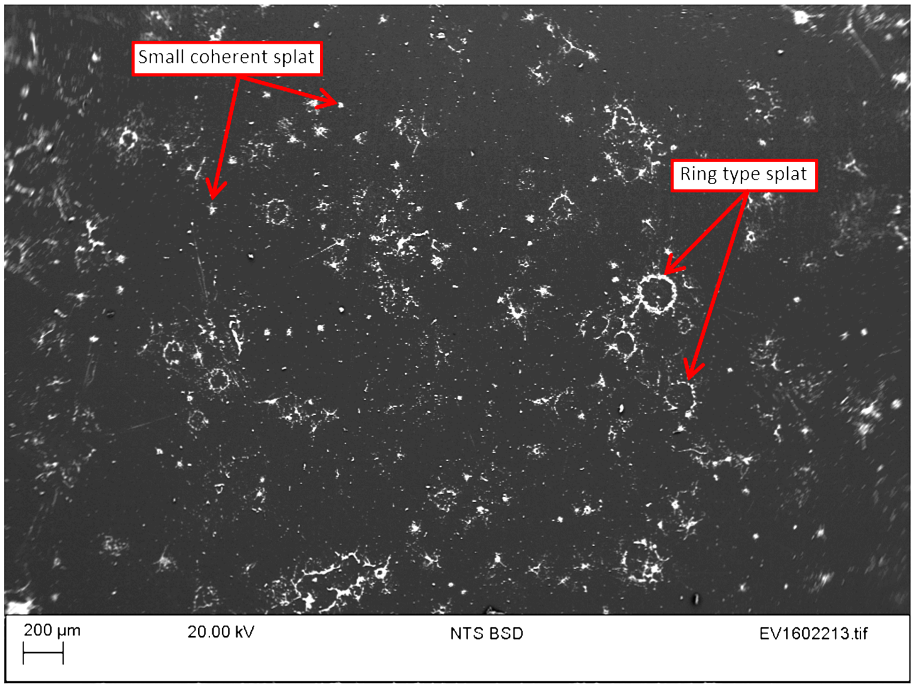


Figure 5.10: Low magnification BSE image of Al splats on Epoxy substrate. Showing mainly large ring type splats

splats are shown in figure 5.12; these images have been focus stacked to allow sharp detail to be seen across the sample. The undersides of the splats contain large hollow voids which are relatively smooth except for possible elongated markings. Figure 5.13 shows an optical image, height image and profile trace of a void in a representative splat showing that the depth of the void is approximately 5 µm. These voids presumably match up with the bulbous regions of the splat as indicated by figure 5.14. This shows a carefully prepared cross section of a single splat deposited on as received CF-epoxy. In addition to the large voids in the centre of the splat, figure 5.12 and figure 5.13 show that there is some roughness around the periphery of the underside of the splat, which may be associated with smaller voids, or mirroring topographical roughness caused by thermal damage.

A representative ring type splat deposited on a polished epoxy substrate is shown in figure 5.15. This image is representative of ring splats deposited on as received CF-epoxy wipe tests. The image clearly shows an outer ring as well as a small irregular inner splat with sub-micron sized drops of aluminium radiating out from it. The outer half of the ring is in good contact with the substrate and the inner half is not attached to the substrate and angled upwards; this is also suggested by the cross section of the splat ring figure 5.16. In addition there are often ligaments of varying size radiating out from the outer ring. It is also of note that polishing marks are still clearly visible within the ring in secondary electron mode (figure 5.17).

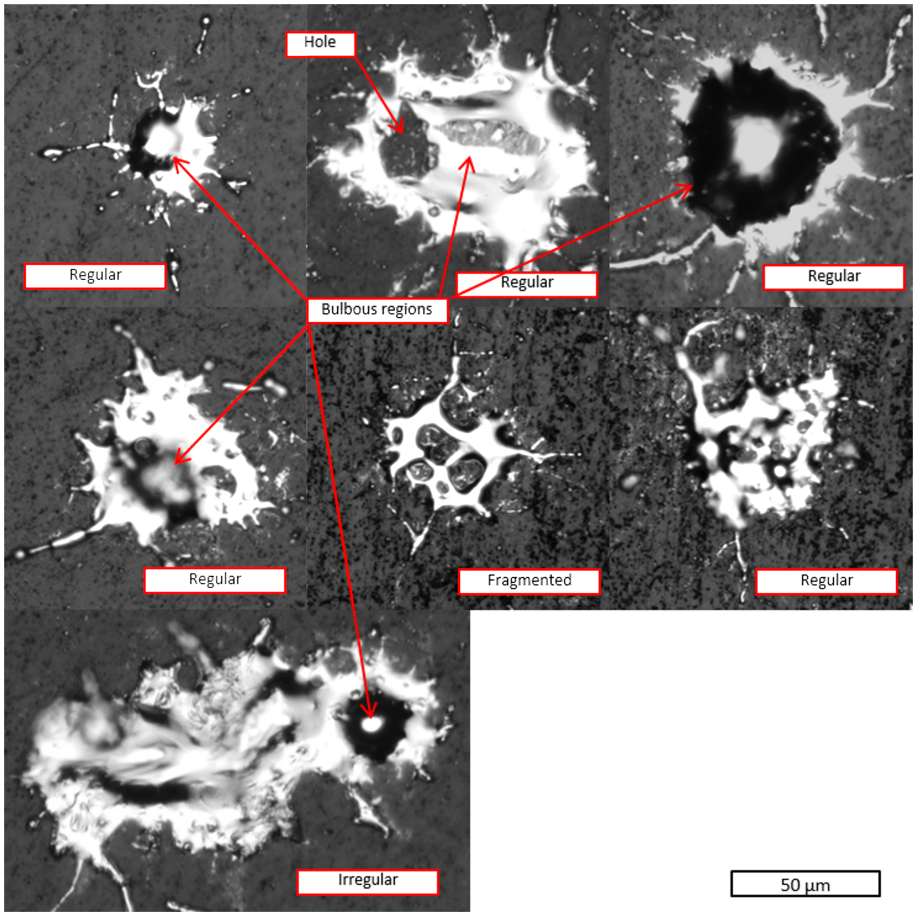


Figure 5.11: OM images of non-ring type splats on epoxy substrate, showing bulbous regions and holes. Images are NOT focus stacked and the blurey areas indicate height

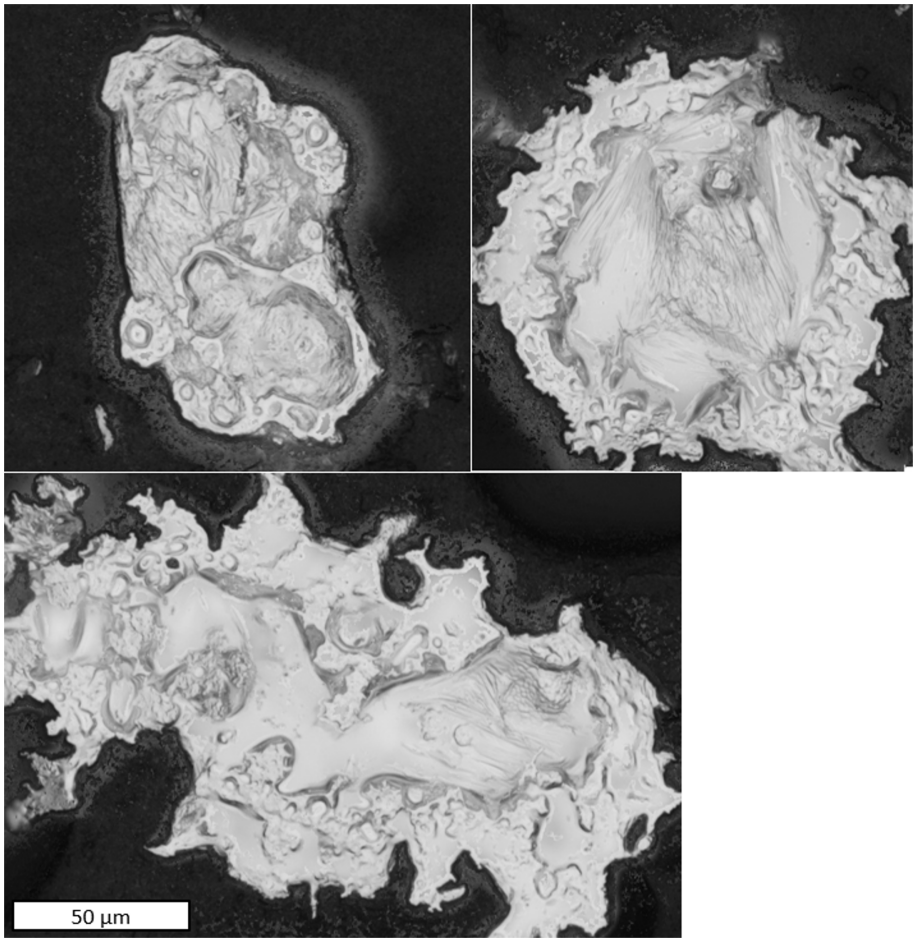


Figure 5.12: OM images of underside of non-ring type splats removed from epoxy substrate showing the detail of the large bulbous regions. Images are focus stacked

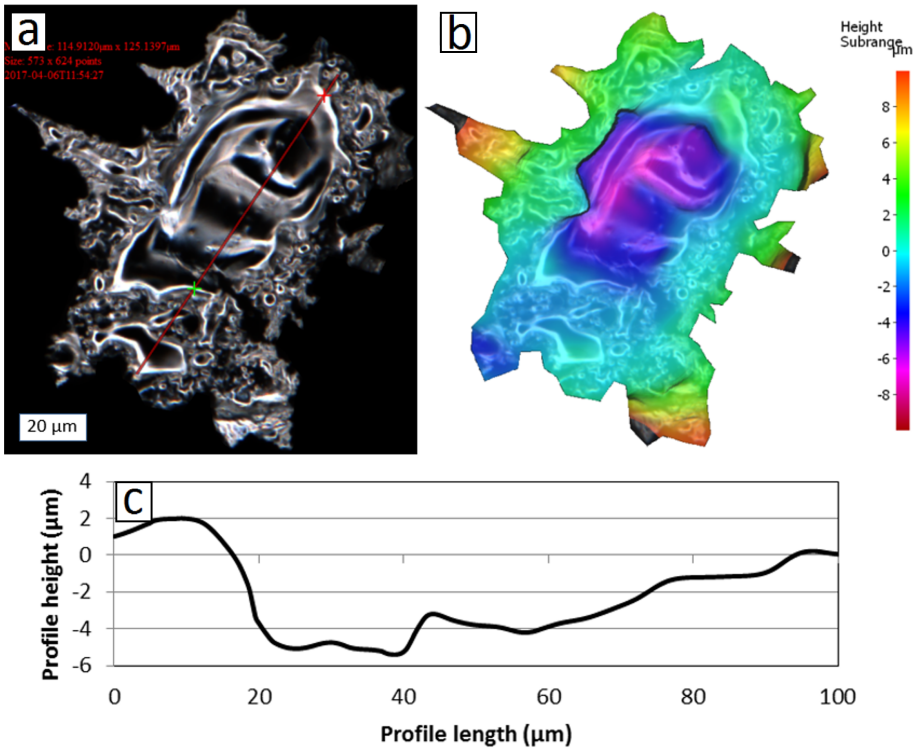


Figure 5.13: Example splat underside removed from polished epoxy (a) Optical image, (b) Height image and (c) line profile trace showing depth of the bulbous region

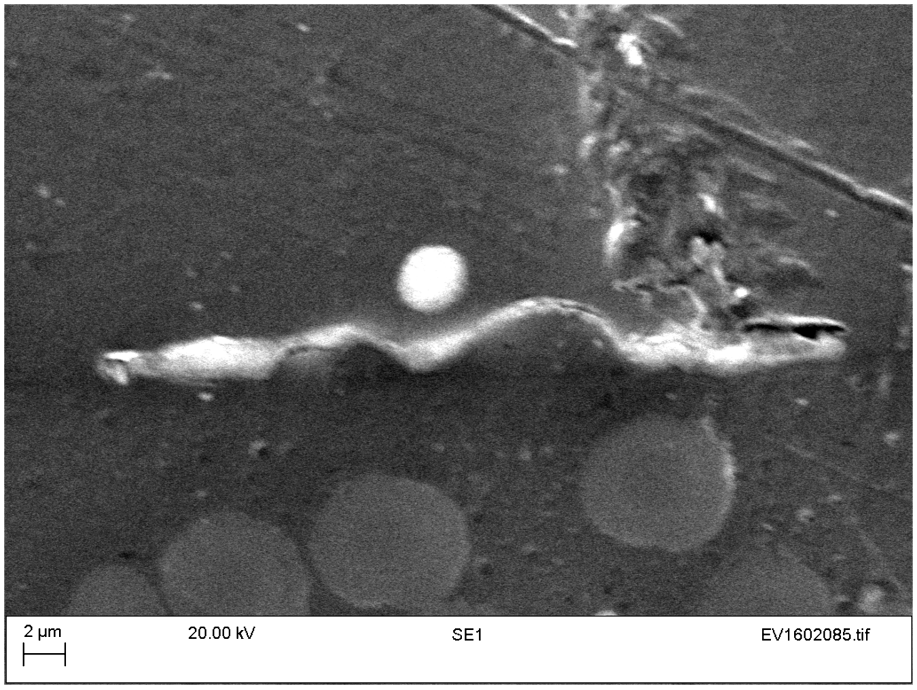


Figure 5.14: SE SEM image of a cross section through an Al splat on an as received CF-Epoxy cross section showing voids in the centre of the splat

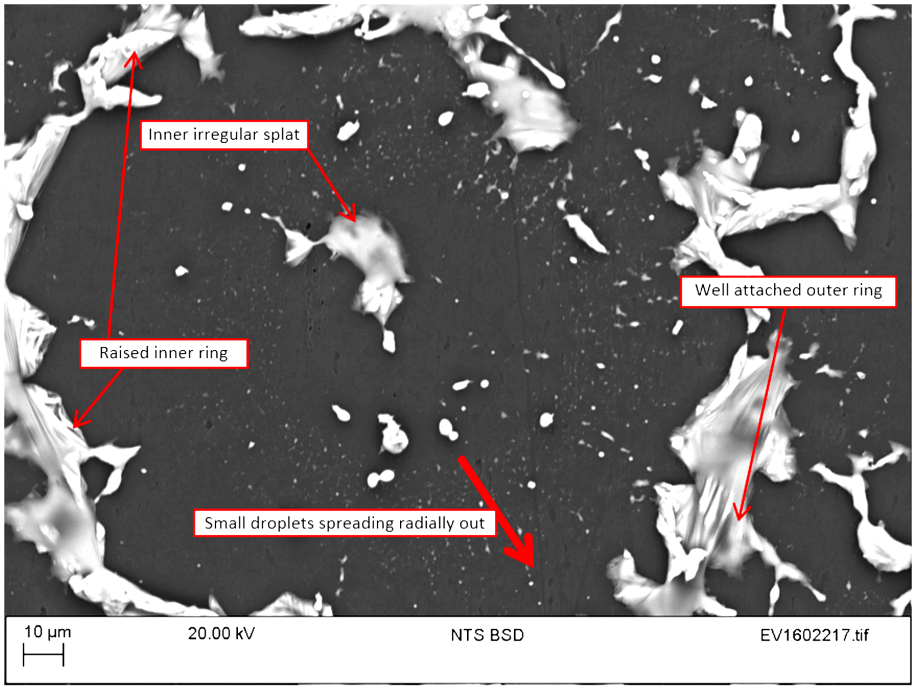


Figure 5.15: Representative BSE image of ring type Al splat on epoxy substrate showing raised inner edges, well attached outer edge and debris radiating outwards

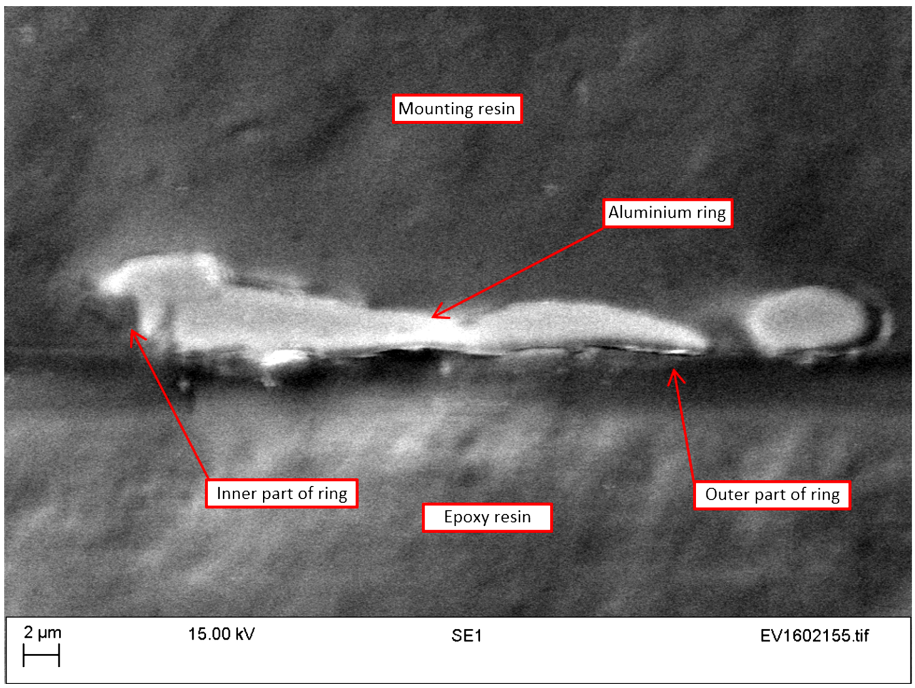


Figure 5.16: SE SEM image of a cross section of part of a Al ring splat on polished epoxy substrate showing a raised and a well adhered adge

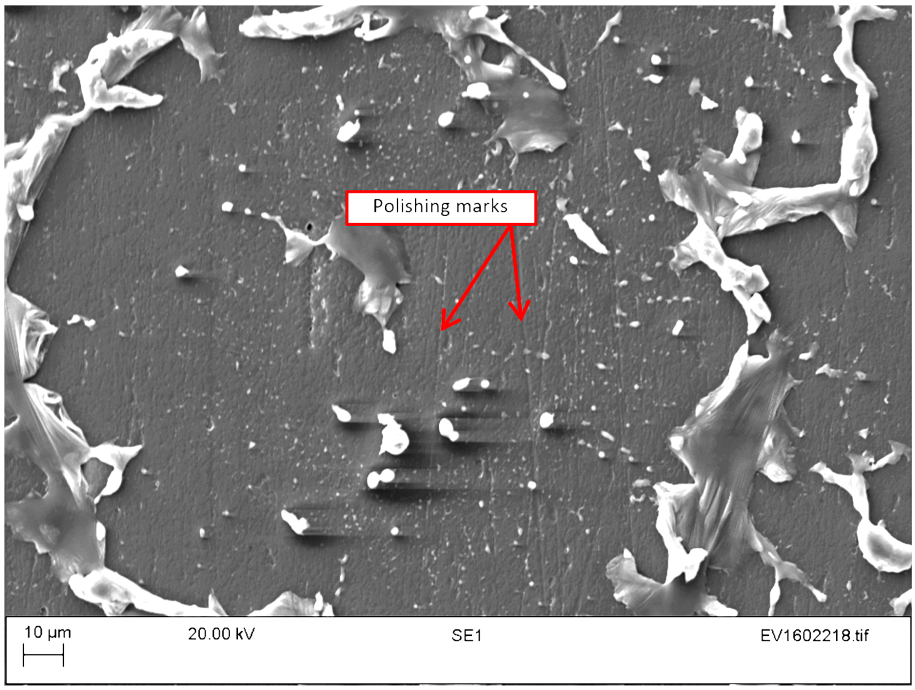


Figure 5.17: SE image of Al splat on polished epoxy substrate shown in figure 5.15 showing polishing marks on surface

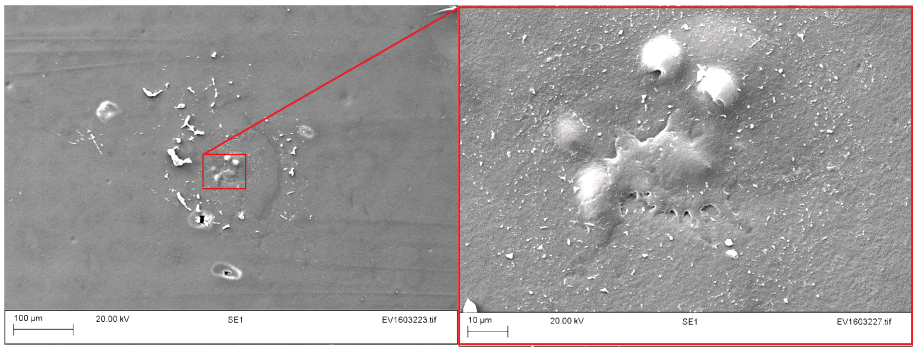


Figure 5.18: SE SEM image of substrate area after removal of splat on as received CF-Epoxy wipe test. Area in the red box is shown in greater detail inset. The figure shows damage caused to the substrate due to the particle

The individual splats had relatively low adhesion and were effectively removed with adhesive carbon tape. Figure 5.18 shows the CF-epoxy substrate after the removal of a ring type splat. The carbon tape removed most of the aluminium from the area; however, the outline of the splat is still clearly visible. This may be partially due to the fact the samples were sputter coated before and after splat removal; thus, the portion of the substrate without the splat was gold coated twice. However, detailed images of the area, such as Figure 5.18 (inset), show pores which indicate possible damage to the substrate. This damage may either have occurred as a result of thermal damage to the sample during spraying, from removing the splat, or a combination of the two.

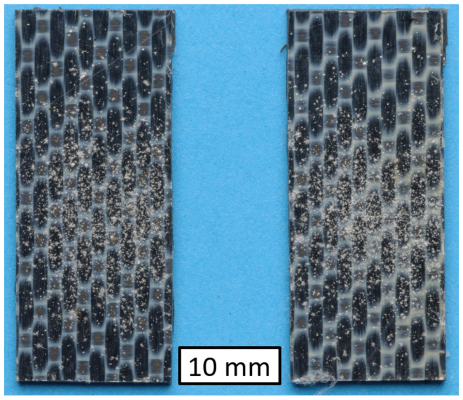


Figure 5.19: Photograph of representative CF-PEEK wipe tests showing splats deposited onto CF-PEEK substrate. Fibre weave clearly visible

PEEK / as received CFR-PEEK

As mentioned in section 5.5.3 the surface of the as received FRP and polished polymer substrates are both completely covered in polymer, thus the splats deposited onto the PEEK and CF-PEEK are very similar, and as such are dealt with together in this section.

Aluminium splats were successfully deposited onto a polished PEEK and as received CF-PEEK substrates (shown in figure 5.19 for as received CF-PEEK). The proportions of ring and fragmented splats deposited were similar for the PEEK (4 and 1% respectively) and as received CF-PEEK (3 and 2% respectively). However, the polished PEEK had a marginally higher percentage of regular splats compared to as received CF-PEEK (46 and 33 % respectively) (figure 5.3).

A majority (54 and 53% for PEEK and CF-PEEK respectively) of the splats had bulbous regions this proportion increased to 70 and 78% respectively when only including regular splats, and around 20% of splats deposited on these substrates had a holes identified in the OM survey (table 5.3 and table 5.4). Examples of bulbous regions and holes in the splats deposited onto polished PEEK are shown in Figure 5.20, though similar images could equally have come from a CF-PEEK sample. The undersides of the removed splats show significant voids; a representative splat underside is shown in Figure 5.21 alongside a line trace which show a depth of around 5 µm. These voids likely coincide with the bulbous regions on the top of the splat. A more detailed image of a splat underside is shown in Figure 5.22; this splat was removed by applying an epoxy mounting compound before pulling it off hence the voids are filled up with resin. This image shows in detail multiple voids of varying size throughout the splat, the largest ones toward the centre of the splat.

After removal of the splats from the substrate, SEM images clearly indicate that there had been a change to the substrate surface (figure 5.23 & figure 5.24). Where the

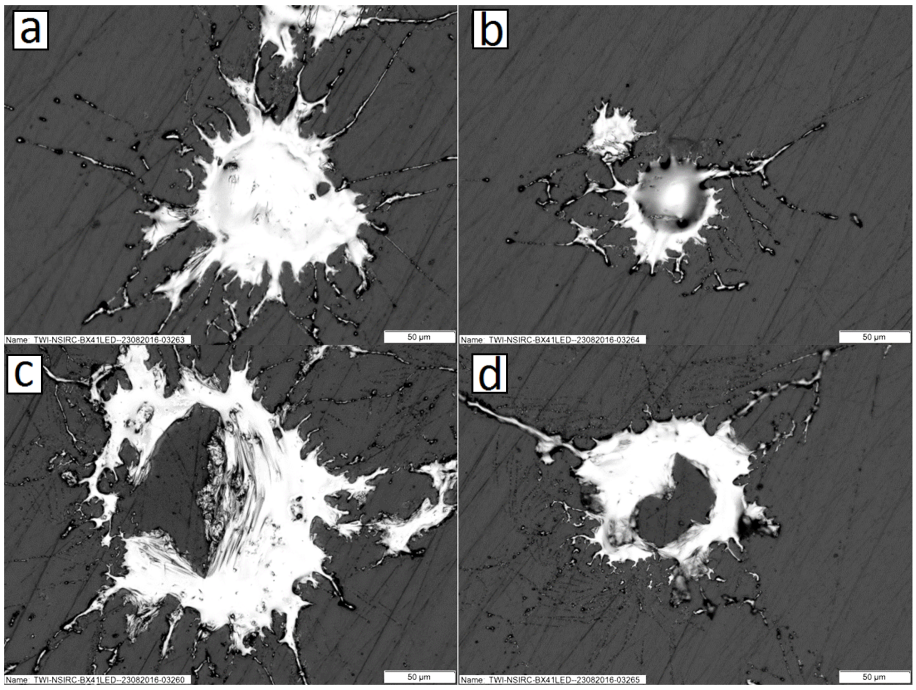


Figure 5.20: Optical microscopy images of different splats showing the development of large hole in the centre of splats on a polished PEEK substrate

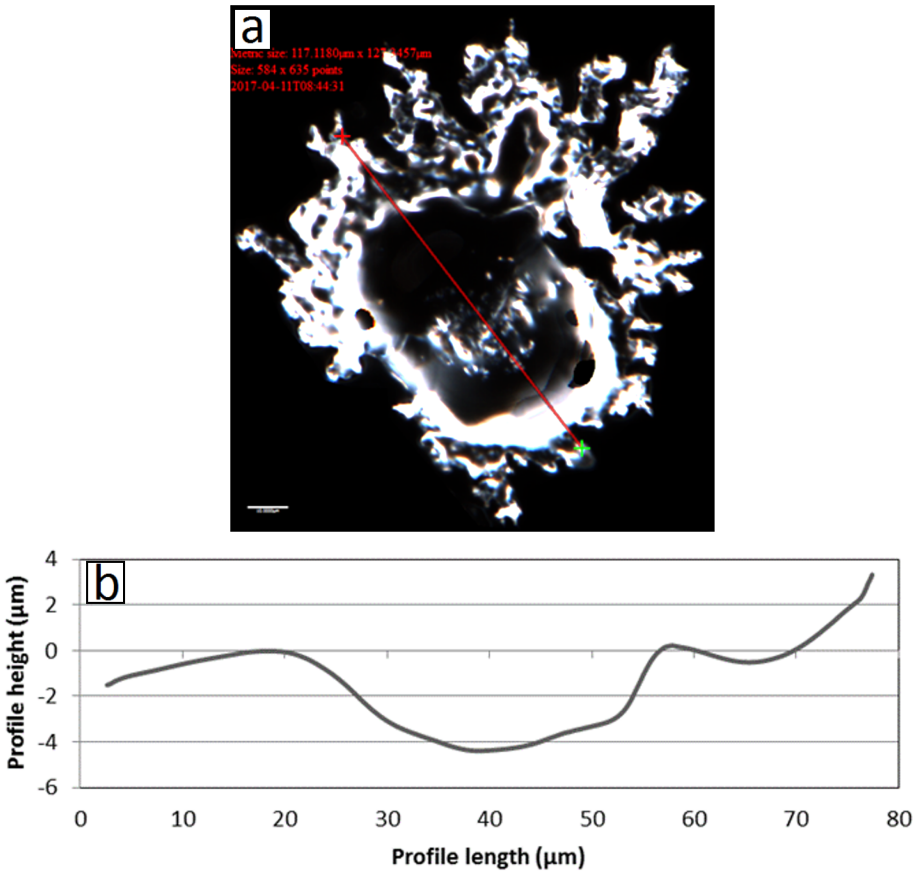


Figure 5.21: Example splat underside removed from polished PEEK (a) Optical image and (b) height line profile trace showing depth of the bulbous region

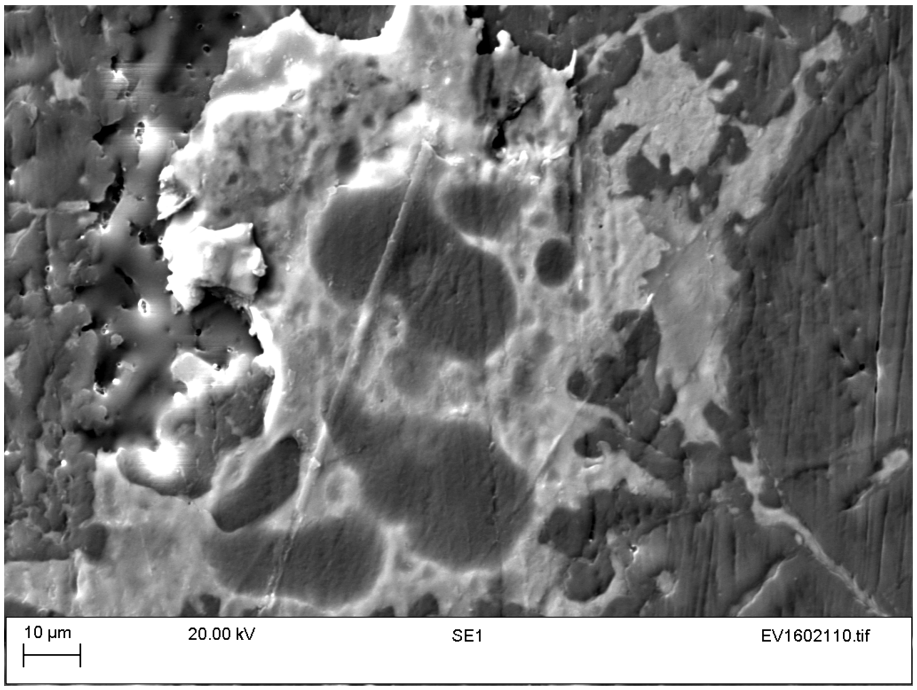


Figure 5.22: SE SEM image of the underside of a splat deposited onto a polished PEEK substrate showing the voids coincident with the bulbous regions. Due to the method of splat removal voids have been filled up with mounting resin

splats had previously been, the area was rougher and there was some signs of damage or melting. This point is reinforced by comparing those (figure 5.23 & figure 5.24) to an unaffected areas e.g. figure 5.25. In addition, figure 5.23 shows an area within the centre of the splat area where this change in surface was not so evident. Given the general morphology of the splats this may have been coincident with a large bulbous region.

In addition to the features described above, many of the splats deposited onto the PEEK and CF-PEEK substrates also had long ligaments extending outwards from their periphery. Figure 5.26 shows a representative SEM image of splats on a polished PEEK substrate displaying these extending ligaments. Under SEM examination, covered voids can be seen, which would not have been evident from the OM survey, but would likely match up with the small voids shown in the SEM image of the splat underside.

Splats deposited on the epoxy and PEEK substrates have some similarities in their morphologies, i.e. the both have significant numbers of splats containing a large bulbous region. However, splats deposited on the epoxy substrate are more likely to form ring and fragmented splat types than those deposited onto PEEK. In addition, splats are shown to modify the topography of both substrates. In the case of the PEEK based substrates, at least part of this appears to be though melting the substrate surface.

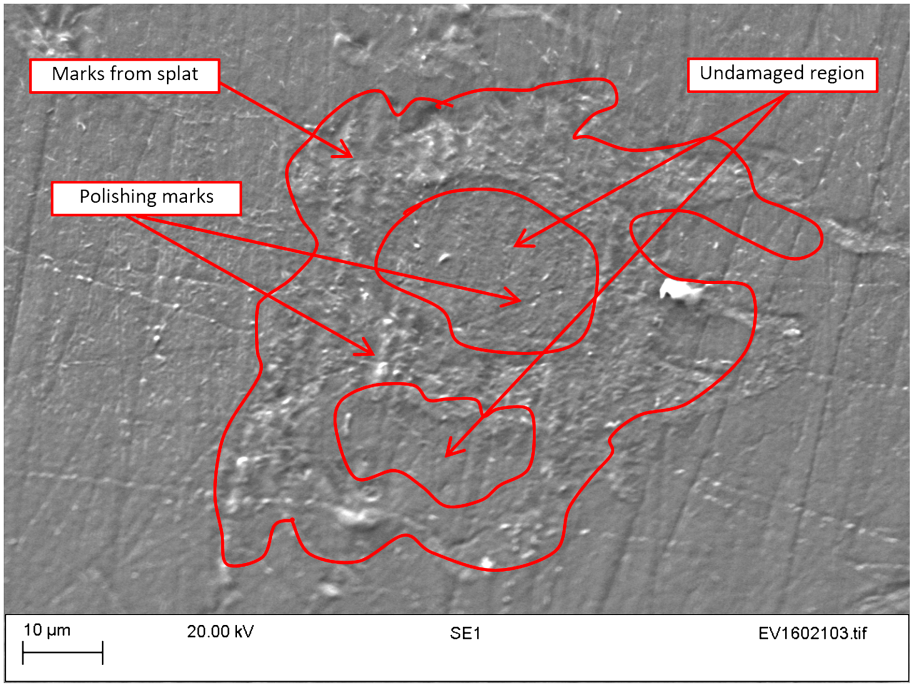


Figure 5.23: SEM image of area where Al splat was removed from PEEK substrate (30° angle) showing damage to the substrate where to splat had been and unaffected region likely coincident with bulbous region of splat

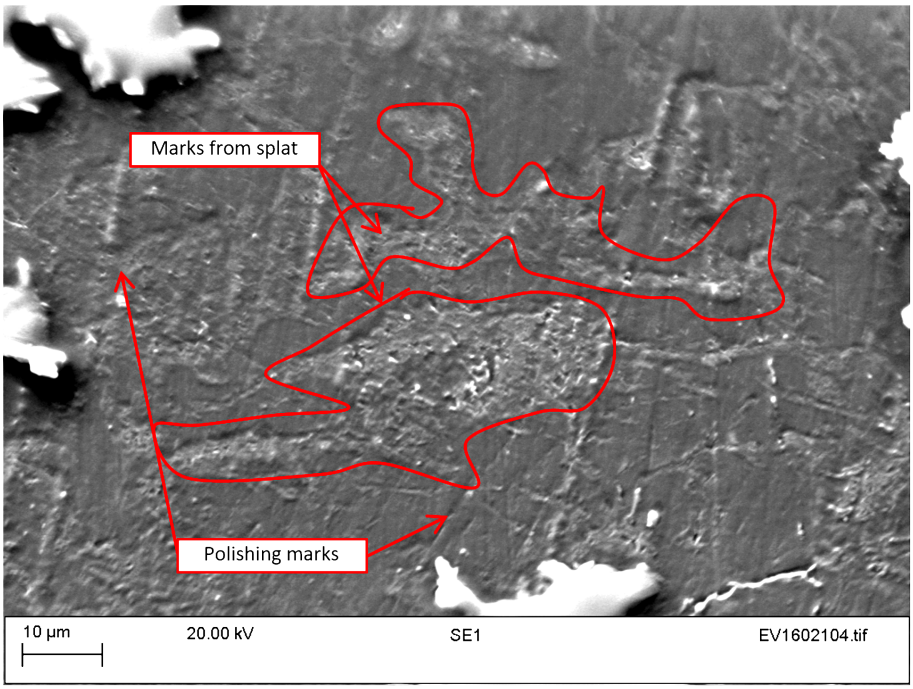


Figure 5.24: BSE SEM image of area where Al splat was removed from PEEK substrate (30° angle) showing damage to the substrate

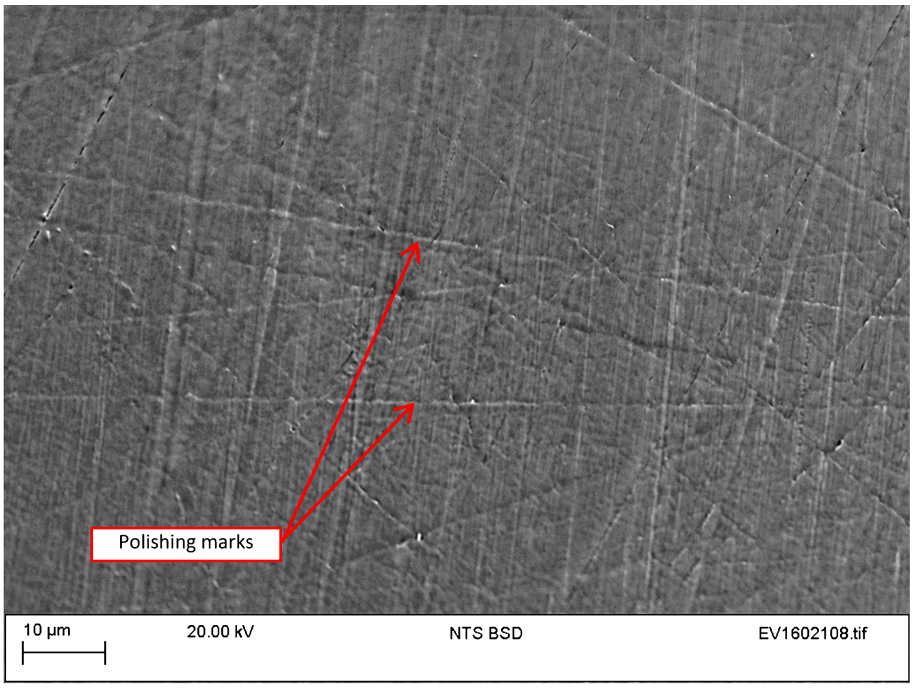


Figure 5.25: SE SEM image of area on PEEK substrate where no splat was previously deposited (image included for comparison) (30° angle)

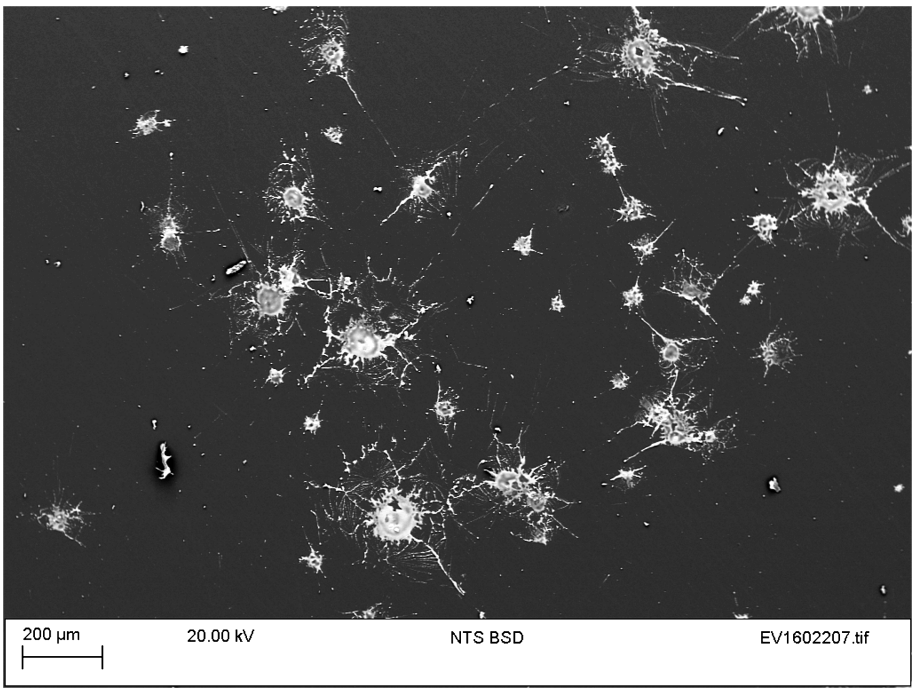


Figure 5.26: SE image of area of an area from a polished PEEK wipe test showing bulbous regions and ligaments radiating from the centre of splats

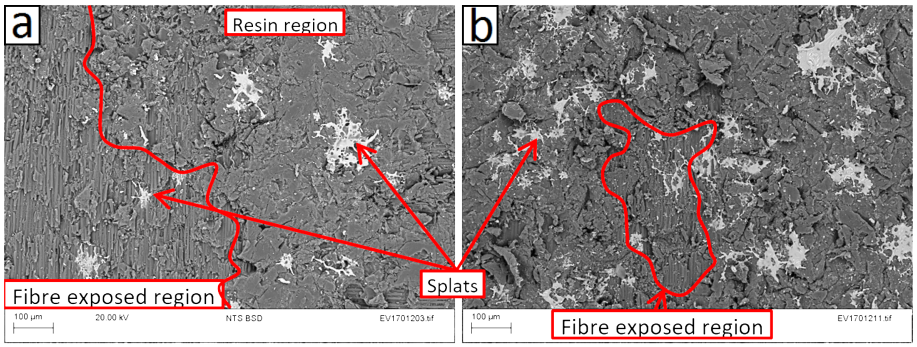


Figure 5.27: BS SEM image of deposited splats on (a) LGB CF-epoxy and (b) LGB CF-PEEK wipe tests showing that splats are deposited on both resin and fibre exposed areas

5.5.4 Roughened FRPs

Upon grit-blasting the FRPs, the substrates are roughened and fibres are exposed. The extent of fibre exposure and roughening is different on the different substrates (this is discussed in detail in chapter 6). However, the general observations as to how the particles interacted with the grit-blasted FRPs and formed splats are similar between the FRP types. Thus, splat morphology on grit-blasted CF-epoxy and CF-PEEK are discussed together.

Splats were successfully deposited on CF-epoxy and CF-PEEK substrates in a LGB state. The splats were successfully deposited in both fibre and resin regions (Figure 5.27). Within the fibre regions, it is not possible to tell whether splats are adhering to fibres or small areas of resin within the fibre area as appears to be happening in Figure 5.28. The shape of the splats is irregular and they appear to follow the topography of the underlying substrate as demonstrated by Figure 5.29. There are also indications that there are gas pockets beneath the surface of the splat with only a thin aluminium film covering them (Figure 5.30). There appear to be more of these pockets in splats which are deposited on resin areas for example in Figure 5.31. In addition there is also surface rippling possibly due to the solidified skin being deformed during cooling.

5.5.5 Reinforcement fibres

Splats were shown to deposit effectively onto dry carbon fibre cloth (figure 5.32a). At higher magnifications it is clear that the aluminium splats deform around the loose fibre cloth and fill up gaps between the individual fibres (figure 5.32b). In some cases there is evidence that the splats are wetting the fibres, figure 5.33.

Although glass fibres are not a main part of this study, it was interesting to observe the behaviour of splats on dry GF cloth substrates. Splats were shown to have deposited

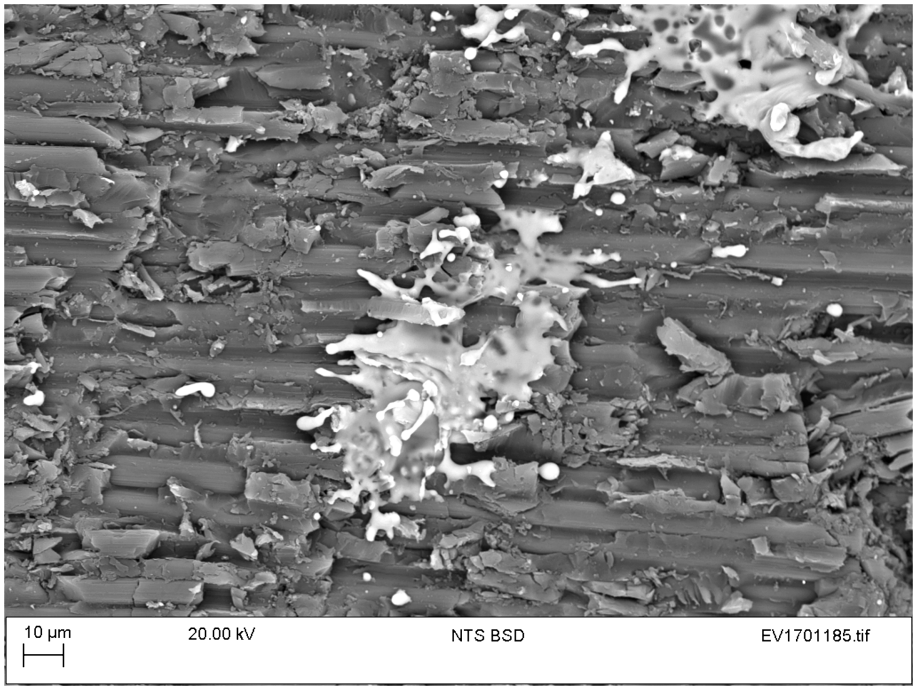


Figure 5.28: BS SEM image of deposited splats on LGB CF-epoxy showing splats on fibre exposed area possibly adhering to resin

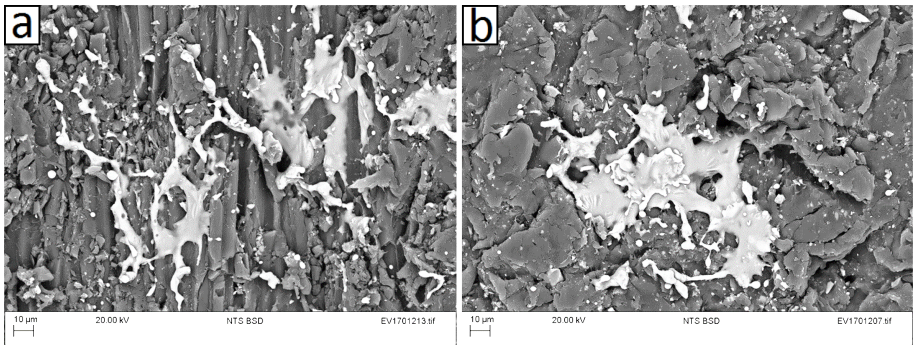


Figure 5.29: BSE images of a LGB CF-PEEK wipe test with splats deposited on (a) fibre phase and (b) resin phase showing splat filling the underlying substrate topography

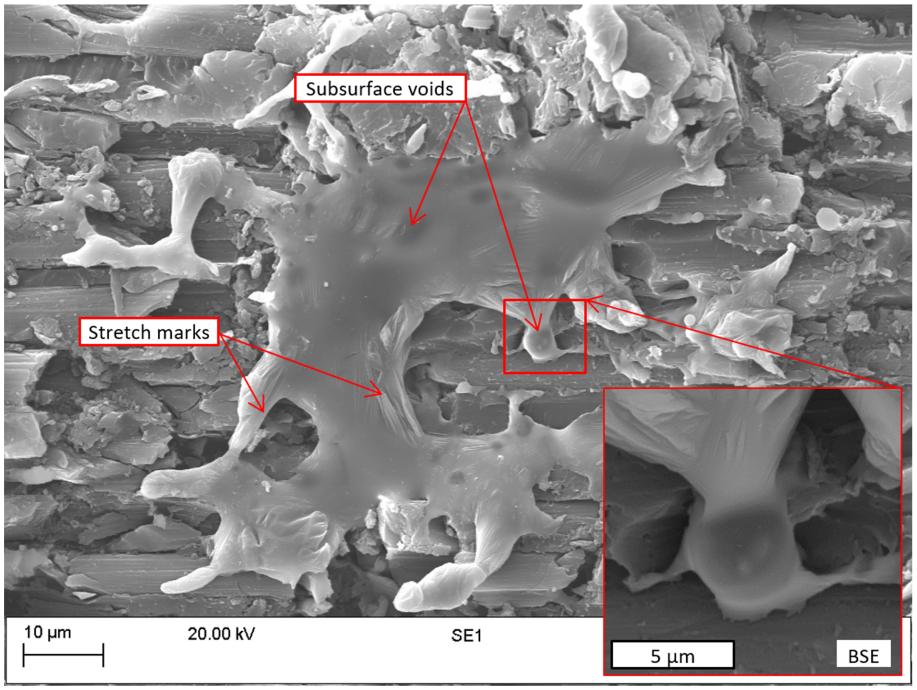


Figure 5.30: SE/BS SEM image of deposited splat on LGB CF-epoxy showing splat following the topography of the substrate, surface elongated ripples and gaseous subsurface voids

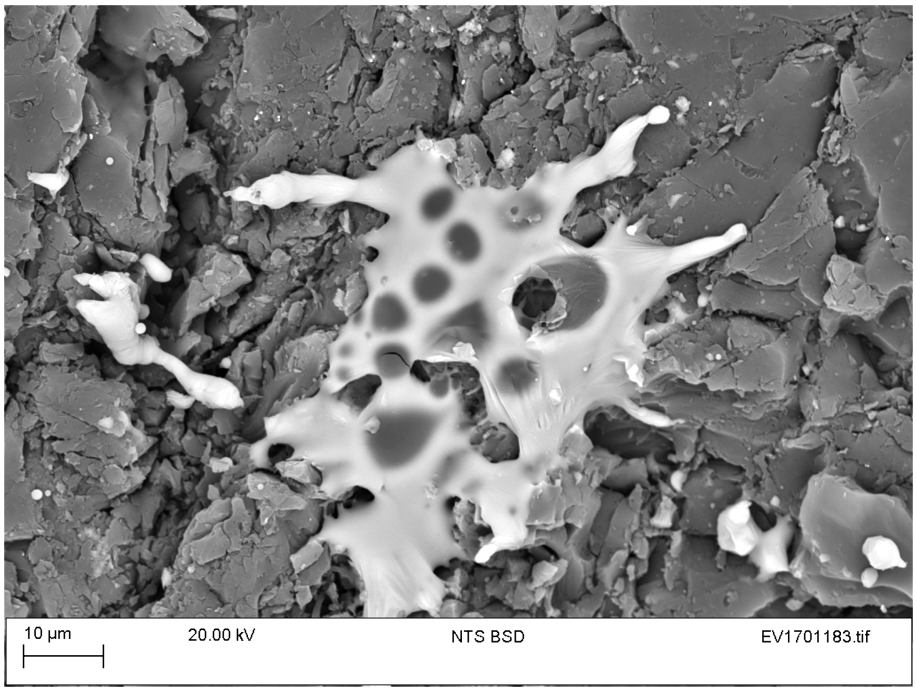


Figure 5.31: BSE SEM image of deposited splat on resin region of LGB CF-epoxy showing surface stretch marks and gaseous subsurface voids

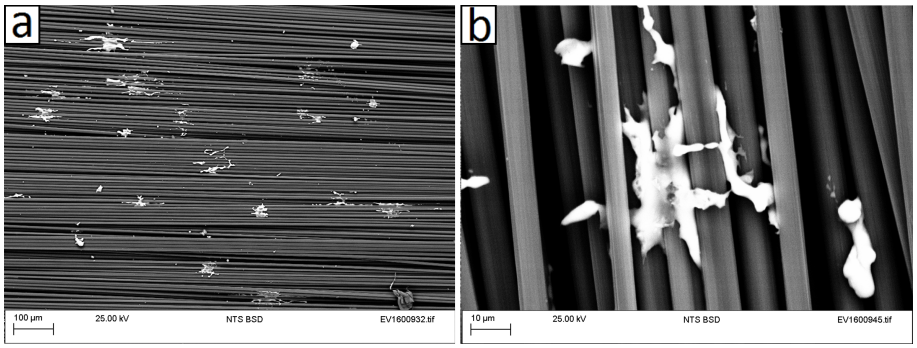


Figure 5.32: BSE image of area of dry CF cloth wipe test (a) general area (b) detail of splat wrapping around loose fibre

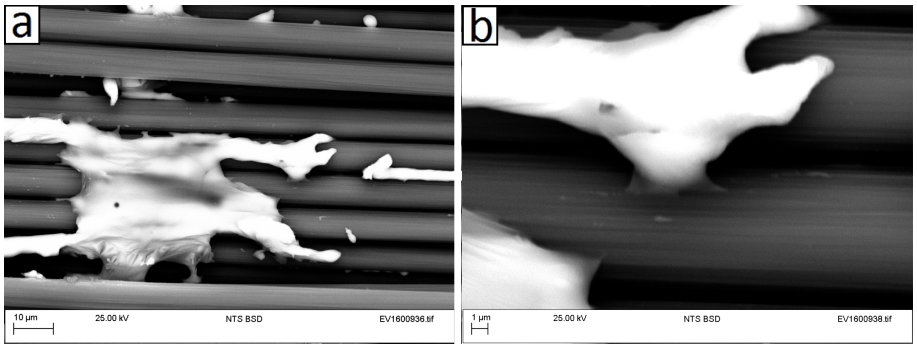


Figure 5.33: BSE image of Al splat on dry CF cloth wipe test (a) general detail (b) showing wetting of Al to fibres

onto dry glass fibre cloth (figure 5.34a), although there were far fewer splats per unit area than on the CF cloth. At higher magnifications it is clear that the aluminium has failed to wet and spread on the glass fibre; instead large splats have balled up. In addition, there are many small balls of aluminium on the surface of the fibres (figure 5.34b). The larger splats in the image also have not spread and are indicative of non-wetting behaviour.

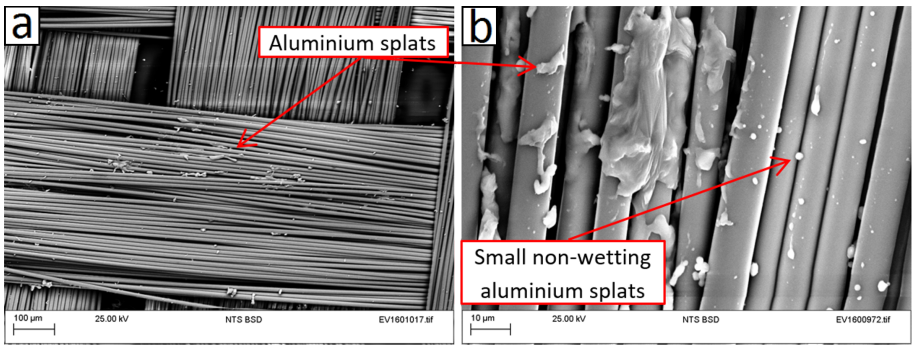


Figure 5.34: BSE image of Al splats on dry GF cloth wipe test (a) general detail (b) showing lack of spreading/wetting of splats

5.6 Discussion

The morphology of every observed splat in this study indicates that the particles were fully molten as they impacted onto the substrate surface. The molten nature of the particles on impact means that they can be interpreted in line with the bulk of the available literature (where particles are typically fully molten on impact).

5.6.1 General description/Flattening behaviour

An early description of an individual thermal spray particle impact and deformation is given by Madejski in [151] and provides a mathematical framework for understanding the process. The process is seen in terms of an overall energy balance, with the sum of the potential and kinetic energy, as well as the work done against internal frictional forces is constant throughout. Prior to the droplet impacting the substrate the kinetic energy is simply given by equation 5.1, potential energy by equation 5.2 and no work has been done against friction, where D = droplet diameter, V = droplet velocity, ρ = density and σ = aluminium surface energy. As the droplet impacts on the substrate, it deforms and the surface area increases, as does the potential energy as implied by equation 5.2. Deformation also requires work to be done against frictional forces. Alongside these processes solidification starts to occur from the centre of the splat. Combining these, the flattening ratio of the splat (splat diameter/droplet diameter) can be determined with respect to time. Differentiating this gives a maximum flattening ratio. Exact analytical solutions cannot be determined but different limiting cases e.g. high Reynolds and Weber numbers have been calculated.

$$KE(t=0) = \frac{V_{drop}}{2}\frac{\pi}{6}D^3\rho_{liquid} \tag{5.1}$$

$$PE(t=0) = \pi\sigma D^2 \tag{5.2}$$

Assuming that the particles impacting the substrate were at their melting temperature (660°C), the theory determines that the size of the splats on the polymer substrates should be approximately 180 µm in diameter, and those on the steel substrates should be ≈50 µm in diameter. The splat diameter estimated for the splats on the steel substrate is a small overestimation, but close to the observed value. However, the effect of changing the substrate material predicted by Madejski's model is opposite to what is observed. The model suggests that because the cooling rate of the splat is slower on the polymer

substrates (due to lower substrate thermal conductivity), the splats should be larger than those on steel. The present observations show that this is not the case and that the splats are marginally smaller than those observed on steel substrates. The disparity could be associated with many different phenomena which are not captured in the modelling. For example, the modelling assumes solidification initiates from the centre of the splat at the splat substrate interface. However, due to the low thermal conductivity, solidification may also initiate on the top of the splat retarding the spreading of the splat. There is some limited evidence for this occurring from the ripple marks present on the top of some of the splats which suggest an initially solidified film is deformed. An alternative explanation could be poorer wetting of the aluminium on the polymer surface, resisting the liquid flow and flattening of the splat.

Whatever the reason for the model not reflecting the observed results, it highlights necessarily simplifications/assumptions inbuilt within it. One such assumption is that the splats have a perfectly round morphology. However, the morphologies observed in this study show that this is not the case. Morphological features are described and explained in the discussion below.

5.6.2 Morphology

As noted in the results section, significant proportions of the splats deposited onto polymer based substrates contained large bulbous regions. Imaging cross sections and the underside of these splats indicated that the large bulbous regions were coincident with large voids. These voids/bulbous regions appear to be formed by a development of gas underneath the splat which, whilst the splat is still molten, form large gas pockets. The mechanism for gas formation is unclear and will be discussed later in the section.

In addition to bulbous regions, a significant proportion of the splats deposited onto polymer based substrates contained holes. It seems likely that the holes were formed in a similar manner to the bubbles. Except, in the case of holes the gas pressure overcomes the surface tension of the aluminium and bursts the bubble revealing the underlying substrate. This development is well depicted in Figure 5.20a-d which shows a series of splats whose morphology moves from a regular splat with a bulbous region to a regular splat with a hole. Figure 5.20a is especially illustrative in showing the rupture of the aluminium on top of the void.

The ring type splat can also be seen in the same context, as a splat where a proportionately very large bulbous region breaks, leaving a ring around the periphery and only debris of the dome in the centre. This is demonstrated by figure 5.15 and figure 5.16

which show how the outer part of the ring is flat and well attached to the substrate, whereas the inner part is raised and looks to be the remnants of a dome/bubble. The ligaments around the outer ring could also be remnants of the central splat propelled by the busting of the bubble.

Given the proposed mechanism, a bulbous region, large hole and ring type splats form a continuum with the specific properties of the particle and amount of gas generated determining the morphology. Therefore it is interesting that the epoxy substrate had a higher proportion of ring type splats than the CF-epoxy, PEEK and CF-PEEK substrates but a lower proportion of bulbous features of holes. This may indicate that that more gas, due to a higher rate of gas evolution was developed when spraying onto epoxy than the other substrates.

The other significant difference between splat morphology on the different polymers is the formation of the fingers protruding from the splats deposited on the PEEK based substrates as shown in Figure 5.26. These protruding fingers could be formed by jetting of material from the central splat during spreading, as was shown to happen in [44] when spraying Ni onto polished metallic substrates. An alternative explanation is that (as modelled and imaged in [49]), the splat initially spreads out in a circle over the entire area encompassed by the ligaments but the slower cooling at the periphery allows time for the outer part of the splat to fragment - presumably to reduce surface energy - causing these ligaments. The second of these explanations seems unlikely given that there was shown to be an observable change in the PEEK surface where molten aluminium had been present, and this change was not evident around the ligaments. This surface modification is discussed again later in the section.

Splats deposited onto the polished steel substrate were shown not to contain these large bulbous regions, or for that matter have large holes or form rings. The splats did have evidence of smaller pores, akin to nano-pores. These have been noted in the literature before, e.g. [44] [47] and [27]; in these studies they were formed on the underside of nickel spats deposited on metallic substrates due to gas formation.

5.6.3 Gas formation mechanism

The nano-pores discussed in [44] (which are similar to those in the splats on the steel substrates) were found not to form when thermal spraying was conducted under low atmospheric pressure. This led the study to suggest that gas stemmed from adsorbents on the substrate surface [44] and that by having the substrate in a low pressure atmosphere the adsorbents were removed. However, in [47], similar pores were observed even after

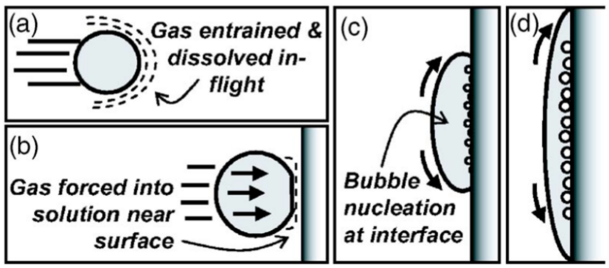


Figure 5.35: Schematic of particle in flight/splatting on substrate indicating how (a) gas gets entrained in the particle during flight, (b) gas dissolved into droplet due to high pressure at impact, (c) nucleation out of solution into bubbles after impact as the pressure is reduced and (d) solidification of the bubbles in place [152]

preheating the substrate surface prior to spraying. Pre-heating would have a similar effect to spraying in a low pressure atmosphere, i.e. it would also remove adsorbents from the surface. In [47], it was suggested that the gas may be absorbed into the particle at impact due to high pressures induced at the interface. After impact, the pressures are reduced and the gas becomes supersaturated within the particle/splat. Whilst the splat is still molten, bubbles nucleate at the splat/substrate interface. This process is diagrammatically illustrated in figure 5.35 [152] [47]. If this is the mechanism for pore creation, then the elongated bubbles shown in some of the splats sprayed onto steel are indicative of a fast cooling rate, as it shows the splat was still solidifying as it was spreading [47]. A fast cooling rate is also indicated by the rough top surfaces of the splats deposited onto steel as it shows that the outer surface of the splat has not had time to smooth (to reduce total surface energy) before solidification occurred.

The volumes of voids in splats deposited onto polymer substrates are significantly greater than those deposited onto steel ones. It has previously been shown in the literature that a slower cooling rate can lead to larger pores [47]. Given the respective thermal conductivities of the substrates (literature values of around 0.19 for epoxy and 43 $W.m^{-1}.K^{-1}$ for low carbon steel), the solidification of splats on polymer should be substantially slower than on steel and thus the pores should be larger. The slower cooling rate of the splats is also indicated by the smoother morphology and the ripple marks present on the splat surfaces, which possibly form when a thin initially solidified layer is distorted as the bulk of the material cools leaving marks on the surface. However, it is not believed that this difference in cooling rate would fully account for the large voids in the splats deposited onto the substrates. The reason for the larger pores at slower cooling rates mentioned in [47] is that at slower cooling rates, smaller pores coalesce to form larger ones, and thus this mechanism would not explain the large total volume of the voids found in the splats (> 3000 μm^3 for the splat shown in figure 5.13). Thus, the

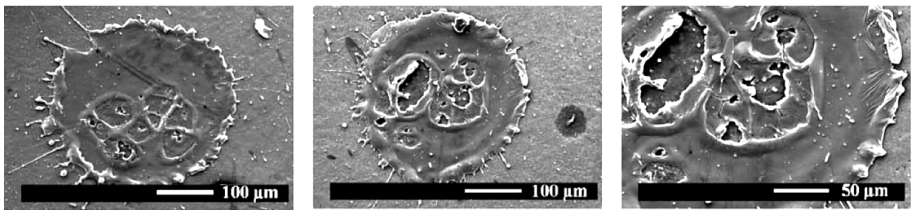


Figure 5.36: SEM images of plasma sprayed 316L splats onto preheated 1040 steel substrates at different magnifications showing possible deflated bubble features [42]

extra gas volume must come from another source.

The most similar morphologies to those found on polymers in this study are in [35] (figure 2.5a) when spraying Ni-Cr onto prepated polished metallic substrates and [42] when spraying 316L onto a preheated steel substrate (figure 5.36). In the latter case, the features may have been associated with an oxide induced substrate topography which trapped large amounts of gas during particle impact and would mean that a large amount of gas would be available to form bubbles.

Two possible sources of the extra gas in the splats are released adsorbed gases from the substrate surface and volatile gases given off during polymer thermal degradation. Given the low thermal conductivity of the polymer substrates, the local interface temperature will be raised to that almost of the impinging Al particle (>660°C). This is in line with the calculated interface temperature using the methodology outlined in [153]. At these temperatures adsorbates on the surface would be released and significant amounts of gas would be given off as the polymer starts to degrade. This is illustrated for the PEEK substrate by thermo-gravimetric analysis (TGA) carried out in [154] which shows that when heating in air there is significant mass loss (through gas evolution) at temperatures of 520 – 530°C. TGA has also been conducted in air for a range of different epoxy polymers. The results showed that a 5% mass loss occurred at temperatures ranging from 170 – 360°C, with the exact temperature depending on the epoxy composition [155].

5.6.4 Substrate features following splat removal

Removal of the splats from the steel substrate often resulted in fracture within the centre of the splat, this was evidenced by remnants of the aluminium splat on the substrate surface as well as an internal fracture face on the removed splats. This was typically in the central region of the splat and so indicated that a significant proportion of the adhesion of the splat on the steel substrate stems from the central portion. This has implications for the splats deposited onto the polymer based substrates, as often the central region of the splat is not in contact with the substrate meaning there can be no

adhesion at that location.

Upon removal of splats from the polymer based substrates, there was evidence for changes on the surface where the splat had been. This was true for both the epoxy (figure 5.18) and PEEK (figure 5.23 & figure 5.24) based materials although the changes were different in each case. On the epoxy substrates, the surface remained relatively similar to the original, the major difference being in some regions there were some small holes which may have been caused by outgassing.

The change in the PEEK based substrate was more distinct; areas where splats had previously been were slightly depressed and underlying fine topography on the structure was slightly distorted. Although not mentioned in the results, unsuccessful attempts were made to quantify the depth of this depression using FVM and tilting the sample within the SEM. The unsuccessful nature of the measurements suggests that the depressions are very shallow, and within the range of the underlying surface roughness.

The marks could be a result of mechanical damage during splat removal. However, the more likely explanation, especially given the effect was only shown on the PEEK (thermoplastic) substrates, is that they are as a result of the substrate very briefly and locally melting from the heat input of the splat.

In some of the areas where splats had been removed, the central portion was unaffected by the change. These unaffected regions perhaps coincide with the site of a bubble, hole or a centre or a ring. These areas being unaffected show that the bubbles started forming very soon after impact and there was not enough time for melting to occur, or that thermally released gas caused the central portion of the splat to never achieve full contact with the substrate.

5.6.5 Abraded CFRPs

Spats successfully deposited onto both the resin and the fibre phases on the abraded CFRPs. There is some indication that there is a slight preference for adhesion to the polymer surface. This is in contrast to [52] where Cr was effectively plasma sprayed onto a FRP and there was preferential adhesion to the fibres. The particle temperature of Cr during plasma spraying is $\approx$ 1900°C, and the high temperature Cr would severely damage any polymer phase it came into contact with, releasing volatile gases causing splats not to form. Any splats that did start to form may severely degrade the polymer from the heat flux as they cooled, resulting in the resin debonding from the underlying resin. In fact, in this case the thermal spray effectively removed the matrix phase before depositing onto the fibres. The same preference was demonstrated for arc sprayed Al

splats in preliminary work for this thesis. This preliminary work is outside the scope of this study, but a brief summary is included as appendix C. The work involved arc spraying aluminium onto a lightly grit-blasted substrate. The results showed that arc spray deposits were exclusively built up on the fibre exposed areas of the substrate. These results suggest that for high temperature splats having a surface with exposed fibres is required, whereas for lower temperature processes more polymer phase is allowable.

Dry reinforcement cloth

Due to the results being ambiguous as to whether the splats were depositing directly onto the fibre phase, wipe tests were conducted directly onto dry carbon fibre cloth. Glass fibre cloth was also tested as some literature [97] suggested that glass is a better reinforcement phase for thermal spray adhesion. It was shown that splats were successfully deposited onto both of the dry fibres. In both cases, the splats partially wrapped around the fibres, a bonding mechanism that would not be available once the cloth is partially encased with resin. However, in the case of the carbon fibres, there was some evidence of aluminium wetting and spreading on the fibres, indicating that aluminium should be able to bond to the fibres. Wetting on glass fibres appeared to be poorer than on carbon fibres and there were less deposited splats in total. This is interesting as some literature suggests that glass fibre composites are preferable for thermal spray deposition. It could be concluded that the proper surface preparation and ideal substrate is probably dependent on the properties of the particle impacting the substrate.

5.7 Conclusions

- Wire flame sprayed Al splats on polymer based substrates have a propensity to form gas bubbles in the centre of the splat. These bubbles appear larger and more pronounced than those typically reported in the literature for metal substrates. These are possibly the result of gas evolution from the substrate stemming from thermal degradation of the polymer and/or evolution of adsorbents.

- Bubbles within the splat often appear to explode causing ring shaped splat morphologies to form. This is more prevalent on the epoxy based substrates than PEEK based substrates.

- The surface of the thermplastic PEEK subsrate after splat removal showed evidence of local melting and the splat sinking into the substrate. The depth of this sinking is limited and could not be reliably measured (i.e. <1 µm).

- Adhesion of splats on polymer substrates comes from the periphery of the splat with little effective adhesion over the central bubble reducing the effective bonding area. This contrasts with splats on a steel substrate where most of the adhesion would come from the centre of the splat.
- WFS Al splats can deposit on both the fibre and resin phases of roughened composites. This is in contrast to hotter splats which have been shown (in literature and appendix C) to require exposed fibres to adhere onto.

Chapter 6

Effect of Surface Preparation on Metallic and Non-Metallic Substrates

6.1 Introduction

Several adhesion mechanisms are said to contribute to thermal spray adhesion (i.e. metallurgical bonding, physical bonding and mechanical anchorage) [10, p. 128] [156]. However, it is believed that the major bonding mechanism (without highly elevated temperatures) is that of mechanical anchorage [156], i.e. the spray particles are sprayed onto a keyed surface, and the splats solidify around topographical asperities holding them in place. Thus a sufficiently keyed/roughened surface is required to form a well adhered thermal spray coating. Typically, this keying is achieved by grit-blasting the substrate prior to thermal spraying [156, p. 79].

Grit-blasting typically leaves a random roughened surface on traditional monolithic substrates. This can be statistically characterised as discussed in section 3.9.1. Even on traditional monolithic substrates, relating the results of this statistical analysis to final coating properties (e.g. coating adhesion) has been challenging; work into this is briefly mentioned in section 6.2.2. In contrast to monolithic materials, the surface of grit-blasted FRPs are complicated by their multi-phase nature (fibre reinforcement and resin). Little published work seeks to comprehensively characterise the surfaces of FRPs prior to thermal spray, and this chapter seeks to address this. FRP composites are prepared for spraying with different grit-blasts and characterised such that information

Table 6.1: Different roughness parameters (from BS EN ISO 4287:1998 [127])

Roughness parameter	Calculation	Description
Ra	$\frac{1}{n}\sum_{i=1}^{n}\lvert z_i\rvert$	The average absolute height of perturbations on the surface from the average profile height. This measure is also known as the Arithmetic Average (AA)
Rz	$\lvert z_{min}\rvert + \lvert z_{max}\rvert$	This is the height difference between the lowest valley and the highest peak in the sample length.
Rq	$\sqrt{\frac{1}{n}\sum_{i=1}^{n} z_i^2}$	This is the Root Mean Squared (RMS) value of the surface height over the sampling length
Rsk	$\frac{1}{R_q^3}(\frac{1}{n}\sum_{i=0}^{n} z_i^3)$	This is the skewness of the distribution of the points measured along a sampling length. i.e. whether it is positively or negatively skewed. This highlights the effect of isolated features

can be drawn as to which surface features are beneficial when subsequently applying thermal spray coatings.

6.2 Literature Review

6.2.1 Characterising monolithic materials - Roughness parametrisation

By their very nature, roughened surfaces (e.g. grit blasted surfaces) are irregular and not easily characterised. Even up until the 1980s, subjective visual inspection was the most common method of surface evaluation [157]. With the advances in profilometry, and more widespread adoption, quantitative measures of characterising the substrate are used [158] e.g. Ra & Rz. These roughness metrics are defined and discussed in the experimental methods chapter (Chapter 3), however, a non-exhaustive table of common R values is reproduced in table 6.1.

6.2.2 Relationship between roughness and coating adhesion

Although the surface of the substrate is understood to be of great importance to the overall adhesion of the thermal spray coating, the relationship between the surface characteristics and coating adhesion is not fully understood; even on more traditional metallic substrates. Several studies, both empirical and theoretical, have been carried out looking into this relationship. Studies looking at metallic substrates tend to agree that higher roughness values (higher Ra or Rz) tend to lead to a higher adhesion e.g. [159] [158] [160] [161]. However, the literature suggests that there are no surface parameters that act as an ef-

fective predictor for coating adhesion. Effectively investigating these relationships is difficult, not least because there is not an effective parsimonious way of parametrising all the details of these surfaces. When spraying onto polymer and composite substrates, the surface topography becomes even more important, as it has been observed that without roughening, no (or very little) coating build-up is possible [51].

6.2.3 Surface preparation of polymers and FRPs

Despite concerns about grit-blasting the surface of FRPs expressed in [105], it appears to be the de-facto standard surface preparation method used prior to initial thermal spray coating and has been used by many researchers. [97] [162] [3] [91] [107] [100] [101] [92] [50] [114]. Some have used abrasive papers in lieu of grit-blasting [3] [98] [99]. However, the majority of researchers use an abrasive process to roughen the surface prior to initial thermal spray. Despite this, few studies report characterisation of the surface prior to spraying. Those that do typically simply report a Ra value (ranging from 1.8 µm [98] to 9.3 µm [50]) and little else. It is rare for studies to comment on the proportion or distribution of the resin / reinforcement phases on the surface of the substrate or the morphology of the prepared surface. The former is presumably an important factor as it completely defines what sort of material the thermal spray particles are actually adhering to. Huang et al. [98] made the comment that their abrasive papers removed most of the resin leaving exposed fibres, but this cursory statement is a rarity in the literature.

Although there appears to be little work in the thermal spray literature characterising the surface morphology prior to coating, there is work investigating solid particle erosion of polymers and fibre-reinforced polymers in the wear literature which is briefly reviewed below.

6.2.4 Solid particle erosion

A functional definition of wear is the removal of material from a surface through its interaction with another surface or material. There are several different types of wear defined in the literature including adhesive and abrasive. Sometimes subsumed within the abrasive category is solid particle erosion [163, p. 2]. This type of wear occurs when solid particles entrained within a fluid impinge upon a surface causing material removal; thus, grit-blasting can be seen as a practical application of this form of wear. Much of the literature in this topic is concerned with understanding the how erodent and material properties effect the mass of material removal.

Erosion rate (ER) is often used when comparing the resistance of different materials

to solid particle erosion. It is defined as the mass or volume loss of material divided by the mass of erodent. The erosion rate of a target material (i.e. the material being eroded) is partially a function of the angle of particle impingement of the erodent particles. The dependence of erosion rate on this angle is dictated by whether the material is ductile or brittle. Ductile materials have a maximum erosion rate at low angles, while brittle materials have a maximum erosion rate at normal angles [164, p. 199] [165]. Ductile materials also have initial embedment of erodent into the material leading to an initial mass gain before erosion, termed the incubation period. These brittle and ductile distinctions do not necessarily correspond to typical groupings [166].

When particles impact a target material at right angles, energy from the particle is typically dissipated through an elastic/plastic deformation in the material, and associated heat loss. Ductile materials will survive significant plastic deformation before fracture and so are resilient to erosion at these angles. Brittle materials will not plastically deform; thus, cracks will form and coalesce resulting in material removal. This is why brittle materials have a maximum erosion rate at 90° [166]. When particles impact a target material at an acute angle, (in addition to elastic/plastic deformation), the particles scratch the surface. In soft ductile materials, this leads to the erodent digging into the surface causing cutting and ploughing damage. Hard brittle materials resist this deformation and thus only the normal component of the particle momentum is seen to contribute to erosion. This is why they have a minimum erosion rate at these angles [166].

Due to the reasons outlined above, solid particle erosion from brittle materials (e.g. ceramics and brittle polymers) is characterised by cracks forming and joining together. For ductile materials (e.g. soft metals and ductile polymers), it is characterised by significant plastic flow on the surface [164, p. 200].

Solid particle erosion mechanisms for polymeric substrates are similar to those for other monolithic materials and are outlined in several places in the literature e.g. [167] [166] and [168, p. 210 - 220]. The predominant material removal mechanism depends on a multitude of factors including whether the polymer substrate behaves in a ductile or brittle manner. Those polymers exhibiting a brittle mode lose material through cracks propagating and joining together (figure 6.1b) and brittle fractures figure 6.1c [right] causing surface removal. Such mechanisms lead to surface cracks, scratches and delamination on the surface of the substrate. Images of such surfaces can be found in [169] [170]. Polymers wearing in a ductile mode lose material through ploughing (figure 6.1a) and deform plastically and chip (figure 6.1c [left]) to remove surface material. These mechanisms lead to obvious plastic deformation and scars from ploughing and cutting

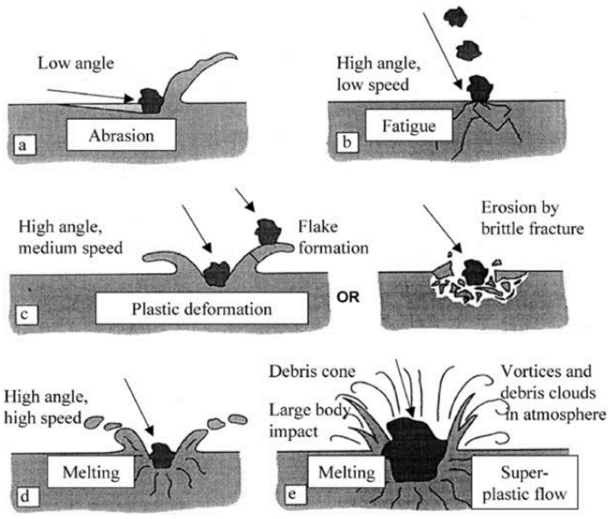


Figure 6.1: Solid particle erosion mechanisms in polymers (taken from [166] originally in [172])

on the eroded substrate surface, as shown in for un-reinforced PEEK in [171].

There is some indication that amorphous polymers behave in a more brittle manner than crystalline ones. Rajesh et al. [173] conducted erosion tests on a variety of different polyimide substrates, where it was found that only the amorphous polymer tested did not exhibit an incubation period (incubation periods are typically associated with ductile materials). The angular dependence of erosion rate still indicated that the amorphous polyimide was ductile (i.e. ER(90°) < ER(30°)); however, the difference between the erosion rate at these angles was the least, indicating that out of the polyimides tested, this was the most brittle. The review article [166] cites two additional studies stating that amorphous polymers behave in a more brittle manner than semi-crystalline ones. There have been attempts to correlate physical properties of polymers to their erosion behaviour. However, as commented in [173], polymer behaviour is a function of the strain rate and in erosion, strain rates can be in the order of 10^4 - 10^5 s^{-1}, thus correlating with quasi-static properties may be problematic.

It is recognised in the literature that FRPs behave differently to pure resin systems. Work in this area typically seeks to determine how material or testing parameters affect erosion rate; however, in addition (and more relevant to this investigation), mechanisms and morphologies are discussed. Several studies e.g. [174] [171] [175] show that FRPs typically have a lower erosion resistance than pure polymers, and typically as fibre content increases, so does the erosion rate [166] [176] [175]. In one of the earliest papers found on solid particle erosion of FRP (Zahavi and Schmitt) [177] described the general erosion process on FRPs. In this paper, the behaviour of several different FRPs subjected to sand particles ≈200 – 300 µm with a velocity of ≈40 $m.s^{-1}$ was investigated. Given that

measured grit velocities in grit-blasting literature range from ≈ 50 - 100's $m.s^{-1}$ [168, p. 94-108], these conditions can be seen as akin to a very light grit-blast with 50-80 mesh grit. The authors observed that fibre and resin phases eroded differently. Initially, resin material was removed, which exposed the reinforcement fibres which cracked and broke into fragments. These fragments detached from the supporting resin material. This meant that after erosion, the weave structure was still evident and that there were both resin and fibres exposed on the surface. Also, depending on the level of erosion, there would be differential amounts of the different phases present on the surface. This model of FRP erosion also explains the observations made in other studies including [176] and [178] that showed increased bonding strength between the fibre and resin phases increased the erosion resistance of the FRPs. As the fibres are better bonded to the resin, they are more resilient to fracture and removal.

The addition of the fibres within the polymer changes the response of the ER with erodent impingement angle. Most of the modern literature suggests that the when the polymer is impregnated with fibres, the angle which yields the maximum erosion rate becomes 45 - 60° [179]. This has been shown for a variety of polymers; for example CF-PEEK (thermoplastic) has been shown to have a maximum ER at 45° [178] and 60° [175], and a CF-epoxy (thermosetting) has been shown to have maximum ER at 60° [180]. The behaviour is likely because the matrix is relatively ductile and the fibres brittle, so an intermediate angle of impingement will be the most effective at removing a combined brittle (fibres) and ductile (resin) material.

One review article [181] somewhat contradicts the above statements, citing multiple studies including Zahavi and Schmitt [177] (discussed above); it states that although thermoplastic based FRPs have a maximum ER at 40 - 50°(semi-ductile behaviour), thermosetting polymer based FRPs have maximum erosion at high angles (brittle behaviour). The implication is that the thermosetting polymer resins are themselves brittle and thus also have a maximum erosion rate at high angles. This means that there is no need an an off-normal component to the erodent velocity to remove ductile material. The different conclusion is likely due to differences in the specifics of the thermosetting polymers. However, it could be noted that the studies cited by [181] supporting the claim are typically older (published between 1969 and 1989) than the studies they somewhat contradict; perhaps the more modern thermosetting resins trialled are tougher.

6.2.5 Literature review summary

- Roughened surfaces are typically defined using statistical parameters, typically Ra.

- Thermal spray coatings typically adhere better to roughened surfaces although there is not an effective predictive parameter for adhesion.
- The two-phase morphology of FRPs likely complicates the roughening and characterisation of the materials.
- There is very little literature characterising FRP materials prior to thermal spray. However there is discussion of erosive wear of FRPs (a very similar process). This literature suggests that grit-blasting the FRPs will lead to a complex two phase rough surface.

6.3 Motivation

Thermal spray particles cannot be assumed to behave the same on the different phases (fibre and resin) of the FRPs, as partially demonstrated in chapter 5. This is likely to complicate understanding of the process, and thus understanding the surface in as greater detail as possible is essential to understanding the substrate/spray interaction. This section of work aims to do that, by characterising the surfaces of fibre reinforced polymer composites to understand how their surface is modified by preparations used in thermal spraying (specifically grit-blasting).

6.4 Objective

The objective of this chapter is to characterise the effect of grit-blasting on the surface of the polymer and FRP substrates.

6.5 Approach

The approach taken in these investigations is to first investigate and characterise the reinforced and unreinforced polymers in their as-received state. The substrates are then treated by grit-blasting them with different grit-blasting parameters. The polymers have been characterised in terms of their mass and volume loss, surface roughness, topography and morphology. In addition to the work carried out with Epoxy, PEEK and FRP systems, some additional work had been carried out on a carbon steel substrate as a comparison.

6.6 Experimental methods

6.6.1 Substrate materials

Unreinforced polymers

In these investigations, unreinforced epoxy (Easy composites EL2) and PEEK were used. These substrates are referred to as epoxy and PEEK respectively. See experimental methods chapter for further details on these materials. Prior to preparing the surface in any way, the samples were polished to 1/4 µm finish and cleaned with industrial methylated spirits (IMS).

Carbon reinforced polymers

In these investigations, carbon fibre (CF)-epoxy (Tencate E722) and CF-PEEK were used. These materials are referred to as CF-epoxy and CF-PEEK respectively. See experimental methods chapter for further details on these materials. Prior to preparing the surface in any way, the samples were cleaned with industrial methylated spirits (IMS).

Steel

Steel (D50) substrates were investigated see experimental methods chapter for further details on this material. Prior to preparing the surface in any way, the samples were polished to 1/4 µm finish and cleaned with industrial methylated spirits (IMS).

6.6.2 Surface preparation

Grit blasting

The grit-blasting was carried out as described in the experimental methods chapter; two levels namely light grit-blast (LGB) and heavy grit-blast (HGB) were used. Parameters defining these are outlined in the experimental methods chapter. Angular 80 mesh brown alumina (hardness 9 MM [182] $\approx$ 2000 HV) was used as the erodent; an image of this is shown in figure 6.2.

6.6.3 Surface characterisation / analysis

Surface profilometry

Surface topography was characterised using a non-contact focus variation profilometer, the Alicona infinite focus SL. This instrument is discussed in the experimental methods chapter and its results verified against a contact profilometer in appendix B. Prior to

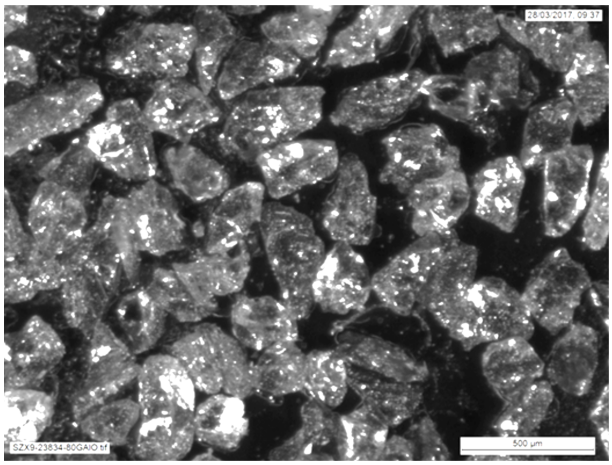


Figure 6.2: Optical microscopy of erodent showing its angular morphology and size of ≈100 - 300µm

Table 6.2: Selected 2D roughness parameters of untreated substrates

	Non-reinforced		Carbon fibre reinforced	
	Epoxy	PEEK	CF-Epoxy	CF-PEEK
Ra (µm)	0.066	0.145	0.230	0.844
Rsm (mm)	0.051	0.137	0.279	0.262
Rdq	0.027	0.035	0.026	0.081

measurement, polymer/composite samples were sputter coated to account for possible transparency issues identified in appendix B.

6.7 Results

6.7.1 Characterisation of substrates prior to treatment

Optical and height images of the untreated polymer substrates are shown in figure 6.3. As can be observed, other than fine scratches from the polishing there is little texture on the surface of the samples. In addition to the scratches, the surface of the epoxy polymer appears to exhibit a small amount of porosity at the surface of the sample. The general smoothness of the polymer materials is confirmed by secondary electron images (figure 6.4). Despite the fine surface features mentioned above, the surfaces are considered to be smooth on all measured roughness metrics (table 6.2). For example, the Ra values of the epoxy and PEEK substrates were 0.066 and 0.145 µm respectively.

The surface of the CF reinforced polymers are made up almost exclusively of the polymer matrix phases (figure 6.4). This layer of polymer follows the texture of the underlying reinforcement weave with the height of the surface changing as fibre bundles approach the surface of the substrate (figure 6.3). This is clearest on the CF-PEEK

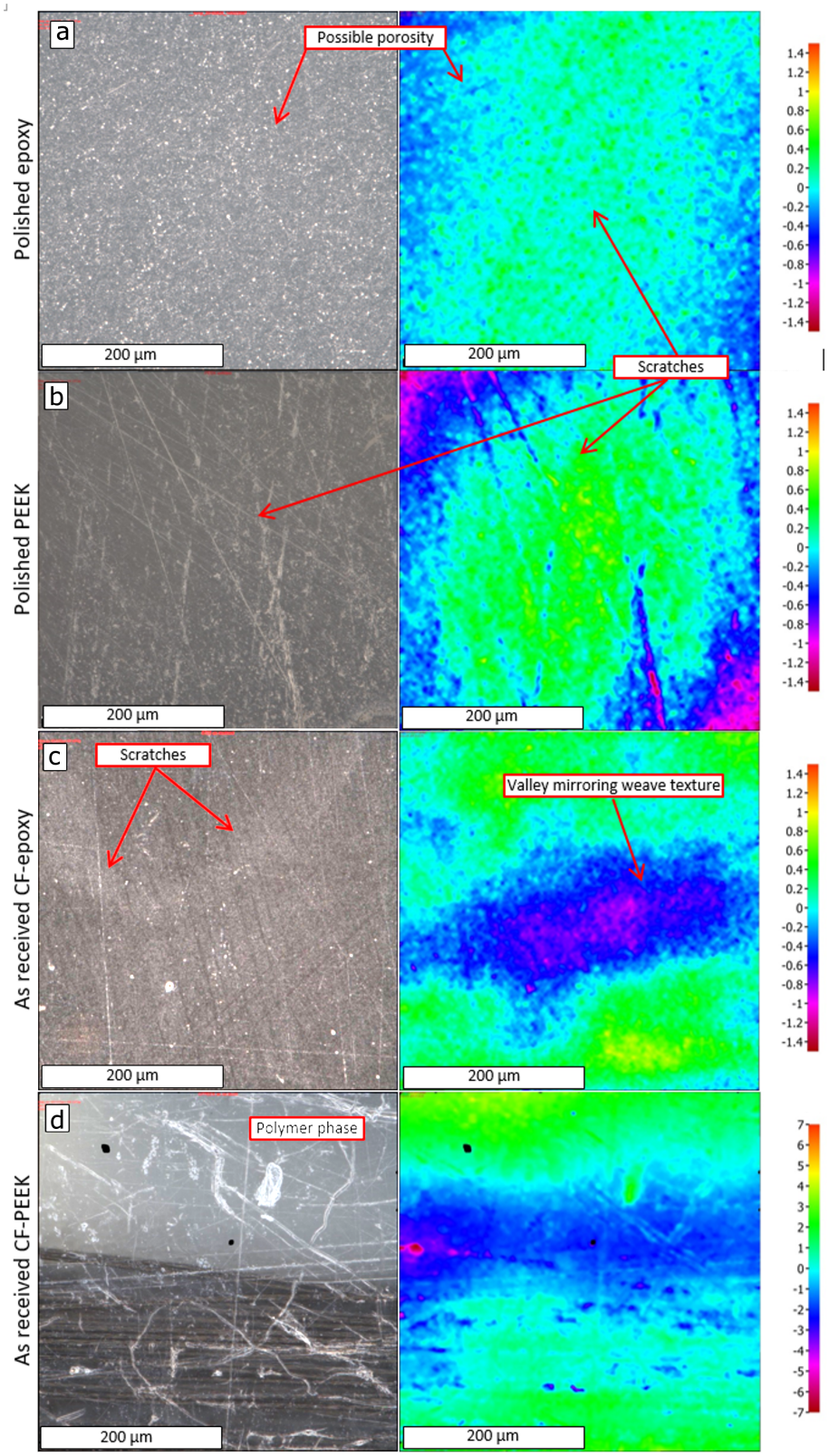


Figure 6.3: Optical (left) and height/FVM (right) images of (a) polished epoxy, (b) polished PEEK, (c) as received CF epoxy and (d) CF PEEK showing all are smooth with only minor scratches and porosity

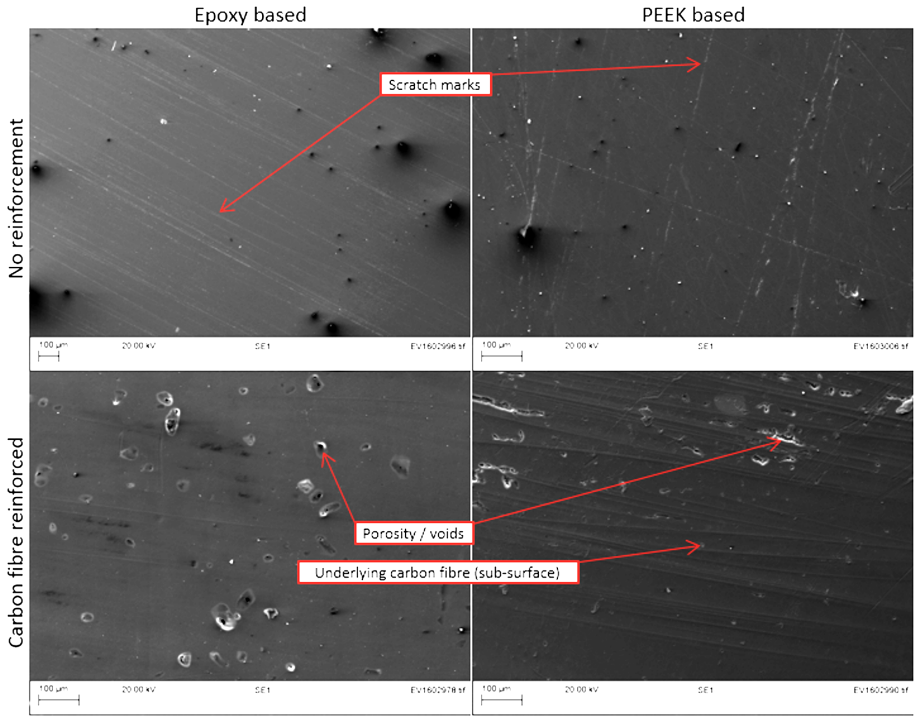


Figure 6.4: SEM SE images of the surfaces of polished/as received polymer and FRP substrates showing that they are all smooth with only minor scratches and porosity

which has higher amplitude features; thus, in figure 6.3 the z-axis in the figure set to a greater dynamic range than the other samples. The surface of the CF epoxy and CF-PEEK show some porosity on the surface which in some cases appears to be associated with fibres near the surface of the substrate (figure 6.4), which are the only areas where some reinforcement may be exposed. Despite these features, roughness metrics indicate that the as received CF substrates are generally smooth (table 6.2). The Ra of all of the reinforced and non-reinforced polymers in the order of 0.1 – 0.2 µm; only the CF-PEEK had a slightly higher Ra of 0.8 µm. The spacing parameter RSm was shown to be low, ranging from 0.05 to 0.28 mm. The surface gradient parameter, Rdq was also shown to be relatively low generally being 0.02 – 0.04[1], being slightly higher for the CF-PEEK (0.08).

Sectioning the CF-epoxy and CF-PEEK prior to treatment reveals the thickness of the resin coating above the CF reinforcement in the as received state. Images of these sections are shown in figure 6.5 and figure 6.6 respectively. The thickness of the resin phase above the reinforcement fibres on average was 23 and 18 µm for CF-epoxy and CF-PEEK respectively (summarised in table 6.3). The variability in the resin's local thickness is greater in the CF-PEEK than in the CF-epoxy with a range of 116 and 64 µm respectively. These are due to thick resin regions in the CF-PEEK substrate

[1]Rdq is dimensionless

Table 6.3: Summary of carbon fibre cross section analysis showing the average minimum and maximum resin thickness showing that CF-PEEK has a greater range of resin thickness

	Carbon fibre reinforced	
	CF-Epoxy	CF-PEEK
Resin thickness above fibres		
Average (min, max) [µm]	23 (9, 73)	28 (1, 117)
Resin fraction (%)	8	14

Table 6.4: Mass loss of grit-blasted samples (negative mass loss represents mass gain) Non reinforced epoxy samples had a different geometry

		Non-reinforced		Carbon fibre reinforced	
	Steel	Epoxy	PEEK	CF-Epoxy	CF-PEEK
LGB					
Average (g)	-0.0006	-0.0012	-0.0002	0.0275	0.0133
Normalised average ($g.m^{-2}$)	-0.4	-0.9	-0.1	17.2	8.3
Standard deviation ($g.m^{-2}$)	0.2	0.6	0.2	0.4	1.2
HGB					
Average (g)	0.0027	0.0020	0.0015	0.1741	0.1394
Normalised average ($g.m^{-2}$)	1.7	1.6	0.9	108.8	87.1
Standard deviation ($g.m^{-2}$)	0.4	0.14	0.2	3.1	3.8

associated with the 0° bundles crossing the 90° bundles. There are also more, and larger regions of resin within the CF-PEEK demonstrated by the almost double area resin content compared to the CF-epoxy (table 6.3). Higher magnification images of the fibre-bundles show that resin has infused between the bundles and there are very few voids present.

6.7.2 Effect of grit-blasting

Un-reinforced substrates

Steel The steel substrates have no significant mass change when grit blasted with the LGB settings. There is a slight mass increase (0.4 $g.m^2$) which is not deemed significant given the accuracy of the measurement. Grit-blasting with the HGB settings led and a small mass loss of 1.7 $g.m^2$ (table 6.4). Height images of the steel substrates (figure 6.7) show that the surface of both the LGB and HGB steel is homogeneously roughened in a random manner. The HGB substrate appears rougher than the LGB substrate. Histograms of the local surface height (figure 6.8) back up these observations. The surface forms a normal distribution around the mean height, and the HGB surface forms a wider bell curve (indicating the rougher surface). The Ra values of the grit-blasted steel are 2.7 and 4.3 µm for LGB and HGB respectively (table 6.5) and the kurtosis of the LGB settings is greater, indicating the sharper peak in the distribution.

SEM images of the steel substrates show that the surface has been abraded by both the

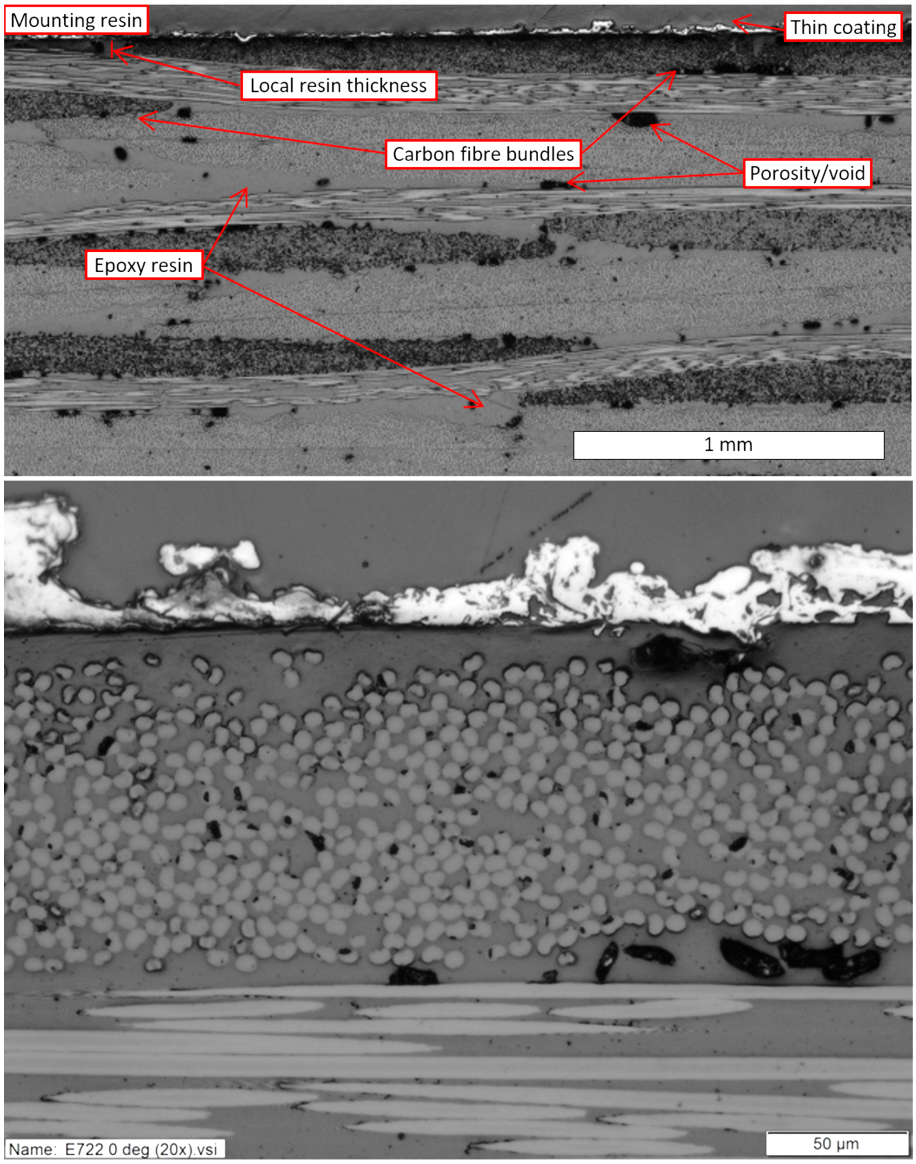


Figure 6.5: Optical microscopy images of cross section of as received CF epoxy (There is a thin layer of aluminium deposited onto the CF-Epoxy substrate in order to highlight the boundary between the substrate and the metallographic mount). Images show local resin thickness and resin infused in fibre bundles.

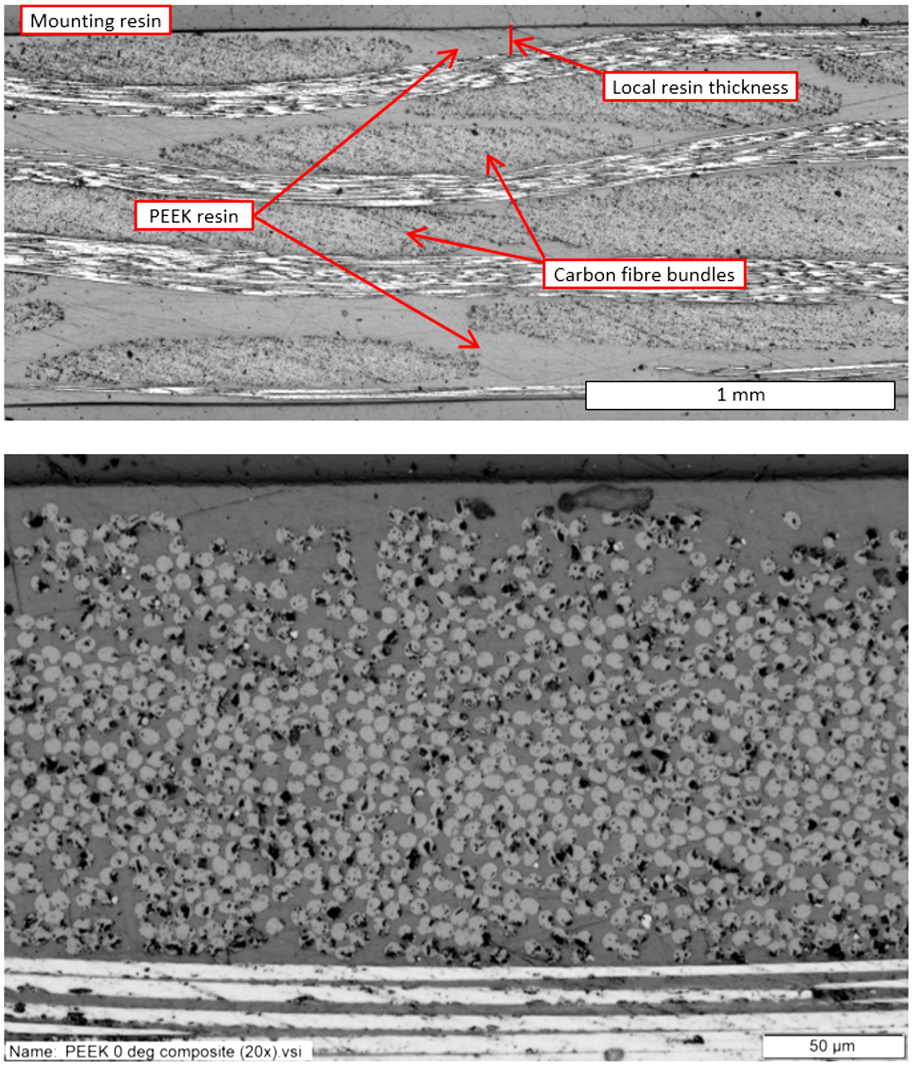


Figure 6.6: Optical microscopy images of cross section of as received CF PEEK (top) low magnification (bottom) high magnification. Images show local resin thickness and resin infused in fibre bundles.

Table 6.5: Selected 2D and 3D roughness parameter of unreinforced substrates

		Steel		Epoxy		PEEK	
		LGB	HGB	LGB	HGB	LGB	HGB
2D parameters							
Ra	(µm)	2.7	4.3	1.6	2.7	2.8	4.3
Rsm	(µm)	149.1	208.7	621.1	604.4	209.1	266.3
Rsk		-0.5	-0.3	-2.4	-2.5	0.0	0.1
Rku		4.2	3.8	14.1	12.8	3.5	3.1
Rdq		0.4	0.5	0.2	0.3	0.3	0.3
Lc	(mm)	2.5	2.5	0.8	2.5	2.5	2.5
3D parameters							
Sa	(µm)	2.7	4.4	1.5	3.1	3.0	4.6
Ssk		0.6	-0.3	-3.0	-3.0	0.3	0.1
Sku		18.1	4.4	18.2	15.7	11.4	3.3
Sdq		0.5	0.7	0.3	0.4	0.4	0.5
Sdr	%	13.1	21.8	3.3	8.5	6.9	8.9
FLTt	(µm)	118.6	125.3	52.1	89.4	163.9	76.1
Lc	(mm)	2.5	2.5	0.8	2.5	2.5	2.5

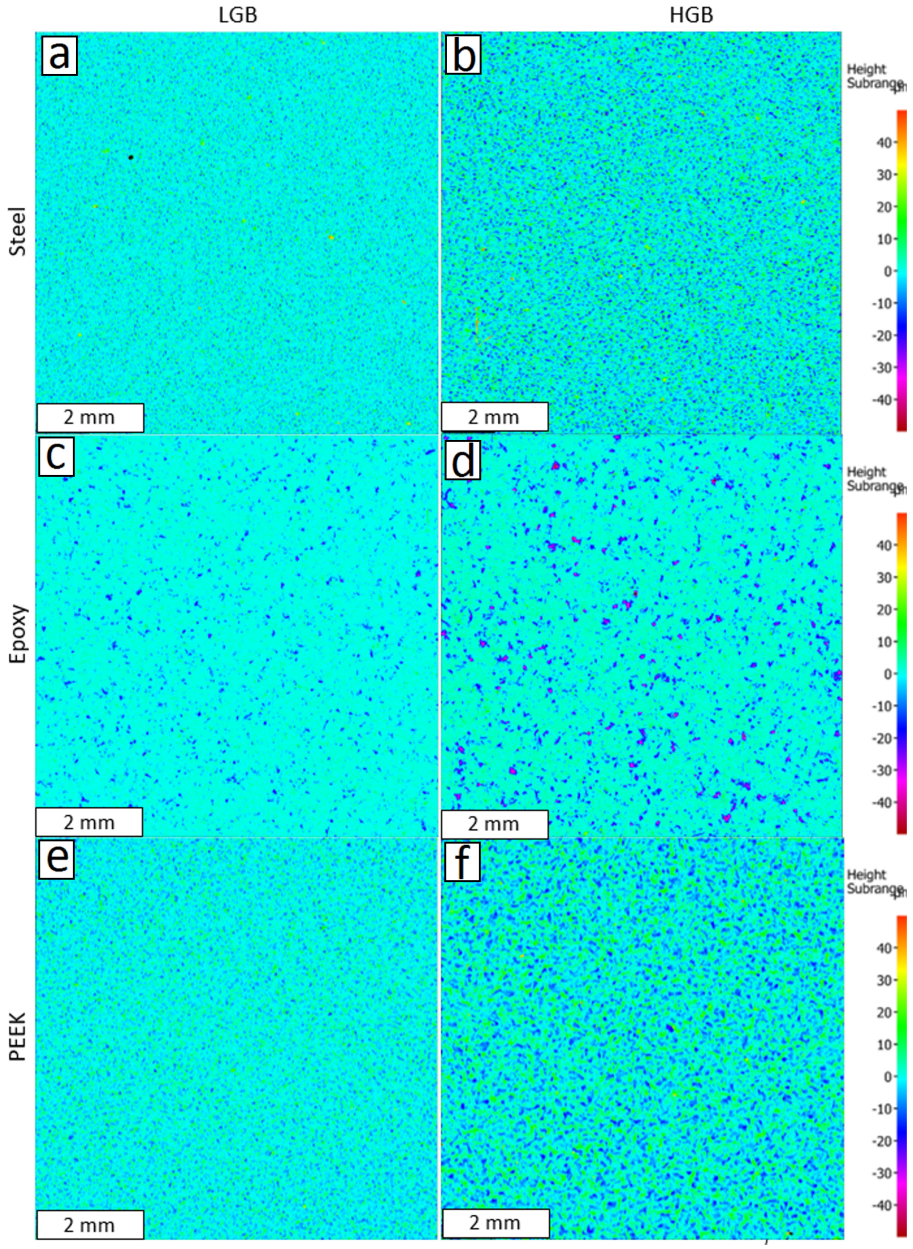


Figure 6.7: Height/FVM images of grit-blasted substrates steel, (a) LGB, (b) HGB, epoxy (c) LGB, (d) HGB, PEEK (e) LGB and (f) HGB. Image highlights how in contrast to steel and PEEK, the epoxy substrates remains generally smooth with small deep furrows

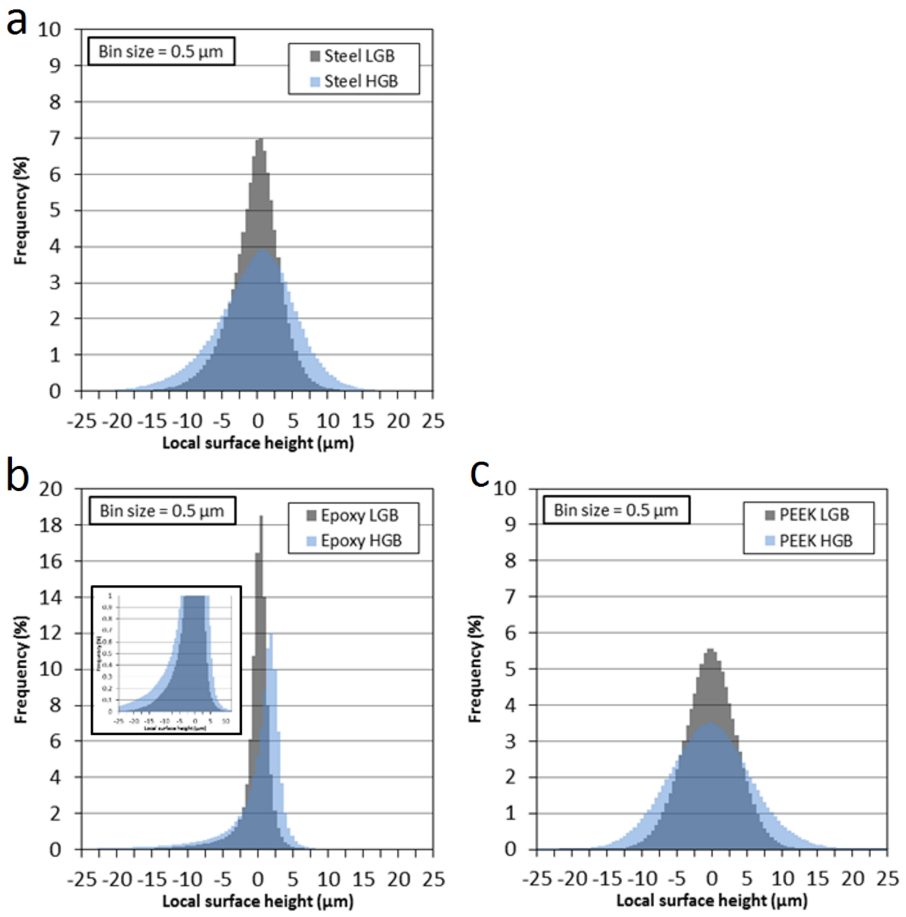


Figure 6.8: Histograms of local surface height of (a) steel (b) epoxy and (c) PEEK substrates. Figure highlights how local height is normally distributed in steel and PEEK and skewed in the epoxy substrate

cutting action of the angular grit and though significant plastic deformation (figure 6.9 and figure 6.10) and there is some embedded grit present on the surfaces.

Epoxy A small mass increase was observed in the LGB epoxy substrate (0.9 $g.m^2$) and a small mass reduction was associated with HGB settings (1.6 $g.m^2$). Height images of the epoxy substrates (figure 6.7) show that the surface of the LGB epoxy substrate is relatively flat interspersed with 10 - 15 µm furrows around 100 µm long. The HGB epoxy has a similar surface morphology; however, there are a greater number of these furrows and some are deeper, up to 20 - 30 µm. This is reflected in the higher Ra of the HGB surface compared to the LGB surface (2.7 and 1.6 µm respectively). Histograms of the local surface height (figure 6.8) agree with these observations. Most of the data-points fit a tight normal distribution around the mean; however, remaining data points (associated with the furrows) form a small tail skewing the distribution negatively (Rsk = 2.4 for LGB epoxy).

Higher magnification images of the epoxy substrate surfaces show that much of the surface is made up of flat 'islands' with the furrows/pits distributed over the surface (figure 6.11). At higher magnifications, a network of fine cracks are evident, which appear to separate relatively flat islands and run partially connect the deeper furrows. In addition to this, there is a large amount of debris visible. Back scattered electron images indicate that much of this debris is made up of small (1 – 5 µm) embedded grit in the surface. SEM images of the HGB Epoxy (figure 6.12a) show similar features, cracks forming that separating flat islands and some furrows. There is some indication that there is slightly more variability between the heights of these islands in the HGB treatment. As with the LGB settings, the debris appears to be made up of alumina grit figure 6.12b.

PEEK Negligible mass change was observed for the LGB PEEK (0.1 $g.m^{-2}$ mass gain). However for the more aggressive settings, a small mass loss was measured 0.9 $g.m^{-2}$ (table 6.4). Height images of the PEEK substrates (figure 6.7) show that the surface of the both the LGB and HGB PEEK substrates are homogeneously roughened in a random manner. Histograms of the local surface height confirm these observations, with the data points being normally distributed around the average surface height. The HGB surface has a wider distribution than the LGB surface indicating that the HGB surface is rougher than the LGB surface. This is confirmed by the fact that the roughness parameters (Ra) for the surfaces are 1.8 and 4.2 µm for LGB and HGB surfaces respectively.

Low magnification images of the unreinforced grit-blasted PEEK (figure 6.13) show

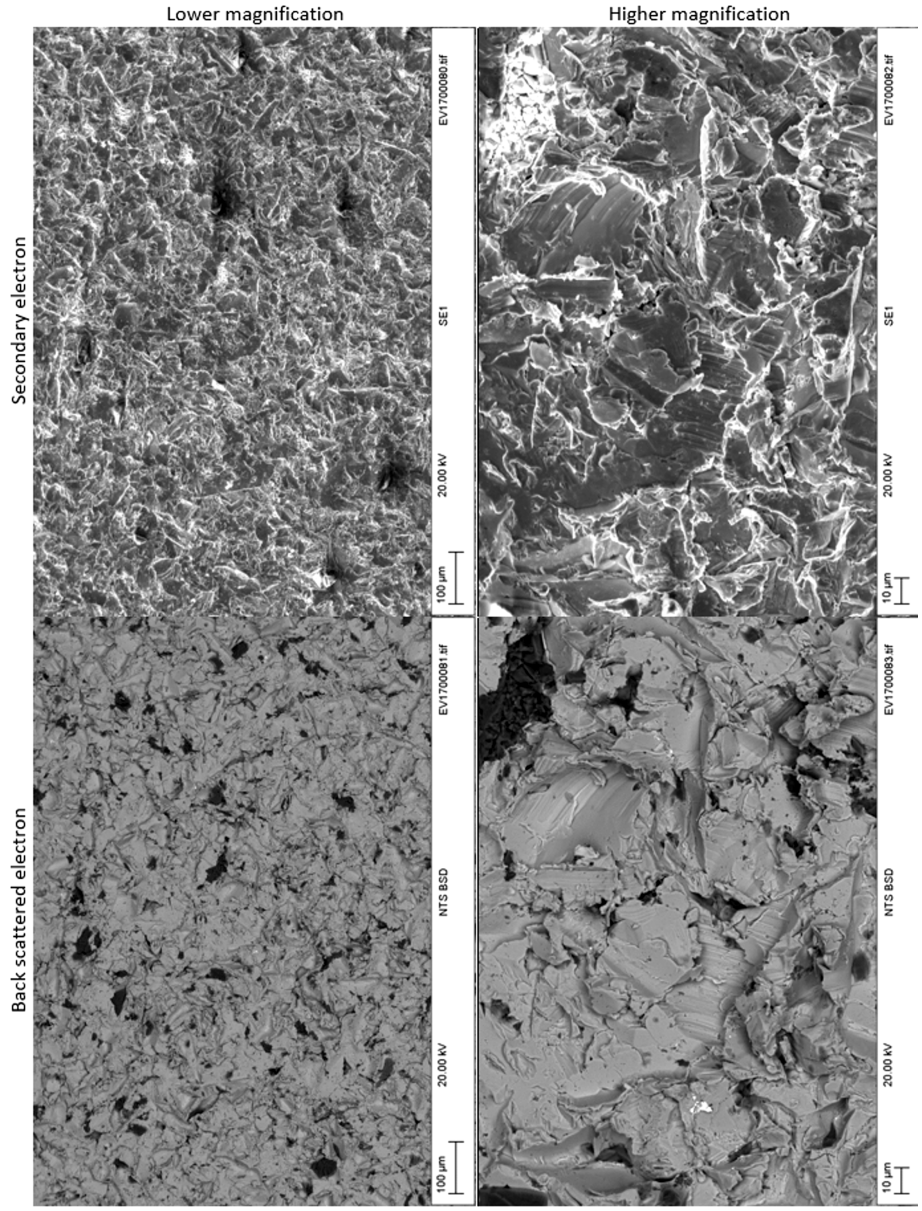


Figure 6.9: SEM images of LGB grit-blasted steel substrates. Images show possible plastic deformation and a small amount of alumina embedment (dark areas in BSE images)

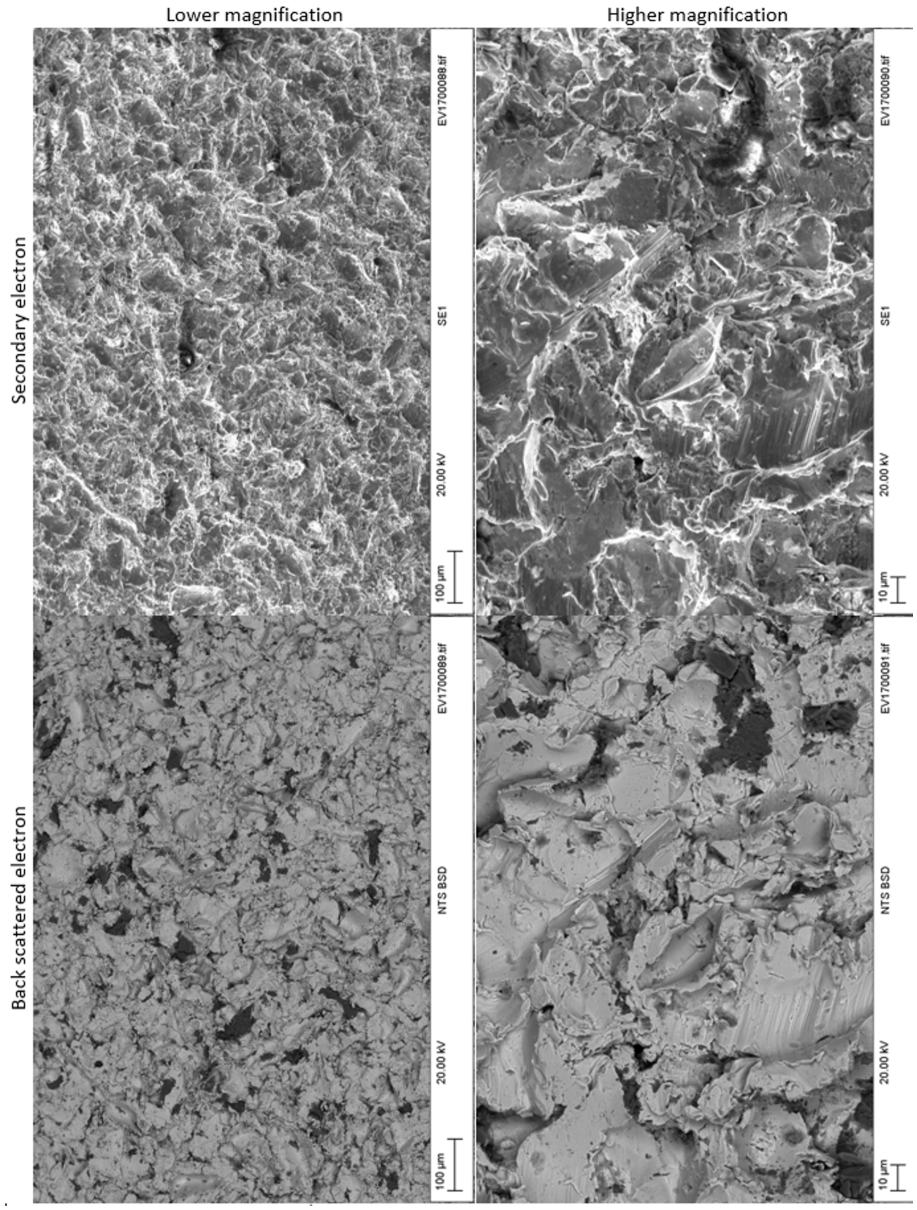


Figure 6.10: SEM images of HGB grit-blasted steel substrates. Images show similar featured to LGB steel, posible plastic deformation and a small amount of alumina embedment (dark areas in BSE images)

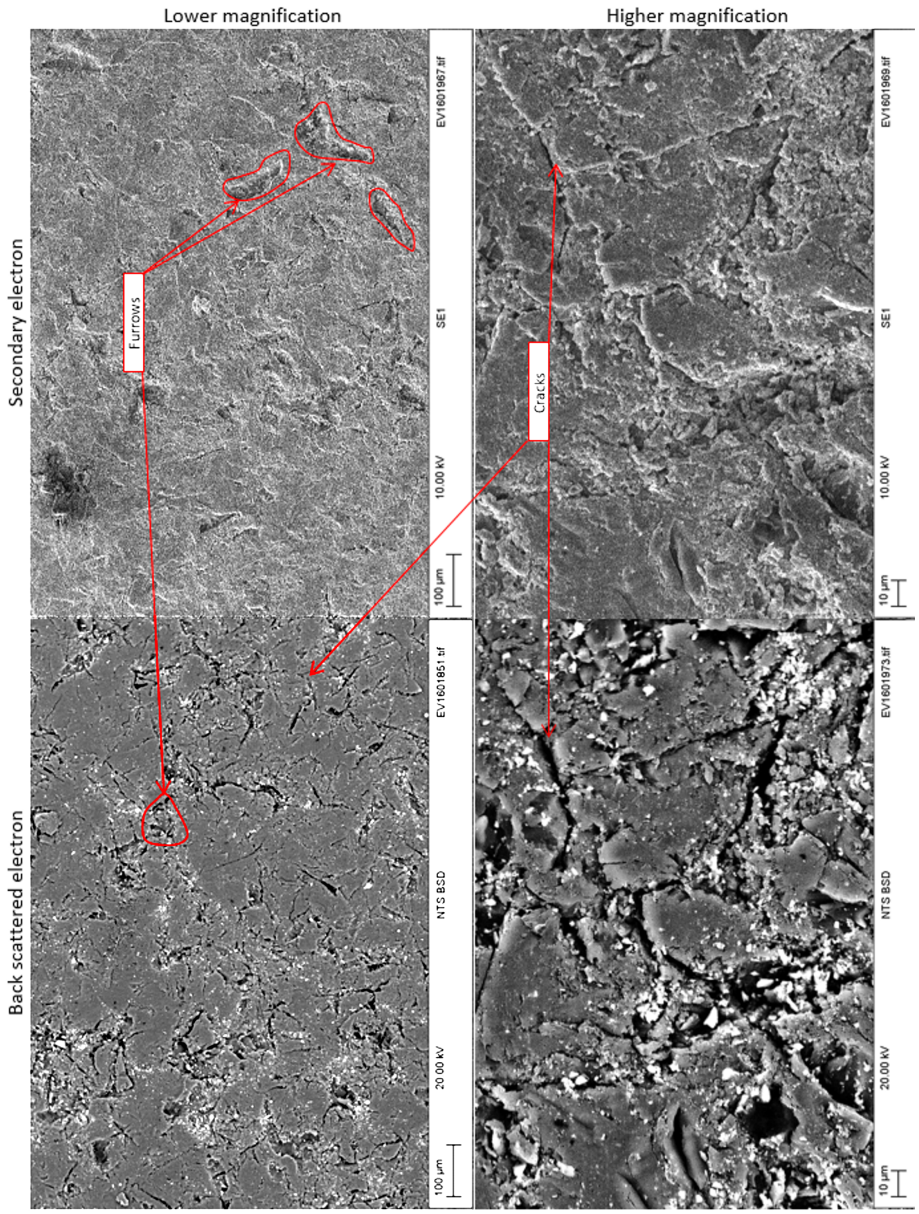


Figure 6.11: SEM images of LGB grit-blasted epoxy substrates. Images show a generally smooth surface with cracks, furrows and alumina contamination

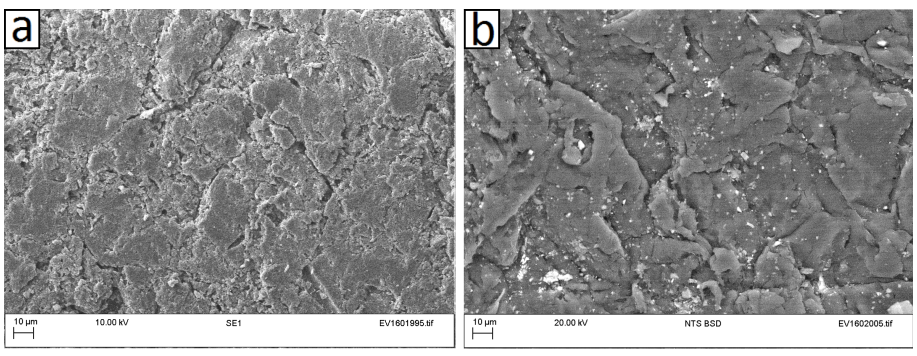


Figure 6.12: High magnification (a) SE and (b) BSE images of HGB epoxy substrates showing relatively smooth substrates and alumina imbedment

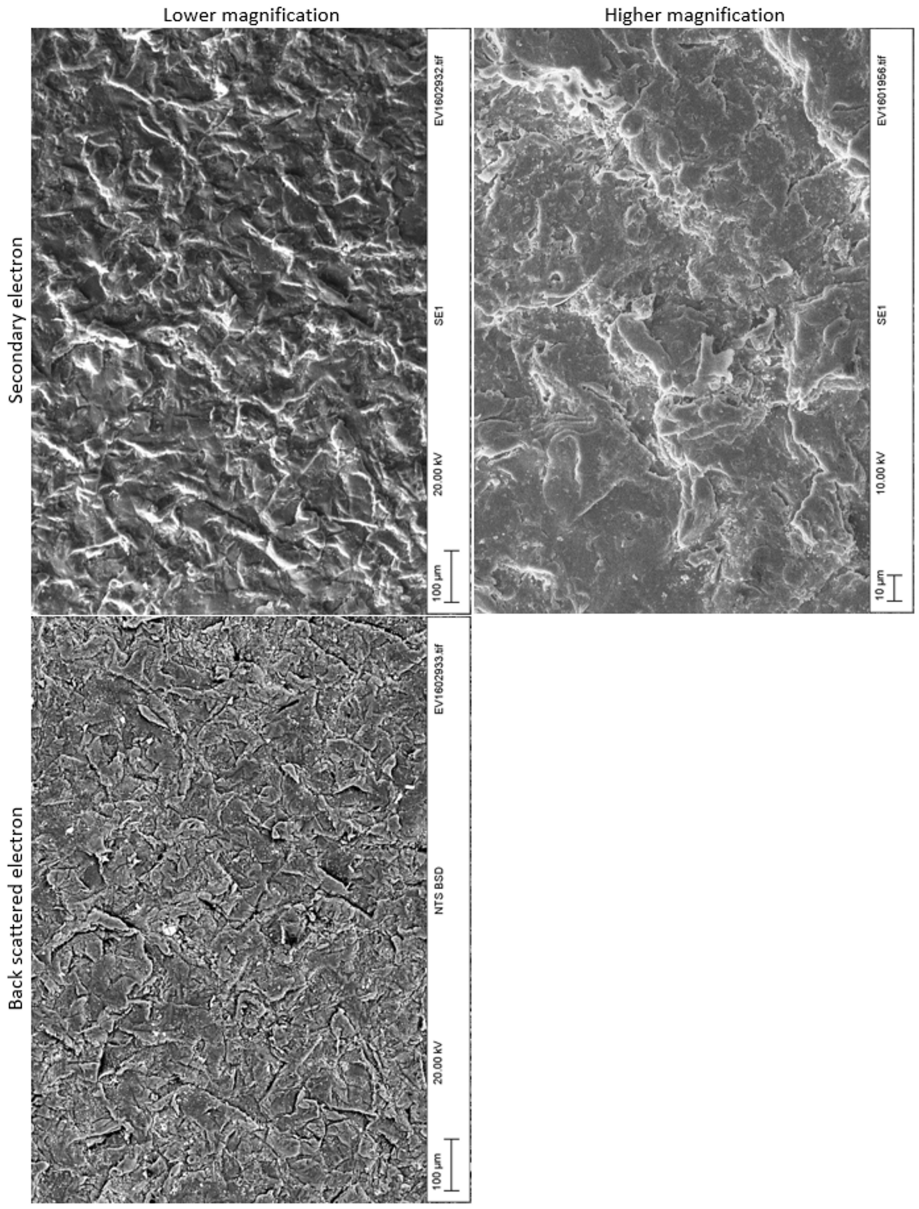


Figure 6.13: SEM images of LGB grit-blasted PEEK substrates showing ductile roughness deformation and limited alumina embedment

that the surface is covered in peaks and troughs which appear to be formed from plastic deformation. At higher magnifications, a few possible cracks are evident; however, extensive cracking is not apparent. The HGB PEEK surface shows similar features to the LGB PEEK surface; however the features are more pronounced (figure 6.14). In both the HGB and LBG PEEK surface, there is evidence of embedment of grit.

Fibre reinforced polymers

CF-Epoxy Grit-blasting the CF-epoxy resulted in a relatively large mass loss of 17 and 106 g.m^{-2} for the LGB and HGB settings respectively (table 6.4). The substrates' Ra after grit-blasting were 5.2 and 15.2 µm for the LGB and HGB settings respectively (table 6.6).

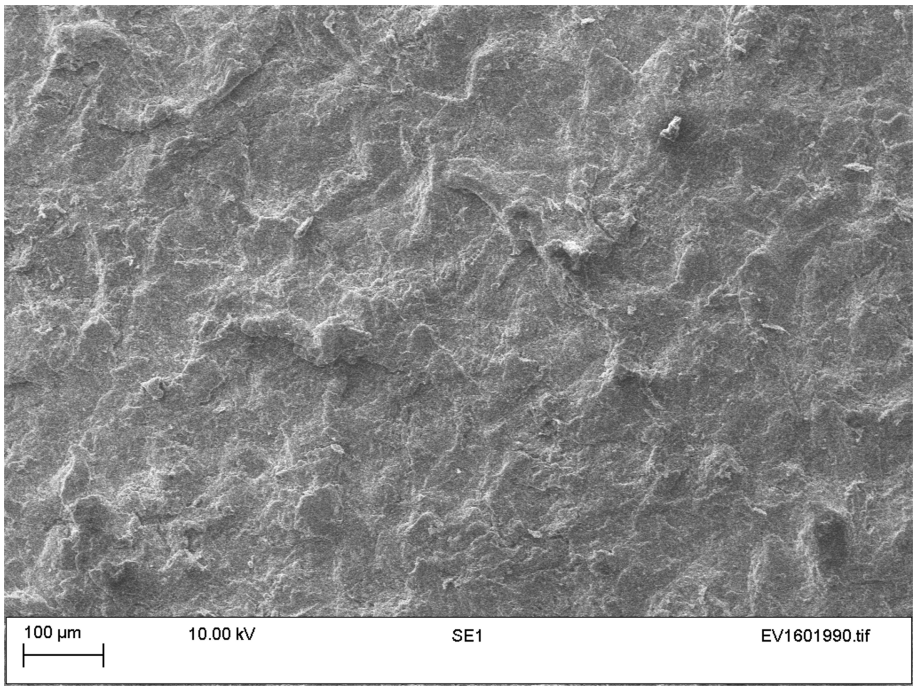


Figure 6.14: SEM image of HGB PEEK substrate showing roughend surface is the result of plastic deformation

The optical and height images of the grit-blasted CF-epoxy substrate (figure 6.15) clearly show the weave pattern of the underlying reinforcement. Areas where fibre bundles are near the surface of the substrate have been eroded to a greater extent than where the waft and weft bundles cross (i.e. where there was a thicker resin layer). This led to the original weave pattern being evident at the macro scale after grit-blasting. The surface area fraction associated with sunken valleys is subjectively greater for the HGB CF-epoxy than the LGB CF-epoxy. The height difference between the ridges and valleys is also greater for the HGB CF-epoxy; around 120 µm as opposed to 50 µm for the LGB CF-epoxy. It is clear from the optical and height images that the ridges are composed of resin, and that for the LGB settings, the ridges contain relatively un-eroded areas. These features are evident when looking at histograms of local surface height. The local height levels have a distinct bi-modal distribution (figure 6.16), with each modal peak being associated with either a resin 'ridge' or fibre 'valley' region. The two peaks are closer together and tighter in the LGB settings than the HGB settings.

The surface of the grit-blasted substrate is shown in figure 6.17. The resin 'ridge' regions on the LGB CF-epoxy exhibit a network of cracks and some furrows. These features are most evident in BSE mode; there appears to have been little volume loss in the areas between the cracks. The SEM images confirm that the area associated with these resin ridges is reduced in the HGB settings (figure 6.18). Away from these resin regions, exposed fibres have been subjected to extensive damage; fibres are fractured

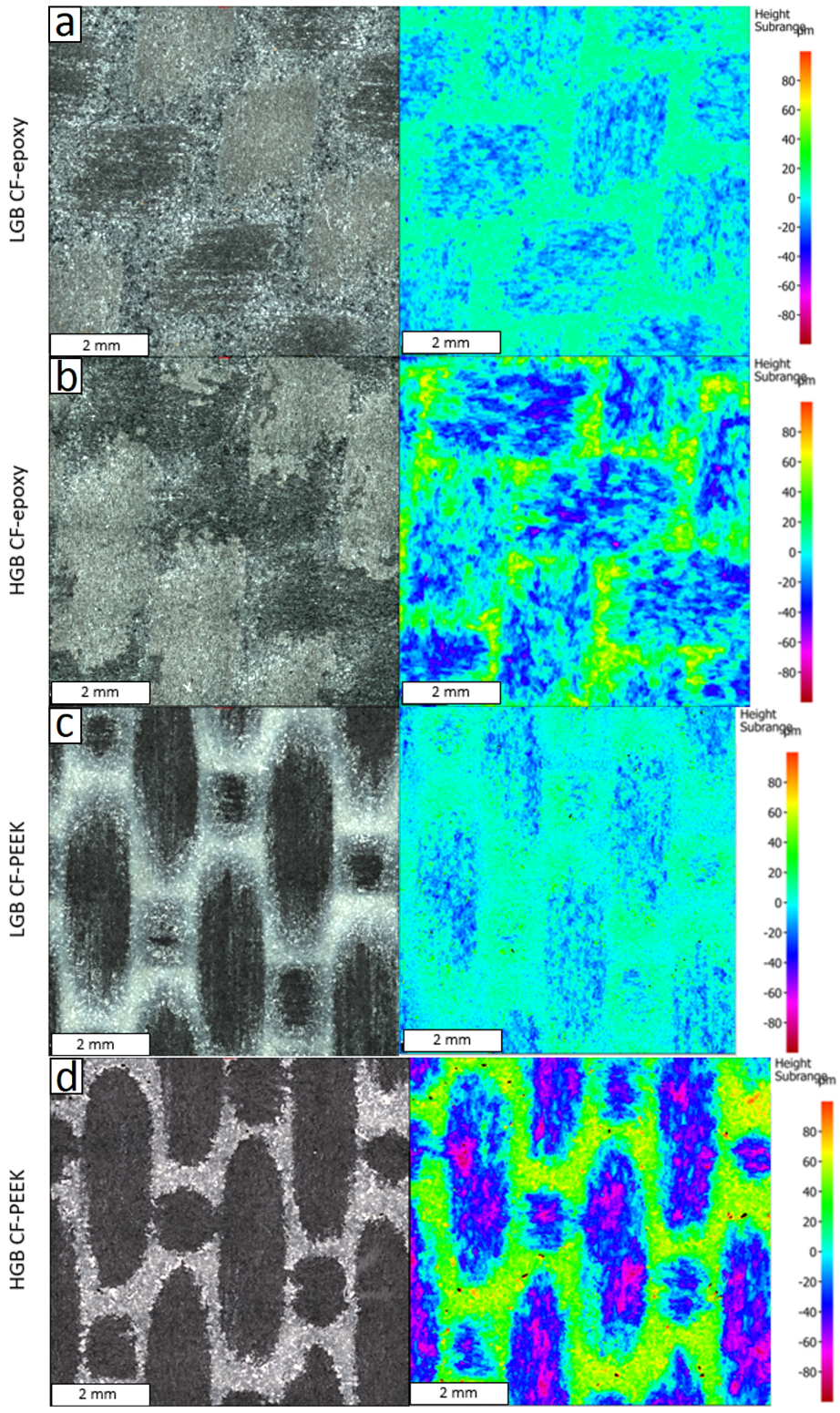


Figure 6.15: Optical (left) and height (right) images of (a) LGB CF-epoxy, (b) HGB CF-epoxy, (c) LGB CF-PEEK, and (d) HGB CF-PEEK

Table 6.6: Selected 2D and 3D roughness parameters of LGB and HGB carbon fibre reinforced polymers

		CF-epoxy		CF-PEEK	
		LGB	HGB	LGB	HGB
2D parameters					
Ra	(µm)	5.2	15.2	5.0	25.2
Rsm	(µm)	363.7	1074.8	351.4	1478.6
Rsk		-0.7	0.7	-0.3	0.3
Rku		3.2	3.3	4.5	2.2
Rdq		0.3	0.4	0.4	0.6
Lc	(mm)	2.5	8.0	2.5	8.0
3D parameters					
Sa	(µm)	5.9	17.7	5.7	32.3
Ssk		-0.8	0.6	0.0	0.0
Sku		3.3	3.0	4.5	1.9
Sdq		0.5	0.7	0.7	1.1
Sdr	(%)	9.2	17.9	20.4	42.7
FLTt	(µm)	62.9	139.0	112.3	256.8
Lc	(mm)	2.5	8.0	2.5	8.0

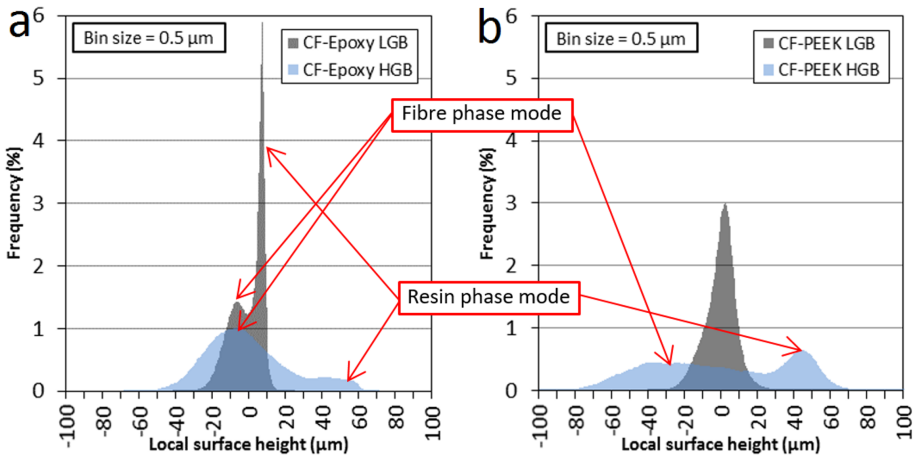


Figure 6.16: Histograms of local height of (a) CF-epoxy and (b) CF-PEEK substrate from unfiltered 3D profilometry data. plots show the two phase bi-modal nature of the subsrates

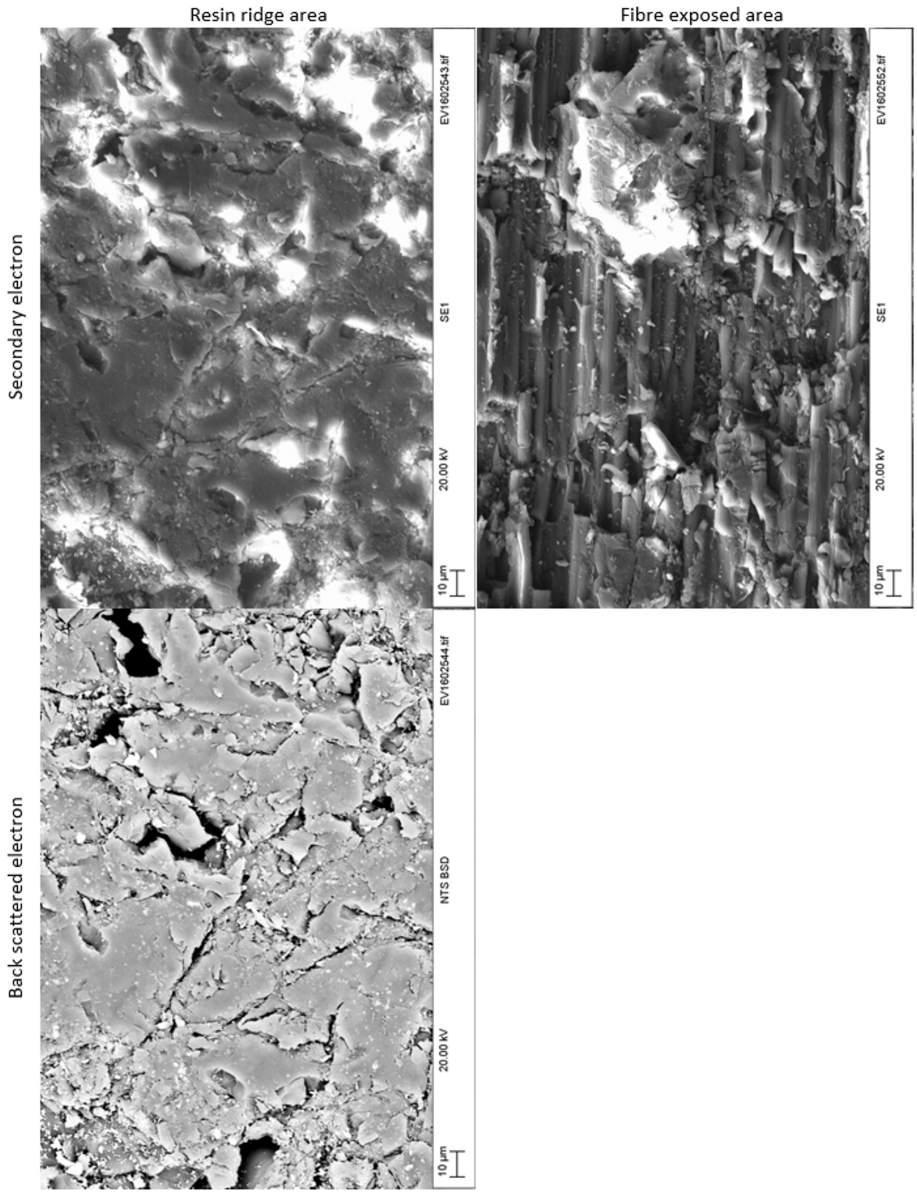


Figure 6.17: SE SEM images of LGB CF-Epoxy showing resin 'ridge' and fibre exposed area

and held in place by the remaining resin infused between individual fibres. The damage is greater in the HGB CF-epoxy substrate where there is less resin remaining and the surface is more uneven.

CF-PEEK Grit blasting the CF-PEEK resulted in a relatively large mass loss of 8.3 and 87.1 $g.m^{-2}$ for the LGB and HGB settings respectively (table 6.4). The Ra induced by the treatments was 5.0 and 25.2 µm for the LGB and HGB settings respectively (table 6.6). Like the CF-epoxy, the optical and height images of the grit-blasted CF PEEK (figure 6.15) show the underlying weave pattern of the reinforcement. Sunken valleys are associated with areas with a local thin surface layer of resin, where the fibre-

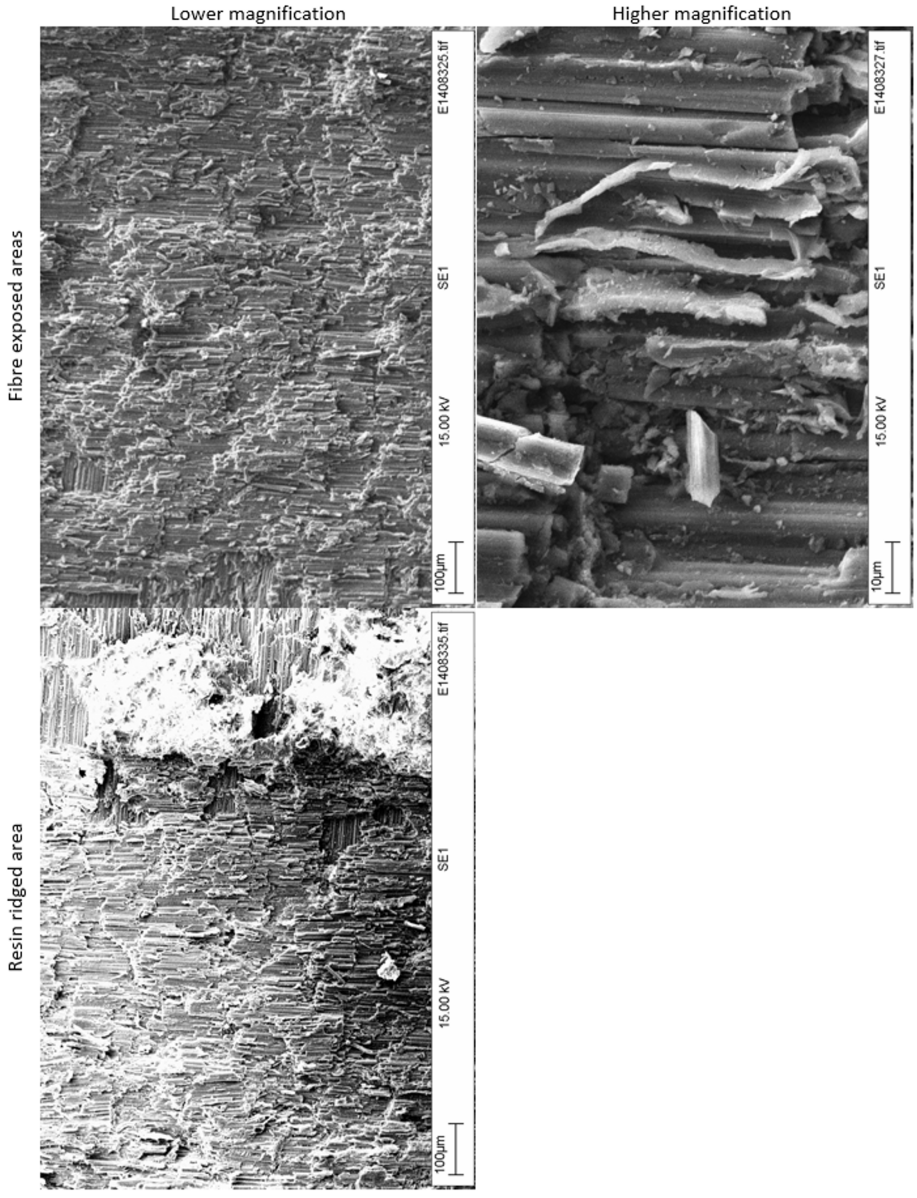


Figure 6.18: SEM images of HGB CF-Epoxy showing resin 'ridge' and fibre exposed areas

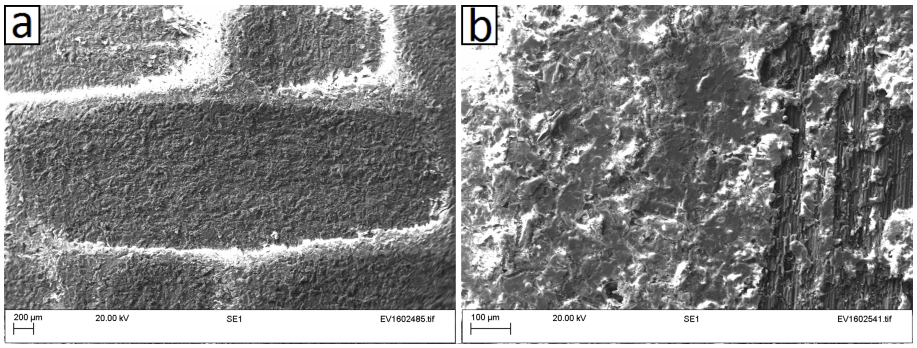


Figure 6.19: (a)SE SEM image of LGB CF-PEEK showing resin ridges (white from sample charging) and fibre rich regions (black) (b) close up of resin region

bundles were initially near the surface. Raised resin ridges are associated with areas with a thick local resin layer, i.e. in the corners where the waft bundles crossed the weft bundles. The areas where resin remains are clear in the optical image and it is clear that the HGB settings only resulted in a slight reduction in the resin areas remaining over the LGB settings. However, the HGB settings resulted in much deeper valleys, with the height difference between the peaks and valleys for the HGB being around 160 µm compared to around 60 µm for the LGB settings. The two phase morphology of the HGB CF-PEEK surface is clearly shown by the bi-modal distribution in figure 6.16b; however, this feature is not evident in the LGB surface.

SE SEM images of the surface of the grit-blasted surfaces clearly show the distinction between the raised resin ridges and the fibre-rich depressed valleys and how they clearly follow the pattern of the weave (figure 6.19a). The raised resin ridges appear to be relatively flat (figure 6.19b), and somewhat interspersed with a network of cracks and furrows (figure 6.20). Within the fibre rich areas of the LGB, there is a large amount of resin in amongst the fibres, such that at low magnification, few fibres are evident. At higher magnification it can be observed that there is resin and fibre debris as well as continuous fibres still intact.

More exposed fibres are observed in the fibre rich areas of the HGB substrate although there is still a significant amount of polymer and polymer debris present surrounding the visible fibres (figure 6.21). Investigating, the newly exposed fibres seem to be encased within a protective polymer matrix (figure 6.22).

6.8 Discussion

In many ways the controlled grit-blasting carried out in this investigation is very similar to erosion experiments. Solid particle erosion tests effectively involve controlled grit-blasting

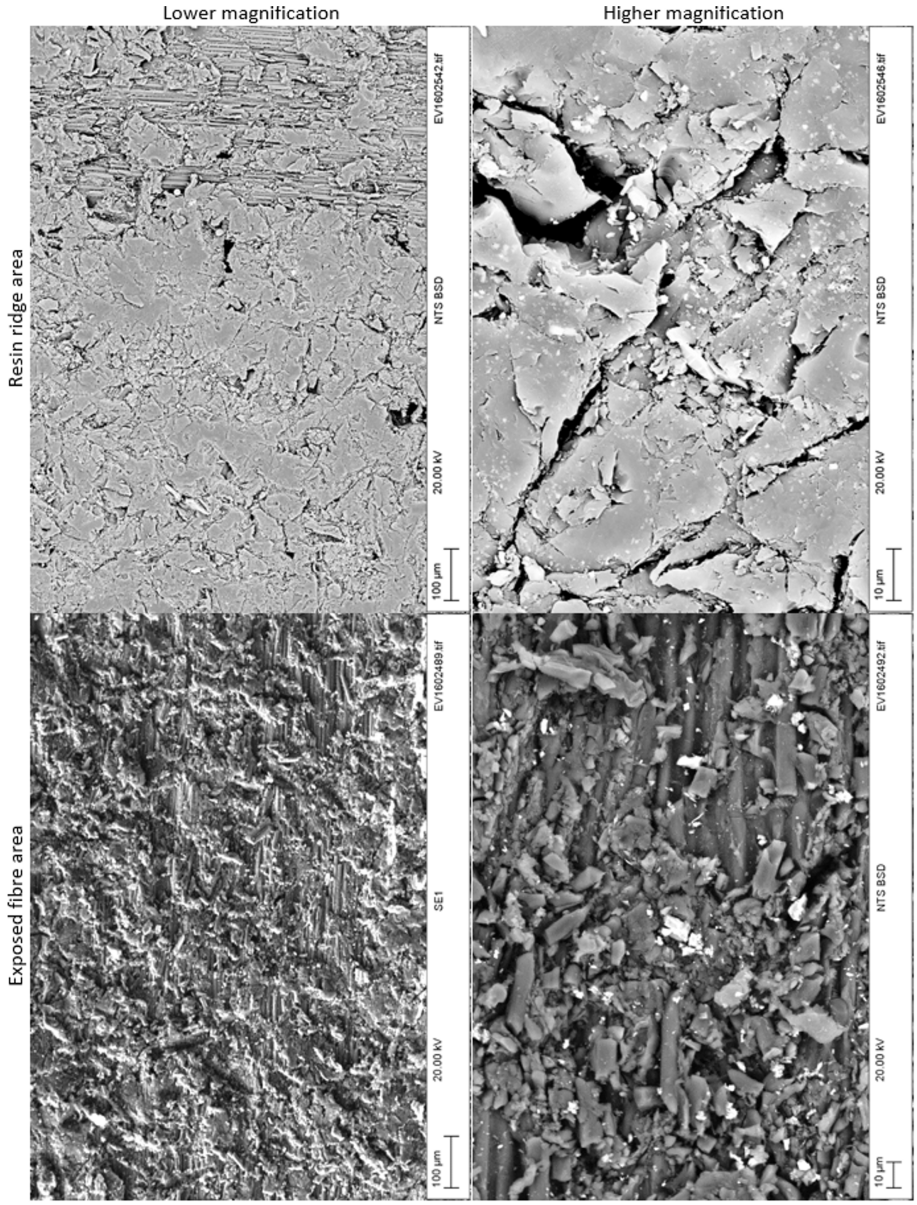


Figure 6.20: SEM images of LGB CF-PEEK showing resin ridge and exposed fibre areas

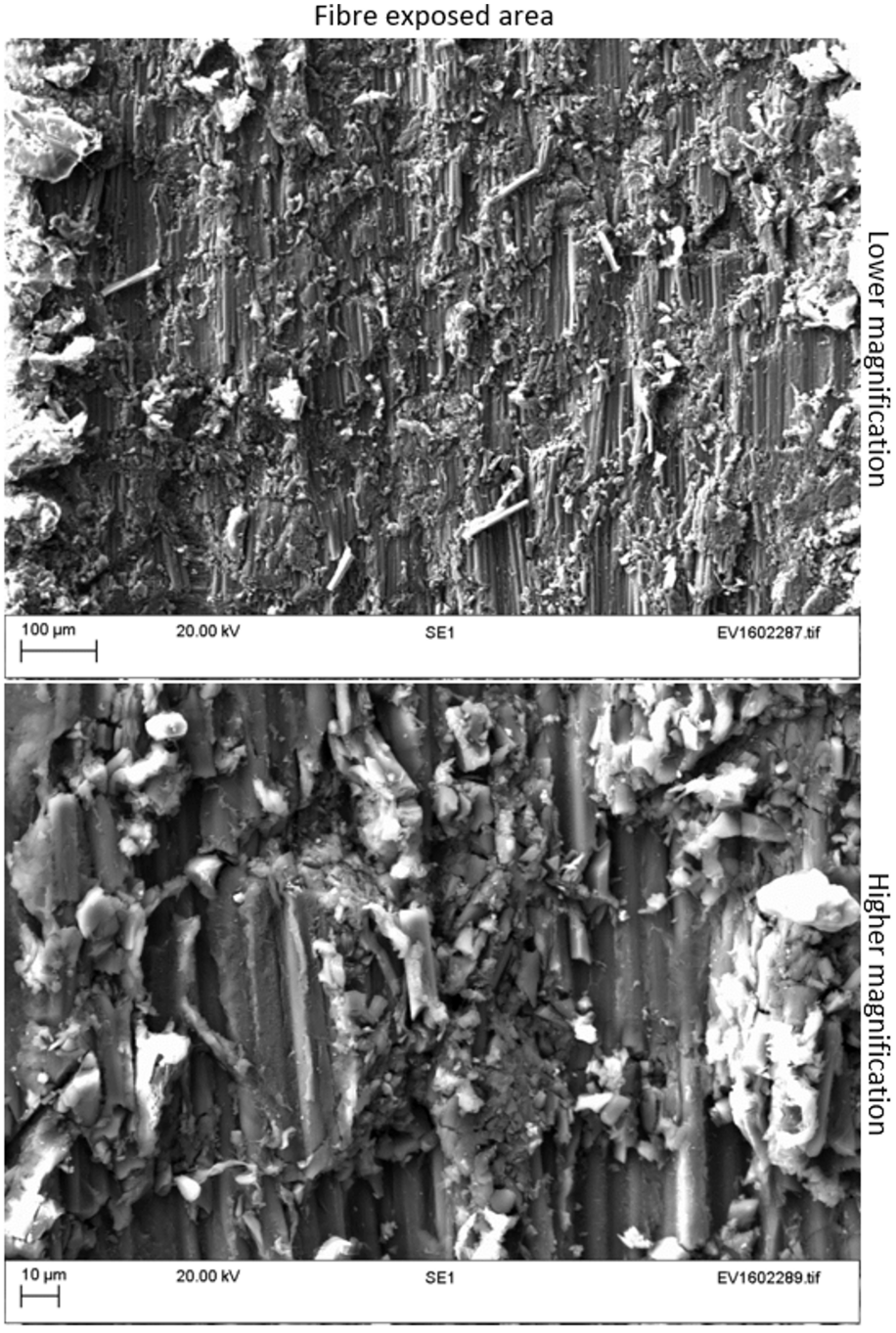


Figure 6.21: SE SEM image of HGB CF-PEEK showing detail of fibre rich region

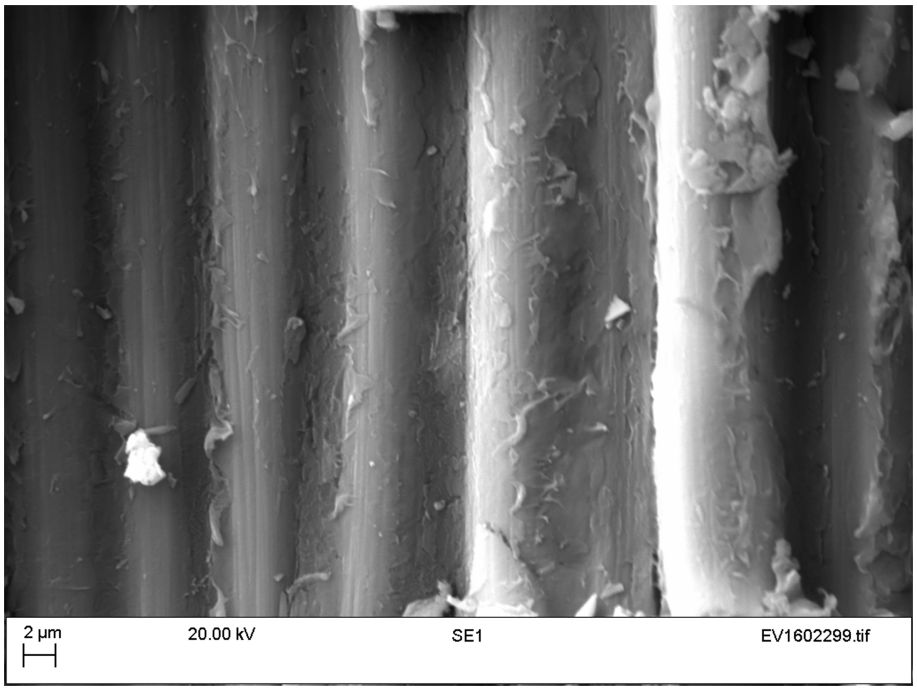


Figure 6.22: SE SEM image of HGB CF-PEEK showing resin on exposed fibres

of a material. The ASTM G76-13 test method for conducting erosion tests involves "delivering a stream of gas containing abrasive particles which [impact] on the surface" [183] and effectively involves a small stationary grit-blaster. However, the investigations carried out in this chapter do not have the same goals as typical wear tests, and thus there are differences in what investigations have been carried out. In the investigations outlined in this chapter, the grit-blasting nozzle was always orientated at right angles to the sample. This means the particle stream was also nominally at right angles to the sample. Due to divergence in the stream, the particles will not all impact at a normal angle to the sample; however, they will typically be at a high angle. This single (normal) angle of attack does not lend itself to determining the angular dependence of erosion, something which is commonly calculated in the erosion literature to classify the material as ductile or brittle. The other major distinction between these sets of experiments and typical erosion experiments is that the nozzle was moved parallel to the sample in a raster pattern during erosion. This was to ensure that the surface was evenly eroded; however, this is not typical in erosion literature and makes it difficult to directly compare results obtained in anything but their generality.

All of the substrates in this investigation started relatively smooth (either as received or polished), and as would be expected, all were roughened by the grit-blasting process. The metallic substrate surfaces behaved as would be expected. They had a low amount of mass loss and the surface was characterised by significant plastic deformation. Thus

the surface was roughened surface without significant mass loss.

The epoxy substrates appeared to behave in a brittle manner and the eroded surfaces looked somewhat similar to the brittle surfaces discussed in [169] [170]. The particle impacts created cracks on the surface which joined and segregated islands. These islands – likely undermined by subsurface cracks – could then be removed by further particle impacts. This is the likely mechanism for furrows being formed and is consistent with the literature characterising behaviour of brittle materials in an erosion environment. The energy of the grit particles seem to dissipate by cracking the substrate as the epoxy could not plastically deform significantly. Within the islands, there was little material removal or roughening, and the substrate was fairly resistant to the grit-blasting. This is reflected by the low measured mass changes (similar to those of the tested steel), low Ra and the narrow sharp peak in the surface height distribution. The effect of the deep furrows is then superimposed on this surface (Figure 6.8) causing the negative skewness. Thus, although the Ra for the surfaces was low, there are deep features on the surface. A more severe grit-blasting treatment would likely remove a greater proportion of the islands to form furrows, until the predominant surface morphology feature became these rough deep furrows significantly roughening the surface. The surface of the grit-blasted epoxy substrates has the lowest roughness of all the measured surfaces, implying that coating adhesion will be the lowest on this substrate.

The PEEK surface was more severely roughened by the grit blasting than the epoxy despite having similar (or less) mass removal. The energy of the grit caused plastic deformation on the surface as evidenced by the surface morphology in Figure 6.13 and Figure 6.14. This can be seen as relatively surprising given the high strain rate of the impact and the strain rate dependant nature of the substrate. It is in contrast to the epoxy which could not plastically deform and so cracked, as seen in the Figure 6.11 and Figure 6.12. The surface morphology of the PEEK is similar to that of particle eroded ductile materials and previously reported results for PEEK [171]. Thus, the surfaces of the two tested polymers have little in common; the epoxy surface is typical of a brittle material and the PEEK is typical of a ductile material when eroded at normal angles. This may be in part due to the thermoplastic nature of PEEK allowing a greater ductility.

The grit-blasted carbon fibre reinforced polymers have a very different morphology and a much greater mass loss than the plain polymers discussed above. They are much rougher (in terms of Ra) than the polymer substrates. This is due to the fibre-reinforcement bundles being much less resilient to the grit-blasting process. On both CF-epoxy and CF-PEEK, the resin which was still in place on the substrates had similar

morphological features to the epoxy substrate, i.e. networks of cracks were present. This implies that the presence of the fibres near the surface of the CF-PEEK undermine the ductility of the PEEK resin making it behave in a more brittle fashion; in thicker areas of PEEK substrate, the effect is likely less important and the surface behaves in a ductile manner. The most striking statistical feature of the surface is the bi-modal distribution (Figure 6.16), the different modal peaks representing the resin and fibre phases. This two phase morphology likely evolves in the following manner. Initially, the surface of the resin is eroded relatively uniformly such that it will appear similar to a non-composite, as with the LGB CF-PEEK; thus the bi-modal distribution is not clear in Figure 6.16. Then, in areas where the resin coverage is thin, brittle fibres will start to be exposed. These, and any subsequently exposed fibres, will be preferentially eroded leading to two distinct components, making up the roughness (as with LGB CF-epoxy and HGB CF-PEEK). Then eventually, the remaining resin rich areas will become less significant and the surface will be mainly rough, damaged brittle fibre (as with HGB epoxy). This speculated series of events is consistent with literature [177].

The CF-PEEK is the slower of the two FRPs to show the bi-modal distribution. The substrate also shows a lower mass loss than the CF-epoxy for the same grit-blasting conditions; these two factors are likely connected. PEEK resin has been shown to be resilient to the grit-blasting process; thus, brittle fibres remain effectively protected from impinging grit particles for longer. Thus, the CF-PEEK requires more erosion to occur before significant amounts of brittle fibres are exposed with their associated high erosion rates. This is why the LGB CF-PEEK only has 48% of the mass loss associated with the CF-epoxy. In the LGB conditions, most of the erosion involves removing resin, and is thus slow. However in the HGB conditions the CF-PEEK has 80% of the mass loss associated with the CF-epoxy. This is because the more severe settings lead to more of the erosion being on the brittle carbon in which case the CF-PEEK and the CF-epoxy are likely similar. That being said, the CF-PEEK has larger regions of the resin phase throughout its volume which mean it has 75% more resin phase than the CF-epoxy. Thus, the CF-PEEK is likely to continue to have marginally increased erosion resistance throughout its entire volume/depth, and as the conditions become more severe. No work has been conducted investigating the adhesion of the fibres to the resin so the effect of this cannot be commented on in this investigation, but if a reduced erosion rate was desired, then increasing the adhesion between the two phases would likely improve the erosion resistance as was the case in [178].

Despite the discussion above, the erosion rates are not of primary concern in this

investigation as the aim is to understand the surface morphology and its likely effect on the behaviour of thermal spray coatings. The grit-blasted FRPs are much rougher than the polymer substrates, and so on the face of it would be expected be the most effectively prepared for thermal spray. However, the large valleys associated with the fibres have a large amount of fibre phase exposed, and this may well completely change the bonding behaviour of the thermal spray to the substrate. It can also be observed statistically and by interrogating the surface of the substrates that the two broad areas (resin ridges and fibre valleys) have distinct roughness characteristics, and thus statistical based surface roughness characteristics for the substrate (Ra, Rsm, Sku etc.) are essentially averages of the distinct areas and of perhaps limited usefulness, especially given there is no particular reason why the a thermal spray coating should adhere to both in a similar manner, and the previous chapter (chapter 5) suggests that they do not. In addition to this, the surface of the substrate has been damaged, particularly for the FRP samples. Even if the thermal spray coating does adhere well to either the resin or the fibres, the top surface is not necessarily adhered well to the resin or fibres beneath them risking cohesive failure within the substrate.

The results of this section have several important implications; not least to highlight an identical grit-blast does not affect the surfaces of the different substrates in the same way. So that although the substrates in this investigation have been identically prepared, it does not mean that they have been affected by the grit-blasting in the same way and that the presence of two phases in the material means that careful investigations of any fracture faces will be required to understand on which phase and how the coating failed. In carrying out these observations, information can be inferred as to how and what thermal spray particles adhere to.

6.9 Conclusions

The PEEK substrate behaves in a similar manner to a ductile metallic substrate, with the local surface normally distributed around the average surface height. The epoxy resin appears to behave in a more brittle manner and there is little wear. Material loss appears to occur by cracks forming on the surface segregating the surface into islands. These islands become compromised and are removed from the surface. This leaves a hole or furrow in the surface much deeper than the rest of the surrounding substrate surface, causing the negative skew on the surface.

The CF reinforced polymers have a much greater wear rate and roughness than the

plain polymer samples. This is because the presence of this less resilient phase increases the average wear rates. The surfaces are also characterised by a bi-modal height distribution. This is because the less resilient fibre phase is lost quicker than the resin phase thus two distinct wear regimes are present.

Chapter 7

Deposited Coatings

7.1 Introduction

The work up to this point in the thesis has involved characterising the WFS plume, observing and analysing the way in which the individual spray particles interact with the substrate and determining how the substrate is modified through grit-blasting. This chapter combines all these aspects, describing deposition and analysis of WFS aluminium coatings sprayed directly onto polymer and fibre reinforced polymer substrates. These aluminium coatings could serve as functional coatings in themselves, or bond coats for functional top coats which would not otherwise adhere to the substrate. However, the broader aim of the chapter - and for that matter this thesis - is to understand the underlying processes and bonding mechanisms to draw out insights that can be applied more broadly rather than just optimising a specific coating/substrate system.

Literature concerning thermal spraying onto FRP/polymer substrates is discussed in chapter 2; below are some of the conclusions from this review relevant for contextualising this chapter.

There is strong evidence (with very few counter examples) that without abrasion of the substrate, coatings will not develop, thus the coatings are thought to adhere predominantly by mechanical keying. However, abrading the substrates has been shown to reduce the substrates' cohesive strength and the damaged substrate has become the failure locus in several studies. Thus, there is a balance in determining an effective surface preparation. There is little conclusive evidence as to the optimal surface topography or level or abrasion. Some studies suggest exposing fibres is beneficial whilst others reject this idea.

Thermal spraying can damage the resin of even heat tolerant FRPs. Some feedstock

materials have melting temperatures that are too high to be directly sprayed onto polymer based substrates and attention must be given to this.

There is little reported literature about thermally spraying coatings onto thermoplastic FRPs. However, there are indications that doing so may result in higher adhesion compared to thermoset FRPs.

7.2 Objective

- To identify the features/properties which are associated with differences in adhesion of WFS coatings on polymer and FRP substrates

7.3 Approach

The approach taken in this chapter was to deposit WFS Al onto different CFRPs (epoxy and PEEK based) substrates as well as pure epoxy and PEEK polymer substrates and investigate the effect of the surface finish on coating adhesion for both types. In all cases, the samples were either smooth (as received or polished for CFRP and polymer respectively), lightly grit-blasted (LGB) or heavily grit-blasted (HGB). These surfaces were extensively characterised previously in chapter 6. The coatings were sectioned for microstructural investigation and adhesion tests performed on specially prepared samples. The sectioned samples and the fracture faces of the adhesion test samples after failure were examined and insights drawn. In addition to this, several other subsidiary investigations were performed to draw out insight including the application of aluminium WFS coatings onto dry fibre reinforcement cloth.

7.4 Experimental methods

7.4.1 Substrate materials

The substrate materials coated in this chapter are listed below. Details on these substrates can be found in chapter 3. The square brackets after the substrate material denote which surface preparations were tried for each substrate. LGB and HGB denote high grit-blast and low grit-blast settings (as defined in chapter 3), polished denotes that the substrate was polished to 0.25 µm finish and as received means that the substrate was sprayed in the state that the substrate was received from the manufacturer. Detailed surface characterisation of the substrates can be found in chapter 6.

- Steel (C15) [LGB & HGB]
- Unreinforced polymers
  - Epoxy Easy composites (EL2) [polished, LGB & HGB]
  - PEEK [polished, LGB & HGB]
- Dry Reinforcement fibres
  - Carbon fibre [As received]
  - Glass fibre [As received]
- CFRP
  - CF-epoxy (TenCate E722) [As received, LGB & HGB]
  - CF-PEEK (TenCate Certex® TC1200) [As received, LGB & HGB]

7.4.2 Sample tests processing

Thermal spray

Thermal spraying was carried out with a Metallisation Mark 73 wire flame spray gun with parameters outlined in chapter 2. The gun was rastered over the surface with a 10 mm increment and a stand-off distance of 160 mm at a speed of 1000 $mm.s^{-1}$. The coatings on all of the substrates consisted of 7 passes which typically gave a coating thickness of approximately 120 µm.

Adhesion tests

ASTM C633 Adhesion tests have been carried out in accordance with a modified ASTM C633-13 standard. Coatings were deposited onto 40 x 40 mm coupons. 1" (25.4 mm) diameter studs were glued on either side of the samples, the coating cut around the stud and pulled in accordance with the standard (figure 7.1) at a loading rate of 1 $mm.min^{-1}$ using an Instron 8801. The coatings tested had a thickness of ≈120 µm which is below the recommended thickness for this standard but the coatings were all sectioned and seen to be dense prior to testing, showing that there was little chance for glue infusion.

ASTM D4541 Where it was not possible to perform adhesion tests to ASTM C633-13 due to practical difficulties, ASTM D4541-09e1 tests were performed. 14 mm diameter test studs were glued to the coating, the coating was cut around and a portable adhesion

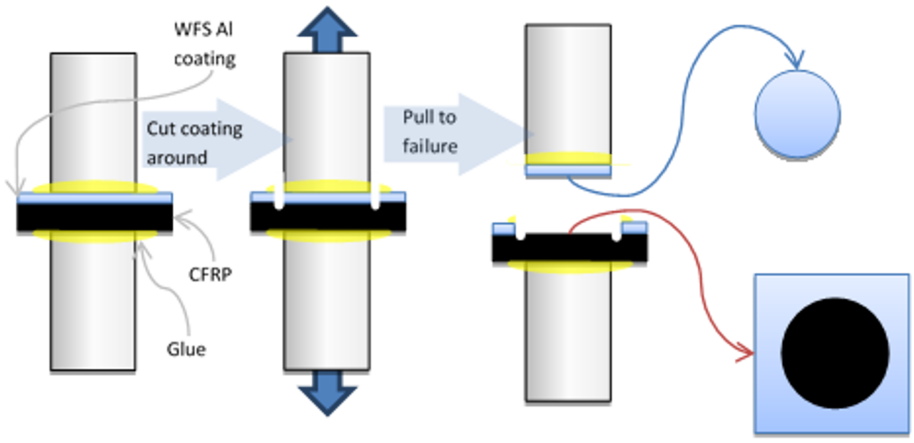


Figure 7.1: Schematic of modified ASTM C633 adhesion test to test samples sprayed on 40 x 40 mm coupons. Samples are glued to studs, excess coating is cut and they are pulled to failure

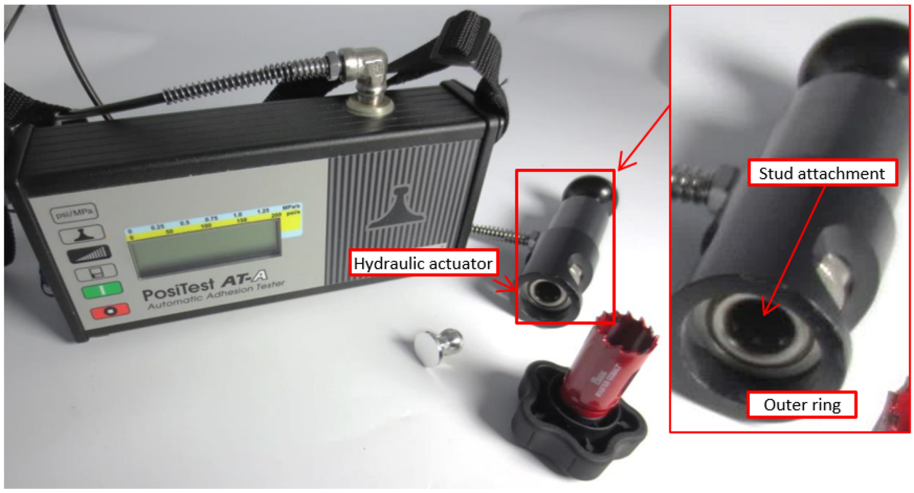


Figure 7.2: Photograph of the portable adhesion tester (PAT) used to conduct ASTM D4541 tensile adhesion tests (TATs). The hydraulic actuator clipped on the stud and pulled to failure.

tester (PosiTest AT-A) (figure 7.2) was used in accordance with the standard. It is known that this test method is prone to shear/peel effects and thus can result in less consistent adhesion values than those produced with the ASTM C633 adhesion test standard.

Fracture surface characterisation

Analysis of the fracture faces created in the tensile adhesion tests were carried out. Several techniques were used i.e. OM/SEM imaging, EDX analysis and variable focus microscopy (FVM); these techniques are outlined in chapter 3.

Table 7.1: Coating thickness measurements of WFS Al coatings on different substrates and preparations (Mean value from multiple measurements)

Material	AR/polished		LGB		HGB	
	Mean thickness (µm)	Standard deviation (µm)	Mean thickness (µm)	Standard deviation (µm)	Mean thickness (µm)	Standard deviation (µm)
Steel	-	-	100	10	134	9
Epoxy	-	-	118	13	98	11
PEEK	130	13	108	10	113	10
CF-epoxy	-	-	123	10	136	16
CF-PEEK	128	12	134	16	120	20

Table 7.2: Coating mass measurements of WFS Al coatings on different substrates and preparations. Where single/few samples were tested, statistics are not included

Material	AR/polished		LGB		HGB	
	Mean mass ($g.m^{-2}$)	Standard deviation ($g.m^{-2}$)	Mean mass ($g.m^{-2}$)	Standard deviation ($g.m^{-2}$)	Mean mass ($g.m^{-2}$)	Standard deviation ($g.m^{-2}$)
Steel	-	-	285	25	309	25
Epoxy	-	-	284	24	291	-
PEEK	315	9	296	23	338	60
CF-epoxy	-	-	319	5	325	9
CF-PEEK	313	6	322	12	302	31

Chemical coating removal

Coatings on a selection of the PEEK materials were removed by chemical means. This was done to deconvolute the effects on the substrate surface of the coating application and the physical removal process. It was carried out by placing the coated substrates in low concentration (0.1 M) sodium hydroxide (NaOH) solution for several hours until the aluminium was completely removed from the substrate. A low concentration was used to mitigate any risk of the exothermic nature of the reaction damaging the substrate. An additional uncoated polished test piece was put in each preparation to ensure that there was no damage to the PEEK from the solution.

7.5 Results

7.5.1 Coating thickness and weights

All of the different substrates and preparations had similar coating thicknesses (around 120 µm) and masses (around 308 $g.m^{-2}$) these are illustrated in table 7.1, table 7.2 and and figure 7.3.

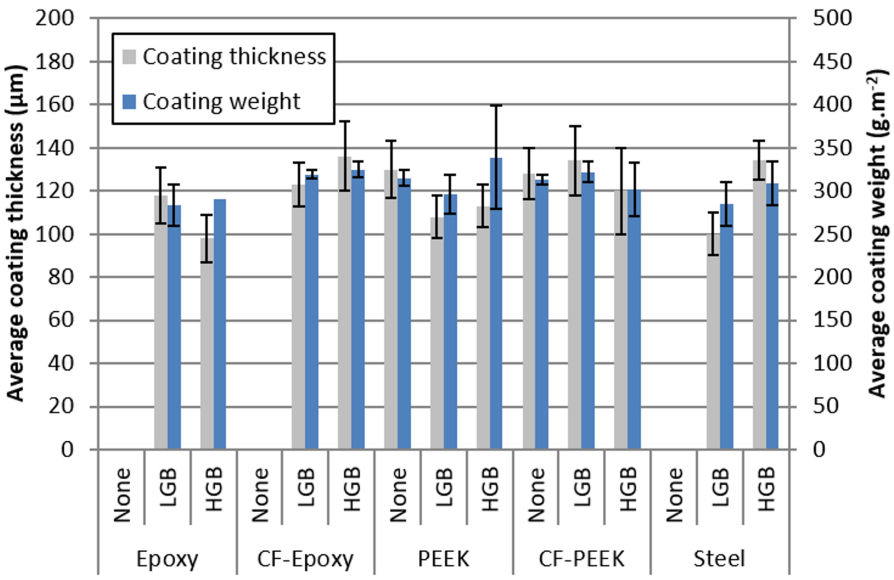


Figure 7.3: Bar chart showing the coating thicknesses and weights of the aluminium coatings deposited on the different substrates indicating that they are all broadly similar, error bars represent +/- one standard deviation

7.5.2 Tensile adhesion tests

The results of the TATs are outlined in table 7.3 and figure 7.5; where possible these are ASTM C633 tests. It was not possible to perform ASTM C633 tests on the coatings deposited onto the epoxy substrates or the as received CF-epoxy substrates. The coatings on the former had extensive cracking on the surface (figure 7.5) without an area free from cracks large enough to adhesively bond a 25 mm stud to. The coatings on the latter were not sufficiently bonded to the substrate to allow ASTM C633 sample preparation without debonding. In both these cases ASTM D4541 TATs (portable adhesion test) were performed instead. Sample preparation was delicate and one successful test was performed per sample type. The test was mainly conducted to reveal a fracture face for examination. However the single adhesion test values are included in table 7.3 and figure 7.4. Due to the different nature of the tests and the single samples taken these results are only indicative and the certainty of any conclusions drawn directly from them reflects this.

Failure modes

Examining the fracture faces of the TATs show that on a macro level the coatings failed adhesively (i.e. at the coating - substrate interface) and there is no obvious coating remaining on the substrate (or vice versa) as shown in figure 7.6. Thus, the measured value in each case is an indication of the interfacial tensile adhesion strength (TAS) of

Table 7.3: Measured tensile adhesion strength for WFS Al coatings on the different substrates and preparations

Substrate	Prep	Adhesion results MPa Min	Mean	Max	Std dev	# of tests	Mode	Test type
Steel	None	-	-	-	-	-	-	-
	LGB	9.8	10.9	12.0	0.9	5	Adhesive	C633
	HGB	14.4	16.8	20.2	2.3	5	Adhesive	C633
Epoxy	None	-	2.3	-	-	1	Adhesive	D4541
	LGB1	-	4.3	-	-	1	Adhesive	D4541
	HGB1	-	4.5	-	-	1	Adhesive	D4541
CF-epoxy	None	-	1.0	-	-	1	Adhesive	D4541
	LGB	7.0	9.6	13.0	2.1	9	Adhesive	C633
	HGB	5.5	7.6	11.0	1.9	14	Adhesive	C633
PEEK	None	2.8	4.5	5.8	1.3	5	Adhesive	C633
	LGB	8.8	12.8	15.9	2.2	10	Adhesive	C633
	HGB	6.3	14.4	18.2	3.7	8	Adhesive	C633
CF-PEEK	None	11.1	13.3	14.8	1.4	6	Adhesive	C633
	LGB	15.4	17.5	21.7	2.4	8	Adhesive	C633
	HGB	10.9	13.0	17.2	2.9	4	Adhesive	C633

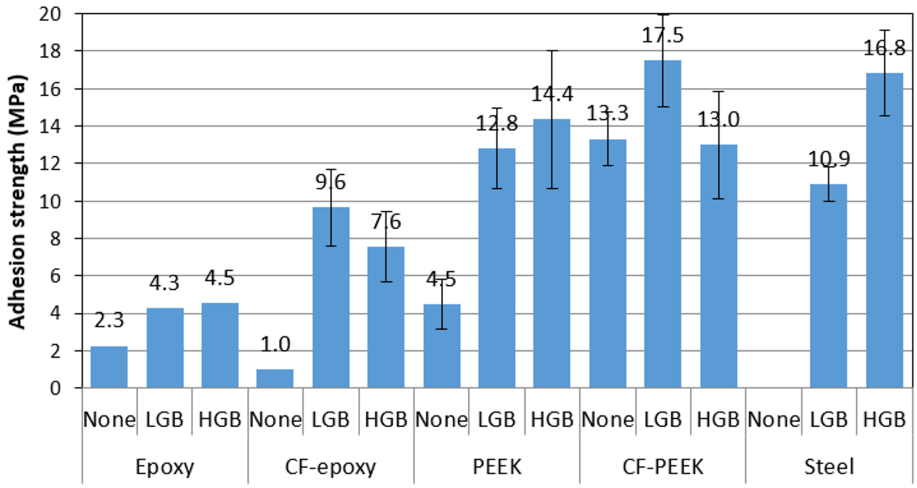


Figure 7.4: ASTM C633/D4541 adhesion test results for WFS aluminium coatings deposited onto polymer and CFRP substrates. Error bars represent +/- one standard deviation, thus not included for single sample tests

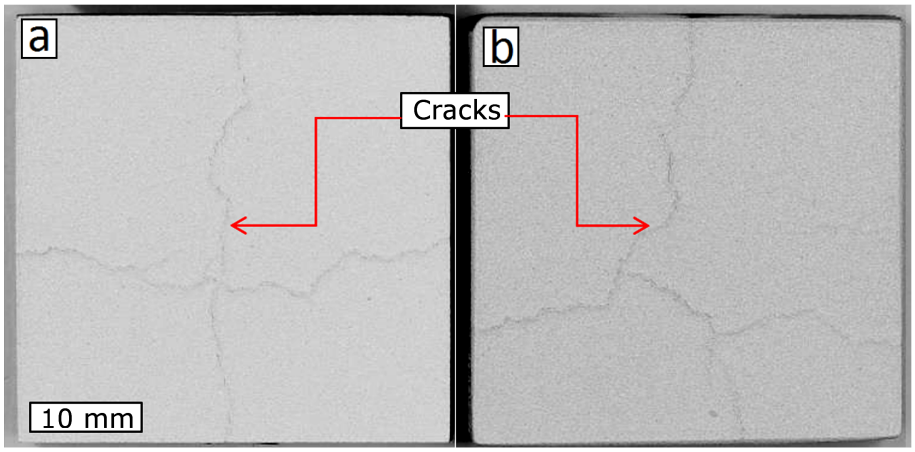


Figure 7.5: Photographs of wire flame spray coating on (a) LGB and (b) HGB non-reinforced epoxy coatings showing prominent cracks on surfaces

the coating, and not the cohesive strength of the coating or substrate.

Trends in adhesion strength

The polymer and metallic substrates (i.e. the non-fibre reinforced substrates) experienced an increase in TAS with the increasing severity of the grit-blast. On the metallic substrate, the increase in adhesion between LGB and HGB was seen to be significant. However, within the coatings on polymer substrates, the increase in TAS adhesion between the LGB and HGB preparation was relatively small. For the PEEK substrate, this increase was 1.6 MPa, which is well within one standard deviation for the collected results. For the epoxy substrate the difference is smaller (0.2 MPa) and thus very likely within the experimental-scatter, although this is impossible to judge this with the single collected data point per epoxy preparation. Where spray was attempted onto smooth substrates (as in the case of epoxy and PEEK), the adhesion recorded was low (2.3 and 4.5 MPa for epoxy and PEEK respectively)

The trend was somewhat different for the FRP substrates. The tensile adhesion strength of the FRP substrates was shown to improve compared with the as received sample by a light grit-blast (LGB). However, the values then decreased (with respect to the LGB TAS) when the grit-blasting was more severe. In the case of the CF-PEEK, increasing the grit-blast intensity to the HGB settings reduced the TAS to its value for as received CF-PEEK, though this result is probably a function of the smooth CF-PEEK having a particularly high adhesion value.

The coatings deposited onto the thermoplastic PEEK polymers and PEEK FRPs had significantly greater TAS than those on the similarly prepared epoxy based substrates. It is important to point out that different test methods were used to measure TAS of the coatings on the PEEK (ASTM C633) and epoxy (ASTM D4541) substrates. This means that the comparison between the polymers is not precise; however, the differences in adhesion measured are very large (averaging around 7.3 MPa for the polymers). The observation that the PEEK substrates have higher TAS than the epoxy substrates is also supported by the fact that coatings deposited on AR CF-epoxy substrates (which is likely very similar to the polished epoxy) were too poorly adhered to prepare an ASTM C633 sample and deboned when this was attempted. The same trend (of higher TAS for the PEEK based substrates) was also seen in the FRPs and the coatings prepared on CF-PEEK had a higher TAS than those on similarly prepared PEEK. This was especially apparent on the unprepared FRPs where the adhesion on CF-PEEK was 13 times greater than that on CF-epoxy.

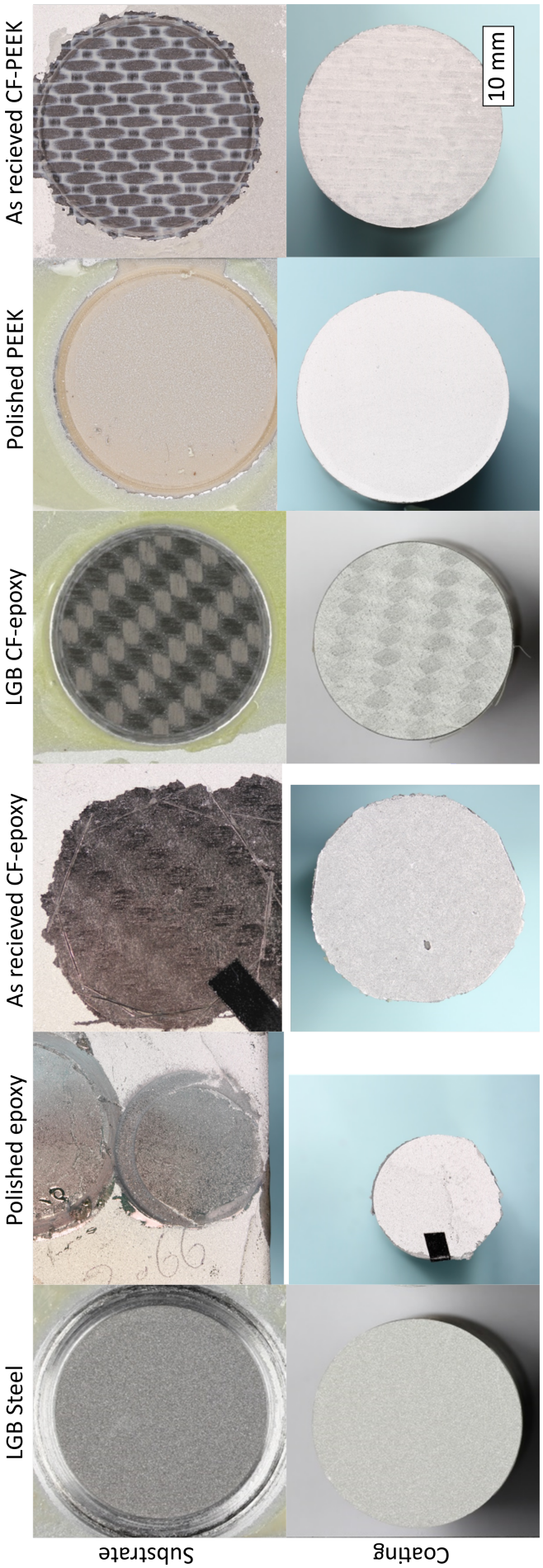


Figure 7.6: Photographs of selected of adhesion test fracture faces (top) substrate and (bottom) coating fracture faces. Images shows the failure was adhesive at the substrate coating interface

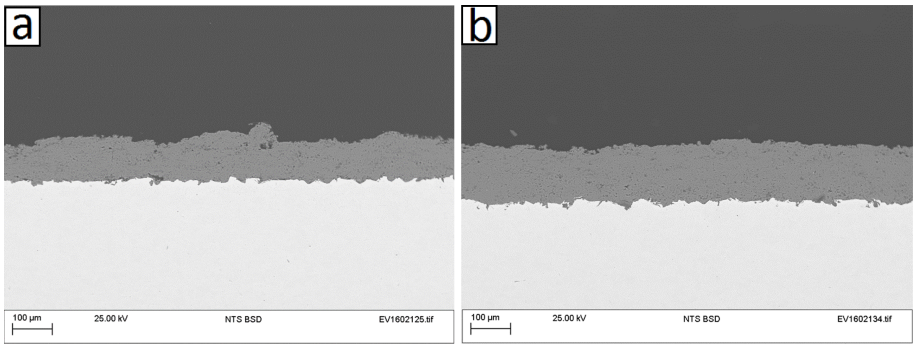


Figure 7.7: BSE SEM image of sectioned WFS coating on (a) a LGB steel coupon and (b) a HGB steel coupon showing the microstructures of the coatings are very similar

The FRP substrates typically have a higher TAS than the similarly prepared polymer substrates. This is especially true for the epoxy based substrates; however, the issues surrounding the different test methodology also apply for this comparison. The higher TAS of the CF-PEEK over the similarly prepared PEEK is less significant and mostly within one standard deviation. The only substrate preparation where the difference (between CF-PEEK and PEEK) is large is for the smooth samples (AS received CF-PEEK and polished PEEK) where the difference in TAS is 8.8 MPa.

7.5.3 Coating characterisation

Metallic substrates

WFS aluminium coatings were successfully deposited onto both the LGB and HGB steel substrates; coatings were not attempted onto polished steel samples because in prelimanary trials such coatings did not adhere. The coatings appear to be relatively dense with few large pores of areas of oxide (figure 7.7). The macro images of the fracture faces show test specimens failed adhesively (figure 7.6). However, observing the fracture faces at higher magnification in back scattered mode shows that on both the LGB and HGB (figure 7.8) there are small areas of aluminium remaining on the substrate as well as evidence of areas of steel substrate material in the fracture face of the aluminium coating. There are some indications that there are more areas of aluminium remaining on the HGB substrate than on the LGB substrate.

Epoxy

Epoxy polymer WFS coatings initially sprayed well onto the unreinforced epoxy substrates, forming continuous coatings on the surface. As the coating thickness increased and additional layers were added, large cracks started forming in the coating on all of

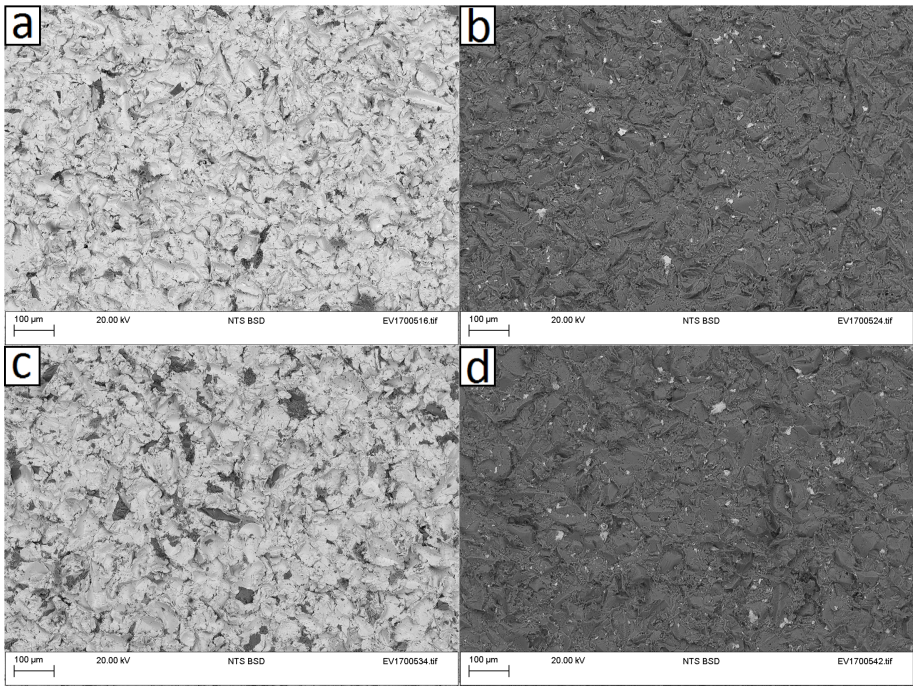


Figure 7.8: BSE SEM images of Steel adhesion test fracture faces (a) LGB substrate, (b) LGB coating, (c) HGB substrate and (d) HGB coating. Images show residual Al on steel and residual steel on Al (light areas represent steel and dark areas represent Al)

the differently prepared epoxy substrates (figure 7.5). In addition, the coating on the polished epoxy debonded and spalled off of the substrate. Sections of the LGB and HGB epoxy substrates show clear interfacial debonding at the cracks (figure 7.9(a and c)), in both cases the cracks occur at a particularly large surface feature. Given that cracks were seen on the surface of the substrate before sectioning the samples, it is likely that these features are real and not due to metallographic sample preparation. In addition to the cracks evident from the surface, the cross sections show subsurface cracks within the coating (e.g. figure 7.10); these are also believed to be real features, not preparation artefacts. Except for the features discussed above, the bulk of the LGB and HGB coatings appear relatively dense with few large pores of areas of oxide (figure 7.9(b and d)) and coating thicknesses and weights in line with the other substrates (figure 7.3).

Examining the fracture face of the epoxy substrates after coating removal revealed two features of note. Firstly, there were a few remnants of aluminium on the surface. Secondly, there was a change in the surface morphology of the substrate; there are large circular crater shapes on the surface (around 100 µm in diameter). These features are particularly evident on the surface of the polished substrate (figure 7.11a). The respective aluminium fracture face (figure 7.11b) shows large (10 – 100 µm) irregular areas of thin carbon deposit after coating removal. In addition small (1 – 5 µm) pores are visible on the coating.

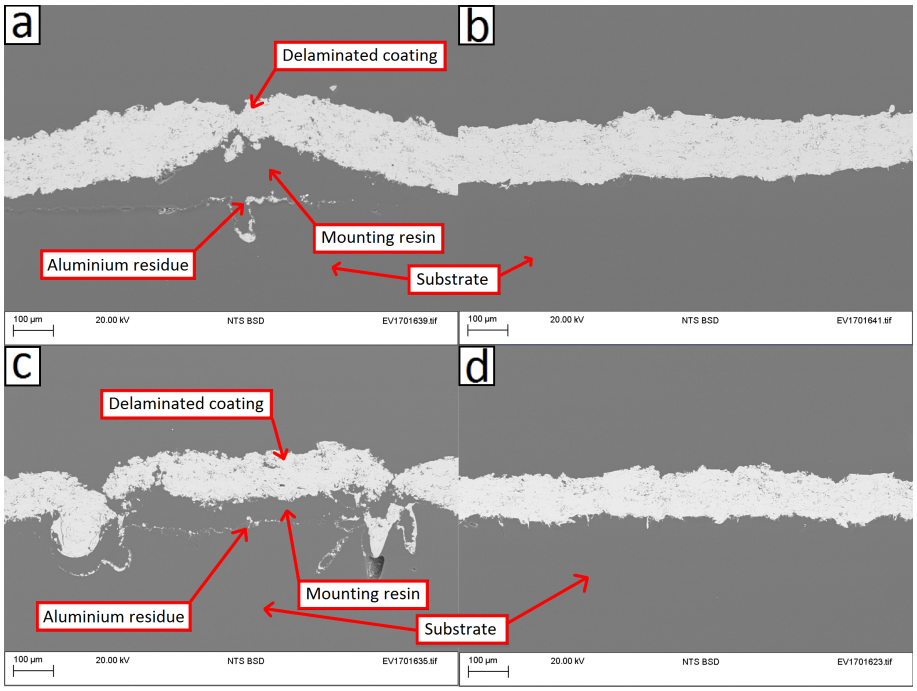


Figure 7.9: BSE images of sectioned WFS coating on (a and b) LGB epoxy substrates and (c and d) HGB epoxy substrates, showing (a and c) cracked region and (b and d) well adhered region

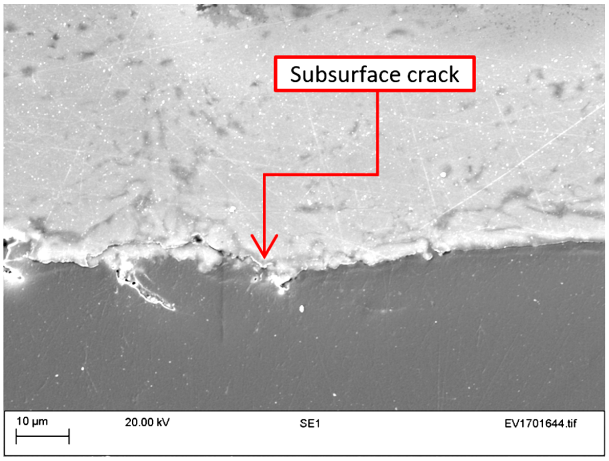


Figure 7.10: SE image of sectioned WFS coating on LGB epoxy substrate showing subsurface crack at the coating/substrate interface

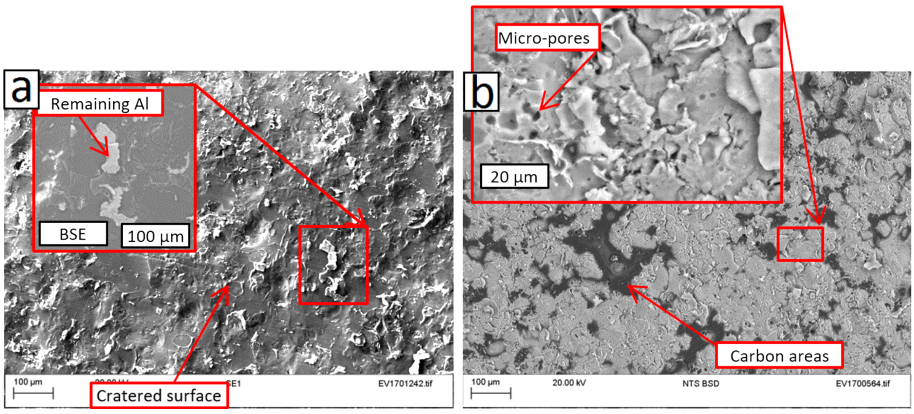


Figure 7.11: SE/BSE SEM images of polished epoxy adhesion test fracture faces (a) substrate (b) coating. Light areas in BSE images represent Al and dark areas represent C

Epoxy FRP WFS coatings initially deposited onto the as received CF-epoxy substrates, but after several passes the coatings would debond and spall off as a mostly continuous mass. Some coatings remained attached; however, they typically had large debonded areas and could not readily be sectioned. Thick (≈100 µm) WFS Al coatings were reliably deposited onto both the LGB and HGB CF-epoxy substrates. Sections of these coatings show a good quality bulk coating. However, at high magnification, interfacial cracks parallel to the substrate surface could be observed. These were typically observed where the fibre phase came directly into contact with the coating both en masse (figure 7.12) and individually (figure 7.13a). Less common, but in some areas, there were cracks normal to the surface extending through the resin to the fibres (figure 7.13b). The cracks like those described above could be a result of damage during sectioning of the samples. However, after mounting the samples, they were ground back extensively before polishing. After observing the features they were re-prepared by grinding back further and re-polishing and the features were still present indicating that the features are probably not a preparation artefact.

Optical microscopy of the as received substrate after coating removal shows that there were pores at the surface of the substrate clustered around the thicker regions of resin (figure 7.14). SEM images of the same substrate (figure 7.15) show very similar features to the polished epoxy after coating removal i.e. small aluminium deposits, craters and blisters. SE SEM images of the coating's fracture face (figure 7.16) show that it contained depth indicating that the coating was deposited to a slightly roughened surface. BSE images show that the coating also contains large area of thin carbon deposits on the fracture face.

Topographical data from the fracture faces of the grit-blasted CF-epoxy adhesion tests

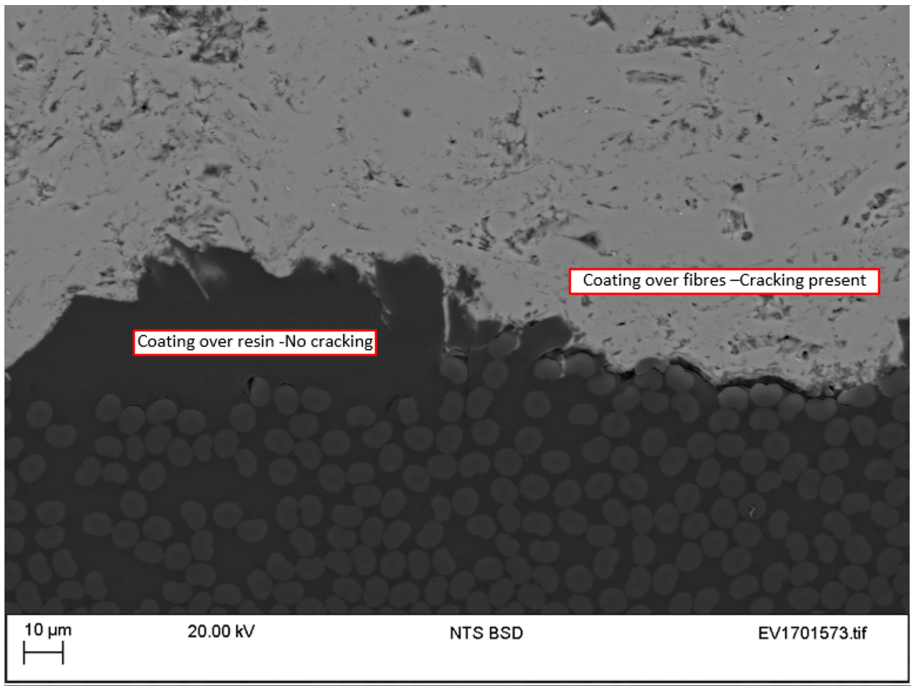


Figure 7.12: BSE imaging of a cross sections through a wire flame spray coating on CF Epoxy HGB highlighting interfacial cracking over fibre areas

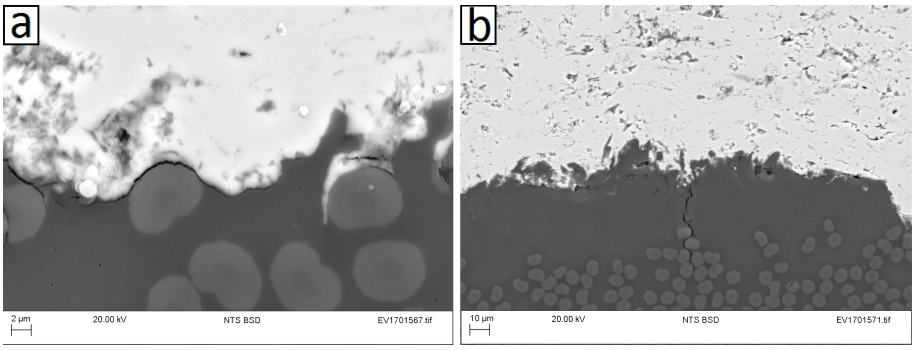


Figure 7.13: BSE Cross sections of wire flame spray coating on CF Epoxy HGB showing (a) crack around coating and (b) crack from fibres to coating

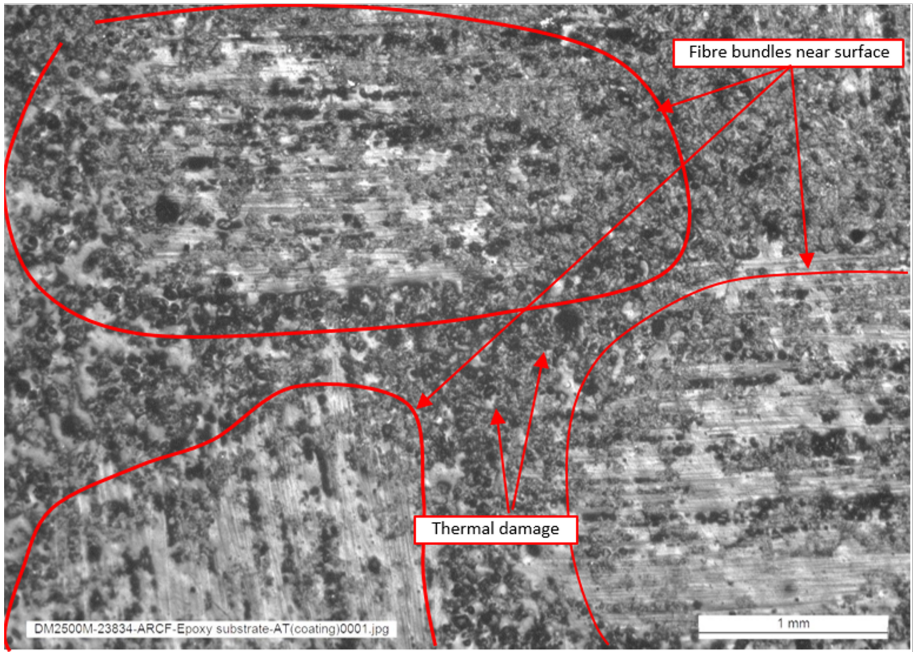


Figure 7.14: Optical microscopy of substrate after coating removal on AR CF-epoxy substrate showing pores on surface clustered around thick epoxy regions

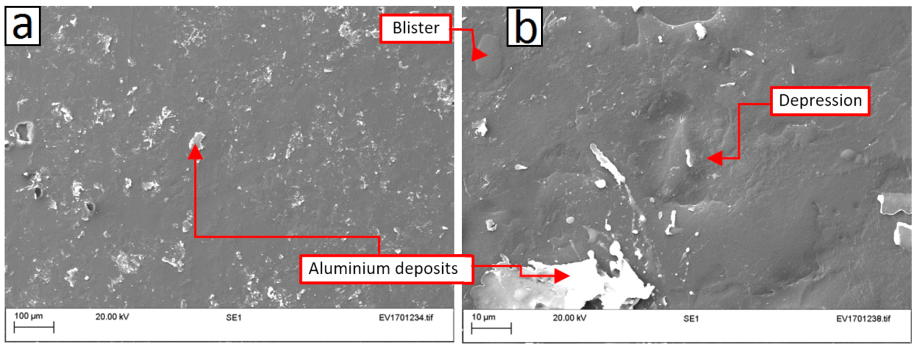


Figure 7.15: SE SEM images of substrate after coating removal on AR CF-epoxy substrate at (a) low and (b) high magnifications showing remaining aluminium on surface and substrate damage

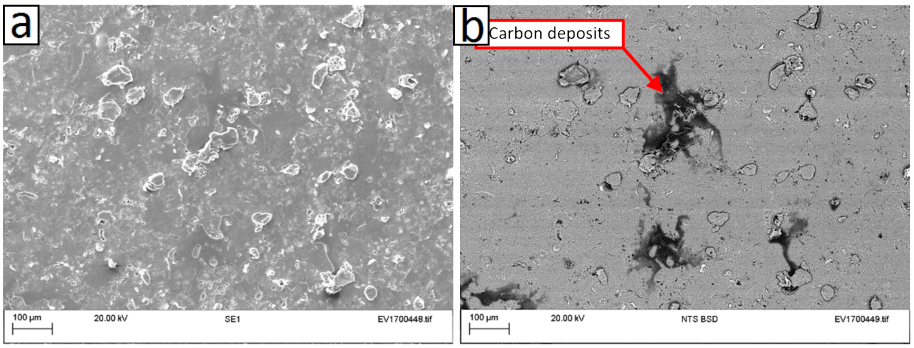


Figure 7.16: SEM images of WFS Al coating removed from AR CF-epoxy substrate (a) SE showing roughness on surface and (b) BSE showing carbon deposits on coating underside

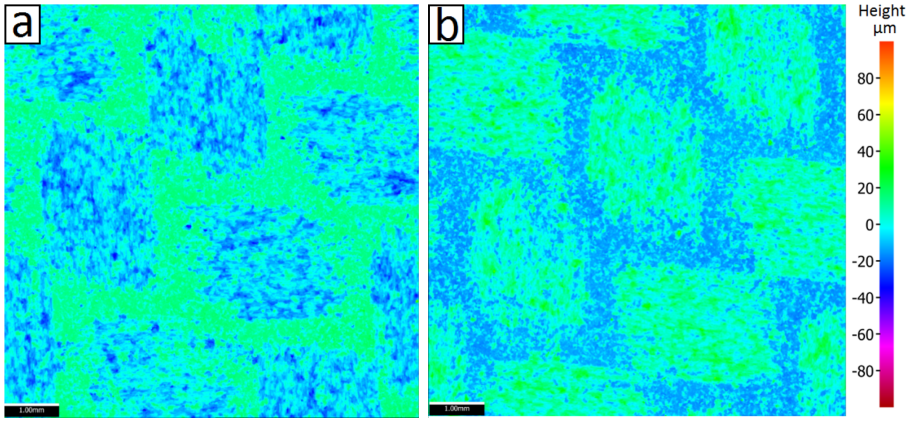


Figure 7.17: Representative height image of 7.5 mm square (a) LGB CF-Epoxy substrate and (b) removed coating after TAT showing the carbon fibre of the carbon fibre weave on both surfaces

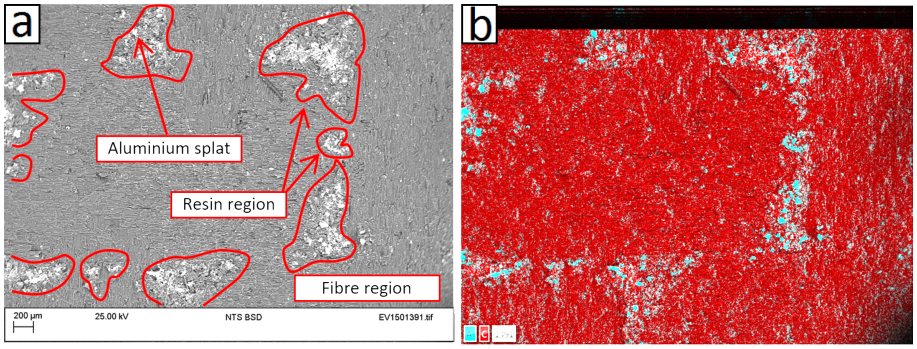


Figure 7.18: SEM imaging of HGB CF-epoxy adhesion test (substrate) fracture face (a) BSE shows areas of remaining resin and (b) EDX map shows that remaining aluminium is concentrated in these resin areas

show that the aluminium coating replicated the topography of the surface it adhered to, i.e. the resin ridged/sunken valley texture was replicated in the coating (figure 7.17). BSE SEM images of the substrates indicate that small (typically < 50 µm) remnants of coating remain on the fracture face of the substrate. These remnants are present on both the LGB and HGB samples and in both cases concentrated on the resin rich area of the sample (figure 7.18a). EDX mapping of the HGB sample confirms that the bright regions are in fact aluminium (figure 7.18b). It also highlights that although the aluminium is predominantly located within the resin ridges there are some smaller deposits within the fibre exposed areas. Closer examination of the aluminium deposits in fibre-exposed area indicate that they are often associated with small areas of resin within that area e.g. figure 7.19a. Within the resin rich areas, aluminium appears to concentrate within the rougher areas of resin, although aluminium is still present in the smoother areas figure 7.17b.

A representative BSE SEM image of the coating fracture face is shown in figure 7.20. The borders between resin and fibre exposed areas were superimposed on the image with

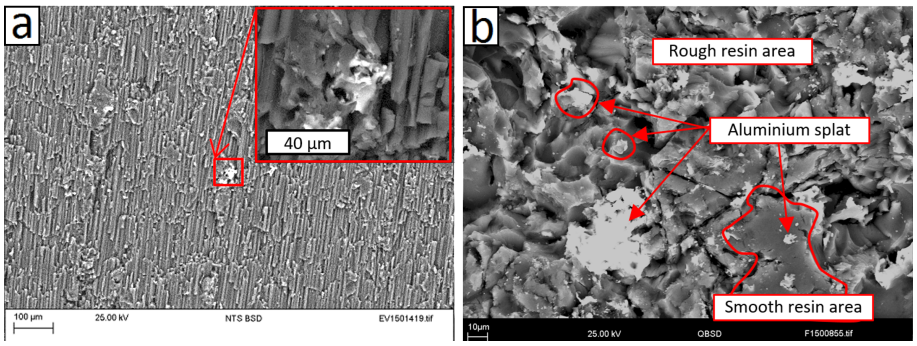


Figure 7.19: BSE SEM images of fracture faces of LGB CF-epoxy substrate (a) showing aluminium residue on epoxy in fibre region and (b) showing aluminium coating residue on rough and smooth resin regions.

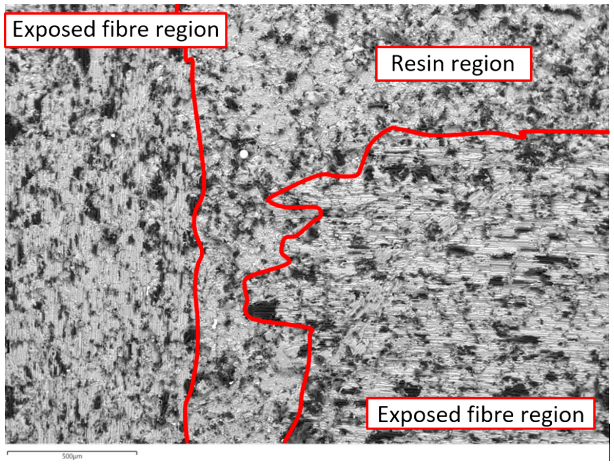


Figure 7.20: BSE image of fracture face of (coating) removed from LGB CF-epoxy. Black areas are indicative of carbon. Red lines separate areas deposited over exposed fibres and resin regions.

reference to SE image of the same area. There are carbon rich deposits (represented by the black colour) present in both the fibre rich and carbon rich areas. Examining the dark areas in more detail show that some of the pull-off from the substrate is made of fibres (figure 7.21a) and some of resin (figure 7.21b); in both cases, the pull off is flush with the surrounding coating indicating that the pull off represents the base of an asperity which was surrounded by, and pulled off with the coating. The bulk of the coating surface is purely aluminium with no residual substrate attached. However it is interesting to note that the aluminium coating mirrors the underlying substrate texture (fibre and resin) as highlighted in figure 7.21. Thus, it must have been in intimate contact. Examining the surface of the coating in detail, it is also clear that there is some porosity on the coating at the coating/substrate interface (figure 7.22). Very similar observations were made on the HGB coating.

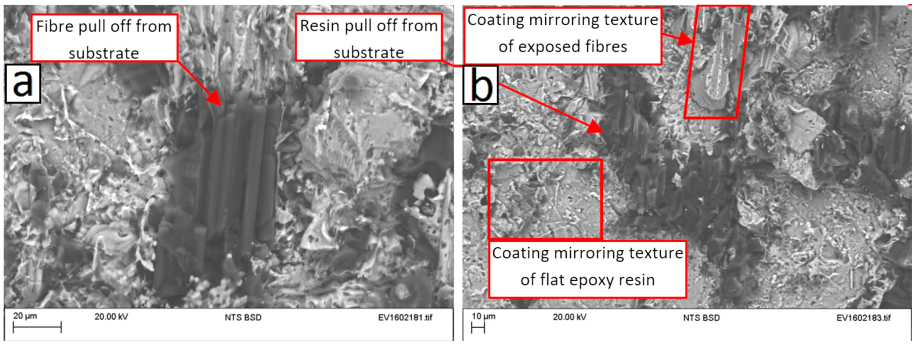


Figure 7.21: BSE images of the aluminium coating fracture face removed from LGB CF-epoxy. Images show (a) fibres removed from the substrate and (b) fibres removed from the substrate.

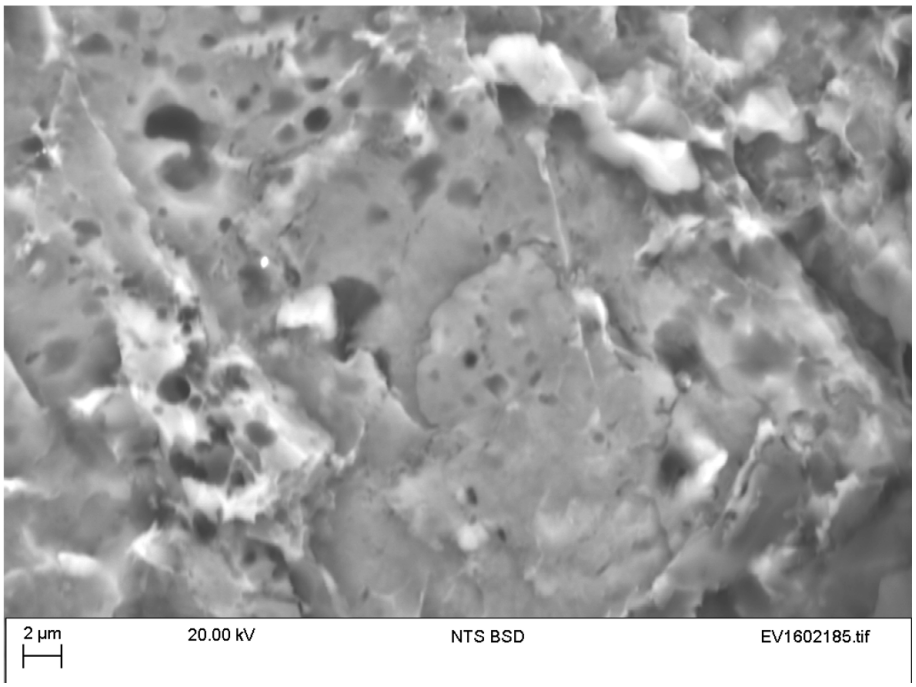


Figure 7.22: BSE images of the aluminium coating fracture face removed from LGB CF-epoxy. Image shows porosity on the surface of the aluminium coating.

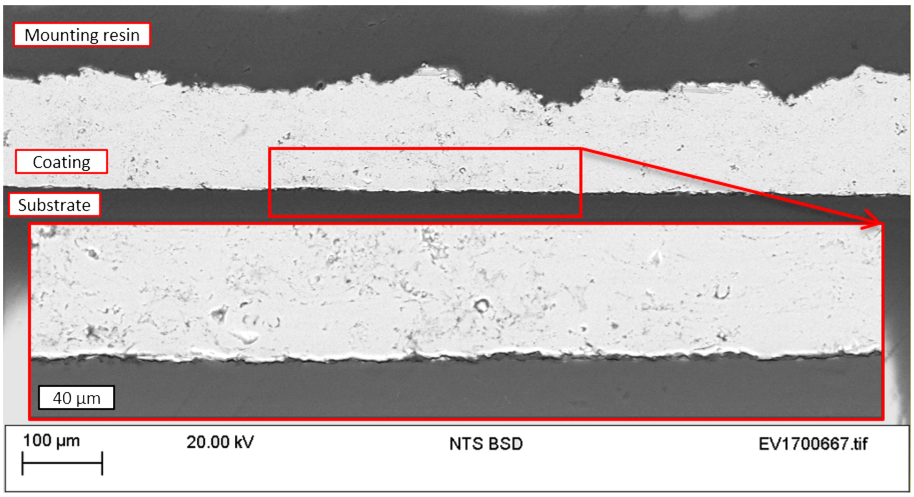


Figure 7.23: SEM BSE image showing sross sections of wire flame spray coating on non-reinforced polished PEEK. At high magnification some de-bonding is observed.

PEEK

PEEK polymer WFS aluminium coatings were successfully deposited onto the polished, LGB and HGB PEEK substrates. Coating thicknesses and weights were in line with the other samples (figure 7.3) and the bulk of the coatings were similar to those deposited on the other substrates. The cross-section of WFS coating on the polished PEEK substrate (figure 7.23) shows that there is extensive debonding at the substrate/coating interface across the entire section. This may be due to extensive debonding occurring whilst cutting the sample (because of the poor adhesion of the coating). Even grinding far away from the area which was sectioned did not expose a bonded region. In some cases, sectioning the coated polished PEEK sample induced complete coating debonding (figure 7.24). The sectioned LGB and HGB coatings show that the coatings are in good contact with the coating; only very limited areas of the section show crack cracking at the interface (figure 7.25).

Optical and height images of the polished PEEK's fracture face (figure 7.26) show that there are remaining areas of aluminium on the PEEK surface which are up to 5 µm higher than the surrounding substrate; however remaining aluminium areas are not necessarily associated with high points in the height image. In addition, the optical images indicate two distinct regions of colouration on the surface of the substrate. The darker areas of the substrate are associated with higher areas on the height image, whilst the lighter areas are typically lower topographically. Examining the lighter areas in detail, it is clear there is some porosity in these lighter areas.

Similar images of the aluminium fracture face (figure 7.27) show that there are small voids (up to 100 µm in diameter) in the coating (2-5 µm deep), which may be associated

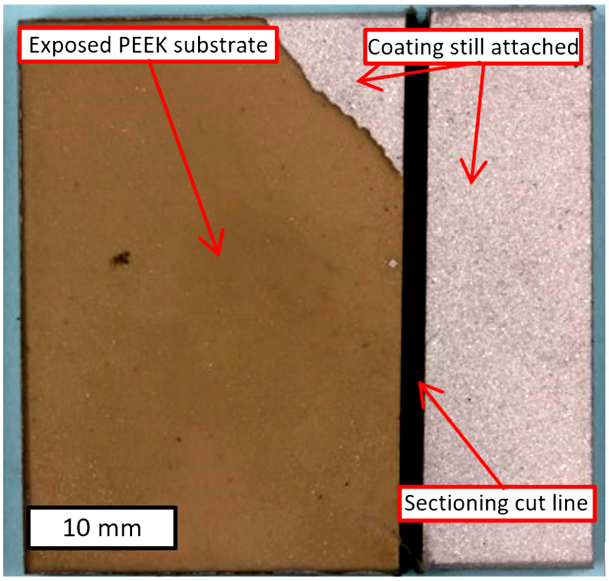


Figure 7.24: Photograph of wire flame spray coating on polished non-reinforced PEEK coatings after debonding due to sectioning.

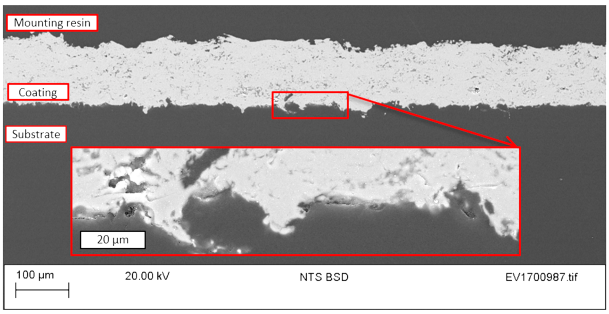


Figure 7.25: BSE SEM image of a cross section of wire flame spray coating on non-reinforced PEEK LGB showing very limited cracking at the interfacial interface.

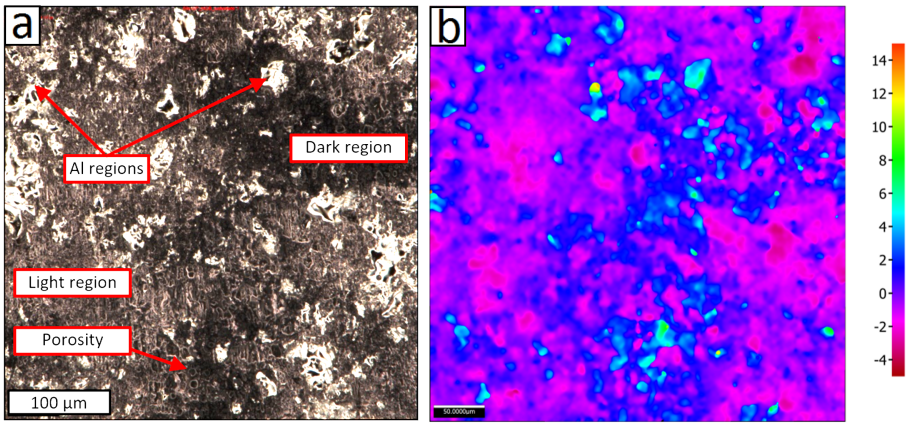


Figure 7.26: (a) Optical and (b) height/FVM images of substrate fracture face of failed ASTM adhesion studs on polished PEEK substrates showing remaining aluminium deposits, light regions and dark regions of substrate.

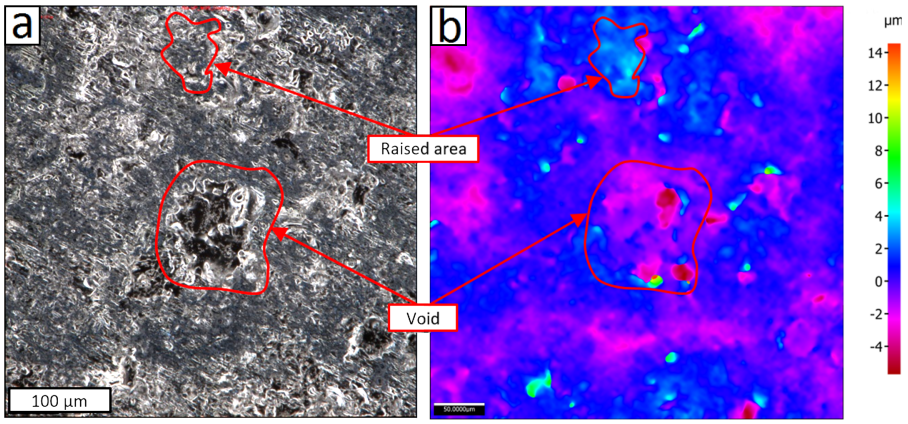


Figure 7.27: (a) Optical and (b) height/FVM images of coating fracture face of failed ASTM adhesion studs on polished PEEK substrates showing voids in coating and high regions which would penetrate the surface of the substrate

with large scale porosity at the coating substrate boundary or where the coating has failed at the splat boundary leaving an individual splat on the surface. There are also raised areas in the coating which may have sunk into the substrate during spraying.

Figure 7.28 shows an SEM image of the substrate fracture face for polished PEEK at a similar scale to the optical and height images in figure 7.26. As with the optical image, the SEM image shows remaining aluminium as well as two distinct regions of the substrate. One of these regions is characterised by surface porosity (this equates to the light region of the optical image) and the other by undamaged substrate (the dark region on the optical image). Examining the damaged region in more detail (figure 7.28 (inset)), it appears that the porous regions have flakes of PEEK on them.

Figure 7.29 shows an SEM image of the underside of the coating for polished PEEK at a similar scale to the optical and height images in Figure 7.30. The SEM image shows many of the same features as the optical/height images i.e. there are splat sized voids visible and smaller scale porosity. In addition, the BSE SEM image also highlights areas of carbon. Interrogating these in greater detail (figure 7.31), it can be seen that these are the same porous structure seen on the substrate. The EDX map shows relatively categorically the carbon rich deposits make up these structures and thus are likely from the PEEK substrate. The structures are shown to be well adhered to the aluminium with Figure 41 showing a crack in the Al coating at the interface of the porous PEEK structure. The porous PEEK structure also contains broken ends where the carbon structure debonded from the PEEK. Almost identical surface morphology was observed on the surface of polished PEEK substrates after the removal of the coating through chemical means (NaOH) as shown in figure 7.34.

The LGB and HGB fracture faces show very similar features to the polished PEEK

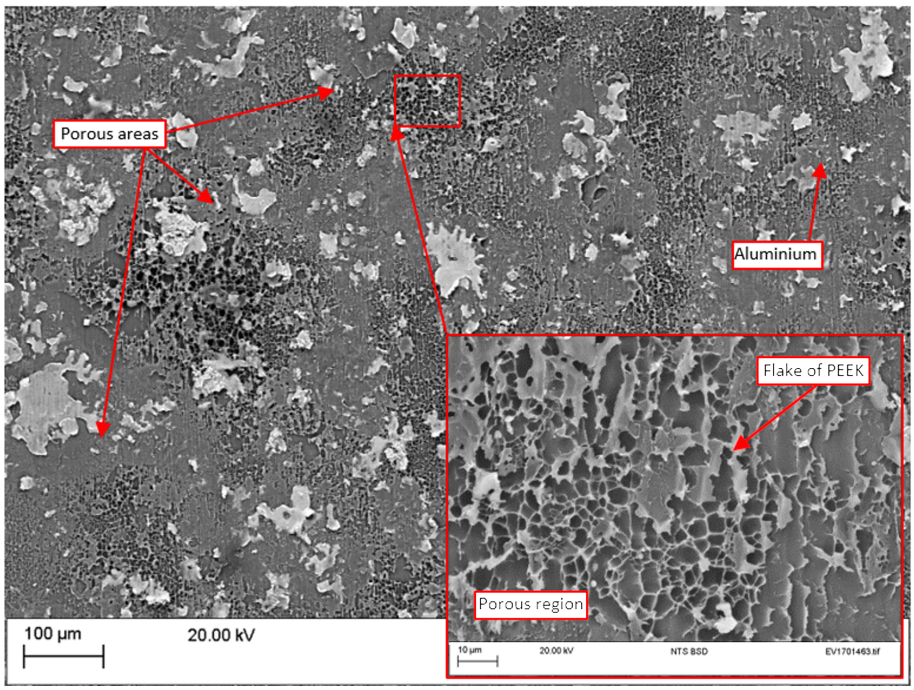


Figure 7.28: BSE image of substrate (fracture face) of polished PEEK substrate after coating removal, showing remaining aluminium, highly porous areas and smooth areas. Detail of porous area (inset) show flake features.

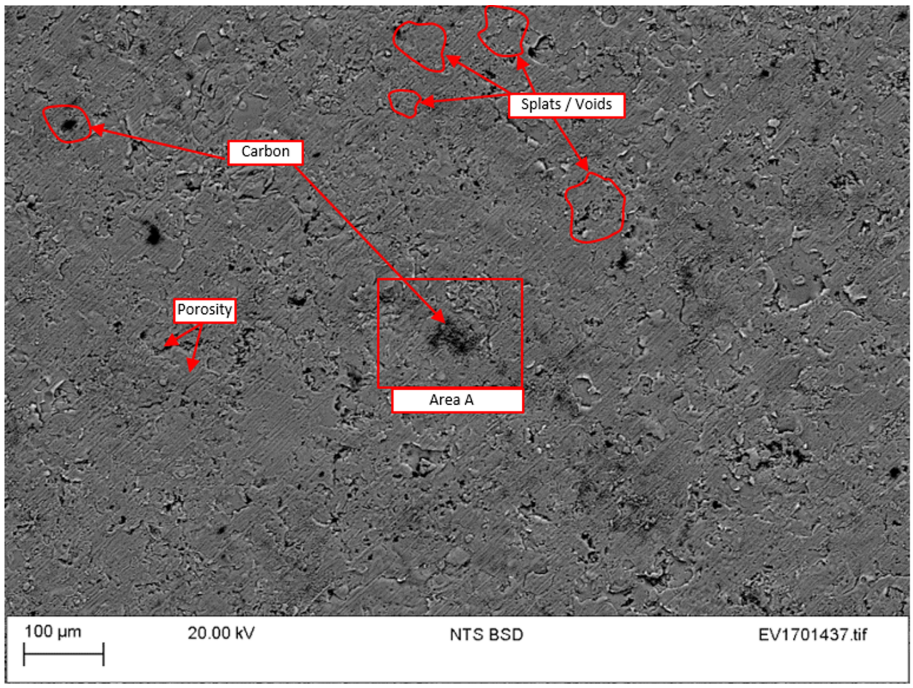


Figure 7.29: BSE image of underside (fracture face) of removed Al coating from polished PEEK substrate. Showing smooth surface with some porosity, voids and carbon areas

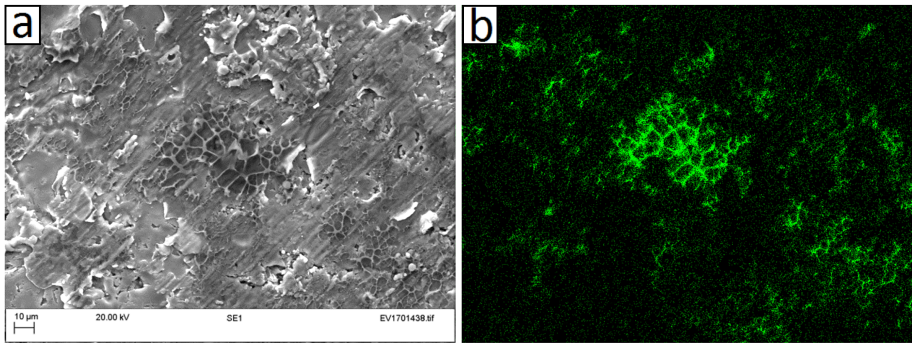


Figure 7.30: Underside (fracture face) of removed Al coating from polished PEEK substrate showing morphology of carbon area (Area A in figure 7.29). (a) SE image and (b) shows carbon EDX map of the same area. The images illustrate the porous nature of the thin carbon deposits on the coating

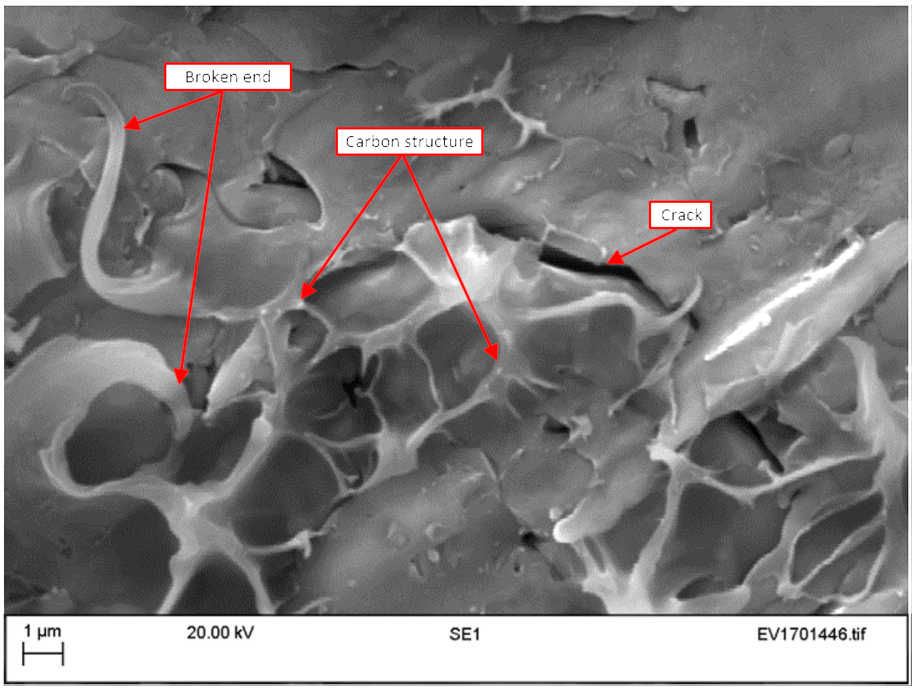


Figure 7.31: SE image of edge of carbon area on underside (fracture face) of removed Al coating from polished PEEK substrate, showing crack in coating at edge of carbon deposit and structure of carbon deposit

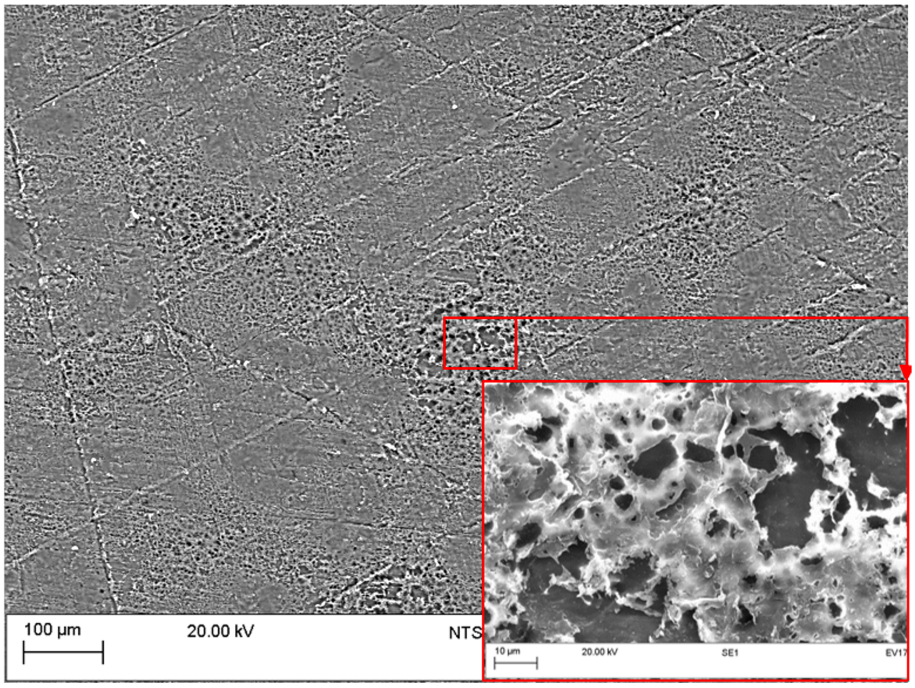


Figure 7.32: BSE/SE image of substrate of polished PEEK substrate after coating removal with NaOH solution showing highly porous and smoother areas.

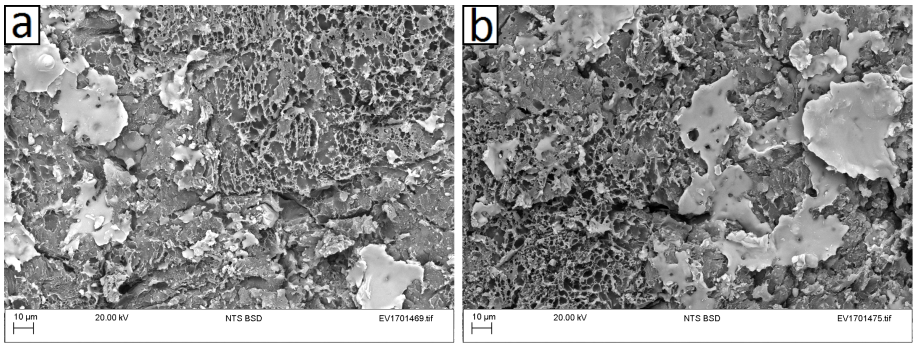


Figure 7.33: BSE image of substrate (fracture face) of PEEK substrate after coating removal for (a) LGB and (b) HGB, showing similar features to polished sample.

substrate (figure 7.33 and figure 7.34). The main differences are that the effects of roughness are superimposed onto the substrate and that with increasing severity of grit-blast, there is more remaining aluminium on the substrate.

PEEK FRP WFS aluminium coatings were also successfully deposited onto the as received, LGB and HGB CF-PEEK substrates. Coating thicknesses and weights were in line with the other samples (figure 7.6) and the bulk of the coatings were similar to those deposited on the other substrates. The as received CF-PEEK coatings had many of the same features as the polished non-reinforced PEEK substrate, including debonding at the interface in the cross section. The fracture face of the coated as received CF-PEEK substrate shows similar features to the polished PEEK samples (figure 7.35 &

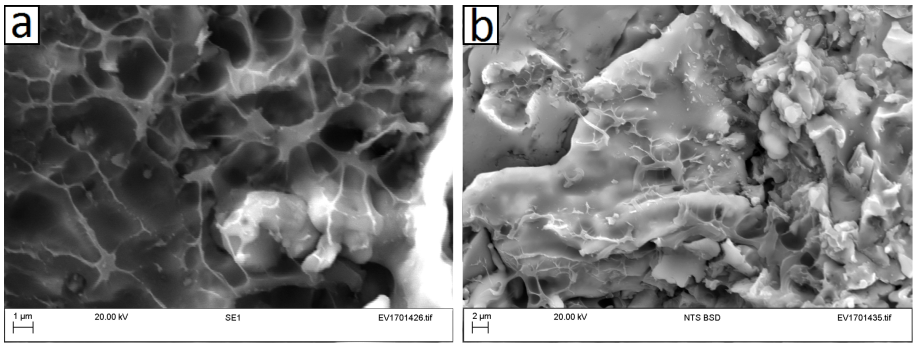


Figure 7.34: BSE image of underside (fracture face) of removed Al coating from PEEK substrate for (a) LGB and (b) HGB, showing similar features to polished sample.

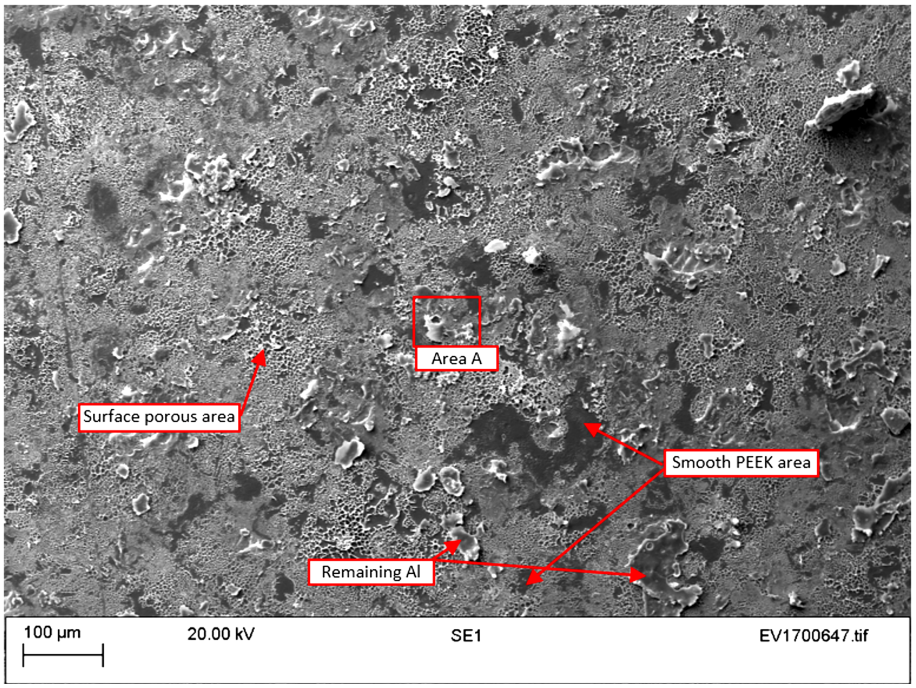


Figure 7.35: SE SEM image of as received CF-PEEK substrate after coating removal showing a porous surface morephology and some remaining aluminium

figure 7.36) i.e. aluminium deposits and porous structures. The porous structures appear more prevalent in the CF-PEEK than the PEEK substrate. In addition, in some areas, the porous areas expose small areas of underlying fibres (figure 7.37).

The porous structures were also more evident when removing the coating though chemical means (NaOH). Tilting this sample in the SEM revealed that the porous structures are around 1 µm high and form cliff edges (figure 7.38). These samples also revealed that there are cracks in the surface associated with fibres close to the surface (figure 7.39).

The associated aluminium coating fracture face is shown in figure 7.40. There are large (50 – 100 µm) thin deposits of carbon on the fracture face as well as several large voids on the surface as highlighted in the figure. At higher magnifications, there is a pore-like morphology on the coating at a similar scale to the porosity on the substrate

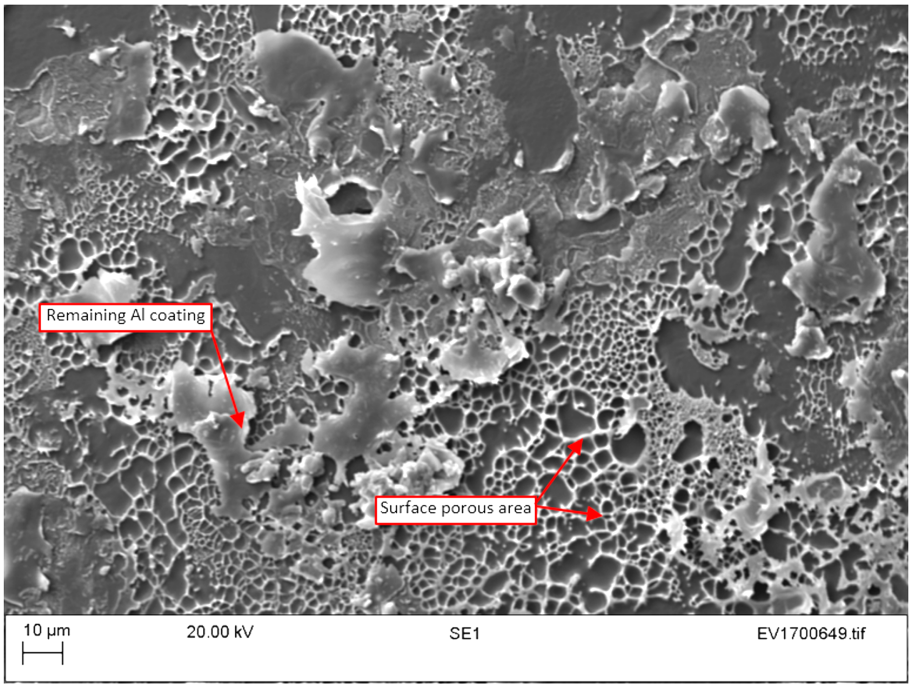


Figure 7.36: SE SEM image of as received CF-PEEK substrate after coating removal (close up of area A in figure 7.35 showing porous surface and remaining aluminium in greater detail

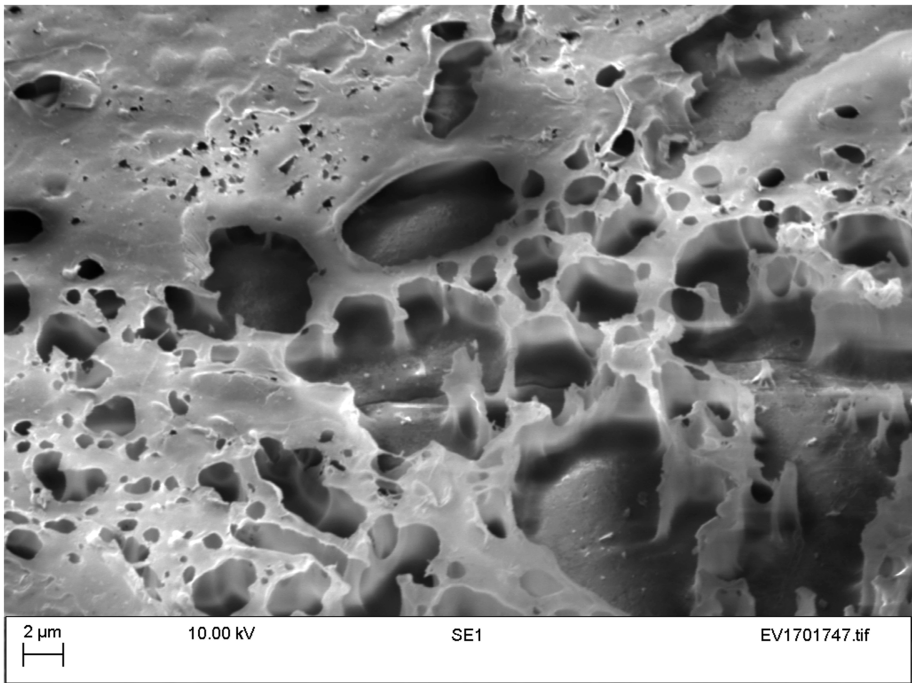


Figure 7.37: SE SEM image of as received CF-PEEK substrate after coating removal showing exposed underlying fibres underneath porous structures in CF-PEEK

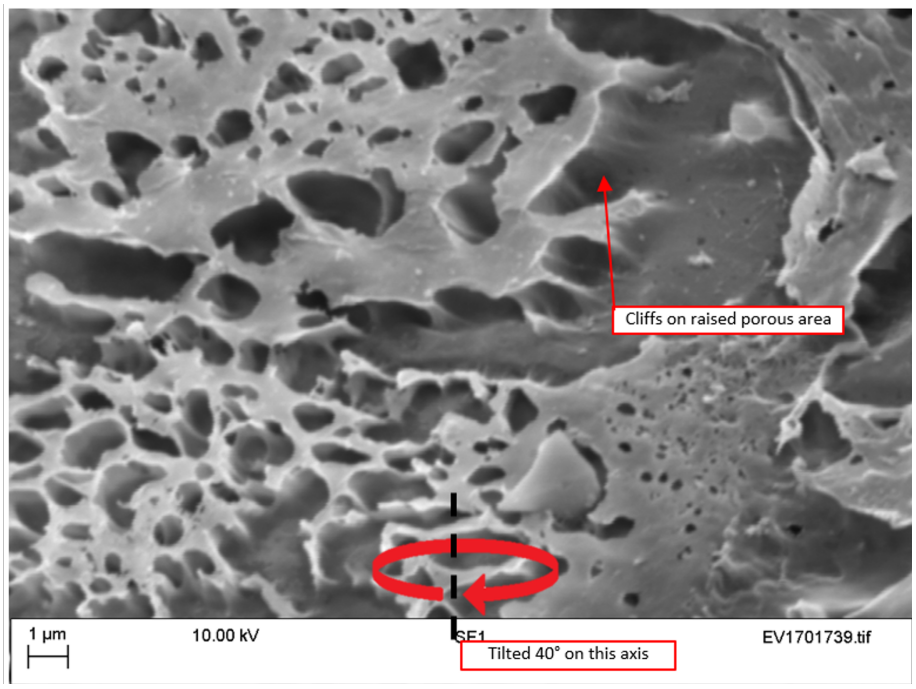


Figure 7.38: SE image of substrate of as received CF- PEEK substrate after coating removal with NaOH solution showing high magnification image of highly porous morphology (angled at 40 degrees in axis shown thus micron marker is indicative only)

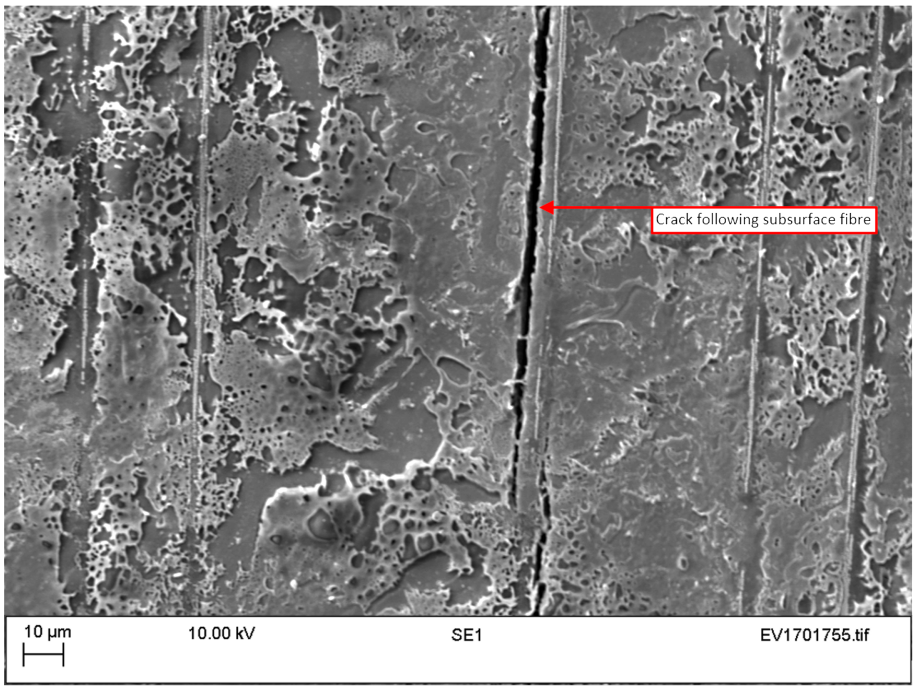


Figure 7.39: SE image of substrate of as received CF- PEEK substrate after coating removal with NaOH solution showing highly porous morphology and crack in surface

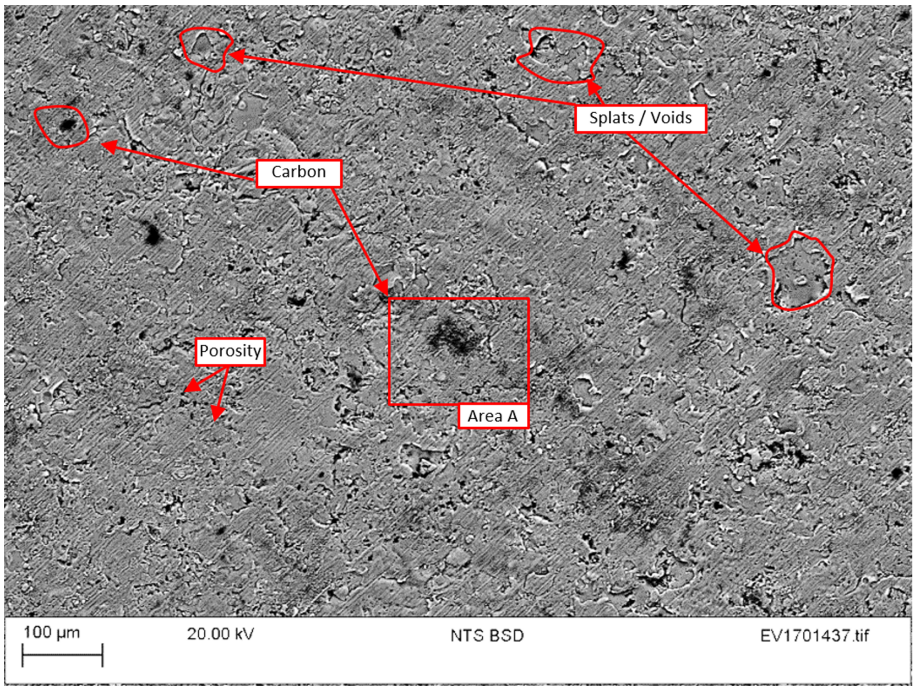


Figure 7.40: BSE SEM image of Al coating removed from as received CF-PEEK substrate showing carbon voids and carbon deposits

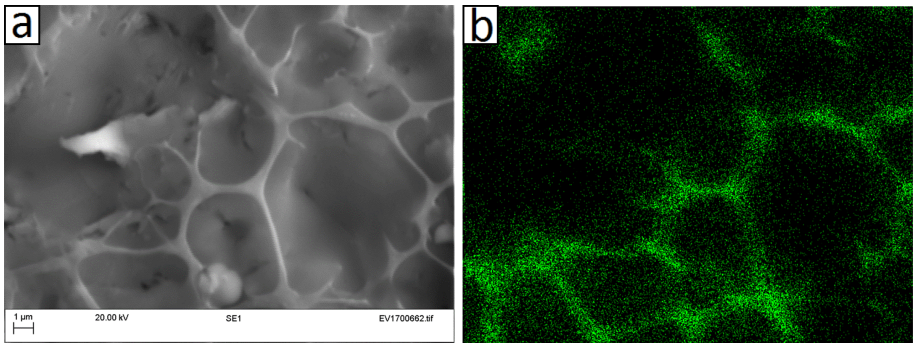


Figure 7.41: Underside of Al coating removed from as received CF-PEEK substrate (a) SE and (b) carbon EDX map images show carbon rich areas around porosity

(figure 7.41a). EDX of the area (figure 7.41b) shows that the prominent edges of the features have carbon deposits on them.

The cross-sections through LGB CF-PEEK show well adhered coatings on the substrate with very little cracking at the interface figure 7.42. There are few fibre exposed areas thus little area where the coating comes directly into contact with the coating. Even within these areas, few cracks are present; figure 7.43 shows an example of the limited cracking in these areas. The HGB CF-PEEK has more areas of exposed carbon fibre where the coating comes into direct contact with the fibres. In these areas, there are cracks present at the interface (figure 7.44), though most of the interface (even in fibre areas) does not contain cracks (e.g. figure 7.45) and there are fewer cracks than in the CF-epoxy samples.

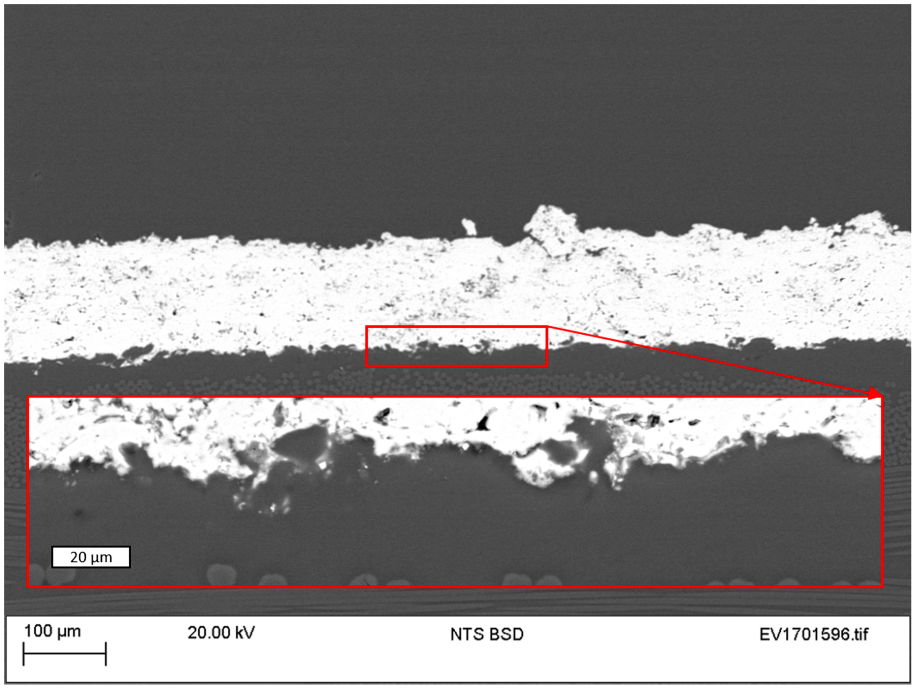


Figure 7.42: BSE SEM image of a cross section of wire flame spray coating on thin resin layer of CF PEEK LGB showing coating with no obvious cracking present

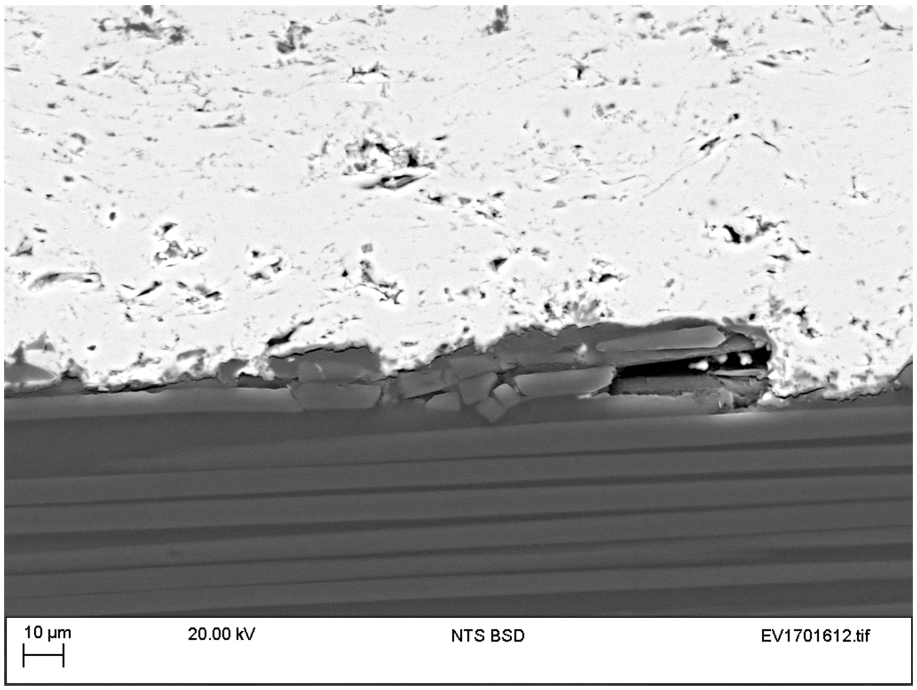


Figure 7.43: BSE SEM image of a cross section of wire flame spray coating on CF PEEK LGB highlighting cracking at the substrate/coating interface on the fibre phase

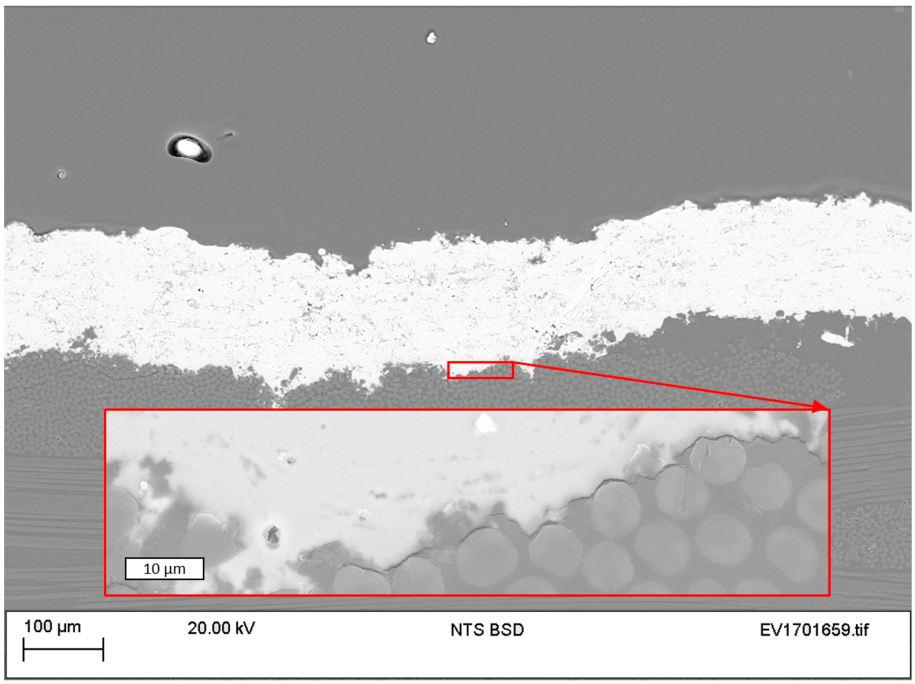


Figure 7.44: BSE SEM image of a cross section of wire flame spray coating on CF PEEK HGB showing interfacial and interphase cracking above fibres

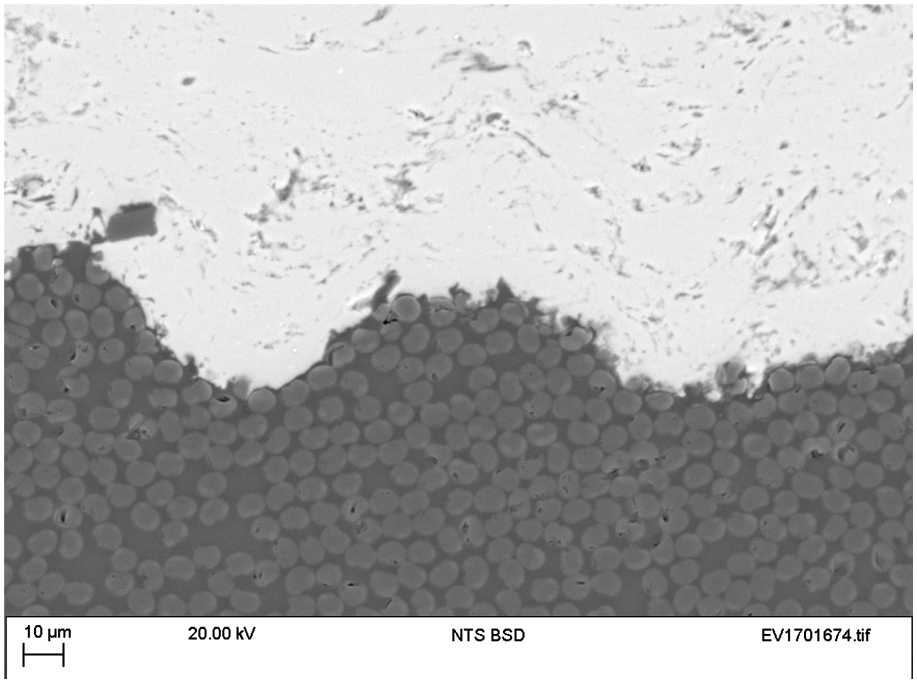


Figure 7.45: BSE SEM image of a cross section of wire flame spray coating on CF PEEK HGB highlighting representative area where there is no cracking on at the interface

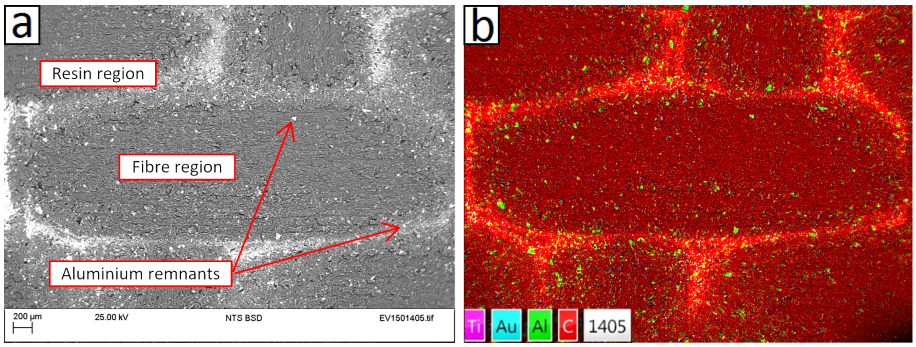


Figure 7.46: SEM images of a LGB CF-PEEK substrate fracture face (a) BSE and (b) EDX map

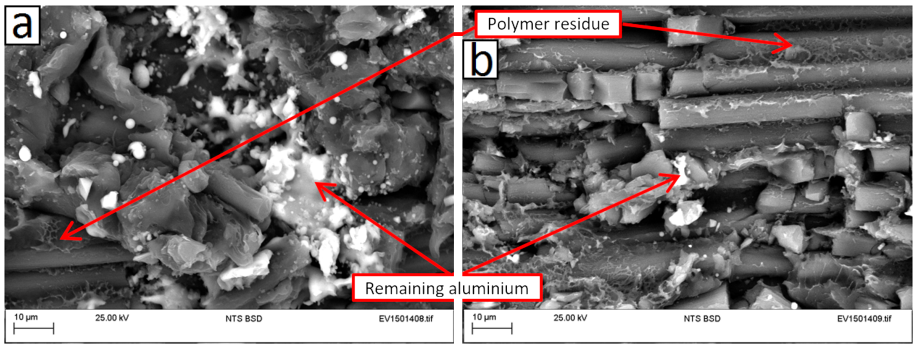


Figure 7.47: BSE SEM close up of remaining aluminium deposits on CF-PEEK in fibre exposed area and polymer film on fibres

BSE SEM images and EDX of grit-blasted PEEK FRP indicate that there are remnants of aluminium on the substrate after TAT testing (figure 7.46). From the images, it is clear that there is a higher concentration of remaining aluminium in resin rich areas. Closer examination of the aluminium deposits in fibre-exposed area indicate that they are typically associated with small areas of resin within that area e.g. Figure 7.47. Examining the fibres in the fibre exposed areas, it is clear that they often contain a polymer film with a similar porous morphology described above or it is present in the surrounding resin.

The fracture face of the aluminium coating shows dark regions, which are representative of carbon rich substances (i.e. carbon fibres or PEEK). The location of the regions mirrors the areas of exposed fibres (figure 7.48). Investigating these regions at higher magnification shows that these dark regions are made of both carbon fibres and resin, which have broken off of the substrate and are embedded in aluminium coating (figure 7.49), although the former is more prevalent. Where the aluminium is visible, it is clear that the coating is mirroring the texture of the underlying substrate, whether that be fibre or resin.

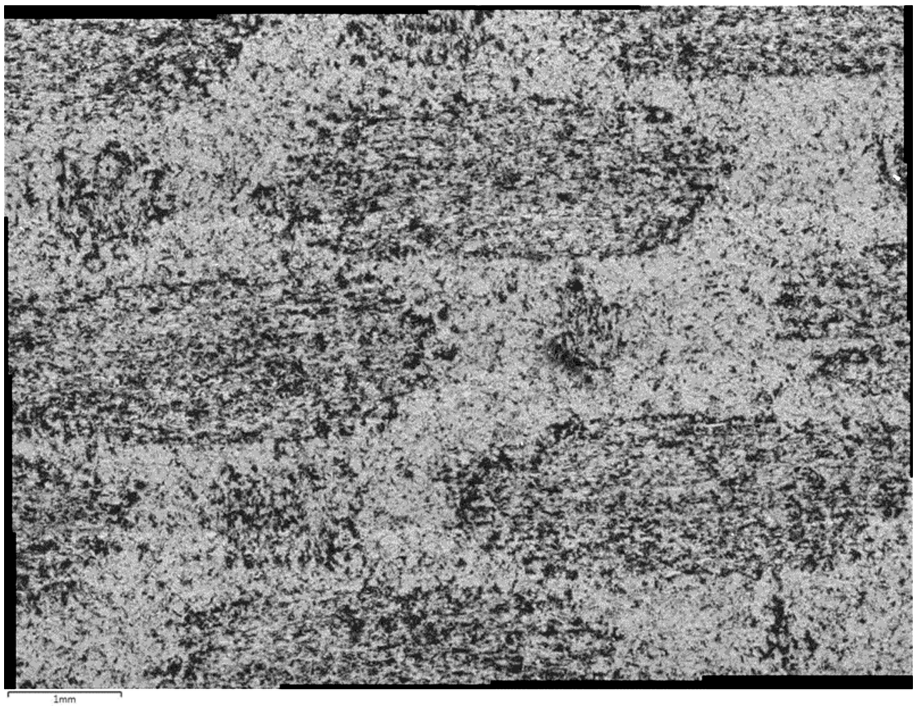


Figure 7.48: BSE SEM of coating fracture face after being removed from LGB CF-PEEK. The dark areas show areas of carbon residue from the substrate surface

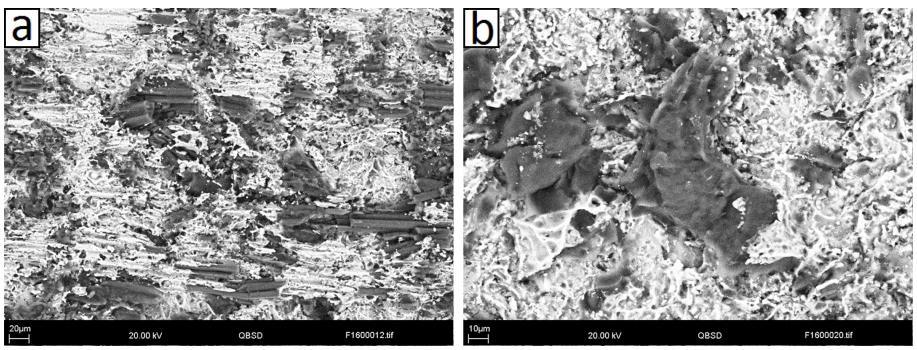


Figure 7.49: BSE SEM image of the underside of WFS Al coating removed from LGB CF-PEEK substrate showing (a) fibre and (b) resin pull off from substrate

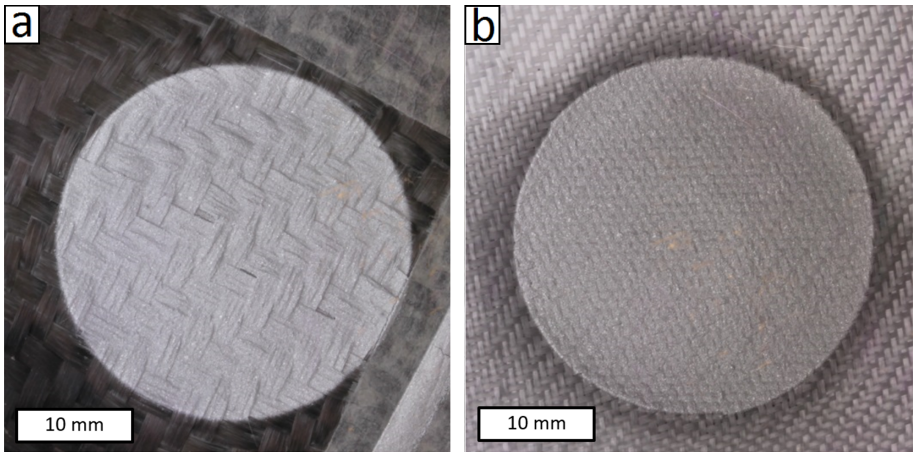


Figure 7.50: Photographs of coated (a) carbon fibre cloth and (b) glass fibre cloth

Reinforcement fibres

Thick (100 µm) WFS aluminium coatings were successfully deposited onto both the GF and CF cloth (figure 7.50). Coatings were deposited on both sides of the cloth substrate to aid adhesion testing. The deposited coatings were 121 and 118 µm thick for GF and CF respectively (the weights were not measured). Sectioning the samples showed that the aluminium has infiltrated into the loose fibres acting as a very effective key (figure 7.51). The glass fibre shows some of the coating material from one side joining up with the coating on the reverse side. This is not evident in the carbon fibre section. In both coatings there is evidence of tearing of aluminium within the coating; this could be a feature of the coating, but more likely due to the fragility of the coating/substrate system leading to damage prior to sectioning. These samples were not tested to ASTM C633; however they were bonded to a steel plate and tested with a single ASTM D4541 test. The obtained adhesion results were 3.53 and 1.28 MPa for the glass and carbon fibre respectively. Images of the tested adhesion samples are shown in figure 7.52. The glass fibre shows a neat fracture face, whereas the CF weave has come apart on the substrate with some fibres attaching to the edge of the stud. Due to practical considerations, only the fracture face on the underside of the stud could be imaged in the SEM. These images and accompanying EDX maps of the fracture faces are shown in figure 7.53 and figure 7.54 for the carbon and glass fibre respectively. They show that the texture of the fracture faces followed the pattern of the weave; however, both were almost entirely composed of the Al coating material with very few fibres present indicating an almost entirely interfacial failure.

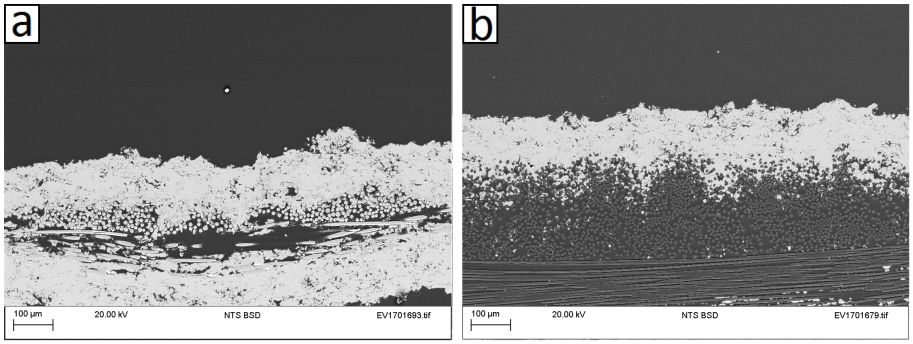


Figure 7.51: BSE SEM image of a cross section of wire flame spray coating on dry (a) glass fibre and (b) carbon fibre cloth (coating deposited on both sides). Images show infilration of aluminium coating into the fibres



Figure 7.52: Photograph glass fibre (Left) and Carbon fibre (right) tested D4541 samples

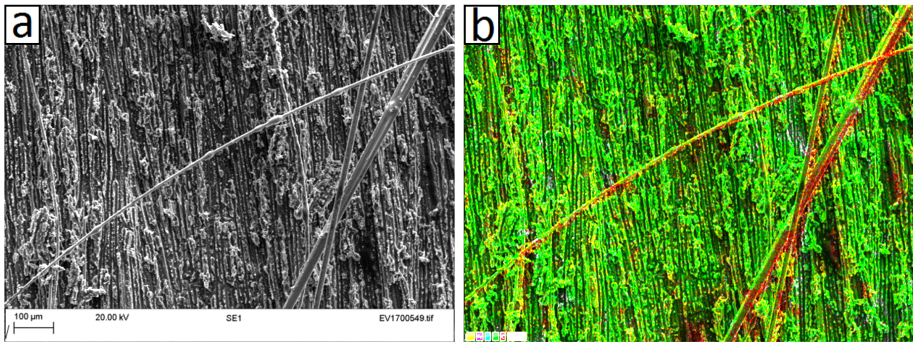


Figure 7.53: (a) SE SEM image and (b) EDX map of fracture face (coating side) of dry carbon fibre adhesion test. Green represents Al and Red C

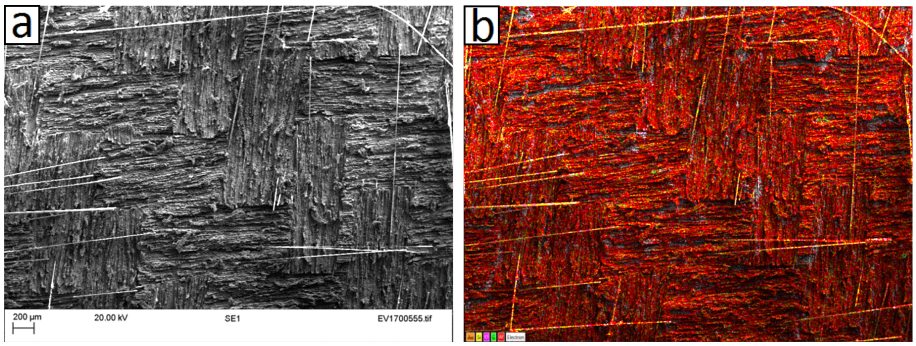


Figure 7.54: (a) SE SEM image and (b) EDX map of fracture face (coating side) of dry glass fibre adhesion test. Red represents Al and yellow Si

7.6 Discussion

7.6.1 Introduction

This chapter investigated the properties of fully developed WFS Al coatings on steel, polymer and FRP substrates. The investigations primarily focused on the tensile adhesion strength of coatings deposited onto differently prepared substrates. This discussion draws insight from how the coatings failed and what influenced their failure in order to understand adhesion mechanisms. As such, it can be seen as encompassing the work up until this point. Due to the summary nature of this discussion, it is useful to reiterate some of the major findings of the previous chapters in order to help build up a model of the overall process.

The wire flame spray process consists of the melting, atomisation and propulsion of the feedstock wire towards the prepared substrate. The individual splats impact, deform and solidify onto the prepared substrate surface and en masse start to form a coherent coating. These processes were investigated in chapters 4 – 6. The investigations outlined in chapter 4 showed that the measured particles were travelling faster than the previous literature would suggest (on average 250 - 300 $m.s^{-1}$). The work also demonstrated that the temperatures of the in-flight particles were < 1000℃, and that during coating, the bulk of the substrate temperature does not increase above 90℃.

Observing the morphology of isolated splats on the substrate, it was clear that they were fully molten upon impact which implies that the particles were >660℃. The morphology of the splats deposited onto polymer surfaces indicated that there was a significant amount of gas evolution causing large bubbles to form underneath the surface of the splat. In many cases these were shown to explode and cause ring type splats. In addition, after removal of the splat there was noticeable change in the surface topography. On the PEEK surfaces this appeared to be due to very local melting of the surface,

whereas on the epoxy substrate this may have been caused by thermal degradation and out-gassing. In this chapter, it was also shown that splats could be deposited on fibre and resin phases, though there was some indication of a preference for the resin phase.

The surface prior to coating was extensively characterised, and it was shown that the PEEK thermoplastic substrates eroded in ductile way with extensive plastic deformation leading to little material loss but high roughness. The epoxy polymers behaved in a hard brittle manner, staying relatively smooth except for cracks which joined together to undermine the surface, causing material loss and furrows to be formed. The different phases of the FRPs were shown to have different responses. The resin was relatively resilient to erosion and the fibres (when exposed) were quickly eroded leading to a very rough texture. This formed a bi-model height distribution and a surface consisting of exposed fibres and resin.

7.6.2 Coating development

As more splats are deposited onto the surface, particles impinge onto previously deposited splats and thick coherent coatings start to be formed. This chapter investigated the properties of these fully developed coatings. The coatings deposited onto the different substrates all had similar microstructures with all of the coatings deposited onto different substrates having similar thickness (after 7 passes) of $\approx$ 120 µm, weights of $\approx$ 308 g.m^{-2} and having limited porosity. This limited porosity is in contrast to [94], in which gas evolved from the substrate led to porosity within the sprayed coating. In the present study there was limited porosity despite there being clear evidence of gas evolution at the surface during spraying which led to large bubbles forming in the individually observed splats.

As the thickness of the coatings increased, the residual stresses within the coating also increased and started to become significant. These stresses were probably responsible for many of the features and properties of the coatings discussed below.

Cracking on epoxy substrates

The only significant difference between the microstructure of the coatings on the different substrates was exhibited in those deposited onto the epoxy polymer substrate. In these coatings, cracking normal to the substrate was observed, as shown in figure 7.9. These were formed due to the greater CTE of the epoxy resin. This meant that as the samples cooled there were significant compressive stresses acting on the coating, leading to this folding and cracking of the coating which relieved the stresses.

Grit-blast severity

Steel and polymers The other significant difference between the coatings deposited on the different substrates was their different adhesion strengths. On all of the monolithic substrates (steel, epoxy and PEEK), increasing the grit-blast severity led to an increase in the adhesion strength of the subsequent coating. This is unsurprising as the increased grit-blast severity led to higher roughness in all different roughness metrics. Although literature is not in agreement as to exactly which roughness parameters are most predictive of adhesion strength, there is broad agreement that generally increasing the roughness of a substrate will lead to greater adhesion.

The increase in adhesion associated with a more severe grit-blast was shown to be relatively large for coatings deposited onto the steel substrate, whereas the increase in adhesion on the polymer substrates was slight and typically within one standard deviation. Comparisons between the epoxy and steel are difficult due to the differences in test procedure as well as the limited number of samples and very different surface morphology of the epoxy substrates. However, comparisons between the PEEK and steel substrates seem more valid as the same test methods were used, more tests were conducted and the grit blasting led to similar surface morphologies on the two substrates. Thus, the difference in the response can be more attributed to differences in material properties.

A possible reason for the only marginal increase in adhesion strength on the more severely grit-blasted PEEK substrate (compared to the LGB PEEK substrate) is that the impacting thermal spray particles modified the surface of the substrate. They modified it to such an extent that the difference in surface morphology between the (LGB and HGB) substrates was not as significant as it was for the steel. This modification is evidenced by the marked change in surface morphology on the polished PEEK substrate after chemical and physical coating removal, as shown in figure 7.32. On the thermoplastic PEEK, this consisted of the addition of approximately 1 µm deep pores in patches across large areas of the surface. These features are probably due to the heat input from the impinging particles, and thus are likely a result of thermal degradation and melting.

It is believed that the majority of the morphology is the result of the surface layer of PEEK melting, and thus wicking/wetting onto the underside of the aluminium coating (due to surface energy considerations). It is also believed that the melted PEEK locally flows in reaction to the local stress fields caused by the coating. These two factors are likely to increase the adhesion strength of the coating as it allows for greater contact between the substrate and coating and for the release of residual stresses. The final

factor modifying the surface of the substrate (i.e. thermal degradation) is likely to char the substrate surface causing gas evolution and a deterioration of mechanical properties for the affected region.

EDX of the underside of PEEK coating showed carbon rich areas which broadly followed the morphology of the porous structures (figure 7.41). This could either evidence thermal damage compromising the local cohesive strength of the polymer at these points, or effective bonding of the PEEK to the coating (due to polymer flow into the coating). Figure 7.31 implies the latter, showing well attached ligaments of polymer (mirroring the porosity), and a fracture in the coating as the ligaments subside. This fracture likely occurred due to the shear stresses developed during testing. As one part of the coating was pulling away from the substrate, the other (well adhered) section resisted causing a shear stress to develop and a crack to initiate.

It is interesting to note that the surface morphological features observed here after coating removal were not evident when impacting a isolated particles onto the substrate. These impacts did lead to surface melting which may have allowed for splats to embed within the substrate. This is indicated by the marks left on the polished PEEK substrates after splat removal from the wipe test samples figure 5.23, though they were too shallow to effectively measure. This implies that the porous surface morphology was formed after a significant coating was already deposited and the surface heated sufficiently.

The surface of the epoxy was also shown to be modified and roughened by the impingement of hot particles (figure 7.11a), although in this case the mechanism was not melting and was likely due to thermal degradation. As stated above, thermal degradation and charring would likely compromise the mechanical properties of the affected region, but in the case of a smooth polymer substrate, it also roughens it enough to allow a coating to develop.

In both cases (PEEK and epoxy), the surface modification induced by the thermal spray particles allowed for coatings (even if poorly adhered) to be deposited onto the polished polymer substrates. Those deposited onto the polished PEEK substrate appeared to have better adhesion than those deposited onto the polished epoxy. The different test methods make direct comparison between adhesion results difficult. However, the as received CF-PEEK was also shown to have higher adhesion than the as received CF-epoxy. In fact, the CF-PEEK substrate had very good adhesion for an unprepared substrate (13.3 MPa), whereas the CF-epoxy substrate did not manage to develop a coherent coating which could be tested with an ASTM C633 adhesion test. The as received CF substrates were both fully covered with smooth resin and thus presented a similar surface

to the thermal spray particles as the polished polymers, backing up the general point that the PEEK thermoplastic polymers allow for greater adhesion.

FRPs Although the polished polymers and as received FRPs presented a similar surface for thermal spray, upon grit-blasting the surfaces significantly diverged. The FRPs became significantly rougher and fibre phases were present on the surface. The significant increase in roughness is the likely cause for the higher adhesion of coatings on FRPs when compared to their respective polymer substrates. Despite the fact that some fibres were imbedded within the pulled-off coating it is believed that having exposed fibres was detrimental to coating adhesion. This is one probable reason that the coating adhesion decreased with increased grit-blast severity (from LGB to HGB) for the FRP substrates as it exposed more fibres. The other likely reason is the increase in damage caused to the substrate by the heavier grit-blast.

The evidence for exposed carbon fibres being detrimental to adhesion strength is twofold. Firstly, the fracture face of the dry CF-cloth adhesion test showed that the failure was completely interfacial (as shown in figure 7.53); this was unexpected as it was believed that the relatively loose fibre weave would come apart leaving fibres on both fracture faces. This did not occur which indicates poor interfacial adhesion despite the aluminium coating wrapping around the fibres (a bonding mechanism which is not available when the fibre is encased in polymer resin). Secondly, imaged cross sections of the coated CF substrates showed that where fibres were in direct contact with the coating, there was a high propensity for interfacial cracks as demonstrated in figure 7.12. This indicates that having a rough, polymer only surface promotes adhesion. These findings are in contrast to Wang et al. [92] which suggested that broken fibres in the pulled off coating indicated that they were positive for adhesion. However, it is important to state that in [92], spray deposition was achieved with a TWAS system. It was shown in Appendix C that TWAS coating build-up occurred almost exclusively on fibre exposed areas. This indicates that for these hotter particles, exposed fibres are positive for coating build-up and presumably adhesion. The reason for this is probably that when spraying hotter particles, significant thermal degradation and destruction of thermally sensitive polymers can occur. This thermal degridation is also the likely reason for the removal of polymer phase and splats only developing on the fibre phase when spraying Cr onto CFRP in [52]. Despite any benefit that may occur from spraying onto a polymer phase, if the polymer cannot handle the heat input, the more heat tolerent carbon phase is preferable for adhesion. This implies that using a lower temperature process (such as

WFS Al) and having a roughened polymer surface should allow for the greatest adhesion. This is perhaps why the adhesions obtained in this study are in line with some of the highest reported in the literature.

The reasons for the interfacial cracking occurring over the fibre region may well be in part due to the poor surface which the fibres present for adhesion. Although having fibres within the polymer increases the gross roughness of the substrate, on a local level (at a fibre scale) the fibres are not typically roughened by the grit-blasting (figure 6.22). Instead erosion damage (from grit-blasting) typically leaves the fibres relatively smooth with cracks present, which is not necessarily an appropriate surface for keying. This is in contrast to the polymers, especially the PEEK, which are heavily deformed leaving a favourable surface for adhesion (figure 6.13). The interfacial cracking may also be associated with the complex stress field at the interface caused in part be due to the differences is CTE and stiffness between the carbon and polymer phases. Carbon fibres have low/negative CTEs (3.8 - 11.5 $\mu.K^{-1}$ across the fibre and -0.4 - -1.4 $\mu.K^{-1}$ along the fibre [184]), PEEK has a CTE of 50 - 85 $\mu.K^{-1}$ [120] [74, p. 789] and epoxies generally have a CTE of 80 - 120 $\mu.K^{-1}$ [74, p. 789]. These CTE values should be seen as indicative especially seeing as CTEs vary with temperature and the structure of a thermal spray coating means that its CTE will be different from that of the feedstock material. This being said, the values indicate that CTE mismatch will induce tensile stresses in the coating over fibre regions and compressive stresses over polymer regions as represented in figure 7.55. More locally, other stress fields could be present i.e. compressive fields associated with resin in fibre regions. This non-uniform stress field is further complicated because of the much lower stiffness of the polymer phase ($\approx$2 GPa [74, p. 778]) compared to the carbon fibre (230 - 290 GPa [74, p. 778]) or aluminium ($\approx$70 GPa [74, p. 778]) coating. The lower stiffness of the polymer phase may lead to lower residual stresses in the coating over the polymer regions. This is because the missfit may cause the low stiffness polymer to deform, relieving stresses in the coating. In addition, the low stiffness of the polymer would lead to low amounts of stored energy associated with its strain. However, such a complicated stress field would require involved testing and an FEA approach to properly resolve it, which was not attempted in this work. The build up of complicated stress and strain fields may lead to local shearing forces at the substrate/coating interface. These could lead to the interfacial cracking at an area of poor adhesion, likely the fibre phase, especially if that area has high local residual stresses acting against adhesion.

The presence of fibres close to the interface led to interphase cracking between the stiff fibres and more compliant ductile polymers slightly below the surface, as shown in

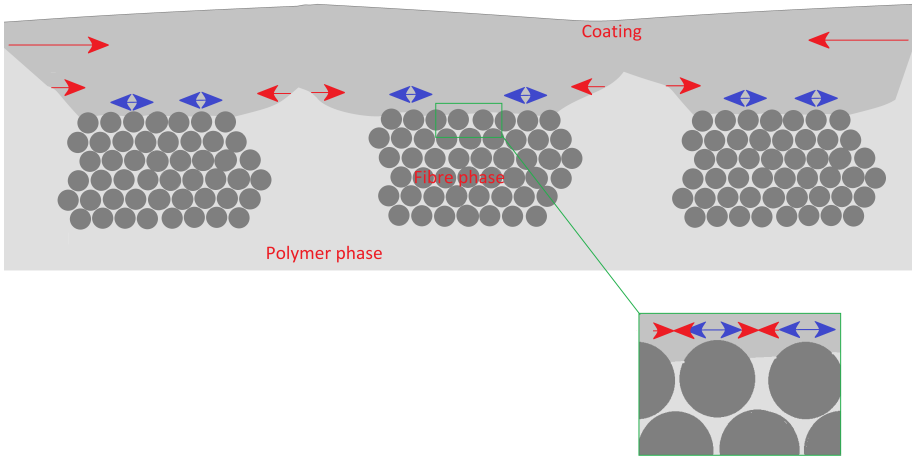


Figure 7.55: Schematic representation of simplified stress field within coating showing in compressive stresses (in red) over polymer phase and tensile stresses over fibres (in blue), local compressive stresses are shown in the fibre region associated with polymer (green box)

figure 7.44; it was likely this which led to the cracking on the CF-PEEK surface shown in figure 7.39. This is probably due to stresses transferred from the coating causing a shear stress across the fibre-polymer interface. This indicates that a high strength fibre-polymer interface can be important for good coating adhesion.

Another result of interest is that the difference in adhesion between the PEEK and CF-PEEK substrate was less stark than that between epoxy and CF-epoxy substrates, although the differences in roughness were of a similar magnitude. Possible reasons for this are that the PEEK substrate presented a similar topography to the steel substrate which was likely positive for adhesion and in fact coatings deposited onto the PEEK based substrates had comparable adhesion to the steel substrates. Also, the fact that the particles could impinge into the substrate, modify the topography and flow to relieve residual stresses meant that the lower roughness was less of a barrier to coating adhesion.

7.6.3 Coating development model

The experiments above help build a qualitative model of wire flame spray onto polymer/FRP substrates, which can likely be extrapolated to other thermal spray processes. Initial splats are deposited onto the substrate, and upon impact gases are evolved on the surface. These may be the result of volatile products of thermal degradation, or from absorbents and condensates on the surface. In either case, on a smooth substrate these can cause large bubbles which may reduce the effective bonding area of the coating. The temperature of the splats in WFS is great enough to damage/roughen the substrate and

(it the case of thermoplastic substrates) and locally melt it leading to shallow embedment. After the splat solidifies and is effectively in place, it cools which leads to residual quenching stress. When the polymer is a thermoplastic, the top layer of the substrate flows and can wick up and wet more of the underside of the coating and flow to relieve residual stresses in the system.

The splats either deposit onto the substrate or impact and rebound off of it. Impacting particles cause damage to the surface, causing topographical asperities to form. These act as keying sights for coatings to start to form. Once the coating is deposited onto the substrate and the coated substrate starts to cool, the different CTEs of the coating and the substrate will lead to a system of residual stresses. This complex stress field is not characterised here but the stresses may cause interfacial cracking over fibre regions. This localised cracking shows that for low temperature particles (e.g. WFS Al), it is preferable for a predominantly polymer surface. For a higher temperature process, exposed carbon fibres are preferable as they are more heat tolerant than the polymers phase. However, the higher temperature splats and coatings are likely subject to greater residual stress levels as the higher temperature necessarily leads to greater quenching and CTE mismatch stresses, lower temperature processes and feedstock materials are preferable from a residual stress perspective.

7.7 Conclusions

- At a macro scale the coatings failed at the interface between the coating and the substrate, and thus the tensile adhesion strength results were indicative of the interfacial adhesion strength of the coatings.

- Well adhered coatings with similar microstructures were deposited onto prepared steel, CF-epoxy, PEEK and CF-PEEK substrates with tensile adhesion test results ranging from 7.6 MPa for HGB CF-epoxy to 17.5 MPa for LGB CF-PEEK. Coatings deposited onto epoxy polymer (not CF-epoxy) substrates had extensive through coating cracks. This cracking was likely caused by low interfacial adhesion and CTE differences between the epoxy substrate and the WFS Al coating.

- The adhesion strengths of WFS coatings deposited onto PEEK (thermoplastic) based substrates were shown to be generally greater than those deposited onto epoxy (thermosetting) based substrates and steel. Adhesion strengths of up to 13.3 MPa could be achieved even on unprepared (smooth) CF-PEEK substrates; however, very low coating adhesion ($\approx$1 MPa) was achieved on unprepared (smooth)

CF-epoxy substrates. This high adhesion is in contrast to previous work which states coatings would not develop on unprepared (smooth) substrates.

- WFS was shown to modify the surface of the polymers, causing roughening on the epoxy substrate and unusual porous morphologies on the PEEK surface.
- It is believed that the unusual surface morphologies and the high adhesion exhibited by the PEEK based substrates is because of the thermoplastic nature of the PEEK. This allowed for limited substrate melting and flow. It is believed that this flow increased the bonding area and allowed for stress relief which caused the unusual surface morphology.
- Interfacial cracks were observed in CFRP coating cross sections where the deposited coating had come into direct contact with the fibre-phase. It is proposed that this is due to the locally smooth surface of the fibres being less conducive to local adhesion than the locally rougher polymer phase.
- Adhesion of coatings onto the roughened CFRP substrates was greater than onto the identically treated polymer substrate. It is believed that this is because the prepared CFRPs were significantly rougher than the polymers, and despite the exposed fibres which are likely to be detrimental to adhesion.

Chapter 8

Conclusions

This study investigated the wire flame spraying of pure aluminium onto polymer and carbon fibre reinforced polymer (CFRP) substrates. Two different types of polymer matrix were investigated, namely epoxy and PEEK. A systematic study was undertaken of the following topics: (i) the characteristics of wire break-up and plume properties in the wire flame spraying; (ii) the deposition of individual splats onto polymer and CFRP substrates prepared in different ways; (iii) the effect of a common surface preparation process (grit blasting) on polymer/CFRP surface features such as roughness; (iv) the structure and adhesion strength thick, multi-pass flame sprayed coatings on polymer and CFRP substrates following different grit blasting surface treatments. The following conclusions can be made in relation to the different topic areas.

8.1 Wire flame spray plume

- The study imaged the wire breakup of WFS aluminium. The breakup was shown to be very similar to anode breakup in TWAS, namely that a thin extruded sheet of molten aluminium was broken up in a Rayleigh non-axisymmetric manner. The way in which this broke up was shown to be insensitive to +/- 20% changes in atomising gas flow.

- Detected particles in the spray plume were shown to follow a log-normal distribution and have a mean particle size of ≈25 µm.

- The particle diagnostic system could not detect particles smaller than 50 µm. This meant that only the largest particles could be detected, accounting for ≈30% of particles in the spray plume by volume. It is important to be aware of this limitation when analysing the results.

- The velocities of (measurable) particles in the plume were shown to be greater than is generally reported for this process at ≈250 - 300 m.s^{-1}. The particle velocities were also shown to be relatively insensitive to +/- 20% changes in atomising gas flow and changes in stand-off distances.

- The small amount of infra red emission from the in-flight particles meant that without external lighting, they could not by detected by the particle diagnostic system. This indicated that their temperature is less than 1000℃.

- The temperature of the substrate was measured during spraying, and it was shown that the temperature of the substrate 1 mm from the surface does not exceed 90℃ during a 10 surface layer coating.

8.2 Interaction of individual splats with the substrate

- The morphologies of the splats indicated that they were liquid on impact which indicates that they were >660℃. As such, it can be concluded that they were between 660 - 1000℃ on impact.

- The splats deposited onto smooth polymer/CFRP substrates had large bubbles in their centre; these had often apparently exploded leaving a ring morphology of deposited material. This indicated that there was probably significant gas evolution at the particle-substrate surface upon impact. Deposited particles on epoxy based substrates were more likely to form exploded ring splats than those on PEEK substrates, indicating a greater tendency for gas evolution from the epoxy.

- Individual particles impinging on the substrates modified its surface and in the case of the PEEK thermoplastic, they somewhat sunk into the substrate. En masse, the heat from particles significantly changes the temperature, and thus properties of the surface of the substrate, facilitating coating deposition even onto polished substrates. However, the surface layer affected by the heat was very thin and the bulk of the substrate (≥ 1 mm from the surface) did not experience temperatures greater than 90℃.

- WFS Al splats adhered to both the polymer and the fibre-rich areas of the CFRP substrate surfaces. This appears to be in contrast to TWAS coatings, where coatings appear to only adhere to the fibre phase.

8.3 Effect of grit blasting on substrate surfaces

- The two different polymers behaved very differently under the action of grit blasting which causes material removal by erosion. The thermoplastic PEEK behaved in ductile manner, with significant plastic deformation, whereas the epoxy behaved in a brittle manner, remaining relatively smooth with material losses due to crack propagation.
- The different phases of the CFRP substrate behaved differently under grit-blast (particle erosion) conditions. The fibre phases were very brittle, and thus they were fractured and quickly removed. Damaged fibres were typically held in place by the remaining polymer phase. Despite the removal, the local morphology of the remaining fibres was relatively smooth. The polymer phase was more resilient to the grit-blasting, and was not eroded away as quickly but, it was more significantly roughened than the fibre phase. The differential erosion led to a bi-modal height distribution which led to a very rough surface on the macroscopic scale.

8.4 The adhesion strength and structure of multi-pass thick coatings

- At a macro scale the coatings failed at the interface between the coating and the substrate, thus the tensile adhesion strength results were indicative of the interfacial adhesion strength of the coatings.
- Well adhered coatings with similar microstructures were deposited onto prepared steel, CF-epoxy, PEEK and CF-PEEK substrates with tensile adhesion test results ranging from 7.6 MPa for HGB CF-epoxy to 17.5 MPa for LGB CF-PEEK. Coatings deposited onto epoxy polymer (not CF-epoxy) substrates had extensive through coating cracks. This cracking was likely caused by low interfacial adhesion and CTE differences between the epoxy substrate and the WFS Al coating.
- The adhesion strengths of WFS coatings deposited onto PEEK (thermoplastic) based substrates were shown to be generally greater than those deposited onto epoxy (thermosetting) based substrates and steel. Adhesion strengths of up to 13.3 MPa could be achieved even on unprepared (smooth) CF-PEEK substrates; however, very low coating adhesion ($\approx$1 MPa) was achieved on unprepared (smooth) CF-epoxy substrates. This high adhesion is in contrast to previous work which states coatings would not develop on unprepared (smooth) substrates.

- WFS was shown to modify the surface of the polymers, causing roughening on the epoxy substrate and unusual porous morphologies on the PEEK surface.
- It is believed that the unusual surface morphologies and the high adhesion exhibited by the PEEK based substrates is because of the thermoplastic nature of the PEEK. This allowed for limited substrate melting and flow. It is believed that this flow increased the bonding area and allowed for stress relief which caused the unusual surface morphology.
- Interfacial cracks were observed in CFRP coating cross sections where the deposited coating had come into direct contact with the fibre-phase. It is proposed that this is due to the locally smooth surface of the fibres being less conducive to local adhesion than the locally rougher polymer phase.
- Adhesion of coatings onto the roughened CFRP substrates was greater than onto the identically treated polymer substrate. It is believed that this is because the prepared CFRPs were significantly rougher than the polymers, and despite the exposed fibres which are likely to be detrimental to adhesion.

Chapter 9

Further work

- The PIV system used to capture inflight particle properties required the particles to be relatively large in order to be detected. It was shown by other means that the majority of the particles in the plume were smaller than this. Re-running some of this work with a higher resolution PIV system could allow smaller particles to be detected and greater confidence that the smaller particles have similar locations/velocities to the larger ones which were detected in this study.

- This study focused on wire flame spraying of aluminium onto different substrates. General points were extracted from this study; however, in order to reinforce the generality of the points it would be useful to spray with different melting temperature feedstocks. Higher melting temperature feedstocks which can by sprayed using WFS might include Cu and NiCr. In order to spray higher melting temperature materials than these, a different thermal spray process would need to be employed (such as plasma spray). Similarly spraying onto polymer based substrates with different melting and glass transition temperatures would be useful, as it would help determine if these are important factors.

- In order to be more confident about the exact particle dynamics upon particle impact, high speed video of the impact could be taken. This may show bubbles forming and bursting. The setup required would be rather involved, and a useful result may not be obtained. However, if successful it would give direct insight into the splat dynamics.

- Images of the substrate after coating removal showed that there was damage to the surface. Chemical characterisation of this was not possible within this investigation. However, surface sensitive chemical analysis (such as X-ray photoelec-

tron spectroscopy) may reveal more about the extent and type of surface damage present.

- As mentioned in chapter 7, complex residual stress fields were likely formed within the coating due to CTE differences. This was not fully examined within the scope of this study. A FEA approach to modelling this could help better understand how the residual stressed play a role in coating debonding.

Bibliography

[1] F. Smith, "The use of composites in aerospace: Past, present and future challenges." [Online]. Available: http://aerosociety.com/Assets/Docs/Events/693/Presentations/(7)\%20Dr\%20Faye\%20Smith.pdf

[2] L. S. Norwood, Fibre reinforced polymers. Woodhead publishing limited, 1994, p. 6–69.

[3] A. Liu, M. Guo, M. Zhao, H. Ma, and S. Hu, "Arc sprayed erosion-resistant coating for carbon fiber reinforced polymer matrix composite substrates," Surface and Coatings Technology, vol. 200, no. 9, pp. 3073 – 3077, 2006. [Online]. Available: http://www.sciencedirect.com/science/article/pii/S0257897205000952

[4] J. K. Sutter, K. Miyoshi, C. Bowman, S. K. Naik, K. Ma, R. Sinatra, R. Cupp, R. Horan, and G. Leissler, "Erosion coatings for polymer matrix composites in propulsion applications," High Performance Polymers, vol. 15, no. 4, pp. 421–440, 2003. [Online]. Available: https://doi.org/10.1177/09540083030154003

[5] R. A. Miller, "Thermal barrier coatings for aircraft engines: history and directions," Journal of Thermal Spray Technology, vol. 6, no. 1, p. 35, Mar 1997. [Online]. Available: https://doi.org/10.1007/BF02646310

[6] N. Huonnic, M. Abdelghani, P. Mertiny, and A. McDonald, "Deposition and characterization of flame-sprayed aluminum on cured glass and basalt fiber-reinforced epoxy tubes," Surface and Coatings Technology, vol. 205, no. 3, pp. 867 – 873, 2010. [Online]. Available: http://www.sciencedirect.com/science/article/pii/S025789721000678X

[7] G. England, "Thermal spray coatings on carbon and glass reinforced polymers." [Online]. Available: http://www.gordonengland.co.uk/frpapp.htm

[8] J. Affi, H. Okazaki, M. Yamada, and M. Fukumoto, "Fabrication of aluminum coating onto cfrp substrate by cold spray," MATERIALS TRANSACTIONS, vol. 52, no. 9, pp. 1759–1763, 2011.

[9] B. Rooks, "Robot spraying of helicopter rotor blade ice protection system," Industrial Robot: An International Journal, vol. 28, no. 4, pp. 313–317, 2001. [Online]. Available: http://www.ingentaconnect.com/content/mcb/049/2001/00000028/00000004/art00006

[10] L. Pawlowski, The science and engineering of thermal spray coatings. Chichester, UK: John Wiley and Sons Ltd, 1995.

[11] Œlikon metco, "œlikon metco." [Online]. Available: http://www.oerlikon.com/ecomaXL/files/metco_Thermal_Spray_V4.pdf

[12] Thermal spray technologies, "Flame spray," 2014. [Online]. Available: http://www.tstcoatings.com/flame_spray

[13] S. Zhang and D. Zhao, Aerospace Materials Handbook (Advances in Materials Science and Engineering). CRC Press, 2016.

[14] M. Planche, H. Liao, B. Normand, and C. Coddet, "Relationships between nicrbsi particle characteristics and corresponding coating properties using different thermal spraying processes," Surface and Coatings Technology, vol. 200, no. 7, pp. 2465 – 2473, 2005. [Online]. Available: http://www.sciencedirect.com/science/article/pii/S0257897204008722

[15] D. Crawmer, "Thermal spray processes," in ASM Handbook Volume 5A: Thermal Spray Technology, 10th ed., R. C. Tucker, Ed. Materials Park, Ohio: ASM International, 2013, ch. 2, pp. 33 – 35.

[16] D. J. Varacelle, D. P. Zeek, V. Zanchuck, E. Sampson, K. W. Couch, D. Benson, and G. S. Cox, "Experimental studies of twin-wire electric arc sprayed zinc/aluminum alloy coatings," Journal of Thermal Spray Technology, vol. 7, no. 4, pp. 513–520, Dec 1998. [Online]. Available: https://doi.org/10.1361/105996398770350738

[17] Metallisation, "The process." [Online]. Available: http://www.metallisation.com/process/

[18] A. Scrivani, U. Bardi, L. Carrafiello, A. Lavacchi, F. Niccolai, and G. Rizzi, "A comparative study of high velocity oxygen fuel, vacuum plasma spray, and axial

plasma spray for the deposition of conicraly bond coat alloy," Journal of Thermal Spray Technology, vol. 12, no. 4, pp. 504–507, Dec 2003. [Online]. Available: https://doi.org/10.1361/105996303772082242

[19] G. England, "Hvof." [Online]. Available: http://www.gordonengland.co.uk/HVOF.htm

[20] I. J. Munns and S. A. Shaw, "An evaluation of ndt methods for adhesion testing of thermally sprayed coatings," TWI Ltd, Abington, Cambridge, Tech. Rep., 2002.

[21] F. J. Blunt, "A review of techniques for measuring and ranking adhesion of hvof sprayed coatings," TWI Ltd, Abington, Cambridge, Tech. Rep., 1996.

[22] TWI, "Hvof wire spraying system extends twi facilities." [Online]. Available: http://www.twi-global.com/news-events/connect/2001/january-february-2001/hvof-wire-spraying-system-extends-twi-facilities/

[23] F. P. L. H. J. V. and B. M. I., Thermal spray fundamentals: from powder to part. Springer science and business media, 2014.

[24] R. K. A. and C. T. W., "A simple procedure for the characterization of spray deposition process - the linescan test," Surface and coatings technology, vol. 41, pp. 103–115, 1990.

[25] F. M., K. S., and O. I., "Splat behavior of plasma sprayed particles on flat substrate surfaces," Thermal spraying - Current status and future trends, vol. 41, pp. 103–115, 1995.

[26] S. Chandra and P. Fauchais, "Formation of solid splats during thermal spray deposition," Journal of Thermal Spray Technology, vol. 18, no. 2, pp. 148–180, Jun 2009. [Online]. Available: https://doi.org/10.1007/s11666-009-9294-5

[27] A. Tran, "Effects of surface chemistry on splat formation during plasma spraying," Ph.D. dissertation, University of Auckland, NZ, 2010.

[28] P. Fauchais, A. Vardelle, M. Vardelle, and M. Fukumoto, "Knowledge concerning splat formation: An invited review," Journal of Thermal Spray Technology, vol. 13, no. 3, pp. 337–360, Sep 2004. [Online]. Available: https://doi.org/10.1361/10599630419670

[29] K. Yang, , M. Liu, K. Zhou, and C. Deng, "Recent developments in the research of splat formation process in thermal spraying," Journal of Materials, 2013.

[30] H. Li, S. Costil, H.-L. Liao, C.-J. Li, M. Planche, and C. Coddet, "Effects of surface conditions on the flattening behavior of plasma sprayed cu splats," Surface and Coatings Technology, vol. 200, no. 18, pp. 5435 – 5446, 2006. [Online]. Available: http://www.sciencedirect.com/science/article/pii/S0257897205006821

[31] M. Fukumoto, T. Yamaguchi, M. Yamada, and T. Yasui, "Splash splat to disk splat transition behavior in plasma-sprayed metallic materials," Journal of Thermal Spray Technology, vol. 16, no. 5, pp. 905–912, Dec 2007. [Online]. Available: https://doi.org/10.1007/s11666-007-9083-y

[32] N. Sakakibara, H. Tsulcuda, and A. Notomi, "The splat morphology of plasma sprayed particle and the relation to coating property," in Thermal Spray Surface Engineering via Applied Research, C. Berndt, Ed., ASM international. ASM, 2000, pp. 753 – 758.

[33] K. Yang, M. Fukumoto, T. Yasui, and M. Yamada, "Study of substrate preheating on flattening behavior of thermal-sprayed copper particles," Journal of Thermal Spray Technology, vol. 19, no. 6, pp. 1195–1205, Dec 2010. [Online]. Available: https://doi.org/10.1007/s11666-010-9515-y

[34] A. Abedini, A. Pourmousa, S. Chandra, and J. Mostaghimi, "Effect of substrate temperature on the properties of coatings and splats deposited by wire arc spraying," Surface and Coatings Technology, vol. 201, no. 6, pp. 3350 – 3358, 2006. [Online]. Available: http://www.sciencedirect.com/science/article/pii/S0257897206007687

[35] A. Tran, M. Hyland, T. Qiu, B. Withy, and B. James, "Effects of surface chemistry on splat formation during plasma spraying," Journal of Thermal Spray Technology, vol. 17, no. 5, pp. 637–645, Dec 2008. [Online]. Available: https://doi.org/10.1007/s11666-008-9237-6

[36] C.-J. Li, C.-X. Li, G.-J. Yang, and Y.-Y. Wang, "Examination of substrate surface melting-induced splashing during splat formation in plasma spraying," Journal of Thermal Spray Technology, vol. 15, no. 4, pp. 717–724, Dec 2006. [Online]. Available: https://doi.org/10.1361/105996306X146947

[37] C. Escure, M. Vardelle, and P. Fauchais, "Experimental and theoretical study of the impact of alumina droplets on cold and hot substrates," Plasma Chemistry and Plasma Processing, vol. 23, no. 2, pp. 185–221, Jun 2003. [Online]. Available: https://doi.org/10.1023/A:1022976914185

[38] C. Mundo, M. Sommerfeld, and C. Tropea, "Droplet-wall collisions: Experimental studies of the deformation and breakup process," International Journal of Multiphase Flow, vol. 21, no. 2, pp. 151 – 173, 1995. [Online]. Available: http://www.sciencedirect.com/science/article/pii/030193229400069V

[39] M. Fukumoto, E. Nishioka, and T. Nishiyama, "New criterion for splashing in flattening of thermal sprayed particles onto flat substrate surface," Surface and Coatings Technology, vol. 161, no. 2, pp. 103 – 110, 2002. [Online]. Available: http://www.sciencedirect.com/science/article/pii/S0257897202004711

[40] L. Blanchi, A. Grimaud, F. Blein, P. Lucchèse, and P. Fauchais, "Comparison of plasma-sprayed alumina coatings by rf and dc plasma spraying," Journal of Thermal Spray Technology, vol. 4, no. 1, pp. 59–66, Mar 1995. [Online]. Available: https://doi.org/10.1007/BF02648529

[41] M. Vardelle, A. Vardelle, A. C. Leger, P. Fauchais, and D. Gobin, "Influence of particle parameters at impact on splat formation and solidification in plasma spraying processes," Journal of Thermal Spray Technology, vol. 4, no. 1, pp. 50–58, Mar 1995. [Online]. Available: https://doi.org/10.1007/BF02648528

[42] A. Syed, A. Denoirjean, B. Hannoyer, P. Fauchais, P. Denoirjean, A. Khan, and J. Labbe, "Influence of substrate surface conditions on the plasma sprayed ceramic and metallic particles flattening," Surface and Coatings Technology, vol. 200, no. 7, pp. 2317 – 2331, 2005. [Online]. Available: http://www.sciencedirect.com/science/article/pii/S0257897205000356

[43] R. Dhiman and S. Chandra, "Freezing-induced splashing during impact of molten metal droplets with high weber numbers," International Journal of Heat and Mass Transfer, vol. 48, no. 25, pp. 5625 – 5638, 2005. [Online]. Available: http://www.sciencedirect.com/science/article/pii/S0017931005005077

[44] M. Fukumoto and Y. Huang, "Flattening mechanism in thermal sprayed nickel particle impinging on flat substrate surface," Journal of Thermal Spray Technology, vol. 8, no. 3, pp. 427–432, Sep 1999. [Online]. Available: https://doi.org/10.1361/105996399770350386

[45] X. Jiang, Y. Wan, H. Herman, and S. Sampath, "Role of condensates and adsorbates on substrate surface on fragmentation of impinging molten droplets during thermal spray," Thin Solid Films, vol. 385, no. 1, pp. 132 –

141, 2001. [Online]. Available: http://www.sciencedirect.com/science/article/pii/S0040609001007696

[46] C.-J. Li and J.-L. Li, "Evaporated-gas-induced splashing model for splat formation during plasma spraying," Surface and Coatings Technology, vol. 184, no. 1, pp. 13 – 23, 2004. [Online]. Available: http://www.sciencedirect.com/science/article/pii/S0257897203011988

[47] M. Qu and A. Gouldstone, "On the role of bubbles in metallic splat nanopores and adhesion," Journal of Thermal Spray Technology, vol. 17, no. 4, pp. 486–494, Dec 2008. [Online]. Available: https://doi.org/10.1007/s11666-008-9198-9

[48] K. Yang, K. Tomita, M. Fukumoto, M. Yamada, and T. Yasui, "Effect of ambient pressure on flattening behavior of thermal sprayed particles," Journal of Thermal Spray Technology, vol. 18, no. 4, p. 510, Oct 2009. [Online]. Available: https://doi.org/10.1007/s11666-009-9401-7

[49] A. McDonald, M. Xue, S. Chandra, J. Mostaghimi, and C. Moreau, "Modeling fragmentation of plasma-sprayed particles impacting on a solid surface at room temperature," Comptes Rendus Mécanique, vol. 335, no. 5, pp. 351 – 356, 2007, melting and solidification: processes and models. [Online]. Available: http://www.sciencedirect.com/science/article/pii/S1631072107000770

[50] A. Ganesan, M. Yamada, and M. Fukumoto, "The effect of cfrp surface treatment on the splat morphology and coating adhesion strength," Journal of Thermal Spray Technology, vol. 23, no. 1, pp. 236–244, Jan 2014. [Online]. Available: https://doi.org/10.1007/s11666-013-0003-z

[51] M. Fukumoto, A. Ganesan, M. Yamada, and Y. Tsunekaw, "Thick metallic/composite coating on c-frp substrate by plasma spraying," in 21st international symposium on plasma chemistry, Cairns, Australia, 2013.

[52] A. Redza, T. Yasui, and M. Fukumoto, "Deposition of hard chrome coating onto heat susceptible substrates by low power microwave plasma spray," IOP Conference Series: Materials Science and Engineering, vol. 114, no. 1, p. 012030, 2016. [Online]. Available: http://stacks.iop.org/1757-899X/114/i=1/a=012030

[53] G. Marot, J. Lesage, P. Démarécaux, M. Hadad, S. Siegmann, and M. Staia, "Interfacial indentation and shear tests to determine the adhesion of thermal spray coatings," Surface and Coatings Technology, vol. 201, no. 5, pp. 2080

– 2085, 2006, the 2nd International Meeting on Thermal Spraying. [Online]. Available: http://www.sciencedirect.com/science/article/pii/S0257897206003963

[54] S. D. Brown, "Adherence* failure and measurement: some troubling questions," Journal of Adhesion Science and Technology, vol. 8, no. 6, pp. 687–711, 1994. [Online]. Available: http://dx.doi.org/10.1163/156856194X00438

[55] C. Berndt and C. Lin, "Measurement of adhesion for thermally sprayed materials," Journal of Adhesion Science and Technology, vol. 7, no. 12, pp. 1235–1264, 1993.

[56] C. K. Lin and C. C. Berndt, "Measurement and analysis of adhesion strength for thermally sprayed coatings," Journal of Thermal Spray Technology, vol. 3, no. 1, pp. 75–104, Mar 1994. [Online]. Available: https://doi.org/10.1007/BF02649003

[57] Y. Tsui, C. Doyle, and T. Clyne, "Plasma sprayed hydroxyapatite coatings on titanium substrates part 1: Mechanical properties and residual stress levels," Biomaterials, vol. 19, no. 22, pp. 2015 – 2029, 1998. [Online]. Available: http://www.sciencedirect.com/science/article/pii/S0142961298001033

[58] "Standard test method for adhesion or cohesion strength of thermal spray coatings," ASTM International, West Conshohocken, PA, Standard, 2013.

[59] "Thermal spraying. determination of tensile adhesive strength," British Standards Institute, London, UK, Standard, 1994.

[60] "Standard test method for pull-off strength of coatings using portable adhesion testers," ASTM International, West Conshohocken, PA, Standard, 2009.

[61] W. Han, E. F. Rybicki, and J. R. Shadley, "An improved specimen geometry for astm c633-79 to estimate bond strengths of thermal spray coatings," Journal of Thermal Spray Technology, vol. 2, no. 2, pp. 145–150, Jun 1993. [Online]. Available: https://doi.org/10.1007/BF02652022

[62] M. Arrigoni, S. Barradas, M. Braccini, M. Dupeux, M. Jeandin, M. Boustie, C. Bolis, and L. Berthe, "A comparative study of three adhesion tests (en 582, similar to astm c633, lasat (laser adhesion test), and bulge and blister test) performed on plasma sprayed copper deposited on aluminium 2017 substrates," Journal of Adhesion Science and Technology, vol. 20, no. 5, pp. 471–487, 2006. [Online]. Available: http://dx.doi.org/10.1163/156856106777144336

[63] S. Kuroda, T. Inoue, A. Kishi, K. Yokoyama, H. Yumoto, and Y. Gotoh, "Evaluation of adhesive strength of hvof sprayed metallic alloy coatings by a modified

tensile test," in Thermal Spray 2004: Advances in Technology and Applications, ASM international. ASM, 2004, pp. 138 – 147.

[64] M. Riley, personal communication.

[65] T. W. Clyne and S. C. Gill, "Residual stresses in thermal spray coatings and their effect on interfacial adhesion: A review of recent work," Journal of Thermal Spray Technology, vol. 5, no. 4, p. 401, Dec 1996. [Online]. Available: https://doi.org/10.1007/BF02645271

[66] T. C. Totemeier, R. N. Wright, and W. D. Swank, "Residual stresses in high-velocity oxy-fuel metallic coatings," Metallurgical and Materials Transactions A, vol. 35, no. 6, pp. 1807–1814, Jun 2004. [Online]. Available: https://doi.org/10.1007/s11661-004-0089-5

[67] O. Kesler, J. Matejicek, S. Sampath, S. Suresh, T. Gnaeupel-Herold, P. Brand, and H. Prask, "Measurement of residual stress in plasma-sprayed metallic, ceramic and composite coatings," Materials Science and Engineering: A, vol. 257, no. 2, pp. 215 – 224, 1998. [Online]. Available: http://www.sciencedirect.com/science/article/pii/S0921509398008600

[68] Y. Tsui and T. Clyne, "An analytical model for predicting residual stresses in progressively deposited coatings part 1: Planar geometry," Thin Solid Films, vol. 306, no. 1, pp. 23 – 33, 1997. [Online]. Available: http://www.sciencedirect.com/science/article/pii/S0040609097001995

[69] S. Kuroda and T. Clyne, "The quenching stress in thermally sprayed coatings," Thin Solid Films, vol. 200, no. 1, pp. 49 – 66, 1991. [Online]. Available: http://www.sciencedirect.com/science/article/pii/004060909190029W

[70] T. C. Totemeier, R. N. Wright, and W. D. Swank, "Mechanical and physical properties of high-velocity oxy-fuel-sprayed iron aluminide coatings," Metallurgical and Materials Transactions A, vol. 34, no. 10, pp. 2223–2231, Oct 2003. [Online]. Available: https://doi.org/10.1007/s11661-003-0286-7

[71] Zoltek, "What is carbon fiber." [Online]. Available: http://www.Zoltek.com/Carbonfiber

[72] Performance composites, "Mechanical properties of carbon fibre composite materials, fibre / epoxy resin (120°c cure)." [Online]. Available: http://www.performance-composites.com/carbonfibre/mechanicalproperties_2.asp

[73] L. M. Nicholson, K. S. Whitley, T. S. Gates, and J. A. Hinkley, "How molecular structure affects mechanical properties of an advanced polymer," Proceedings of SAMPE, vol. 44, pp. 794 – 808, 1999.

[74] W. D. Callister, Materials Science and Engineering: An Introduction, 4th ed. Wiley, 12 1996.

[75] F. C. Campbell, Matrix resin systems, new ed. ed. ASM International, 11 2010, pp. 63–99.

[76] V. John, Introduction to Engineering Materials, 3rd ed. Palgrave Macmillan, 5 1992.

[77] Vitrex, "High performance paek polymers." [Online]. Available: https://www.victrex.com/\~/media/datasheets/victrex_tds_450g.pdf

[78] Y. Huang and R. Young, "Effect of fibre microstructure upon the modulus of pan- and pitch-based carbon fibres," Carbon, vol. 33, no. 2, pp. 97 – 107, 1995. [Online]. Available: http://www.sciencedirect.com/science/article/pii/000862239400109D

[79] S.-Y. Fu, B. Lauke, E. Mäder, C.-Y. Yue, and X. Hu, "Tensile properties of short-glass-fiber- and short-carbon-fiber-reinforced polypropylene composites," Composites Part A: Applied Science and Manufacturing, vol. 31, no. 10, pp. 1117 – 1125, 2000. [Online]. Available: http://www.sciencedirect.com/science/article/pii/S1359835X00000683

[80] S. Mazumdar, Composites Manufacturing: Materials, Product, and Process Engineering, 1st ed. CRC Press, 12 2001.

[81] H. S. Ingham and A. P. Shepard, The Metco Metallizing handbook. Woking, England: Metallizing engineering Co., inc, 1951.

[82] J. K. Sutter, K. Miyoshi, C. Bowman, S. K. Naik, K. Ma, R. Sinatra, R. Cupp, R. Horan, and G. Leissler, "Erosion coatings for polymer matrix composites in propulsion applications," High Performance Polymers, vol. 15, no. 4, pp. 421–440, 2003. [Online]. Available: https://doi.org/10.1177/09540083030154003

[83] J. K. Sutter, S. K. Naik, R. Horan, K. Miyoshi, C. Bowman, K. Ma, G. Leissler, R. Sinatra, and R. Cupp, "Erosion resistant coatings for polymer matrix composites in propulsion applications," 2003.

[84] K. Miyoshi, J. K. Sutter, R. A. Horan, S. K. Naik, and R. J. Cupp, "Assessment of erosion resistance of coated polymer matrix composites for propulsion applications," 2004.

[85] R. Gonzalez, A. McDonald, and P. Mertiny, "Effect of flame-sprayed al–12si coatings on the failure behaviour of pressurized fibre-reinforced composite tubes," Polymer Testing, vol. 32, no. 8, pp. 1522 – 1528, 2013. [Online]. Available: http://www.sciencedirect.com/science/article/pii/S0142941813002031

[86] R. G. Henriquez, "Flame-sprayed al-12si coatings as damage detection sensors for fibre-reinforced polymer composites," Ph.D. dissertation, University of Alberta, Alberta, 2015.

[87] A. Lopera-Valle and A. McDonald, "Flame-sprayed coatings as de-icing elements for fiber-reinforced polymer composite structures: Modeling and experimentation," International Journal of Heat and Mass Transfer, vol. 97, no. Supplement C, pp. 56 – 65, 2016. [Online]. Available: http://www.sciencedirect.com/science/article/pii/S0017931015303173

[88] J. Sloan, "787 integrates new composite wing deicing system." [Online]. Available: http://www.compositesworld.com/articles/787-integrates-new-composite-wing-deicing-system

[89] E. Lugscheider, R. Mathesius, G. Spur, and A. Kranz, "Mechanical properties of thermal sprayed coatings on cfrp," in Proceedings of the 1993 national thermal spray conference, Anahelm, USA.

[90] W. Kim, A. Argento, and P. S. Mohanty, "Spray deposition of metals over circular cfrp core shafts," Journal of Composite Materials, vol. 43, no. 3, pp. 277–287, 2009. [Online]. Available: "https://doi.org/10.1177/0021998308099222"

[91] A. Liu, M. Guo, J. Gao, and M. Zhao, "Influence of bond coat on shear adhesion strength of erosion and thermal resistant coating for carbon fiber reinforced thermosetting polyimide," Surface and Coatings Technology, vol. 201, no. 6, pp. 2696 – 2700, 2006. [Online]. Available: http://www.sciencedirect.com/science/article/pii/S025789720600421X

[92] R. Wang, D. Song, W. Liu, and X. He, "Effect of arc spraying power on the microstructure and mechanical properties of zn–al coating deposited onto carbon fiber reinforced epoxy composites," Applied Surface

Science, vol. 257, no. 1, pp. 203 – 209, 2010. [Online]. Available: http://www.sciencedirect.com/science/article/pii/S0169433210008986

[93] M. Ducos, "Atmosphere and temperature controlled plasma spraying thick coatings and coating on composite resin fibre," in 12th Internation Thermal Spray Conference, The Welding Institute, Abington Hall, Abington, Cambridge, 1989.

[94] R. H. Henne and C. Schitter, "Plasma spraying of high performance polymers," in Proceedings of the 8th National Thermal Spray Conference, Houston, 1995.

[95] J. D. Reardon, "Plasma sprayed bonding coat for plastic substrates," in Thermal spray coatings proceedings 2nd National conference.

[96] F. Alonso, I. Fagoaga, and P. Oregui, "Erosion protection of carbon—epoxy composites by plasma-sprayed coatings," Surface and Coatings Technology, vol. 49, no. 1, pp. 482 – 488, 1991. [Online]. Available: http://www.sciencedirect.com/science/article/pii/0257897291901045

[97] A. Ashari and R. Tucker, "Thermal spray coatings for fibre reinforrced polymer composites," in Proceedings of the 15th International Thermal Spray Conference, Nice, France, 1998.

[98] W. Huang, X. Fan, Y. Zhao, X. Zhou, X. Meng, Y. Wang, B. Zou, X. Cao, and Z. Wang, "Fabrication of thermal barrier coatings onto polyimide matrix composites via air plasma spray process," Surface and Coatings Technology, vol. 207, no. Supplement C, pp. 421 – 429, 2012. [Online]. Available: http://www.sciencedirect.com/science/article/pii/S025789721200730X

[99] W. Huang, Y. Zhao, X. Fan, X. Meng, Y. Wang, X. Cai, X. Cao, and Z. Wang, "Effect of bond coats on thermal shock resistance of thermal barrier coatings deposited onto polymer matrix composites via air plasma spray process," Journal of Thermal Spray Technology, vol. 22, no. 6, pp. 918–925, Aug 2013. [Online]. Available: https://doi.org/10.1007/s11666-013-9942-7

[100] D. Song, R. Wang, W. Liu, and X. He, "Microstructure and mechanical properties of pbsn alloys deposited on carbon fiber reinforced epoxy composites," Journal of Alloys and Compounds, vol. 505, no. 1, pp. 348 – 351, 2010. [Online]. Available: http://www.sciencedirect.com/science/article/pii/S0925838810014726

[101] S. Guanhong, H. Xiaodong, J. Jiuxing, and S. Yue, "Parametric study of al and al2o3 ceramic coatings deposited by air plasma spray onto polymer substrate,"

Applied Surface Science, vol. 257, no. 17, pp. 7864 – 7870, 2011. [Online]. Available: http://www.sciencedirect.com/science/article/pii/S0169433211005939

[102] M. Ivosevic, R. Knight, S. R. Kalidindi, G. R. Palmese, A. Tsurikov, and J. K. Sutter, "Optimal substrate preheating model for thermal spray deposition of thermosets onto polymer matrix composites," in Thermal spray 2003: Advancing the science and applying the technology. Orlando: ASM International, 2003.

[103] M. Ivosevic, R. Knight, S. R. Kalidindi, G. R. Palmese, and J. K. Sutter, "Erosion/oxidation resistant coatings for high temperature polymer composites," High Performance Polymers, vol. 15, no. 4, pp. 503–517, 2003. [Online]. Available: https://doi.org/10.1177/09540083030154007

[104] M. Ivosevic, R. Knight, S. Kalidindi, G. Palmese, and J. Sutter, "Solid particle erosion resistance of thermally sprayed functionally graded coatings for polymer matrix composites," Surface and Coatings Technology, vol. 200, no. 16, pp. 5145 – 5151, 2006. [Online]. Available: http://www.sciencedirect.com/science/article/pii/S0257897205006432

[105] M. Ivosevic, R. Knight, S. R. Kalidindi, and G. R. Pal, "Microstructure and properties of thermally sprayed functionally graded coatings for polymeric substrates," in Thermal spray 2003: Advancing the science and applying the technology, Orlando, Florida, 2003.

[106] M. Ivosevic, R. Knight, S. R. Kalidindi, G. R. Palmese, and J. K. Sutter, "Adhesive/cohesive properties of thermally sprayed functionally graded coatings for polymer matrix composites," Journal of Thermal Spray Technology, vol. 14, no. 1, pp. 45–51, Mar 2005. [Online]. Available: https://doi.org/10.1361/10599630522765

[107] S. Dixit, M. Chin, and R. Dixit, "Coatings for polymer turbine blades," in Proceedings of the International Thermal spray Conference. Las Vegas: ASM International, 2009.

[108] A. Ganesan, J. Affi, M. Yamada, and M. Fukumoto, "Bonding behavior studies of cold sprayed copper coating on the pvc polymer substrate," Surface and Coatings Technology, vol. 207, no. Supplement C, pp. 262 – 269, 2012. [Online]. Available: http://www.sciencedirect.com/science/article/pii/S0257897212006743

[109] R. Lupoi and W. O'Neill, "Deposition of metallic coatings on polymer surfaces using cold spray," Surface and Coatings Technology, vol. 205, no. 7, pp. 2167

– 2173, 2010. [Online]. Available: http://www.sciencedirect.com/science/article/pii/S0257897210007851

[110] H. Q. Che and S. Yue, "Cold spray of carbon fibre reinforced polymer for lightning strike protection," in Proceedings from the international thermal spray conference, Barcelona, 2014.

[111] J. Affi, H. Okazaki, M. Yamada, and M. Fukumoto, "Fabrication of aluminum coating onto cfrp substrate by cold spray," MATERIALS TRANSACTIONS, vol. 52, no. 9, pp. 1759–1763, 2011.

[112] F. Robitaille, M. Yandouzi, S. Hind, and B. Jodoin, "Metallic coating of aerospace carbon/epoxy composites by the pulsed gas dynamic spraying process," Surface and Coatings Technology, vol. 203, no. 19, pp. 2954 – 2960, 2009. [Online]. Available: http://www.sciencedirect.com/science/article/pii/S0257897209002473

[113] R. Gonzalez, H. Ashrafizadeh, A. Lopera, P. Mertiny, and A. McDonald, "A review of thermal spray metallization of polymer-based structures," Journal of Thermal Spray Technology, vol. 25, no. 5, pp. 897–919, Jun 2016. [Online]. Available: https://doi.org/10.1007/s11666-016-0415-7

[114] L. Zhu, W. Huang, H. Cheng, and X. Cao, "Thermal shock resistance of stabilized zirconia/metal coat on polymer matrix composites by thermal spraying process," Journal of Thermal Spray Technology, vol. 23, no. 8, pp. 1312–1322, Dec 2014. [Online]. Available: https://doi.org/10.1007/s11666-014-0144-8

[115] U. Cvelbar, S. Pejovnik, M. Mozetiè, and A. Zalar, "Increased surface roughness by oxygen plasma treatment of graphite/polymer composite," Applied Surface Science, vol. 210, no. 3, pp. 255 – 261, 2003. [Online]. Available: http://www.sciencedirect.com/science/article/pii/S0169433202012862

[116] B. Henry, F. Borit, V. Guipont, and M. Jeandin, "Residual stresses in inconel 625 coating of organic-based composites obtained by plasma spraying with atmosphere and temperature control (atc)," in Thermal Spray 2003: Advancing the Science and Applying the Technology.

[117] Tencate, "Product e722." [Online]. Available: https://www.tencatecomposites.com/media/6b3fca19-816d-471c-a7f2-805b6908ef16/Rq1puA/TenCate\%20Advanced\%20Composites/Documents/Product\%20datasheets/Thermoset/UD\%20tapes\%20and\%20prepregs/E722_Epoxy_PDS.pdf

[118] ——, "Product tencate certex tc1200." [Online]. Available: https://www.tencatecomposites.com/media/7765d981-1f9f-472d-bf24-69a647412e38/XDoW-A/TenCate\%20Advanced\%20Composites/Documents/Product\%20datasheets/Thermoplastic/UD\%20tapes,\%20prepregs\%20and\%20laminates/TenCate-Cetex-TC1200_PEEK_PDS.pdf

[119] Easy composites, "El2 epoxy laminating resin 500g slow." [Online]. Available: https://system.eu2.netsuite.com/core/media/media.nl?id=54760\&c=3937524\&h=25fbf4b8bcc9a9db3140\&_xt=.pdf

[120] Direct plastics, "Peek sheet." [Online]. Available: http://www.directplastics.co.uk/pdf/datasheets/PEEK\%20Data\%20Sheet.pdf

[121] L. Reimer, Scanning electron microscopy : physics of image formation and microanalysis. Berlin New York: Springer, 1998.

[122] J. Goldstein, Scanning electron microscopy and X-ray microanalysis : a text for biologists, materials scientists, and geologists. New York: Plenum Press, 1981.

[123] Nanoscience instruments, "Sample-electron interaction." [Online]. Available: http://www.nanoscience.com/technology/sem-technology/sample-electron-interaction/

[124] W. Kapłonek, K. Nadolny, and G. M. Królczyk, "The use of focus-variation microscopy for the assessment of active surfaces of a new generation of coated abrasive tools," Measurement Science Review, vol. 16, pp. 42 – 53, 2016.

[125] R. Danzl, F. Helmli, and S. Scherer, "Focus variation – a robust technology for high resolution optical 3d surface metrology," Strojniški vestnik - Journal of Mechanical Engineering, vol. 57, no. 3, pp. 245–256, 2011. [Online]. Available: http://ojs.sv-jme.eu/index.php/sv-jme/article/view/sv-jme.2010.175

[126] Alicona. [Online]. Available: http://www.alicona.com/fileadmin/downloads/InfiniteFocusSL_Flyer_EN.pdf

[127] "Geometrical product specification (gps). surface texture: Profile method. terms, definitions and surface texture parameters," British Standards Institute, London, UK, Standard, July 2000.

[128] Taylor Hobson, Exploring surface texture. Leicester: Taylor Hobson, 2011.

[129] L. D. Chiffre, P. Lonardo, H. Trumpold, D. Lucca, G. Goch, C. Brown, J. Raja, and H. Hansen, "Quantitative characterisation of surface texture," CIRP Annals, vol. 49, no. 2, pp. 635 – 652, 2000. [Online]. Available: http://www.sciencedirect.com/science/article/pii/S0007850607634581

[130] G. D. Lunn, M. A. Riley, and D. G. McCartney, "A study of wire breakup and in-flight particle behavior during wire flame spraying of aluminum," Journal of Thermal Spray Technology, Sep 2017. [Online]. Available: https://doi.org/10.1007/s11666-017-0639-1

[131] T. Turner and N. Budgen, Metal spraying: The origin development and applications of the metal-spray process of metallisation. London: Charles griffin & company limited, 1926.

[132] S. L. Chen, P. Siitonen, and P. Kettunen, "A method for measuring particle velocity in thermal spraying," Surface and Coatings Technology, vol. 64, no. 1, pp. 17 – 20, 1994. [Online]. Available: http://www.sciencedirect.com/science/article/pii/S0257897209900809

[133] F. W. Bach, A. Laarmann, and T. Wenz, Modern Surface Technology. John Wiley & Sons, 2006.

[134] A. Fischer, T. Pfister, and J. Czarske, "Derivation and comparison of fundamental uncertainty limits for laser-two-focus velocimetry, laser doppler anemometry and doppler global velocimetry," Measurement, vol. 43, no. 10, pp. 1556 – 1574, 2010. [Online]. Available: http://www.sciencedirect.com/science/article/pii/S0263224110002058

[135] A. Newbery, P. Grant, and R. Neiser, "The velocity and temperature of steel droplets during electric arc spraying," Surface and Coatings Technology, vol. 195, no. 1, pp. 91 – 101, 2005. [Online]. Available: http://www.sciencedirect.com/science/article/pii/S025789720500037X

[136] J. Bolinder, "On the accuracy of a digital particle image velocimetry system," 1999.

[137] F.-W. Bach, K. Möhwald, T. Rothardt, J. Prehm, L. Engl, K. Hartz, and B. Drößler, "Particle image velocimetry in thermal spraying," vol. 383, no. 1, 2004, pp. 146 – 152, 2nd International erence on Spray Deposition and Melt Atomization and the 5th International Conference on Spray Forming. [Online]. Available: http://www.sciencedirect.com/science/article/pii/S0921509304002187

[138] J. R. Fincke, D. C. Haggard, and W. D. Swank, "Particle temperature measurement in the thermal spray process," Journal of Thermal Spray Technology, vol. 10, no. 2, pp. 255–266, Jun 2001. [Online]. Available: https://doi.org/10.1361/105996301770349358

[139] P. Fauchais and M. Vardelle, "Sensors in spray processes," Journal of Thermal Spray Technology, vol. 19, no. 4, pp. 668–694, Jun 2010. [Online]. Available: https://doi.org/10.1007/s11666-010-9485-0

[140] J. Largo, "High-power diado lasers in spray process diagnostics." in Proc. SPIE 5580, 26th International Congress on High-Speed Photography and Photonics, Alexandria, Virginia, USA, 2005.

[141] N. A. Hussary and J. V. R. Heberlein, "Atomization and particle-jet interactions in the wire-arc spraying process," Journal of Thermal Spray Technology, vol. 10, no. 4, pp. 604–610, Dec 2001. [Online]. Available: https://doi.org/10.1361/105996301770349123

[142] ——, "Effect of system parameters on metal breakup and particle formation in the wire arc spray process," Journal of Thermal Spray Technology, vol. 16, no. 1, pp. 140–152, Mar 2007. [Online]. Available: https://doi.org/10.1007/s11666-006-9006-3

[143] W. Tillmann and M. Abdulgader, "Wire composition: Its effect on metal disintegration and particle formation in twin-wire arc-spraying process," Journal of Thermal Spray Technology, vol. 22, no. 2, pp. 352–362, Mar 2013. [Online]. Available: https://doi.org/10.1007/s11666-012-9870-y

[144] A. P. Abkenar, "Wire-arc spraying system: particle production, transport, and deposition," Ph.D. dissertation, University of Toronto, Toronto, 2007.

[145] H. Liu, Science and Engineering of Droplets. Norwich, NY: William Andrew Publishing, 1999.

[146] TWI, "What are the most common applications of flame spraying?" [Online]. Available: http://www.twi-global.com/technical-knowledge/faqs/process-faqs/faq-what-are-the-most-common-applications-of-flame-spraying/

[147] R. C. Dykhuizen and R. A. Neiser, "Process-based quality for thermal spray via feedback control," Journal of Thermal Spray Technology, vol. 15, no. 3, pp. 332–339, Sep 2006. [Online]. Available: https://doi.org/10.1361/105996306X124310

[148] R. Neiser, I. Brockman, T. O'Hern, M. Smith, R. Dykhuizen, T. Roemer, and R. Teets, "Wire melting and droplet atomization in a high velocity oxy-fuel jet," in Advances in Thermal Spray Science & Technology, C. Berndt and S. Campath, Eds. Houston, TX: ASM International, 1995, pp. 99 – 110.

[149] K. K. Kuo, Recent advances in spray combustion : spray atomization and drop burning phenomena. Volume I. Reston, VA: American Institute of Aeronautics and Astronautics, 1996.

[150] I. F. Bainbridge and J. A. Taylor, "The surface tension of pure aluminum and aluminum alloys," Metallurgical and Materials Transactions A, vol. 44, no. 8, pp. 3901–3909, Aug 2013. [Online]. Available: https://doi.org/10.1007/s11661-013-1696-9

[151] J. Madejski, "Solidification of droplets on a cold surface," International Journal of Heat and Mass Transfer, vol. 19, no. 9, pp. 1009 – 1013, 1976. [Online]. Available: http://www.sciencedirect.com/science/article/pii/0017931076901836

[152] M. Qu, Y. Wu, V. Srinivasan, and A. Gouldstone, "Observations of nanoporous foam arising from impact and rapid solidification of molten ni droplets," Applied Physics Letters, vol. 90, no. 25, p. 254101, 2007. [Online]. Available: http://dx.doi.org/10.1063/1.2749183

[153] L. Li, X. Wang, G. Wei, A. Vaidya, H. Zhang, and S. Sampath, "Substrate melting during thermal spray splat quenching," Thin Solid Films, vol. 468, no. 1, pp. 113 – 119, 2004. [Online]. Available: http://www.sciencedirect.com/science/article/pii/S0040609004006686

[154] P. Patel, T. R. Hull, R. E. Lyon, S. I. Stoliarov, R. N. Walters, S. Crowley, and N. Safronava, "Investigation of the thermal decomposition and flammability of peek and its carbon and glass-fibre composites," Polymer Degradation and Stability, vol. 96, no. 1, pp. 12 – 22, 2011. [Online]. Available: http://www.sciencedirect.com/science/article/pii/S0141391010004167

[155] R.-J. Jeng, S.-M. Shau, J.-J. Lin, W.-C. Su, and Y.-S. Chiu, "Flame retardant epoxy polymers based on all phosphorus-containing components," European Polymer Journal, vol. 38, no. 4, pp. 683 – 693, 2002. [Online]. Available: http://www.sciencedirect.com/science/article/pii/S0014305701002464

[156] H. Fukanuma and N. Ohno, Influences of Substrate Roughness and Temperature on Adhesive Strength in Thermal Spray Coatings. ASM International, 2003.

[157] M. G. Nicholas and K. T. Scott, "Characterisation of grit-blasted surfaces," Surfacing Journal, p. 5–12, 1981.

[158] F. Bahbou, P. Nylén, and S. Trollhättan, Relationship between surface topology parameters and adhesive strength for plasma spraying. ASM International, 2005.

[159] J. Day, X. Huang, and N. L. Richards, "Examination of a grit-blasting process for thermal spraying using statistical methods," Journal of Thermal Spray Technology, vol. 14, no. 4, pp. 471–479, Dec 2005. [Online]. Available: https://doi.org/10.1361/105996305X76469

[160] M. Staia, E. Ramos, A. Carrasquero, A. Roman, J. Lesage, D. Chicot, and G. Mesmacque, "Effect of substrate roughness induced by grit blasting upon adhesion of wc-17% co thermal sprayed coatings," Thin Solid Films, vol. 377, no. Supplement C, pp. 657 – 664, 2000, international Conference on Metallurgic Coatings and Thin Films. [Online]. Available: http://www.sciencedirect.com/science/article/pii/S0040609000014474

[161] M. F. Bahbou, P. Nylén, and J. Wigren, "Effect of grit blasting and spraying angle on the adhesion strength of a plasma-sprayed coating," Journal of Thermal Spray Technology, vol. 13, no. 4, pp. 508–514, Dec 2004. [Online]. Available: https://doi.org/10.1361/10599630421406

[162] D. L. Vasquez, T. Ndalama, D. A. Hirschfeld, and J. K. Sutter, "Effect of surface modification on adhesion of a metal bond coat to pmr composites," High Performance Polymers, vol. 17, no. 2, pp. 293–302, 2005. [Online]. Available: https://doi.org/10.1177/0954008305050677

[163] DEPARTMENT OF Trade and Industry, Wear Resistant Surfaces in Engineering, A Guide to Their Production, Properties and Selection. Hmso, 1986.

[164] C. Kenneth, Wear, 1992, pp. 175 – 333.

[165] G. Sundararajan and M. Roy, "Solid particle erosion behaviour of metallic materials at room and elevated temperatures," Tribology International, vol. 30, no. 5, pp. 339 – 359, 1997, wear of Metals. [Online]. Available: http://www.sciencedirect.com/science/article/pii/S0301679X96000643

[166] N.-M. Barkoula and J. Karger-Kocsis, "Review processes and influencing parameters of the solid particle erosion of polymers and their composites," Journal

of Materials Science, vol. 37, no. 18, pp. 3807–3820, Sep 2002. [Online]. Available: https://doi.org/10.1023/A:1019633515481

[167] A. Patnaik, A. Satapathy, N. Chand, N. Barkoula, and S. Biswas, "Solid particle erosion wear characteristics of fiber and particulate filled polymer composites: A review," Wear, vol. 268, no. 1, pp. 249 – 263, 2010. [Online]. Available: http://www.sciencedirect.com/science/article/pii/S004316480900475X

[168] A. Momber, Blast Cleaning Technology, 2008th ed. Springer, 2 2008.

[169] S. W. Zhang, W. Deguo, and Y. Weihua, "Investigation of abrasive erosion of polymers," Journal of Materials Science, vol. 30, no. 18, pp. 4561–4566, Sep 1995. [Online]. Available: https://doi.org/10.1007/BF01153063

[170] N.-M. Barkoula, J. Gremmels, and J. Karger-Kocsis, "Dependence of solid particle erosion on the cross-link density in an epoxy resin modified by hygrothermally decomposed polyurethane," Wear, vol. 247, no. 1, pp. 100 – 108, 2001. [Online]. Available: http://www.sciencedirect.com/science/article/pii/S0043164800005299

[171] A. Suresh, A. Harsha, and M. Ghosh, "Solid particle erosion of unidirectional fibre reinforced thermoplastic composites," Wear, vol. 267, no. 9, pp. 1516 – 1524, 2009. [Online]. Available: http://www.sciencedirect.com/science/article/pii/S0043164809003068

[172] G. Stachowiak and A. Batchelor, Engineering Tribology, Tribology Series no. 24. Amsterdam, 21821: Elsevier, 1993.

[173] J. J. Rajesh, J. Bijwe, B. Venkataraman, and U. Tewari, "Effect of impinging velocity on the erosive wear behaviour of polyamides," Tribology International, vol. 37, no. 3, pp. 219 – 226, 2004. [Online]. Available: http://www.sciencedirect.com/science/article/pii/S0301679X03000756

[174] N. Miyazaki and N. Takeda, "Solid particle erosion of fiber reinforced plastics," Journal of Composite Materials, vol. 27, no. 1, pp. 21–31, 1993. [Online]. Available: https://doi.org/10.1177/002199839302700102

[175] A. Harsha, U. Tewari, and B. Venkatraman, "Solid particle erosion behaviour of various polyaryletherketone composites," Wear, vol. 254, no. 7, pp. 693 – 712, 2003. [Online]. Available: http://www.sciencedirect.com/science/article/pii/S0043164803001431

[176] J. Bijwe, R. Rattan, M. Fahim, and S. Tiwari, "Erosive wear of carbon fabric reinforced polyetherimide composites: Role of amount of fabric and processing technique," Polymer Composites, vol. 29, no. 3, pp. 337–344, 2008. [Online]. Available: http://dx.doi.org/10.1002/pc.20544

[177] J. Zahavi and G. F. Schmitt, "Solid particle erosion of reinforced composite materials," Wear, vol. 71, no. 2, pp. 179 – 190, 1981. [Online]. Available: http://www.sciencedirect.com/science/article/pii/0043164881903379

[178] M. Sharma, J. Bijwe, K. Singh, and P. Mitschang, "Exploring potential of micro-raman spectroscopy for correlating graphitic distortion in carbon fibers with stresses in erosive wear studies of peek composites," Wear, vol. 270, no. 11, pp. 791 – 799, 2011. [Online]. Available: http://www.sciencedirect.com/science/article/pii/S0043164811000548

[179] S. Arjula and A. Harsha, "Study of erosion efficiency of polymers and polymer composites," Polymer Testing, vol. 25, no. 2, pp. 188 – 196, 2006. [Online]. Available: http://www.sciencedirect.com/science/article/pii/S0142941805001728

[180] U. Tewari, A. Harsha, A. Häger, and K. Friedrich, "Solid particle erosion of carbon fibre– and glass fibre–epoxy composites," Composites Science and Technology, vol. 63, no. 3, pp. 549 – 557, 2003. [Online]. Available: http://www.sciencedirect.com/science/article/pii/S0266353802002105

[181] S. Biswas, A. Satapathy, and A. Patnaik, "Erosion wear behavior of polymer composites: A review," Journal of Reinforced Plastics and Composites, vol. 29, no. 19, pp. 2898–2924, 2010. [Online]. Available: https://doi.org/10.1177/0731684408097786

[182] Guyson, "Blast media data sheet - guyson saftigrit brown." [Online]. Available: http://s3-eu-west-1.amazonaws.com/resources.guyson.co.uk/product-downloads/guyson_brown_saftigrit_datasheet.pdf

[183] "Standard test method for conducting erosion tests by solid particle impingement using gas jets," ASTM International, West Conshohocken, PA, Standard, 2013.

[184] R. Kulkarni and O. Ochoa, "Transverse and longitudinal cte measurements of carbon fibers and their impact on interfacial residual stresses in composites," Journal of Composite Materials, vol. 40, no. 8, pp. 733–754, 2006. [Online]. Available: https://doi.org/10.1177/0021998305055545

Appendix A

Data sheets

easycomposites
share the knowledge

EPOXY LAMINATING RESIN

EL2

Key Features

- Easy to use
- Medium Viscosity Resin
- Outstanding Wetting Abilities
- Good Mechanical Properties
- Choice of Hardener Speed

Product Description

El2 is a high performance general purpose epoxy laminating resin for use in wet-lay or vacuum bagging carbon fibre, aramid or glass lamination.

This medium viscosity epoxy exhibits excellent wetting characteristics especially when used with carbon fibre and aramid fibre (such as Kevlar®) reinforcement making airbubbles in the laminate less likely than with some alternative epoxy systems.

The resin also exhibits excellent cured mechanical properies far in excess of many more traditional epoxy resin brands (as can be seen from the technical data sheets). Improved mechanical properties mean stronger, ligher, higher performance parts.

Recommended Uses

Use as a general purpose laminating epoxy, wet-laying or vacuum bagging composites such as glass fibre, carbon fibre and aramid fibre (Kevlar).

When cured the epoxy exhibits good flexural strength making it will suited to the lamination of structural parts. The resin also exhibits very good clarity making it also suitable for use when laminating unpainted carbon fibre composites.

Properties

The table below shows the typical uncured properties:

Property	Units	Resin	Hardener	Combined
Material	-	Epoxy Resin	Formulated Amine	Epoxy
Appearance	-	Clear Liquid	Amber Liquid	Clear Liquid
Viscosity @20 °C	mPa.s.	1200 – 1800	5 - 80	1000 – 1400
Density @20 °C	g/cm^3	1.13 – 1.17	0.90 – 1.06	1.05 – 1.15

How to Use

EL2 is a chemical product for professional use. It is essential to read and understand the safety and technical information before use.

Follow the guidelines for safe use outlined in the SDS which include the use ofappropriate hand and eye protection during mixing and use.

Mix Ratio

Mix Ratio 100:30 by Weight

EL2 Epoxy Laminating Resin should be mixed with AT30 FAST or AT30 SLOW Hardener at a ratio of 100 parts of resin to 30 part sof hardener, by weight. FAST and SLOW hardeners can be blended to achieve pot-life and demould times anywhere between those stated. However, you must still maintain the correct overall ratio of resin to hardener to ensure a proper cure.

When working with any epoxy resin, it is essential to mix the resin and hardener exactly at the correct mix ratio. Failure to do so will result in a poor or only partial cure of the resin, greatly reduced mechanical properties and possibly other adverse effects. Under no circumstances add 'extra hardener' in an attempt to speed up the cure time; epoxies do not work in this way.

Mixing Instructions

EL2 is a highly reactive (fast curing) resin system. Only weigh out and mix as much resin as you can use within the pot life.

Weigh or measure the exact correct ratio of resin and hardener into a straight sided container. Using a suitable mixing stick begin to mix the resin and hardener together to combine them completely.

Spend at least one minute mixing the resin and hardener together, paying particular attention to the sides and base of the container. Remember: Any resin that has not been thoroughly combined with hardener will not cure.

Once you have finished mixing in one container, it is good practice to transfer the mixed resin into a second container and undertake further mixing of the resin using a new mixing stick. Doing so will eliminate the risk of accidentally using unmixed resin from the bottom or sides of the container.

Pot-Life / Working Time / Cure Time

EL2 is a highly reactive resin system and once the resin has been mixed with the hardener, the reaction will start to give off heat (exotherm) which will further accelerate the cure of the resin, especially when the resin is in the mixing pot.

Transfer the resin from the mixing pot onto the part as soon as possible to extend the working time and avoid the risk of uncontrollable rapid cure in the mixing pot.

As with all epoxies, the pot-life/working time will vary significantly depending on the ambient temperature, the starting temperature of the resin and hardener and the amount of resin mixed.

EL2 can be used in ambient temperatures between 15°C (59°F) and 30°C (86°F). For best results, an ambient temperature of at least 20°C (68°F) is recommended. Ensure that both resin and hardener containers are within this temperature range before use.

The table below gives an indication of pot-life and cure properties:

	Pot-Life @ 25 °C	Gelation @ 25 °C	Demould Time @ 25 °C
AT30 SLOW*	95 - 115mins	8.5 - 10.5hrs	20 - 30hrs
AT30 FAST*	12 - 17mins	2 - 3hrs	4 - 6hrs

*Fast and slow hardeners can be blended to achieve pot-life and demould timesanywhere between those stated above.

PEEK

PEEK (Polyetheretherketone)
Colour: Natural
Density: 1.31g/cm^3

DirectPlastics
...not just a quicker delivery!

Material Data Sheet

Mechanical Properties	Parameter	Value	Unit	DIN/EN/ISO
Modulus of elasticity (tensile test)	1mm/min	4200	MPa	527-2
Tensile strength	50mm/min	116	MPa	527-2
Tensile strength at yield	50mm/min	116	MPa	527-2
Elongation at Yield	50mm/min	5	%	527-2
Elongation at break	50mm/min	15	%	527-2
Flexural strength	2mm/min 10N	175	MPa	178
Modulus of elasticity (flexural test)	2mm/min 10N	4200	MPa	178
Compression Strength	1%/2% 5mm/min 10N	23/43	MPa	604
Compression modulus	5mm/min 10N	3400	MPa	604
Impact strength (Charpy)	Max. 7,5J	N.B.	kJ/m²	179-1eU
Notched impact strength (Charpy)	Max. 7,5J	4	kJ/m²	179-1eA
Ball indentation hardness	-	253	MPa	2039-1

Thermal Properties	Parameter	Value	Unit	DIN/EN/ISO
Glass transition temperature	-	150	°C	53765
Melting temperature	-	341	°C	53765
Heat distortion temperature	HDT, Method A	162	°C	ISO-R 75 Method A
Service temperature	Short term	300	°C	-
Service temperature	Long term	260	°C	-
Thermal expansion (CLTE)	23-60°C, Long	5	$10^{-5}K^{-1}$	11359-1;2
Thermal expansion (CLTE)	23-100°C, Long	5	$10^{-5}K^{-1}$	11359-1;2
Thermal expansion (CLTE)	100-150°C, Long	7	$10^{-5}K^{-1}$	11359-1;2
Specific heat	-	1.1	J/(g*K)	22007-4:2008
Thermal conductivity	-	0.27	W/(K*m)	22007-4:2008

Electrical properties	Parameter	Value	Unit	DIN/IEC
Surface resistance	-	10^{14}	Ω	60093

Other properties	Parameter	Value	Unit	DIN/EN/ISO/IEC
Water absorption	24h/96h (23°C)	0.02/0.03	%	62
Resistance to hot water/bases	-	+	-	-
Resistance to weathering	-	-	-	-
Flammability (UL94)	Listed (value @ 1,5mm)	V0	-	60695-11-10
FDA Approved	-	Yes	-	-

Direct Plastics Ltd. Unit 14 Portland Business Park, Richmond Park Road, Sheffield, S13 8HS
Tel: 0114 2560889 Email: sales@directplastics.co.uk

The following information corresponds with our current knowledge and indicates our products and possible applications. We cannot give a legally binding guarantee of certain properties or the suitability for a specific application. Existing commercial patents must be observed. A definitive quality guarantee is given in our generalconditions of sales.
Unless otherwise stated, these values represent averages taken from injection moulding samples.
We reserve the right of technical alterations.

TECHNICAL DATA

TENCATE ADVANCED COMPOSITES

TenCate E722

Mid temperature curing modified epoxy component prepreg

PRODUCT TYPE

120°C (248°F) cure

Toughened epoxy resin system

TYPICAL APPLICATIONS

- Motor racing
- Marine industries
- General aircraft fittings
- Sporting equipment
- Wide range of engineering applications

SHELF LIFE

Out life
60 days at @ 20°C (68°F)

Storage life
12 months @ -18°C (0°F)

Out life is the maximum time allowed at room temperature before cure.

To avoid moisture condensation:
Following removal from cold storage, allow the prepreg to reach room temperature before opening the polythene bag. Typically the thaw time for a full roll of material will be 4 to 6 hours.

PRODUCT DESCRIPTION

TenCate E722 is a toughened epoxy resin system for cures at 120°C (248°F), pre-impregnated into high performance fibres such as carbon, glass and aramid. It is designed for structural applications in the motor racing and marine industries. TenCate E722 would also suit general aircraft fittings, sporting equipment, and a wide range of engineering applications. TenCate E722 is compatible for co-cure with TenCate EF72, a 120°C (248°F) cure resin film and TenCate Amlite SC72A syntactic core.

TENCATE E722 PRODUCT BENEFITS/FEATURES

- Excellent drapeability – complex shapes easily formed
- Good surface finish
- Medium tack level – easily laminates to mould surface
- Low volatile content – no solvents used during processing
- 60 day shelf life at ambient temperature
- Autoclave, vacuum bag or press curable

TYPICAL NEAT RESIN PROPERTIES

Density .....1.21 g/cm^3 (75.5 lbs/ft^3) at 23°C (73.4°F)
Tg (DMTA) after 1 hour @ 120°C (248°F).....Onset: 120°C (248°F); Peak tan δ: 138°C (280°F)

TYPICAL LAMINATE PROPERTIES

HS0838 – CARBON 205 GSM 2X2 TWILL TR30S T 3K - 0/90° CONFIGURATION WOVEN LAMINATES

Property	Condition	Method	Results	
Tensile Strength (Warp)	RTD	ISO 527-4	595 MPa	86 ksi
Tensile Modulus (Warp)	RTD	ISO 527-4	56.1 GPa	8.1 Msi
Poisson's Ratio (Warp)	RTD	ISO 527-4	0.04	
Tensile Strength (Weft)	RTD	ISO 527-4	580 MPa	84 ksi
Tensile Modulus (Weft)	RTD	ISO 527-4	52.4 GPa	7.6 Msi
Poisson's Ratio (Weft)	RTD	ISO 527-4	0.04	
In Plane Shear Strength	RTD	EN 6031	112 MPa	16 ksi
In Plane Shear Modulus	RTD	EN 6031	3.57 GPa	0.5 Msi
Poisson's Ratio	RTD	EN 6031	0.8	
Compression Strength (Warp)	RTD	EN 2850	567 MPa	82 ksi
Compression Modulus (Warp)	RTD	EN 2850	52.5 GPa	7.6 Msi
Compression Strength (Weft)	RTD	EN 2850	563 MPa	82 ksi
Compression Modulus (Weft)	RTD	EN 2850	49.4 GPa	7.2 Msi
ILSS (Warp)	RTD	ISO 14130	68.1 MPa	10 ksi
ILSS (Weft)	RTD	ISO 14130	68.7 MPa	10 ksi

* Cured 1 hour at 120°C (248°F) at 50% Vf.

PRODUCT DATA SHEET

TENCATE ADVANCED COMPOSITES

TenCate Cetex® TC1200
PEEK Resin System

PRODUCT TYPE
Polyetheretherketone (PEEK)
Thermoplastic Resin System

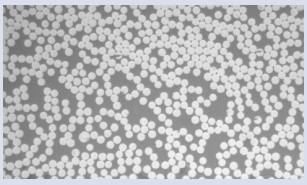
SERVICE TEMPERATURE
Approximately 250°F (121°C)

FEATURES
- Ambient temperature storage
- Flame retardant
- Low moisture absorption
- Good impact resistance
- 3-5 minute thermoforming cycles
- Excellent structural performance
- Outstanding solvent resistance
- Very low void content (<1%)

TYPICAL APPLICATIONS
- Primary Aircraft Structure
- Secondary Aircraft Structure
- Access Panels, Rib Stiffeners, Brackets, Conduit, Flooring

Tg ..... 290°F (143°C)
Tm ..... 649°F (343°C)

PROCESSING OPTIONS
Press,Thermoform,
in-situ ATL or Autoclave



Very low void content, 500x view of single ply Cetex UD prepreg, as produced, without further consolidation. Average void level of <0.2% with even fiber and resin distribution.

PRODUCT DESCRIPTION

TenCate Cetex® TC1200 is a semi-crystalline polyetheretherketone thermoplastic composite available in fabric and unitape form. It offers excellent resistance to chemicals and solvents, is flame retardant and combines outstanding toughness with high temperature performance. TenCate Cetex® TC1200 unitapes are offered with standard or intermediate modulus carbon fiber or S-2 glass fiber. TenCate Cetex TC1200 has a very low void content (<1%). Typical carbon unitape width offered is standard six inch (75 mm) widths with optional 12 inch (305 mm) widths offered too. Alternative narrower slit widths for ATL processing may be available through secondary slitting.

MECHANICAL PROPERTIES - CETEX TC1200 PEEK AS-4

Data generated on AS-4, 146 gsm FAW, resin content of 34% by weight, 59% fiber by volume. Prepreg areal weight 218 gsm.

Property	Condition	Test Method	Result	
Tensile Strength (0°)	RTD	ASTM D3039	330 ksi	2280 MPa
Tensile Modulus (0°)	RTD	ASTM D3039	18.9 Msi	130 GPa
Poisson's Ratio	RTD	ASTM D3039	0.33	
Tensile Strength (90°)	RTD	ASTM D3039	12.5 ksi	86 MPa
Tensile Modulus (90°)	RTD	ASTM D3039	1.4 Msi	10 GPa
Compressive Strength (0°)	RTD	ASTM D6641	188 ksi	1300 MPa
Compressive Modulus (0°)	RTD	ASTM D6641	18 Msi	124 GPa
Compressive Strength (0°)	ETW [1]	ASTM D6641	176 ksi	1210 MPa
Compressive Modulus (0°)	ETW	ASTM D6641	17.6 Msi	121 GPa
In-Plane Shear Strength (±45°)	RTD	ASTM D3518	22 ksi	152 MPa
In-Plane Shear Modulus (±45°)	RTD	ASTM D3518	0.75 Msi	5.2 GPa
Flexural Strength (90°)	RTD	ASTM D7264	22.0 ksi	152 MPa
Interlaminar Shear Strength (SBS) 0°/ 90°	RTD	ASTM D2344	13.7 ksi	94 MPa
Interlaminar Shear Strength (SBS) 0°/ 90°	ETW	ASTM D2344	11.2 ksi	77 MPa
Open Hole Tensile Strength	RTD	ASTM D5766	56.1 ksi	387 MPa
Open Hole Compressive Strength	RTD	ASTM D6484	46.4 ksi	320 MPa

[1] ETW is tested at 180°F/82°C after 14 day soaks in 160°F/71°C water.

Issue Date 31/05/17

Metallisation
Thermal spray equipment and consumables

01E ALUMINIUM (1050A/1350)

Material Data Sheet

Introduction
This data sheet is offered as guidance for our standard range of products. Additional product variants and technical information, Including MSDS sheets, are available from Metallisation

Related Specifications

BS EN 573-3:2013, EN AW-1050A/1350, ISO 209:2007(E), BS EN ISO 14919:2015
AWS C2.25/C2.25M:2012

Typical Composition

Typical composition of material given by % weight.

Element	Minimum	Maximum
Aluminium	99.5	0
Fe	0	0.4
Si	0	0.1
B	0	0.05
Cu	0	0.02
Mg	0	0.05
Zn	0	0.05
Ga	0	0.03
Cr	0	0.01
Mn	0	0.01
V + Ti	0	0.02
Others Each	0	0.03
Others Total	0	0.10

Packaging Form

Packaging	Weight (Kg)	Tolerance (Kg)
Coil	25KG	+/-2KG
MIG (D300)	6KG/10KG	+/-0KG
Spools (H390)	7KG	+/-0.5KG
Drum (Fibreboard)	60KG	+/-0KG

Metallisation Ltd., Peartree Lane, Dudley, West Midlands, DY2 0XH, UK
Tel: +44 (0)1384 252464 Fax: +44 (0)1384 237196
Visit our website at www.metallisation.com
Registered in England No. 270156. Registered office: Peartree Lane, Dudley, DY2 0XH
QSD 4/6/3

Appendix B

Comparing contact and non-contact profilometry

B.1 Introduction

When comparing roughness results obtained through physical (stylus) and optical (focus variation microscopy) methods significant differences in roughness were observed. This short appendix demonstrates this disparity; explains its origin; and shows how to account for it.

B.2 Experimental method

B.2.1 Materials

The experiment was conducted on cured E722 CF-epoxy laminate prepared in three different ways, as received, lightly grit-blasted (LGB) and heavily grit-blasted (LGB). The material and different preparations are described in detail in chapter 3 and 6.

B.2.2 Methods

Long line scans of the surface topography were taken with optical methods using focus variation microscopy (Alicona Infinite Focus) and contact stylus methods (Taylor Hobson Form Talysurf 40). The techniques were used to measure the same locations on each substrate, the samples were then gold sputter coated and the locations re-measured using the optical method. In practice placing the stylus accurately was very difficult so the locations measured with this method were not identical (though close) to those

measured with the optical method. The locational accuracy of the optical method was very good so the areas measured before and after coating are identical.

B.3 Results and Discussion

The results show that the average Ra measured with the optical method (prior to sputter coating) is significantly greater than that measured with the contact method for the as received substrate (figure B.1). For roughened samples there are no significant differences between the average results as shown in figure B.2 and figure B.3 for LGB and HGB respectively. The cause of the increased Ra measurement on the as received (smooth) sample becomes clear when interrogating a false colour height image of the sample with the FVM as shown in figure B.4 (top). The topography of fibres is clearly present below in the image, more that would be expected if their pattern was simply being followed by the overlying resin surface. This indicates that the FVM system is looking though the smooth semi-transparent top resin layer to the rougher carbon fibres below and defining this as the surface. Sputter coating the sample reduces the transparency of the substrate figure B.4 (bottom) and thus reduces the measured roughness bringing it nearer to the value measured with the contact method. Roughening the substrate has a similar effect and thus the LGB/HGB show negligible difference in results obtained by the different methods. This is also seen by interrogating the false colour images of the LGB before and after sputter coating.

B.4 Conclusions

- FVM can overestimate the roughness of the FRP by 'seeing through' the smooth resin to the underlying fibres.
- Roughened substrates to not experience this problem
- Sputter coating the substrate prior to measurement mitigates this problem for smooth substrates

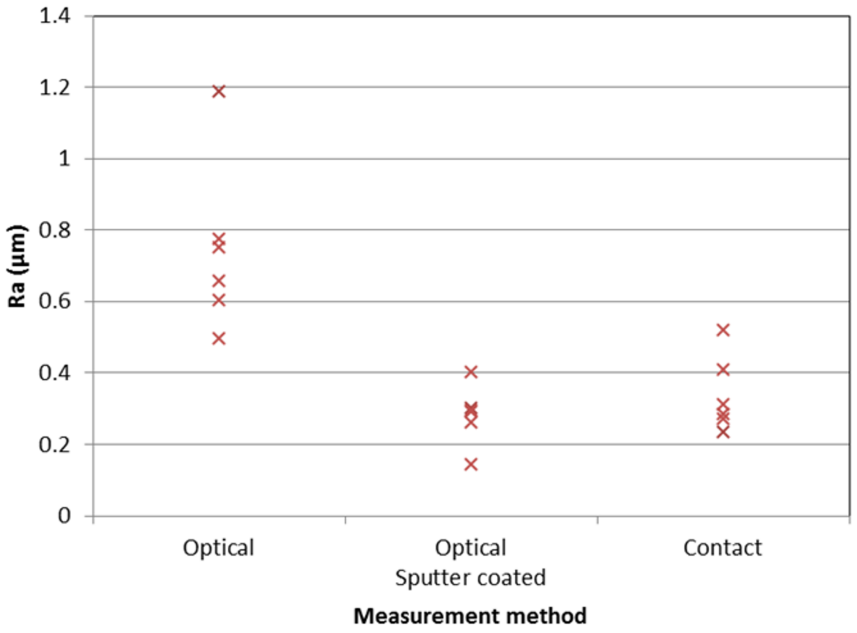


Figure B.1: Plot showing repeated Ra measurements taken on a single (as received) CF-epoxy sample with different methods indicating that the optical method gives significantly higher roughness values than other methods

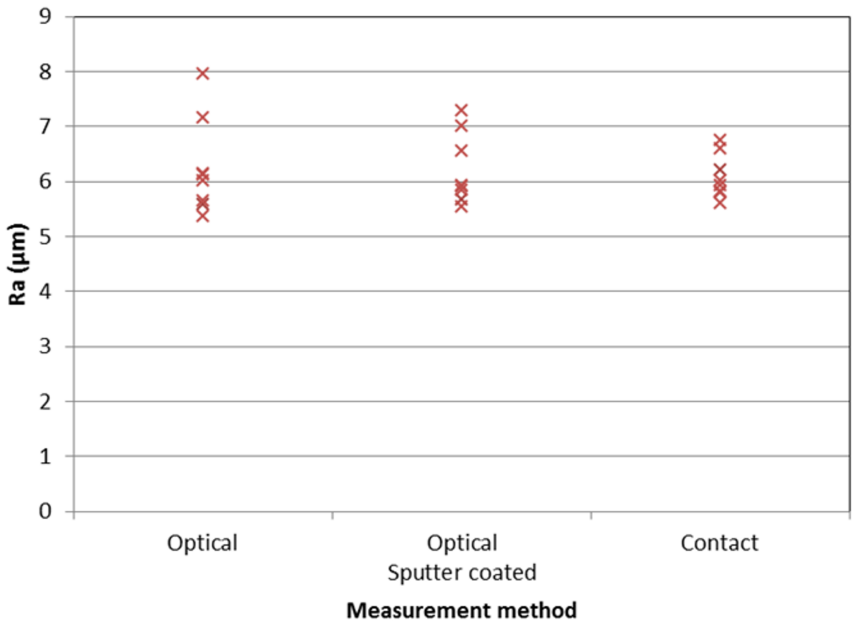


Figure B.2: Plot showing repeated Ra measurements taken on a single (LGB) CF-epoxy sample with different methods indicating that the optical method gives broadly the same measurement as other methods

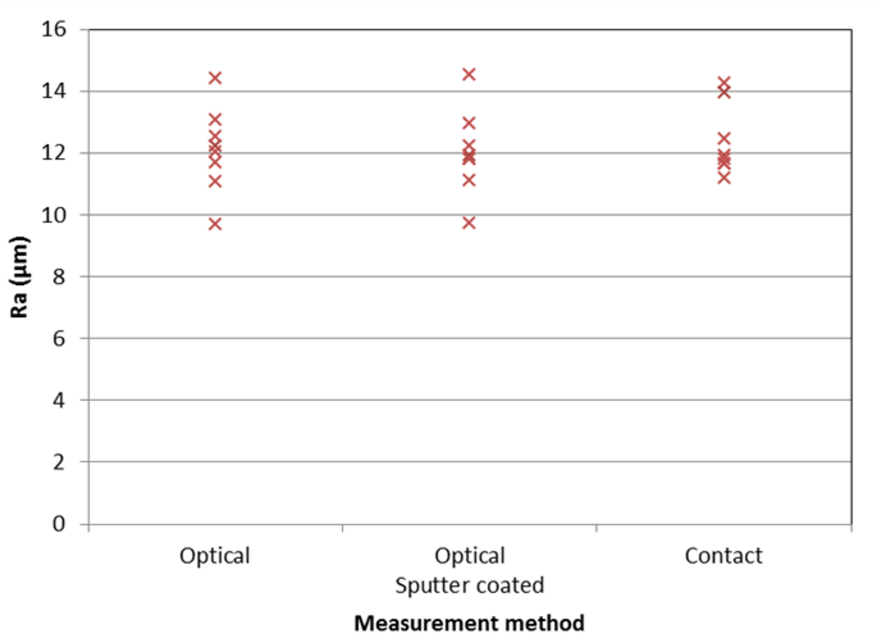


Figure B.3: Plot showing repeated Ra measurements taken on a single (HGB) CF-epoxy sample with different methods indicating that the optical method gives broadly the same measurement as other methods

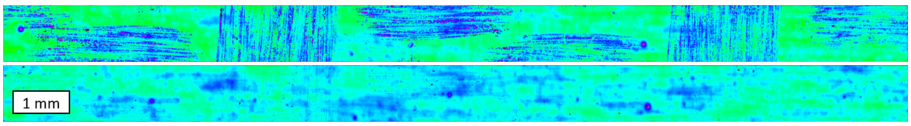


Figure B.4: False colour height images of as received CF-epoxy, the images are at same scale and location before (top) and after (bottom) sputter coating

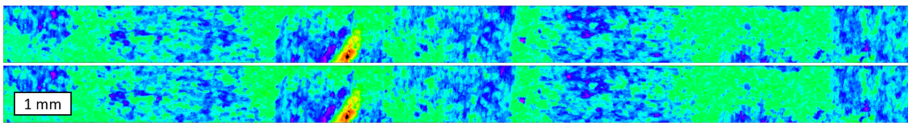


Figure B.5: False colour height images of LGB CF-epoxy, the images are at same scale and location before (top) and after (bottom) sputter coating

Appendix C

TWAS onto CF-epoxy composite

C.1 Introduction

This short appendix discusses some observations during a short package of initial work. It was carried out using twin wire arc spray (TWAS) to deposit aluminium onto prepared CF-epoxy substrates. The work it presented here so that reference can be made to it within the thesis.

C.2 Experimental method

Coatings were deposited onto a cured E722 CF-epoxy laminate at different stand-off distances. The samples were grit-blasted with the LGB settings prior to spraying. The samples were sprayed using a metallisation 528 TWAS gun with metallisation 01E aluminium feedstock. The spraying parameters used are not disclosed here, but they were consistent throughout and typical for the gun model with this feedstock.

C.3 Results

None of the stand-off distances gave well adhered coherent coatings (figure C.1). Instead aluminium preferentially deposited at the areas with carbon fibres exposed. Increasing the stand-off distance seemed to increase the coherence of the coatings up until a stand-off distance of around 260 - 300 mm. Although these coatings were relatively coherent they possessed very low adhesion, evidenced by the fact they were starting to peel from

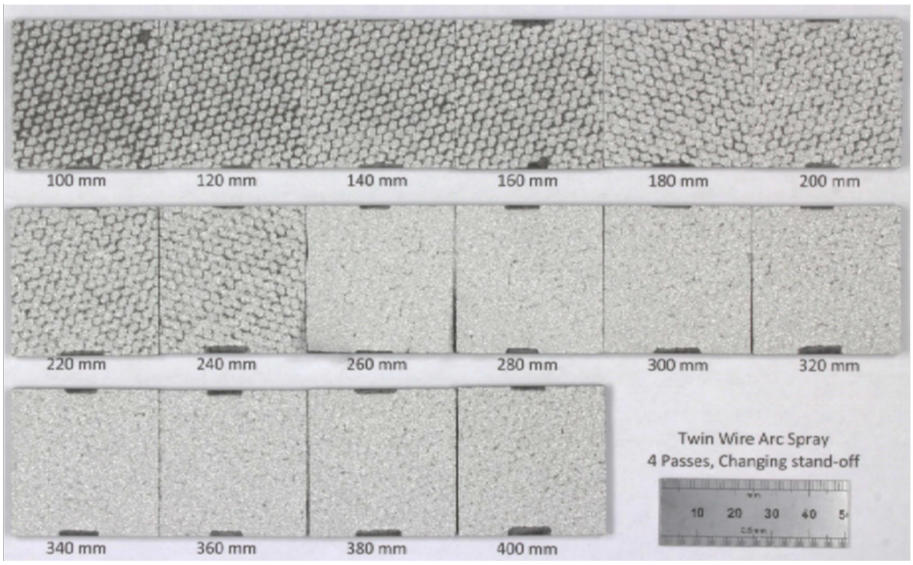


Figure C.1: Photographs of lightly grit-blasted CF-epoxy compostes (Tencate E722) sprayed with TWAS Al (4 passes) showing how coating has preferentially deposited on the fibre regions

the substrate. At a stand-off distance greater than 300 mm the coherence of the coatings appears to start to reduce slightly.